



HAL
open science

Modeling and simulation of droplets growing on patterned substrates during dropwise condensation

Solmaz Boroomandi Barati

► **To cite this version:**

Solmaz Boroomandi Barati. Modeling and simulation of droplets growing on patterned substrates during dropwise condensation. Other. Université de Lyon, 2018. English. NNT : 2018LYSEM018 . tel-02861062

HAL Id: tel-02861062

<https://theses.hal.science/tel-02861062>

Submitted on 8 Jun 2020

HAL is a multi-disciplinary open access archive for the deposit and dissemination of scientific research documents, whether they are published or not. The documents may come from teaching and research institutions in France or abroad, or from public or private research centers.

L'archive ouverte pluridisciplinaire **HAL**, est destinée au dépôt et à la diffusion de documents scientifiques de niveau recherche, publiés ou non, émanant des établissements d'enseignement et de recherche français ou étrangers, des laboratoires publics ou privés.



N°d'ordre NNT : 2018LYSEM018

THESE de DOCTORAT DE L'UNIVERSITE DE LYON
opérée au sein de
MINES Saint-Etienne

Ecole Doctorale N° 488
Sciences, Ingénierie, Santé

Spécialité de doctorat : IMAGE, VISION, SIGNAL

Soutenue publiquement le 09/10/2018, par :
(Boroomandi-Barati Solmaz)

**Modeling and simulation of
dropwise condensation on textured surfaces**

Devant le jury composé de :

Président : Gruy, Frédéric

Harmand, Souad	Professeur, Université Valenciennes	Rapporteure
Mongruel, Anne	Maître de conférence, Sorbonne Université	Rapporteure
Gruy, Frédéric	Professeur, Mines Saint-Etienne	Examineur
Pupier, Christophe	R&D, Institut de Recherches En Ingénierie des Surfaces (groupe HEF)	Examineur
Gavet, Yann	Maître-Assistant, Mines Saint-Etienne	Directeur de thèse
Pinoli, Jean-Charles	Professeur, Mines Saint-Etienne	Co-directeur de thèse
Valette, Stéphane	Maître de conférence, École centrale Lyon	Co-directeur de thèse

Spécialités doctorales
 SCIENCES ET GENIE DES MATERIAUX
 MECANIQUE ET INGENIERIE
 GENIE DES PROCEDES
 SCIENCES DE LA TERRE
 SCIENCES ET GENIE DE L'ENVIRONNEMENT

Responsables :
 K. Wolski Directeur de recherche
 S. Drapier, professeur
 F. Gruy, Maître de recherche
 B. Guy, Directeur de recherche
 D. Graillot, Directeur de recherche

Spécialités doctorales
 MATHEMATIQUES APPLIQUEES
 INFORMATIQUE
 SCIENCES DES IMAGES ET DES FORMES
 GENIE INDUSTRIEL
 MICROELECTRONIQUE

Responsables
 O. Roustant, Maître-assistant
 O. Boissier, Professeur
 JC. Pinoli, Professeur
 N. Absi, Maître de recherche
 Ph. Lalevée, Professeur

EMSE : Enseignants-chercheurs et chercheurs autorisés à diriger des thèses de doctorat (titulaires d'un doctorat d'État ou d'une HDR)

ABSI	Nabil	MR	Génie industriel	CMP
AUGUSTO	Vincent	CR	Image, Vision, Signal	CIS
AVRIL	Stéphane	PR2	Mécanique et ingénierie	CIS
BADEL	Pierre	MA(MDC)	Mécanique et ingénierie	CIS
BALBO	Flavien	PR2	Informatique	FAYOL
BASSEREAU	Jean-François	PR	Sciences et génie des matériaux	SMS
BATTON-HUBERT	Mireille	PR2	Sciences et génie de l'environnement	FAYOL
BEIGBEDER	Michel	MA(MDC)	Informatique	FAYOL
BLAYAC	Sylvain	MA(MDC)	Microélectronique	CMP
BOISSIER	Olivier	PR1	Informatique	FAYOL
BONNEFOY	Olivier	MA(MDC)	Génie des Procédés	SPIN
BORBELY	Andras	MR(DR2)	Sciences et génie des matériaux	SMS
BOUCHER	Xavier	PR2	Génie Industriel	FAYOL
BRODHAG	Christian	DR	Sciences et génie de l'environnement	FAYOL
BRUCHON	Julien	MA(MDC)	Mécanique et ingénierie	SMS
CAMEIRAO	Ana	MA(MDC)	Génie des Procédés	SPIN
CHRISTIEN	Frédéric	PR	Science et génie des matériaux	SMS
DAUZERE-PERES	Stéphane	PR1	Génie Industriel	CMP
DEBAYLE	Johan	MR	Sciences des Images et des Formes	SPIN
DEGEORGE	Jean-Michel	MA(MDC)	Génie industriel	Fayol
DELAFOSSÉ	David	PR0	Sciences et génie des matériaux	SMS
DELORME	Xavier	MA(MDC)	Génie industriel	FAYOL
DESRAYAUD	Christophe	PR1	Mécanique et ingénierie	SMS
DJENIZIAN	Thierry	PR	Science et génie des matériaux	CMP
DOUCE	Sandrine	PR2	Sciences de gestion	FAYOL
DRAPIER	Sylvain	PR1	Mécanique et ingénierie	SMS
FAUCHEU	Jenny	MA(MDC)	Sciences et génie des matériaux	SMS
FAVERGEON	Loïc	CR	Génie des Procédés	SPIN
FEILLET	Dominique	PR1	Génie Industriel	CMP
FOREST	Valérie	MA(MDC)	Génie des Procédés	CIS
FRACZKIEWICZ	Anna	DR	Sciences et génie des matériaux	SMS
GARCIA	Daniel	MR(DR2)	Sciences de la Terre	SPIN
GAVET	Yann	MA(MDC)	Sciences des Images et des Formes	SPIN
GERINGER	Jean	MA(MDC)	Sciences et génie des matériaux	CIS
GOEURIOT	Dominique	DR	Sciences et génie des matériaux	SMS
GONDRAN	Natacha	MA(MDC)	Sciences et génie de l'environnement	FAYOL
GONZALEZ FELIU	Jesus	MA(MDC)	Sciences économiques	FAYOL
GRAILLOT	Didier	DR	Sciences et génie de l'environnement	SPIN
GROSSEAU	Philippe	DR	Génie des Procédés	SPIN
GRUY	Frédéric	PR1	Génie des Procédés	SPIN
GUY	Bernard	DR	Sciences de la Terre	SPIN
HAN	Woo-Suck	MR	Mécanique et ingénierie	SMS
HERRI	Jean Michel	PR1	Génie des Procédés	SPIN
KERMOUCHE	Guillaume	PR2	Mécanique et Ingénierie	SMS
KLOCKER	Helmut	DR	Sciences et génie des matériaux	SMS
LAFORÉST	Valérie	MR(DR2)	Sciences et génie de l'environnement	FAYOL
LERICHE	Rodolphe	CR	Mécanique et ingénierie	FAYOL
MALLIARAS	Georges	PR1	Microélectronique	CMP
MOLIMARD	Jérôme	PR2	Mécanique et ingénierie	CIS
MOUTTE	Jacques	CR	Génie des Procédés	SPIN
NEUBERT	Gilles			FAYOL
NIKOLOVSKI	Jean-Pierre	Ingénieur de recherche	Mécanique et ingénierie	CMP
NORTIER	Patrice	PR1	Génie des Procédés	SPIN
O CONNOR	Rodney Philip	MA(MDC)	Microélectronique	CMP
OWENS	Rosin	MA(MDC)	Microélectronique	CMP
PERES	Véronique	MR	Génie des Procédés	SPIN
PICARD	Gauthier	MA(MDC)	Informatique	FAYOL
PIJOLAT	Christophe	PR0	Génie des Procédés	SPIN
PINOLI	Jean Charles	PR0	Sciences des Images et des Formes	SPIN
POURCHEZ	Jérémy	MR	Génie des Procédés	CIS
ROUSSY	Agnès	MA(MDC)	Microélectronique	CMP
ROUSTANT	Olivier	MA(MDC)	Mathématiques appliquées	FAYOL
SANAUR	Sébastien	MA(MDC)	Microélectronique	CMP
STOLARZ	Jacques	CR	Sciences et génie des matériaux	SMS
TRIA	Assia	Ingénieur de recherche	Microélectronique	CMP
VALDIVIESO	François	PR2	Sciences et génie des matériaux	SMS
VIRICELLE	Jean Paul	DR	Génie des Procédés	SPIN
WOLSKI	Krzysztof	DR	Sciences et génie des matériaux	SMS
XIE	Xiaolan	PR0	Génie industriel	CIS
YUGMA	Gallian	CR	Génie industriel	CMP

Contents

Acknowledgement	xii
List of publications	xiii
Summary	1
Résumé	4
General introduction	6
0.1 General issue	6
0.2 Dropwise and filmwise condensation	8
0.2.1 Effect of topography	9
0.2.2 Effect of chemical coatings	10
0.3 Dropwise condensation	10
0.3.1 Droplets nucleation	11
0.3.2 Droplets growth	17
0.3.3 Steady state	17
0.4 Spatial distribution	18
0.4.1 Poisson point process and Matern hardcore	19
0.4.2 Ripley's function	20
0.4.3 Fry plot	23
0.5 Droplets temporal distribution	24
0.6 Droplets size distribution function	28
0.7 Algorithms for simulating dropwise condensation	33
0.8 The aim of this study	38
0.9 Conclusion	41
0.9.1 English	41
0.9.2 French	41
1 Experimental Procedure	42
1.1 Introduction	42
1.1.1 French	42
1.1.2 English	42
1.2 Experimental set-up	43
1.3 Surface preparation	44
1.4 Surface Characterization	46
1.4.1 Surface characterization of the metallic molds	50
1.4.2 Surface characterization of the polycarbonate samples	53
1.5 Statistical analysis of sinusoidal surface characteristics	62
1.6 Conclusion	68

1.6.1	English	68
1.6.2	French	68
2	Image processing method	69
2.1	Introduction	69
2.1.1	French	69
2.1.2	English	69
2.2	Image processing technique for the droplets on flat and sinusoidal surfaces	72
2.2.1	Preprocessing	72
2.2.2	Segmentation	72
2.2.3	Reconstruction	75
2.3	Image processing technique for the droplets on pillared surface	75
2.3.1	Pillar characterization	77
2.3.2	Image categorization	80
2.3.3	Drop identification	81
2.3.4	Algorithm verification	87
2.4	Conclusion	90
2.4.1	English	90
2.4.2	French	90
3	Modeling and simulation	91
3.1	Introduction	91
3.1.1	French	91
3.1.2	English	92
3.2	Model that considers droplets as spherical-caps	94
3.2.1	Initial nucleation	95
3.2.2	Adsorption	95
3.2.3	Coalescence	99
3.2.4	Nucleation of new droplets	101
3.2.5	Departure of big droplets	102
3.2.6	Drop-size distribution function	102
3.2.7	Algorithm for generating circular droplets on flat substrates	105
3.3	Model that considers droplets as ellipsoids	106
3.3.1	Adsorption	108
3.3.2	Coalescence	110
3.3.3	Algorithm for generating ellipsoidal droplets on pillared substrates	115
3.4	Model that considers droplets as semi-ellipsoids	117
3.4.1	Adsorption of semi-ellipsoidal droplets	119
3.4.2	Coalescence of semi-ellipsoidal droplets	122
3.4.3	Sliding of big droplets and equivalent radius	123
3.4.4	Surface area	123
3.4.5	Algorithm for generating semi-ellipsoidal droplets on sinusoidal substrates	124
3.5	Conclusion	125
3.5.1	English	125
3.5.2	French	125

4	Results and discussion	127
4.1	Summary	127
4.1.1	French	127
4.1.2	English	127
4.2	Results of the spherical-cap model on flat substrates	127
4.2.1	Droplets growth procedure	127
4.2.2	Droplets spatial distribution	130
4.2.3	Effect of wall temperature	131
4.2.4	Effect of initial nucleation site density	134
4.2.5	Drop-size distribution function	135
4.3	Results of the ellipsoidal model on pillared substrates	139
4.4	Results of the semi-ellipsoidal model on sinusoidal substrates	145
4.4.1	Droplets growth procedure	145
4.4.2	Droplets spatial distribution	152
4.5	Conclusion	155
4.5.1	English	155
4.5.2	French	159
	General conclusion	162
	Conclusion générale	165
	perspectives	168

List of Figures

1	(a) Spherical droplets on a flat substrate, (b) ellipsoidal droplets on a textured substrate.	2
2	Schematics of (a) a spherical-cap (b) an ellipsoid (contact angle with surface is 90°), and (c) a semi-ellipsoid (contact angle with surface is θ).	2
1	Light reflection because of droplets formation on the glassy substrates. This phenomenon can happen on the interior side of the car light shields at the foggy days and will reduce the efficiency of illumination.	6
2	Changes in contact angle and radius of the droplet during evaporation [1]. Stage I: the radius of droplet is constant while, its contact angle is decreasing. Stage II: the droplet becomes smaller in the same contact angle. Stage III: both the radius and contact angle decrease at the same time.	7
3	(A) Cassie-Baxter and (B) Wenzel droplets on textured surfaces (image from [2]).	9
4	Optical images of the nucleation and growth of water condensation on various super hydrophobic surface geometries [3].	13
5	Control of droplet coalescence by changing the geometrical features sizes [3].	14
6	Two methods for tessellation the surface of nucleation [4].(a) Voronoi diagram based on the distances to the bubbles' centers (red circles). One Voronoi cell with area A_{vor} associated with the bubble center marked as a filled red circle is shown. (b) Modified Voronoi diagram based on the distance to the bubbles' triple contact lines (pink lines). One modified Voronoi cell with area A associated with the bubble footprint (with area a) colored in pink is shown.	15
7	Effective parameters on the droplets nucleation density [5]. (a) Effect of contact angle without coating, (b) effect of coating layer thickness, (c) effect of contact angle on a coating with $\delta = 0.1\mu m$ and $\lambda = 0.25W/m.K$, (d) effect of thermal conductivity of the coating layer.	16
8	Changes of a specified parameter M during time. The blue level illustrates the amount or value M in the system. If this level does not change during time, the system is at steady state step.	18
9	The main idea of Ripley's function is to count the number of points that are in distance r from center.	21
10	Ripley's L function, the straight line represents the Ripley's L function of Poisson point process. Positive and negative deviations from this line indicate dispersion and clustering of the points.	22

11	(a) Conical and (b) cylindrical elements for K_{dir} function. Meaning that this cone or cylinder sweeps the area around a center point and detects the number of points in the sweeping area. Then, after 360° its radius increases by a small amount like ϵ [6].	22
12	An example of Fry plot with fitted an ellipsoid in the vacant zone at origin. Image from [7].	23
13	Comparison of three PDFs for a certain rain drops within $T = 600min$ and $\mu = 183drops/min$ [8]. The distribution of $P(X = k)$ depends on the shape of $f(\mu(t))$	25
14	The PDF of a Poisson and Poisson mixture distribution for rain drops compared with real observed data over $T = 900min$ and $t = 10min$ in [8].	26
15	Coalescence model of two droplets	32
16	Drop size distribution for condensation of saturated steam at $100^\circ C$ with $N_s = 5 \times 10^6 cm^{-2}$. A, $\Delta T = 1^\circ C$; B, $\Delta T = 4^\circ C$. broken line, experimental data [9].	34
17	Flow diagram of computer simulation used by Earl <i>et al.</i> to simulate droplet growth [10]	36
18	Flow diagram of computer simulation used by Burnside and Hadi to simulate droplet growth [11]	37
19	Comparison of drop distribution between random fractal model and photography. (a) random fractal model, (b) close-up photography of condensing surface [12]	38
20	Determination of P (probability of finding a droplet in a grid) [13]. P can be calculated as the fraction of area covered by the droplets at each instance.	39
21	Differences between shape of droplets on the flat and pillared surfaces, (a) spherical droplets growing on a flat surface, (b) elliptical droplets growing on a micrometric pillared surface. The small points in image (b) are the texturing patterns.	40
1.1	Illustration of experimental set up. (a) Top view, (b) Closer view of the humid chamber and CCD camera. The parts that are marked in (a) correspond to: 1) light for taking high quality images, 2) humid chamber, 3) gas inlet, 4) gas outlet 5) cold substrate, and 6) CCD camera, (c) schematic diagram of the whole system	44
1.2	Four main steps of dropwise condensation including: (a) initial nucleation, (b) growth due to adsorption, (c) growth due to coalescence and nucleation of new small droplets, and (d) departure of big droplets.	45
1.3	Illustration of the injection press system. (a) Polymer granulates, (b) metal mold (the small squares are the sinusoidal surfaces), (c) polymeric textured surfaces that will be used as substrates in dropwise condensation experiments.	46
1.4	Schematic illustration of pillars dimensions that are mentioned in table 1.1.	47
1.5	Optical microscope images of 6 polycarbonate pillared surfaces. The black points represents the pillars with radius and heights according to table 4.1. The size of the substrate in all these images is $3.2mm \times 2.7mm$	48

1.6	Optical microscope images of 6 examples of polycarbonate sinusoidal surfaces. The size of the substrate in all these images is $3.2mm \times 2.7mm$	49
1.7	SEM microscopic images (magnification $\times 311$) of the sinusoidal surfaces. λ and a here are the period and amplitude of the sinusoidal profiles.	51
1.8	Three dimensional images produces by the interferometric microscope. λ and a represent the period and amplitude of the sinusoidal profiles.	52
1.9	Two dimensional roughness profile of the configuration 30-5. This plot can be used to measure the roughness parameters	53
1.10	SEM microscopic images of the sinusoidal surfaces on polycarbonate samples. λ and a here are the period and amplitude of the sinusoidal profiles.	55
1.11	Three dimensional microscopic illustration of 6 pillared substrates with $50\times$ magnification. The colored bar on the right hand side of each image measures the height of the pillars. Meaning that each color on this bar corresponds to a value on μm , so for measuring the height of each pillar it is enough to find the value corresponds with the color of it's top head.	57
1.12	Illustration of two dimensional roughness profile of the six pillared substrates. At each graph, X is the distance between the pillars.	58
1.13	Illustration of two dimensional roughness profile of the six pillared substrates. At each graph, X and Z represent the radius and height of the pillars, respectively.	59
1.14	Illustration of contact angle measurement set-up. (a) the substrate support, (b) the syringe for injection water droplets on the substrate, (c) light source, and (d) the CCD camera that acquires images of droplets sited on the substrate.	61
1.15	Contact angle of droplets on sinusoidal surfaces. λ and a being the period and amplitude of the sinusoidal profiles. In this images the sinusoidal profiles are perpendicular to the base lines of the droplets.	63
1.16	Pareto charts of the effects of λ and a on (a) θ and (b) R_a	65
1.17	Residual plots of θ at $\alpha = 0.05$	67
1.18	Residual plots of R_a at $\alpha = 0.05$	67
2.1	Droplets on the (a) flat and (b) sinusoidal substrates are distinguishable from the substrates. Due to similarity between the images on the flat and sinusoidal substrates, the same segmentation algorithm is used for the images of these two kinds of substrates.	71
2.2	(a) A pillared surface without droplets. (b) Adsorbing and (c) coalescing droplets on the same pillared substrate. The droplets are not easily detectable from the pillars so a more complicated image processing technique is required.	73
2.3	Image pretreatment by Laplacian filtering. (a) Original image, (b) filtered image	74
2.4	Reconstruction step. (a) Binarized image before reconstruction, (b) Distance map, (c) Watershed partitioned image, (d) Binarized image after reconstruction	76

2.5	The segmented images of droplets growing on the flat substrate at different time steps ($t = 10, 300, 700, 5000$ s). These time steps correspond to initial nucleation, adsorption, coalescence, and steady state steps.	77
2.6	Schematic diagram of the image processing algorithm on pillared substrate	78
2.7	Algorithm for pillar characterization	79
2.8	Equivalent circle determination	80
2.9	The changes in number of the major peaks in gray-tone histograms on time. Since the size of droplets is changing, the gray-tone histograms shows different number of peaks at different time steps. Based on the number of these peaks we can categorize the droplets in the four categories: very small, small, medium, and big droplets.	81
2.10	Intensity histogram of (a) very small droplets at $t = 100$ s, (b) small droplets at $t = 200$ s, (c) medium droplets at $t = 500$ s and (d) big droplets drops at $t = 1500$ s.	81
2.11	Image of very small drops on a pillared surface.	82
2.12	Algorithm for very small drops.	83
2.13	Image of small drops on a pillared surface.	84
2.14	Algorithm for small drops.	84
2.15	Image of medium drops on a pillared image.	85
2.16	Algorithm for medium drops.	86
2.17	Image of big drops on a pillared image.	87
2.18	Algorithm for big drops.	88
2.19	Schematic diagram of parameters using for algorithm validation. The blue solid circle represents the real droplets captured in the original image and the red dashed circle is the droplet detected by the image processing algorithm. Therefore, TP represents the part of the real droplet that is detected by the algorithm, FP is the part detected falsely by the algorithm, FN shows the part which is not detected by the algorithm but presents in the initial image, and TN is the part that is not detected by the algorithm and dose not present in the original image.	89
3.1	(a) Spherical droplets on a flat substrate, (b) ellipsoidal droplets on a textured substrate.	93
3.2	A spherical cap is a part of a sphere that is cut by a plain with distance h from the center of sphere and its contact angle with surface is not equal to 90°	94
3.3	(a) Nucleation of the initial droplets that is completely randomly based on Poisson point process. (b) Ripley's L function corresponding to this image is the same as Ripley's L function of Poisson point process ($F(x) = x$).	95
3.4	There are two main heat transfer resistances through a droplet: conduction resistance ($R_{Conduction}$) and convection resistance ($R_{Convection}$).	96
3.5	Thickness of boundary layer d_t at each point P of a sphere with temperature T_s that is immersed in a fluid of temperature T_∞ depends on the angle between P and the bottom of the sphere φ	99
3.6	Multiple coalescence: two big droplets adsorb each other and swallow the small droplets in their between.	101

3.7	Probability density function (PDF) of number of droplets in each size range at three time steps: (a) $t = 200s$, (b) $t = 2500s$, (c) $t = 5000s$	102
3.8	Schematic diagram of the simulation algorithm for generating circular droplets on flat substrate	107
3.9	Comparison between the shape of small and big droplets on a pillared substrate. Small droplets tend to form more elliptical shapes due to adhesion with surface texturing, while big droplets present more spherical shapes in order to occupy less surface. The size of the image is $3.3mm \times 2.7mm$	108
3.10	Schematic of (a) spherical droplets and (b) ellipsoidal droplets in two planes (X - Y) and (X - Z) and their corresponding equations.	109
3.11	(a) The difference between approaching two spherical droplets <i>v.s</i> two ellipsoidal droplets, (b) intersection of two touching ellipsoidal droplets.	111
3.12	Two ellipsoidal droplets approaching on the space between two pillars. For checking coalescence between these two droplets we can verify the existence of intersection between their projected images on each planes X - Y , X - Z and Y - Z . But, this calculation is done if the three dimensional Euclidean distance between the ellipsoids is inferior than the summation of their maximum sizes.	112
3.13	Images of the real droplets growing on a pillared substrate at $t = 100, 200, 400, 800$. Two example zones are highlighted in these images that consist of droplets in touch with pillars. It can be seen that if a droplet touches a pillar, they will stay in touch till the end of process.	114
3.14	Schematic diagram of the simulation algorithm for generating ellipsoidal droplets on pillared substrate	116
3.15	(a) An ellipsoid (contact angle with surface is 90°), (b) a semi-ellipsoid (contact angle with surface is θ). On theory we consider that the semi-ellipsoid is cut of from the head of an ellipsoid.	117
3.16	Semi-ellipsoid with contact angle θ is cut of from a bigger ellipsoid by angle γ and height h	118
3.17	Sinusoidal surface parameters.	124
3.18	Schematic diagram of the simulation algorithm for generating semi-ellipsoidal droplets on sinusoidal substrates.	126
4.1	The evolution of the droplets during dropwise condensation at different time steps ($t = 10 s$ (initial nucleation), $100 s$ (growth due to adsorption), $700 s$ (growth due to coalescence), $5000 s$ (steady state)). (a) Binarized images of experimental results, (b) Results from simulation algorithm.	129
4.2	Changes in (a) droplet size and (b) droplets density during process time for simulation and experiments. The first vertical lines indicate the time that almost the rate of changes in radius and density are lowered (due to opposite effects of coalescence and nucleation of new droplets) and the second lines are the starting time of the steady state step.	130
4.3	Comparison between Ripley's L functions of droplets at steady state relevant to the Poisson point process, experiments and simulation	131
4.4	Average heat transfer coefficient <i>v.s</i> average size of droplets	132
4.5	Minimum size of droplets that are able to grow <i>v.s</i> wall temperature	133

4.6	Evolution of average heat transfer coefficient and total heat flux v.s wall temperature	133
4.7	Percentage of surface coverage at different times.	134
4.8	(a) Droplets size and (b) droplets densities during progress time for different initial nucleation site densities	135
4.9	Surface coverage for different nucleation site densities v.s time	136
4.10	The results of the three models (Rose, Abu-Orabi and empirical models) versus experimental data at different time intervals of adsorption step ($t = 10, 30, 50 s$). The empirical and the Rose models are able to predict the size distribution function of adsorbing and coalescing droplets respectively, while the model of Abu-Orabi is far from the experimental data at earlier stages.	137
4.11	The results of the three models (Rose, Abu-Orabi and empirical models) versus experimental data at different time intervals of adsorption step ($t = 100, 300, 500 s$). The empirical and the Rose models are able to predict the size distribution function of adsorbing and coalescing droplets respectively, while the model of Abu-Orabi is far from the experimental data at earlier stages.	138
4.12	The results of the three models (Rose, Abu-Orabi and empirical models) versus simulation data at $t = 10s$ for 4 different initial nucleation densities.	139
4.13	The results of the three models (Rose, Abu-Orabi and empirical models) versus simulation data at $t = 10s$ for 4 different substrate temperature.	140
4.14	Illustration of 6 pillared surfaces after 1800s. The size of the substrate at each image is $3.3mm \times 2.7mm$	141
4.15	Comparison between growth rate of experimental and simulation droplets on 6 different pillared surfaces.	143
4.16	Comparing the changes in droplets density between experimental and simulation droplets on 6 different pillared surfaces.	144
4.17	Illustration of 6 sinusoidal surfaces at adsorption stage (around $t = 10s$).	147
4.18	Illustration of 6 sinusoidal surfaces at coalescence stage (around $t = 1800s$).	148
4.19	Illustration of 6 sinusoidal surfaces at steady state (around $t = 8000s$).	149
4.20	Comparison between growth rate of experimental and simulation droplets on 6 different sinusoidal surfaces	150
4.21	Comparison between density of experimental and simulation droplets on 6 different sinusoidal surfaces	151
4.22	The evolution of droplets size measured by spherical-cap model and ellipsoidal cap model on 6 different sinusoidal surfaces compared to experimental results	153
4.23	The evolution of droplets density measured by spherical-cap model and ellipsoidal cap model on 6 different sinusoidal surfaces compared to experimental results	154
4.24	Fry plot of droplets spatial distribution on sinusoidal substrates at $t = 1800s$	156
4.25	Zoomed on the origin of Fry plot of droplets spatial distribution on sinusoidal substrates.	157
4.26	Ripley's K_{dir} function of droplets spatial distribution on sinusoidal substrates	158

List of Tables

1.1	Size and distance between the pillars of each substrate. r_t represents the theoretical radius of pillars, d_t is the theoretical center to center distance between the pillars, and h_t is the theoretical height of pillars.	47
1.2	Characteristics of each sinusoidal surface. λ and a being the period and amplitude of the sinusoidal profiles.	47
1.3	Roughness parameters of each sinusoidal surface on the metallic molds. $\lambda(\mu m)$ and $a(\mu m)$ denote the period and amplitude of the sinusoidal profiles respectively, R_a is the average roughness, while $R_t = R_p - R_v$ is the maximum amplitude of the sinusoidal profile and R_z is the average of R_t on the surface. R_q in this table represents root mean square of the roughness profile and finally, E_{ave} here is the average error between R_z and a	54
1.4	Roughness parameters of each sinusoidal surface on the metallic molds using Fourier filter in order to avoid the highest and the lowest points that are not the real peaks and valleys. $\lambda(\mu m)$ and $a(\mu m)$ denote the period and amplitude of the sinusoidal profiles respectively, R_a is the average roughness, while $R_t = R_p - R_v$ is the maximum amplitude of the sinusoidal profile and R_z is the average of R_t on the surface. R_q in this table represents root mean square of the roughness profile and finally, E_{ave} here is the average error between R_z and a	54
1.5	Roughness parameters of each pillared surface.	56
1.6	Roughness parameters of each sinusoidal surface on polycarbonate samples using Fourier filter in order to avoid the highest and the lowest points that are not the real peaks and valleys. $\lambda(\mu m)$ and $a(\mu m)$ denote the period and amplitude of the sinusoidal profiles respectively, while $R_t = R_p - R_v$ will be the maximum amplitude of the sinusoidal profile and R_z will be the average of R_t on the surface. R_q in this table represents root mean square of the roughness profile and finally, E_{ave} here is the average error between R_z and a	60
1.7	Contact angle of droplets on pillared surfaces.	61
1.8	Average contact angle on each sinusoidal substrate.	61
1.9	θ experiments table designed by FFD.	62
1.10	R_a experiments table designed by FFD.	64
1.11	ANOVA table for studying the importance of effect of λ and a on θ for significance level $\alpha = 0.05$	66
1.12	ANOVA table for studying the importance of effect of λ and a on R_a for significance level $\alpha = 0.05$	66

2.1 Performance parameters of the algorithm for several image sets 90

3.1 period and amplitude of the sinusoidal patterns. 124

4.1 The mean and standard deviation of errors of the model for different configurations of pillars. 145

4.2 Comparison between total surface area and density of the initial droplets on 6 configurations of sinusoidal patterns. 146

Acknowledgement

It is a humbling experience to acknowledge those people who have, mostly out of kindness, helped along the journey of my PhD. I am indebted to so many for encouragement and support. This journey would not have been possible without the support of my family, professors and mentors, and friends.

To my family, thank you for encouraging me in all of my pursuits and inspiring me to follow my dreams. I am especially grateful to my parents, my sister and my brother who supported me emotionally and financially.

My sincerest thanks are extended to my advisors Dr. Yann Gavet, Prof. Jean-Charles Pinoli and Dr. Stéphane Valette for their continuous support of my Ph.D study and related research, for their patience, motivations, and immense knowledge. Their guidance helped me in all the time of research and writing of this thesis. I could not have imagined having a better advisors and mentors for my Ph.D study.

Besides my advisors, I wish to thank the members of my dissertation committee: Prof. Frédéric Gruy, Dr. Anne MONGRUEL, Prof.Souad Harmand, and Dr.Christophe Pupier, for generously offering their time, support and guidance throughout the preparation and review of this document.

Last but not the least, to my many friends specially Thomas Cavoué who made the biggest change in my life. Thank you for listening, offering me advice, and supporting me through this entire process. You should know that your support and encouragement was worth more than I can express on paper.

Also I would like to mention that this work was funded by LABEX MANUTECH-SISE (ANR-10-LABX-0075, within the program "Investissements d'Avenir" (ANR-11-IDEX-0007) operated by the French National Research Agency (ANR). The experimental set-up was developed by Nicolas Pionnier during his PhD thesis funded by PSA Peugeot-Citroen in the context of OpenLab VAT@Lyon between Peugeot-Citroen and LTDS laboratory.

List of publications

International journals

1. S. Boroomandi Barati, N. Pionnier, J.-C. Pinoli, S. Valette, and Y. Gavet, "Investigation spatial distribution of droplets and the percentage of surface coverage during dropwise condensation", *International journal of thermal science*, Volume [124], 2018, 356-365.
2. N. Pionnier, S. Boroomandi Barati, E. Contraires, R. Berger, M. Guibert, S. Benayoun, S. Valette, "Design of an environment controlled dew tracking setup to emphasize the role of the relative humidity on breath figures dynamics", *Journal of EPJ Techniques and Instrumentation*, Volume 5[2], 2018.
3. S. Boroomandi Barati, V. Rabiet, J.-C. Pinoli, S. Valette, and Y. Gavet, "Modeling and simulation the growth of ellipsoidal droplets during dropwise condensation on pillared surfaces", accepted for the publication at *Journal of applied thermal engineering*, 2018.
4. H. Martin, S. Boroomandi Barati, N. Pionnier, J.-C. Pinoli, S. Valette, and Y. Gavet, "Segmentation of gray scale images of dropwise condensation on textured surfaces", *International journal of circuits, systems and signal processing*, Volume 12[1], 2018.
5. S. Boroomandi Barati, J.-C. Pinoli, S. Valette, and Y. Gavet, "Differential and average approaches to Rose and Mei dropwise condensation models", *International journal of mathematical models and methods in applied science*, Volume[11], 2017, 40-46.
6. S. Boroomandi Barati, J.-C. Pinoli, S. Valette, and Y. Gavet, "Drop-size distribution function for small droplets during dropwise condensation", will be Submitted to the *International journal of thermal science*, 2018.
7. S. Boroomandi Barati, V. Rabiet, J.-C. Pinoli, S. Valette, and Y. Gavet, "Simulation the growth of ellipsoidal droplets during dropwise condensation on Sinusoidal surfaces", Will be submitted to the *International journal of heat and mass transfer*, 2018.

International conferences

1. H. Martin, S. Boroomandi Barati, N. Pionnier, J.-C. Pinoli, S. Valette, and Y. Gavet, "Segmentation of gray scale images of dropwise condensation on textured surfaces", *The 2018 International Conference on Applied Mathematics and Computational Methods in Engineering*, Venice, Italy April 28-30, 2018.
2. H. Martin, S. Boroomandi Barati, J.-C. Pinoli, S. Valette, and Y. Gavet, "Recognition the droplets in gray scale images of dropwise condensation on pillared surfaces", *7th international conference on computer science, engineering and applications*, 23-24 September Copenhagen, Denmark.
3. S. Boroomandi Barati, J.-C. Pinoli, S. Valette, and Y. Gavet, "Differential and average approaches to Rose and Mei dropwise condensation models", *16th international conference on mathematical methods, mathematical models and simulation in science and engineering*, Athens, Greece, April 9-11 2017.
4. S. Boroomandi Barati, J.-C. Pinoli, S. Valette, and Y. Gavet, "Modeling and simulation of ellipsoidal droplets growing on patterned substrates during dropwise condensation", *XVIII Spanish-French School Jacques-Louis Lions about Numerical Simulation in Physics and Engineering*, 25-30 Juin 2018, Gran Canaria, Las Palmas.

National seminars

1. S. Boroomandi Barati, J.-C. Pinoli, S. Valette, and Y. Gavet, "Mathematical model of dropwise condensation on textured surfaces", *9ème Colloque Science et Technologie des Poudres*, Compiègne, France, 3-5 July 2018.
2. S. Boroomandi Barati, N. Pionnier, J.-C. Pinoli, S. Valette, and Y. Gavet, "Spatial distribution of droplets during dropwise condensation ", *28em Journées Internationales Francophones de Tribologie (JIFT)*, Saint Etienne, France, 27-29 April 2016.
3. S. Boroomandi Barati, J.-C. Pinoli, S. Valette, and Y. Gavet, "Random and geometric model of droplets nucleation on textured surfaces", *Séminaire biennal labex manutech-sise 2017*, Marcoux, France, 12-13 October 2017.

Honors and awards

1. The bourse of the "Société de Mathématiques Appliquées et Industrielles (SMAI)" for participation at summer school of Jacques-Louis Lions about Numerical Simulation in Physics and Engineering, 25-30 Juin 2018, Gran Canaria, Las Palmas.

Summary

Water droplets that are forming on the interior side of the car light shields in humid days reduce the efficiency of the lightening by reflecting the light beams passing through. The formation of these droplets is due to the process of condensation. The aim of this thesis is to develop a numerical simulation model to study the process of dropwise condensation on flat and textured substrates.

Condensation occurs when the temperature of a humid air mixture goes beyond its dew point, like when a cold substrate is in contact with humid air and water droplets start to nucleate and grow on its surface. In this case, condensation can occur either in dropwise or filmwise form. Dropwise condensation is preferred when higher heat transfer coefficient is needed like in heat exchanging devices and power generation refrigeration, when in optical purposes filmwise condensation is favored because of less light reflection.

One efficient and environmentally-friendly way to transit from dropwise to filmwise condensation and vice-versa is by applying special texturing patterns on the substrate. In this regard, we studied the droplets behavior on three types of substrates: flat surface, textured in form of pillars and textured in form of sinusoidal substrates. The experimental part was carried on the polycarbonate surfaces that were duplicated from a metal mold textured using laser technology. Then, the samples are mounted on a home-made condensation set-up developed previously. The results of these experiments are gray scale images that had to be segmented in order to get the information related to droplets growth rate, density and spatial distribution.

Comparison between the gray scale images taken from droplets growing on textured and flat surfaces shows considerable differences. The most important difference is that since the droplets can be easily canalized between the patterns, the shape of droplets changes from spherical to ellipsoidal as is shown in figure 1. These ellipsoidal droplets can grow, contact and coalesce in a three dimensional configuration.

Therefore, three different models were developed during this thesis to describe droplets behavior:

1. a classical method that considers droplets as spherical-caps growing on a flat substrate (figure 2 (a)),
2. a method that considers elliptical droplets (contact angle = 90°) growing on the textured substrates (figure 2 (b)),
3. and a modified method that considers ellipsoidal-cap droplets (contact angle $\neq 90^\circ$) growing on the textured substrates (figure 2 (c)).

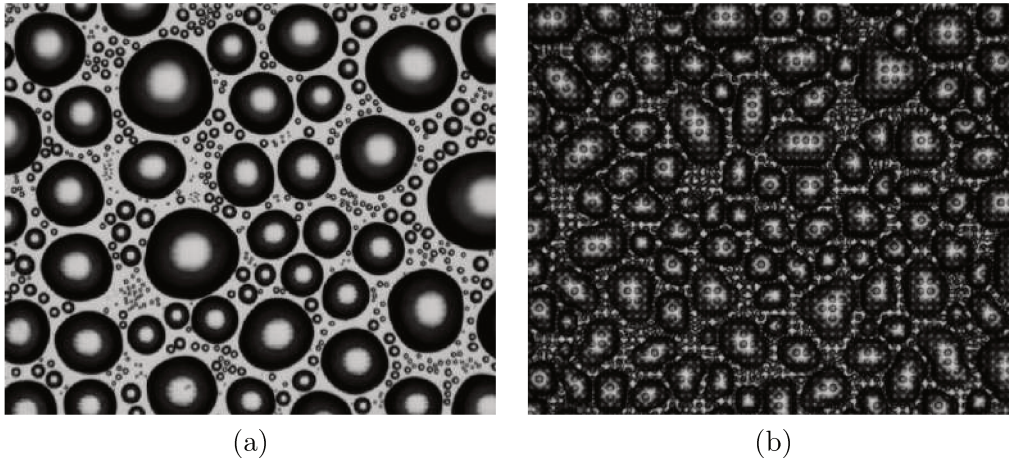


Figure 1: (a) Spherical droplets on a flat substrate, (b) ellipsoidal droplets on a textured substrate.

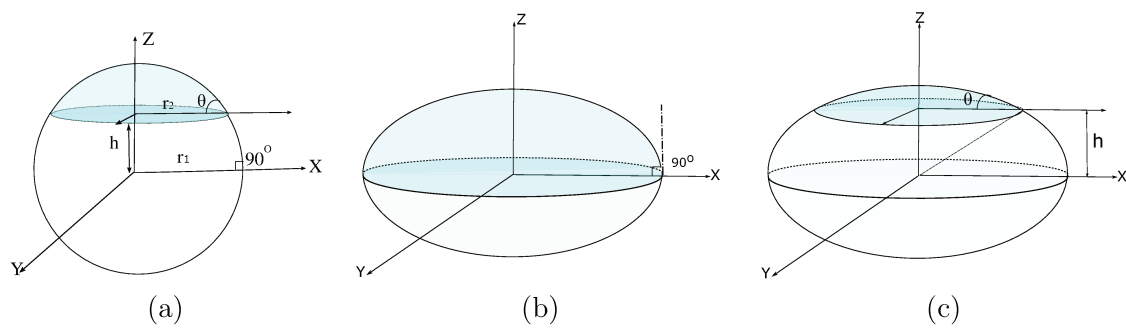


Figure 2: Schematics of (a) a spherical-cap (b) an ellipsoid (contact angle with surface is 90°), and (c) a semi-ellipsoid (contact angle with surface is θ).

The results of these three methods are validated by comparison with experimental data on a flat surface, six different configurations of pillared surfaces, and six configurations of sinusoidal patterns. The spatial distribution of droplets on both flat and textured substrates are studied using Fry plot and Ripley's K directional methods as well. Moreover, a method for studying the density function of small droplets on flat surfaces is proposed by modifying the method of Abu-Orabi for the surface area and by neglecting the periodic surface renewal. Therefore, a simpler but more efficient model is developed to describe the size distribution function of small droplets at earlier stages. Earlier stages here means the time steps before sliding of the big droplets.

As was expected, by making texturing patterns on the substrates, we will be able to control droplets spatial distribution and more importantly their growth rate. Also, the three models proposed here are in acceptable agreement with experimental data with the error less than 10% depending on the model.

Résumé

Les gouttelettes d'eau qui se forment du côté intérieur des phares des voitures pendant les jours humides réduisent l'efficacité de l'éclairage en réfléchissant les faisceaux de lumière passant à travers. La formation de ces gouttelettes est due à la condensation. Le but de cette thèse est de développer un modèle de simulation numérique pour étudier le processus de condensation en gouttelettes sur des substrats plats et texturés.

La condensation se produit lorsque la température d'un mélange d'air humide passe en dessous de son point de rosée, comme lorsqu'un substrat froid est en contact avec de l'air humide et que des gouttelettes d'eau commencent à germer et à se développer à sa surface. Dans ce cas, la condensation peut se produire par gouttelettes ou sous forme de film. La condensation en gouttelettes est préférée lorsqu'un coefficient de transfert de chaleur plus élevé est nécessaire, comme dans les dispositifs d'échange de chaleur et de réfrigération. Au contraire, pour les applications anti-bouée la condensation par film est favorisée afin de limiter la diffusion de lumière par les gouttelettes.

Une manière efficace et écologique de passer de la condensation en gouttelettes à la condensation par film et inversement consiste à appliquer des motifs de texturation spéciaux sur le substrat. À cet égard, nous avons étudié le comportement des gouttelettes sur trois types de substrats : surface plane, texturée sous forme de piliers et sous forme de sinusoïdes. La partie expérimentale a été réalisée sur des surfaces de polycarbonate dupliquées à partir d'un moule métallique texturé par laser. Les échantillons sont montés sur un ensemble de condensation développé précédemment au laboratoire. Les résultats de ces expériences sont des images à niveaux de gris qui ont dû être segmentées afin d'obtenir l'information liée au taux de croissance des gouttelettes, à la densité et à la distribution spatiale.

La comparaison entre les images à niveaux de gris prises à partir de gouttelettes sur des surfaces texturées et plates montre des différences considérables. La différence la plus importante est que, puisque les gouttelettes peuvent être facilement canalisées entre les motifs, la forme des gouttelettes passe de sphérique à ellipsoïdale comme le montre la figure 1. Ces gouttelettes ellipsoïdales peuvent se développer, entrer en contact et se fondre dans une configuration tridimensionnelle.

Par conséquent, trois modèles différents ont été développés au cours de cette thèse pour décrire le comportement des gouttelettes :

1. une méthode classique qui considère les gouttelettes comme des calottes sphériques se développant sur un substrat plat (figure 2 (a)),
2. une méthode qui considère les gouttelettes elliptiques (angle de contact = 90°) croisant sur les substrats texturés (figure 2 (b)),

3. et une méthode modifiée qui considère les gouttelettes à calotte ellipsoïdale (angle de contact $\neq 90^\circ$) croissant sur les substrats texturés (figure 2 (c)).

Les résultats de ces trois méthodes sont validés par comparaison avec des données expérimentales sur une surface plane, six configurations différentes de surfaces à piliers et six configurations de motifs sinusoïdaux. La distribution spatiale des gouttelettes sur les substrats plats et texturés est étudiée à l'aide de la méthode Fry et des méthodes fonctions de K directionnelles. De plus, une méthode pour étudier la fonction de densité de la taille des petites gouttelettes sur les surfaces planes est proposée en modifiant la méthode d'Abu-Orabi pour la surface et en négligeant le renouvellement périodique de surface. Par conséquent, un modèle plus simple mais plus efficace est développé pour décrire la fonction de distribution de taille des petites gouttelettes au début du processus. La phrase début du processus ici signifie les étapes de temps avant le glissement des grosses gouttelettes.

En réalisant des modèles de textures sur les substrats, nous sommes en mesure de contrôler la distribution spatiale des gouttelettes et, plus important encore, leur taux de croissance. De plus, les trois modèles proposés ici sont en accord acceptable avec les données expérimentales avec une erreur inférieure à 10% selon le modèle.

General introduction

0.1 General issue

Moisture formation on the interior side on the windows, eye glasses, light shields and other glassy substrates during the foggy days has been always known as a natural process. But when it comes to lightening and optical devices, the formation of dew can become a serious problem: the water droplets reflect the light beams passing through the surface and can reduce for example the vision of the optical glasses or the efficiency of lightening in light shields. Figure 1¹ shows the light beams reflected by water droplets formed on a glassy substrate. This is what can happen on the interior side of the car light shields at the foggy days or almost all the time in the countries that have humid environment. The formation of dew is because of the well-known process of "condensation".



Figure 1: Light reflection because of droplets formation on the glassy substrates. This phenomenon can happen on the interior side of the car light shields at the foggy days and will reduce the efficiency of illumination.

Condensation generally occurs when the temperature of a saturated air mixture goes below its dew point [14, 15]. The growth or shrinking of droplets depends on the challenge between condensation and evaporation. At first, condensation occurs and water droplets form either on the substrate or as a mixture with vapor phase, but after a while some of the

¹Image from <https://pxhere.com/en/photo/1076373>

water molecules with higher amount of energy move back to the vapor phase. Depending on the rate of the two processes, water droplets can either grow or disappear. Beysens *et al.* did considerable researches on the formation, determination and growth of dew under different situations [15, 16, 17, 18].

Evaporation of the droplets generally occurs in 3 stages according to figure 2. At first, the spreading stage occurs, during which the droplet attains the maximum value of the base diameter and the contact angle reaches the value of advancing contact angle. For simple liquids this stage is very fast and evaporation can be neglected. Therefore, in most studies it is out of consideration and only three consequent stages of evaporation are taken into account [1]. During stage I the contact angle is decreasing while the radius of drop or the length of contact line is constant. Following the process at stage II, the droplet becomes smaller in the same contact angle and in the final stage both the radius and contact angle decrease at the same time [1]. These stages are presented in figure 2.

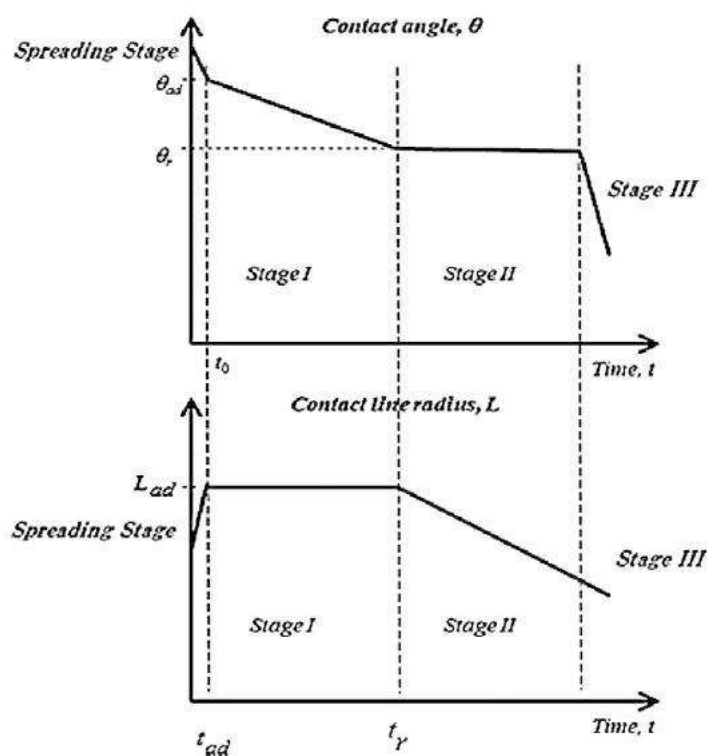


Figure 2: Changes in contact angle and radius of the droplet during evaporation [1]. Stage I: the radius of droplet is constant while, its contact angle is decreasing. Stage II: the droplet becomes smaller in the same contact angle. Stage III: both the radius and contact angle decrease at the same time.

Parsa *et al.* [19] reported two other stages after stage III named the mixed mode and the stick-slip stages. During the mixed mode sometimes both the radius and contact angle decrease simultaneously. In the stick-slip mode, the droplet is in the constant contact radius mode, but the contact line suddenly slips into a new position leading to a smaller

contact radius when the contact angle reaches a threshold, minimum value (corresponding to a slip phase). Then, the droplet is again in the constant contact radius mode (stick phase) until the next depinning occurs.

The transfer point from stage I to stage II (t_r) is related to the surface roughness and hydrophobicity. On rougher surfaces, it is difficult for drops to slide on the surface and the decrease in radius happens later, so evaporation occurs mainly through the radius constant stage. While, for hydrophobic surfaces evaporation goes through the θ constant stage [1].

The problem appears when the rate of evaporation is less than condensation and water droplets do not disappear. Usually when outside is relatively colder than inside area and air relative humidity is high enough, droplets form and grow on the surface of interface between indoor and outdoor that can be a window, a light bubble or simply the eye glasses.

The most important parameters affecting the rate of condensation and evaporation are: both air and substrate temperature, air pressure, air flow velocity [20], solid content and impurities in liquid droplets [21], heat transfer mechanism [22], size of initial droplets, surface hydrophobicity [1], and surface roughness[1]. Therefore, by (1) considering constant temperature for cold substrate and hot air, (2) neglecting the effect of impurities and (3) considering zero velocity of both phases, (4) under atmospheric pressure and (5) on the surface without coating, the only parameter that can be manipulated in order to control the rate of condensation and evaporation is the surface roughness as well as surface topography.

In the following the condensation process on the solid substrates especially in dropwise mode will be presented with more details. Then, different aspect of dropwise condensation that have been studied up to now will be discussed.

0.2 Dropwise and filmwise condensation

Condensation can play a great role in improving the efficiency of the energy utilization systems and relieving pollution problems [23] and is widely used in heat transfer devices, power generation refrigeration, and waste heat recovery stations [24, 25]. There are two main types of condensation: dropwise and filmwise. The efficiency of all the above systems depends on the mode of condensation, because it has been proved that dropwise condensation has considerably greater heat transfer coefficient (about 5 to 7 times) with respect to the filmwise mode [26, 27]. In dropwise condensation the surface of substrate is covered by liquid droplets[28], while the filmwise mode happens when the contact angle of liquid on the surface is low enough to form a stable liquid film [27].

Depending on the goal of process, each of dropwise or filmwise condensation can be more favorable. Dropwise condensation is preferred when higher rate of heat transfer is needed, for example in heat exchangers or when an easy-to-clean surface aims to reduce pollutant adhesiveness [29]. The problem that we are dealing with is the formation of liquid droplets in car light shields, which will cause the light reflection and as a result the decrease in the efficiency of illumination. In such cases, it is preferred to achieve the filmwise regime.

Stylianou and Rose [33] discussed different methods to describe transition mode from dropwise to filmwise condensation like, viscosity-limited coalescence mechanism or nucleation site saturation mechanism. There are several ways to control the ratio of dropwise to filmwise condensations such as using hydrophobic or hydrophilic chemical coatings [34, 35],

changing surface roughness and surface morphology [36].

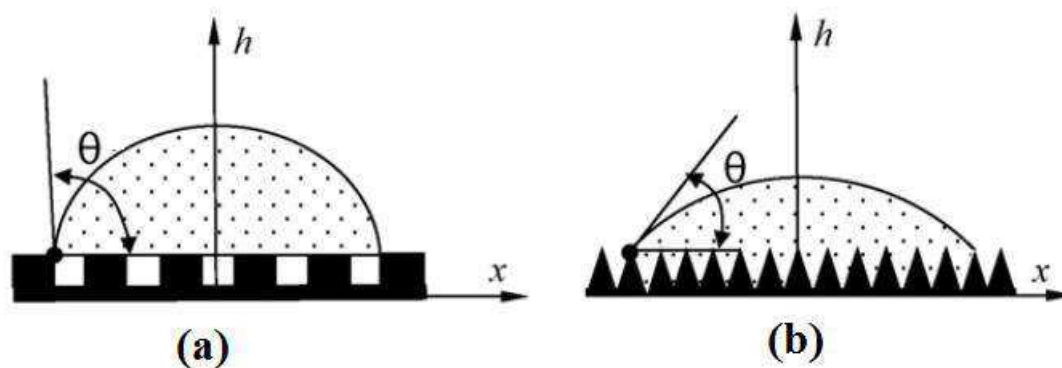


Figure 3: (A) Cassie-Baxter and (B) Wenzel droplets on textured surfaces (image from [2]).

The definition of dropwise and filmwise condensations might bear in mind the concept of Cassie-type [30] and Wenzel-type [31] droplets. Cassie droplets sit on top of the roughness peaks with trapped air underneath, so they can be effectively removed from the surface [32]. Whereas, Wenzel droplets retain intimate contact with the solid surface (figure 3). Usually Cassie droplets lead to dropwise condensation and Wenzel droplets lead to filmwise mode, but it depends on the wettability of the surface as well as size of the texturing patterns. Meaning that, the Cassie and Wenzel drops usually happen on the surfaces with special chemical coatings with preferred wettability or when the size of roughness pattern is far smaller than the size of droplets (usually nano-metric patterns). In the case of the surfaces without chemical coating and bigger texturing patterns (usually micro-metric patterns), comparing Cassie and Wenzel droplets with dropwise and filmwise condensation is not appropriate.

0.2.1 Effect of topography

Medici *et al.* [37] investigated the effect of discontinuities (either due to surface roughness or due to different subcooling properties) on the rate of droplets growth. They stated that both of these discontinuities at outer edges will speed up the droplets growth rate. This is because more water vapor can be collected at the border, whereas geometrical discontinuities at inner edges, where less water vapor is collected will lower the droplet growth. Guadarrama-Cetina *et al.* [38] investigated the nucleation and growth of water droplets on the hexagonal micro-structure surface of desert beetles skin and they found the higher droplet nucleation rate in the valleys where dew forms primarily.

Qian and Ma [39] stated that nano-concave or convex topography can change nucleation pattern of droplets on a rough surface. Chen *et al.* [40] discovered that Cassie droplets are more stable than Wenzel type on the rough surfaces with nano-pillars. However, it is difficult to maintain Cassie droplets on a flat or macro pillared surfaces because the Cassie

state is meta stable and a transition from the Cassie to Wenzel state is often observed by an increase in driving force like temperature or pressure difference [41].

0.2.2 Effect of chemical coatings

Vemuri and Kim [34] reported the increase of about 8 times in condensation heat transfer rate on the hydrophobic coating of *n*-octadecyl mercaptan with respect to complete filmwise condensation under atmospheric pressure. Tiany *et al.* [35] compared the rate of droplets growth on two different coatings: a hydrophilic (contact angle = 73.9°) and a hydrophobic (contact angle = 110.8°) one. Their results show that on the two substrates the condensation starts by dropwise form, no matter how the surface wettability is. Then depending on the wettability of the surface the shape of droplets will be different: on the hydrophobic substrate the droplets will grow in circular shape, while on the hydrophilic substrate droplets will be shapeless after a while. Xiuliang and Cheng [5] studied the effect of coating thickness, thermal conductivity of coating and contact angle on the heat transfer during dropwise condensation. They also improved a thermodynamic model to calculate critical radius for dropwise condensation on a subcooled coated surface [42]. But, using chemical coatings is harmful to environment and wastes water. Therefore, in the current study it is more preferred to investigate the effective parameters on the rate of droplets growth by avoiding use of chemical coatings.

0.3 Dropwise condensation

A huge amount of works have been done up to now to describe theoretically and empirically what happens during the process of dropwise condensation (for example. Generally dropwise condensation includes four main steps: nucleation of initial droplets (homogeneously or heterogeneously), growth due to adsorption, growth due to coalescence and at the same time nucleation of new droplets in vacant area of surface, and sliding of very big drops (in the case of vertical substrate). The result of the last three stages is the change in number of droplets as well as their size. In dropwise condensation, water droplets start to nucleate either in the air mixture or on the cold substrate of chamber walls. Regarding condensation on cold substrate, nucleation can occur uniformly (when there is no preference between different spots for nucleation) or ununiformly (preferentially on the surface imperfections) [44].

After nucleation step, the droplets grow due to two main mechanisms: when the droplets are smaller than critical radius (r_c) they grow by absorbing water molecules from the gas phase, while droplets bigger than r_c grow mainly due to coalescence [45, 46], which means joining of the neighboring drops to form a new bigger drop. The concept of small and big droplets was firstly introduced by Abu-Orabi [47]. He proposed the critical radius as the half-spacing between active sites on the substrate and divided the droplets into small or adsorbing droplets and big or coalescing droplets by comparing their radius with r_c . r_c can be calculated as follows, where N is the number of droplets and L is the side length of the square substrate:

$$r_c = \sqrt{\frac{L^2}{4N}} \quad (0-1)$$

Based on this method of droplets categorizing, Liu *et al.* [5] and Vemuri *et al.* [34] calculated total heat transfer and droplets nucleation density as the summation of these values for each group of droplets. Although coalescence is a mass conservative process, the area covered by daughter droplet is lower than the summation of area covered by its parents. This will lead to forming vacant area around daughter droplet, in which new small droplets can nucleate and grow. Both these steps will change droplets density and lead to a temporal distribution [48].

After a while very big droplets will form that can overcome the friction and slide from the substrate and clean off the droplets on their path. In this situation the droplets will disappear and new small droplets will form at their places. Therefore, there is another important definition in this case, maximum radius (r_{max}), which is the larger radius that is achievable by a drop before sliding (in the case of vertical substrates). This parameter is a completely experimental factor that is in direct relationship with the surface topography, physical features of liquid, and the angle of substrate with horizon. For example Earl *et al.* [10] reported $r_{max} = 0.1cm$ for water droplets sliding from the vertical surface of a condenser. Ghosh *et al.* [172] studied different mechanisms affecting the surface removal step. According to their work, in the case of dropwise condensation from pure vapor the droplets bigger than the capillary radius of water ($0.2Cm$) will slide from the substrate.

In the following, after a brief explanation of different steps of dropwise condensation, the most important aspects of this process based on their roles in droplets growth and heat transfer rate, including droplets nucleation, temporal distribution and droplets size distribution function are going to be discussed. Then, the algorithms that were used for generating droplets will be introduced and finally the goals of this study will be introduced.

0.3.1 Droplets nucleation

Nucleation refers to the process of forming a new thermodynamic phase from a bulk phase that can occur homogeneously or heterogeneously [35]. In dropwise condensation nucleation means formation of small droplets that are ready to grow. These small droplets can form either in the steam or gas bulk (homogeneous nucleation) or on the surface of a substrate or solid particles (heterogeneous nucleation). In this thesis we deal with nucleation of water droplets on substrate or a heterogeneous nucleation.

In dropwise condensation on substrate, if the droplets form on a completely flat surface with no preference, it will be a uniform nucleation. An ununiform nucleation occurs when there are some points due to pollutants or surface topography that are more potential to grow droplets. The arrangement of droplets on the surface plays a very important role in controlling the rate of droplets growth. Configuration of droplets on the surface will change the possibility of contact between droplets and as well, the rate of growth due to coalescence, and consequently the rate of producing vacant area after coalescence that will change the number of new small droplets nucleate at each step. The arrangement of droplets is in close relationship with surface wettability and roughness. Therefore, one of the ways to change droplets arrangement is to apply chemical coatings that can change surface wettability, or to make different topographies on the surface to arrange the places that are more preferred to grow droplets. Both of these parameters will affect the number of droplets that are able to grow on the surface.

All in all one can divide the nucleation process in dropwise condensation into different

types:

- homogeneous nucleation: nucleation on the bulk phase,
- heterogeneous nucleation: nucleation on the cold substrate,
 - uniform nucleation: nucleation on the cold substrate without any preferred points,
 - ununiform nucleation: nucleation on the cold substrate with preferred points (for example on patterned or coated substrates).

Since in this study we are focused on the heterogeneous nucleation, in the following more explanations about the two forms of this process will be presented.

0.3.1.1 Uniform nucleation

Uniform nucleation occurs when the droplets nucleate completely randomly or as is said in the literature their distribution follows the Poisson point process (see section 0.4.1). Kostinski, Jameson and Larsen [49, 50, 8, 51, 52] have published many works in investigating the validity of the Poisson distribution for rain drops. In dropwise condensation on the flat surface also, because the initial droplets are fine and there is no preference between different spots to grow droplets, the assumption of Poisson point process can be considered as true. But, in the coalescence part the droplets in the neighboring volumes are not statistically independent and thus the distribution will not be uniform anymore. Therefore, it can be concluded that the spatial distribution of droplets at initial steps of condensation on flat surfaces can be assumed as uniform distribution, but at coalescence stage it will deviate from uniformity.

0.3.1.2 Ununiform nucleation

Ununiform dropwise condensation on textured surfaces is now more attractive to scientists because of the ability of controlling droplets configuration [53]. Therefore, this idea could also be interesting for optical applications. Indeed, this solution could make drops to form a continuous film or to drain quickly from the surface of headlights or glasses. There are some methods, by which the nucleation sites can form under controlled conditions. One of these methods is the so-called bottom-up approach to create localized hydrophilic tips on super hydrophobic surfaces [27]. In this method a hydrophobic or super hydrophobic surface is chemically treated to have controlled hydrophilic spots. These hydrophilic spots that can be inserted by different geometries will be the nucleation sites for droplets during dropwise condensation. One of the materials that is used for this purpose is polyvinyl alcohol (PVA) due to its ability to be adsorbed onto most hydrophobic surfaces from solution phase [3]. Such unique bottom-up approach can be investigated by other water-soluble polymers as well as aqueous suspension of nanoparticles like AgI instead of PVA [4]. In this method, the main mechanism is based on the Volmer's classical nucleation theory and experimental nucleation studies that predict a higher condensation rate on the hydrophilic surfaces than hydrophobic ones. Thus, hydrophilic spots of PVA on a super hydrophobic surface can function as the spatial nucleation sites.

This spatial configuration can be extended on various topographical geometries, such as blade (figure 4 (A) and (B)), honeycomb (figure 4 (C)) and brick topographies (figure 4 (D)). The two important parameters here are the shapes of geometric features which varies in figure 4 and their size which effects can be seen in figure 5. In figure 4 optical images of the nucleation and growth of water droplets condensation on various super hydrophobic surface geometries are presented. For each geometry the comparison between functionalized with PVA tips and un-functionalized patterns is illustrated. At figure 4 (A) the first row shows an hydrophobic blade geometry without any hydrophilic functionalized tip. As a result, the droplets were formed and grew randomly, resulting in wetting films. The second row of figure 4 (A) shows the hydrophobic blade geometry with the hydrophilic functionalized tips on the top of the blades. The results of condensation on these geometries can be seen in 4 (B). It is obvious that nucleation sites followed the same shape of the PVA pattern and grew from D_{Si} to D_{w1} and D_{w2} . Condensation on 4 (C) honeycomb and 4 (D) brick follows a similar pattern to the posts. At first that there is no functionalized tip, droplets form all around the surface without special interest, but after inserting the hydrophilic tips, the droplets follow the roughness pattern [3].

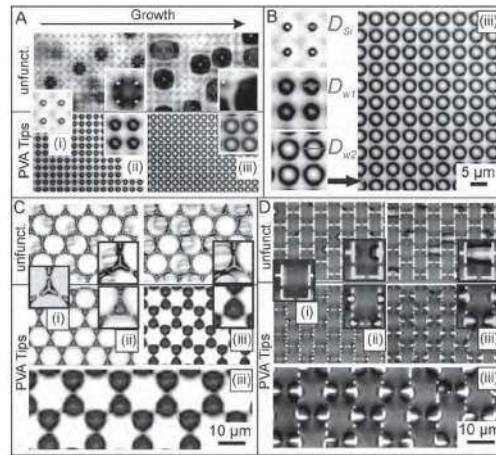


Figure 4: Optical images of the nucleation and growth of water condensation on various super hydrophobic surface geometries [3].

As it was mentioned above, both shape and size of geometry features are important in the shape of droplets spatial distribution. In figure 5, the control of droplet coalescence by changing the geometric features size is presented. PVA tip functionalization in three different sizes of the same geometries results in different droplet condensation patterns. In 5 (A) small blades were studied. In this pattern droplets formed on the middle of each blade, resulting in the uniform condensation of one centered droplet per blade. In 5 (B) blades of intermediate length are shown that lead to two droplets per blade in a dumbbell shape. Figure 5 (C) indicates that a thin film of water nucleates on longer blades, which can break up into smaller droplets. These smaller droplets can coalesce and form large, uniformly positioned single droplets. Thus, it can be concluded that for bigger blades a random pattern of droplets will form, that their shapes and distribution are not under controlled conditions.

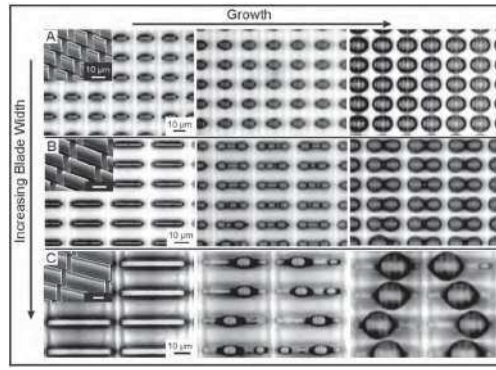


Figure 5: Control of droplet coalescence by changing the geometrical features sizes [3].

Voronoi diagram

Lhuissier *et al.* [4] studied the formation of nano- or micro-gas bubbles that often form on hydrophobic solid surfaces in contact with an aqueous environment. Their mathematical method can also be used to study the nucleation of droplets during dropwise condensation on solid substrates. For studying the spatial distribution of the bubbles, they made two algorithms to track the area of each bubble, that considers a cell around each bubble's zone and grid the surface with respect to these cells. Two methods were used for grinding the surface:

1. the first method is called standard Voronoi diagram, considers a surface with area A_{vor} around each zone based on the distances to its center. So, just the points that are closer to the center of each zone than the center points of the other zones are chosen as area of the bubble.
2. the second one, that is called modified Voronoi diagram (also known as Apollonius diagram), is based on the distances with the boundary of each zone. Therefore, it draws a surface with area A consisting of the points that are closer to the boundary of each zone with respect to the boundaries of the other zones.

These two definitions are equal only if the bubbles have the same size. Figure 6 shows these two methods of grinding the surface. In 6 (a) standard Voronoi diagram is shown, in which the surface with area A_{vor} is considered around the center of the bubbles, while in modified Voronoi, figure 6 (b), the surface was drawn around the boundary of bubbles.

Lhuissier [4] considered the probability distribution function (pdf) of the normalized area of the cells ($x = A/A_{ave}$) for Voronoi diagram as a gamma distribution, which is expected as a case of a random Poisson process for bubbles distribution:

$$P(x) = \frac{343}{15} \sqrt{\frac{7}{2\pi}} x^{5/2} e^{-7x/2}. \quad (0-2)$$

But their experiments resulted in a broader distribution than the gamma process that shows inhomogeneity in the bubbles distribution. They explained this inhomogeneity by the nature of nucleation and growth of bubbles. If some bubbles nucleate and start growing

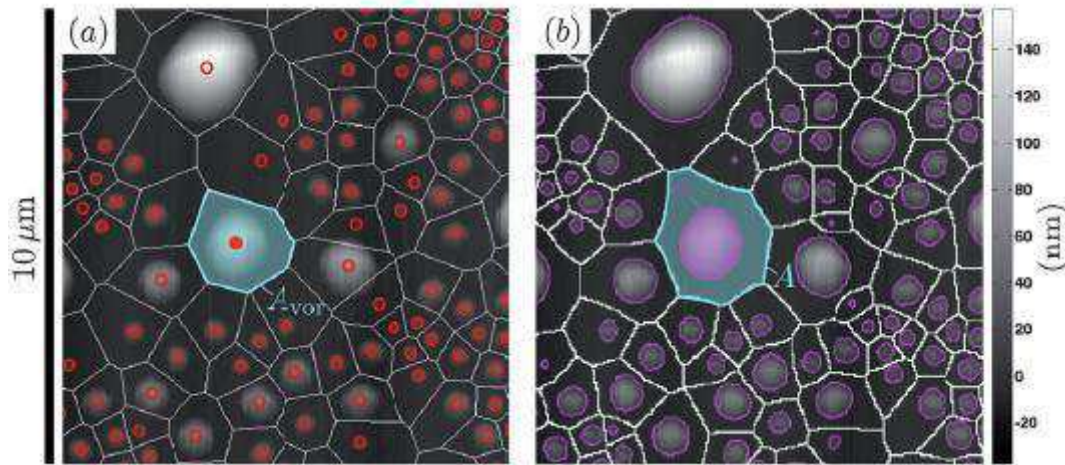


Figure 6: Two methods for tessellating the surface of nucleation [4]. (a) Voronoi diagram based on the distances to the bubbles' centers (red circles). One Voronoi cell with area A_{vor} associated with the bubble center marked as a filled red circle is shown. (b) Modified Voronoi diagram based on the distance to the bubbles' triple contact lines (pink lines). One modified Voronoi cell with area A associated with the bubble footprint (with area a) colored in pink is shown.

before the others, they are likely to reach larger sizes than in the case where all bubbles would nucleate at the same time. So, their difference in size with respect to the mean is going to be more than the amount that was predicted by gamma process. At last, it resulted that the bubbles centers are not uniformly distributed and this shows that they interact with each other during nucleation and growth. More over, the size of bubbles is a strong function of their distance with their neighbors.

Effective parameters on the droplets nucleation density

Liu and Cheng [54] at first developed the Kim and Kim's model [55] of heat transfer through a droplet by adapting population balance model to achieve the critical radius. Then, they developed a new model for dropwise condensation heat flux on a subcooled surface with coatings and used this model to investigate the effect of the following parameters on the droplets nucleation density on a surface with hydrophobic coating [5]:

- Degree of subcooling, which is the difference between gas saturated temperature and substrate temperature ($\Delta T_{sub} = T_{sat} - T_s$)
- Contact angle (θ)
- Coating thickness (δ)
- Thermal conductivity of thickness (λ)

The results of their study can be seen in figure 7. According to this figure for surface without coating, figure 7(a), the increase in contact angle does not affect apparently on the drop nucleation density on high degrees of subcooling, but in ΔT_{sub} lower than $4^\circ C$, by increasing the contact angle the drop nucleation density decreases. This is because by increasing contact angle condensation is more difficult and the number of nucleation sites reduce. While as can be seen in figure 7(b) by adding a $0.1\mu m$ coating, the drop

nucleation density decreases with increasing contact angle. It is also worth pointing out that by increasing coating thickness and decreasing thermal conductivity of coating, drop nucleation density will decrease too. This is because of increasing the thermal resistance between substrate and gas phase. So the rate of heat transfer will decrease as well as the number of droplets by increasing coating thickness and decreasing thermal conductivity.

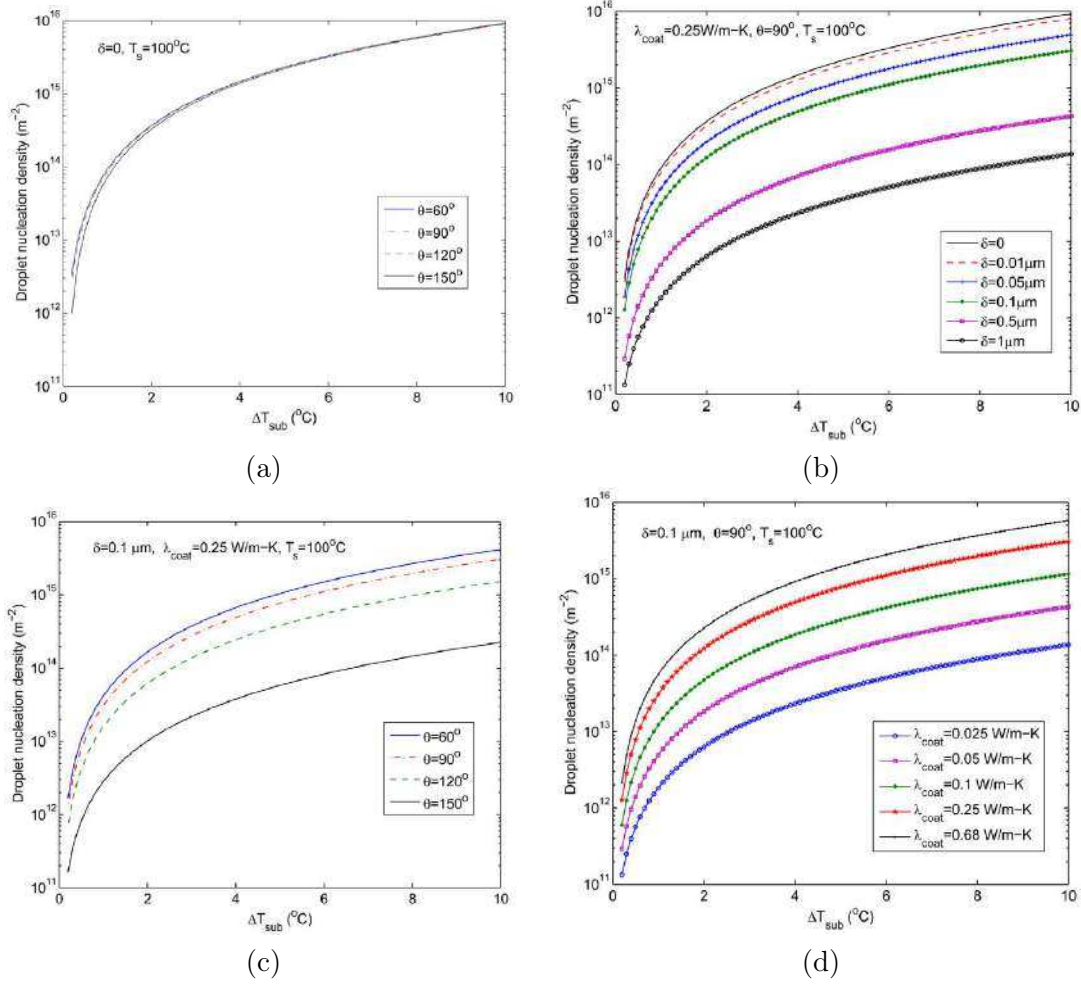


Figure 7: Effective parameters on the droplets nucleation density [5]. (a) Effect of contact angle without coating, (b) effect of coating layer thickness, (c) effect of contact angle on a coating with $\delta = 0.1\mu\text{m}$ and $\lambda = 0.25\text{W/m.K}$, (d) effect of thermal conductivity of the coating layer.

In this part, the uniform and ununiform nucleation process were introduced. Also, some interesting methods that used to achieve non uniform nucleation were explained briefly. This is shown that by applying texturing patterns, we are able to change the nucleation and growth rate of droplets. In this thesis we will use two texturing patterns that are not chemically functionalized to investigate their effect on droplets behavior.

0.3.2 Droplets growth

0.3.2.1 Adsorption

Adsorption is the first mechanism for droplet growth in drop wise condensation and refers to the attracting vapor molecules by droplets due to temperature difference. In other words, vapor molecules in the vicinity of cold droplets loose their energy and condense on the surface of the droplet. Since this is a mass conservative process, the result is growing the size of water droplet. Condensation of vapor molecules in contact with cold droplet is the main reason of growing the initial droplets.

0.3.2.2 Coalescence

The second mechanism for droplet growth as was explained before, is coalescence that is the interaction between two or more droplets. Surface tension is the elastic tendency of a fluid surface which makes it acquire the least surface area possible. At liquid-air interfaces, surface tension results from the greater attraction between liquid molecules (due to cohesion) than attraction between liquid-air molecules (due to adhesion). The net effect is an inward force at interface that causes the liquid to behave like a surface covered with a stretched elastic membrane. In dropwise condensation there is always a tail around each droplet in its interface with substrate [56]. Formation of this tail is due to two reasons, condensation of very small droplets from the dense vapor around each droplet and liquid-solid adhesion. If two droplets are close enough to have a contact in the area of their tails, surface tension in this area will drive them to coalesce.

0.3.3 Steady state

The term steady state describes the situation under which the changes in the characteristic parameters of the system with time are negligible. In process engineering usually, the rate of changes is described as:

$$M_2 - M_1 = \frac{dM}{dt}, \quad (0-3)$$

where, M can be each parameter that describes the system like: total mass, heat, or momentum. Superscripts 2 and 1 show the amount of M that exits from the system and the amount of entrance at time interval $\Delta t = t_2 - t_1$, respectively. But most importantly, the deferential $\frac{dM}{dt}$ represents the accumulation ($\frac{dM}{dt} > 0$) or evacuation ($\frac{dM}{dt} < 0$) of M . These definitions can be seen in figure 8. In this schematic diagram the blue level illustrates the amount or value of parameter M in the system. If this level does not change during time, means that the accumulation term is negligible ($\frac{dM}{dt} = 0$), so ($M_1 = M_2$) and the changes in parameter M is not significant during time. This is the meaning of steady state situation.

In the case of dropwise condensation on solid substrate, if we assume M as the number or size of droplets, then steady state situations achieved when the density and average size of droplets on the substrate are almost constant. In [43] the term of steady is used in opposition to non-steady, in which millions of coalescence occur in a square of $1 \times 1 \text{ cm}^2$ at each second. On the other hand, Tanaka [57, 58] studied the photographs of a vertical condensing surface, and he assumed that steady state achieved in dropwise

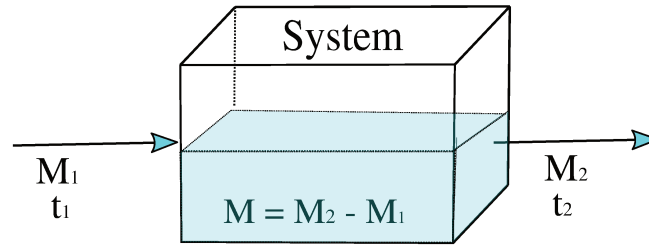


Figure 8: Changes of a specified parameter M during time. The blue level illustrates the amount or value M in the system. If this level does not change during time, the system is at steady state step.

condensation when the surface is cleared off condensate periodically by sliding big drops. These drops sweep the surface, exposing bare strips, on which transient condensation takes place without delay, until the area is swept clean again [47]. Based on these references and the definition that steady state occurs when changes during time are negligible, we interpret steady state as the situation under which the droplets are big and surrounded by vacant area produced by coalescence and sliding of bigger droplets, so they are not able to coalesce rapidly. Moreover, small droplets nucleate in these vacancies and the combination of these two effects will cause a constant pattern in graphs of droplets radius and density and will lead to steady state situation. This can happen before and during sliding the big droplets.

Until now, the physical fundamentals of dropwise condensation have been introduced briefly. In the following, some theoretical aspects of dropwise condensation will be discussed including: spatial and temporal distribution of droplets and drop-size distribution function. Then, some simulation algorithms for generation droplets will be presented.

0.4 Spatial distribution

Spatial distribution describes the position of each point in n -dimensional space. This process has a great importance in some special fields of science. For example, by investigating the three dimensional distribution of the air bubbles trapped inside the Antarctic ice during decades, the ecologists succeeded to study the weather on the earth environment in the past eras [7, 59]. As another example, Teichmann *et al.* [60] used the points spatial distribution methods to study the patterns of deagglomerated alumina particles and the composition of Fontainebleau sandstone.

In dropwise condensation, points distribution can be used to study droplets spatial distribution. The importance of droplets distribution is because it can change both the rate of coalescence and the pattern of droplets at later stages. Meaning that if we manipulate the position of droplets on the substrate and put them closer together, they will coalesce faster and even they can form bigger droplets at later stages that are able to cover the substrate and changes dropwise condensation into filmwise mode.

Marshall *et al.* [61] proposed an empirical model based on the droplets fractal dimensions for the spatial distribution of droplets inside a cloud. According to their model the

probability of finding a droplet in a small element of space depends on its size. They emphasized that they used this method due to non-random nature of droplet distributions especially for big drops that can cluster. They assumed that the probability of finding a drop in a linear space with length l is a power law function with size dependent exponent.

$$P(l) = l^{-D(r)}, \quad (0-4)$$

where $D(r)$ is the power of length in the distribution function. $D(r)$ is a nonlinear function of r that lies between $[0,1]$ and according to probability theory is classified into three classes, $D = 1$ for absolutely continuous distribution, $D = 0$ for clustered or discrete distribution and $0 < D < 1$ for singular distribution. For small drops $D(r) = 1$ and indicates a dense distribution of the droplets, while for a few big drops that are sparsely distributed $D(r) = 0$. $0 < D(r) < 1$ indicates that frequency of droplets with size r reduces for bigger drops, meaning that by increasing r , the probability of finding droplet of size r reduces. Also in this case, the smaller D shows the larger degree of clustering.

It is worth pointing out here that the exponent 1 for small droplets which is well documented in the literature indicates the Poisson distribution for small drops. One of the features of Poisson distribution is that the probability of a single event occurring in the interval l is proportional to l [8] and this is exactly what resulted by $D(r) = 1$ for small drops.

So, the mean number $n(r, V)$ of drops with radius r in a volume V would be like equation below and $\delta(X)$ is the Dirac δ function. Meaning that, its value is zero except at $X = 0$ and its integral is 1 over the whole area [61]:

$$n(r, V) = N_S(V)\delta(r - r_S) + N_B(V)\delta(r - r_B), \quad (0-5)$$

where subscripts S and B denotes small drops and big ones respectively, $N(V)$ is the number of droplets in a volume V , and D as is explained above is the exponent of length in the distribution function .

$$N_S(V) = \rho V^{-D_S}, \quad (0-6)$$

$$N_L(V) = \rho V^{-D_B}, \quad (0-7)$$

So, Marshal *et al.* [61] have discovered that clustering of droplets is a function of their size r and that it can be encapsulated into a single function $D(r)$. Using only $D(r)$ makes it possible to create realizations of the location of every drop on the surface as a function of its size, and all such realizations naturally exhibit clustering of droplets bigger than about $14\mu m$ without introducing such clustering as an arbitrarily imposed constraint.

0.4.1 Poisson point process and Matern hardcore

There are some models that describe the different points spatial distributions. The first and basic model is Poisson point process that describes the completely randomly distributed droplets and is formulated as [62]:

$$P(X = k) = \frac{\mu^k \exp(-\mu)}{k!}, \quad (0-8)$$

where X is an event and k is a random variable like the number of droplets. For such a distribution the mean and variance are equal and represented by μ . A Poisson point process has three main assumptions:

1) The probability of detecting more than one point in a given interval δm is vanishingly small for sufficiently small δm (m can be volume or surface).

2) Points counts in non-overlapping intervals are statistically independent random variables (at any length scale) meaning that the probability of finding a point in each interval is independent of having a point in another intervals.

3) The process is statistically homogeneous which means that the mean and variance of random variable are constant along the domain of observation [49].

This model can describe adsorbing droplets spatial distribution on the flat substrates, because small droplets at initial stages obey all these three assumptions [63, 64]. So, it is possible to consider the distribution of initial droplets on the flat surfaces as a completely random distribution or Poisson point process. But regarding coalescing drops, they cannot satisfy the second assumption because their positions are dependent to their neighbors. Another more adapted model for coalescing drops is Matern II hard core [65]. Matern's classical hard core models can be interpreted as models obtained from Poisson point process, in which a solid ball of fixed radius is considered around each point. In Matern hard core I, a point is retained when its associated ball does not hit any other balls. Meaning that if two balls get in touch, then the two points related to their centers will be deleted from the spatial distribution. Matern hard core II process deletes the point that its random birth time is strictly smaller than the birth times of all balls hitting it [65]. This model can describe dropwise condensation process after coalescence, because if two droplets touch each other, then they will merge and form a bigger droplet. In other words, there are not any connecting couples that stay in touch for a long time unless they coalesce. This process is somehow the same as what happens in a Matern hard core II model: if two points get in touch, one of them (the younger one) will be deleted.

The traditional point pattern analysis was based on two assumptions: stationary and isotropic distribution [7]. The point process $\psi = x_1, x_2, \dots, x_n$ observed in a window $W \subseteq \mathbb{R}^d$ is stationary if its distribution is invariant by shifting \mathbb{R}^d [6]. Anisotropy can come from the changes in spatial distribution with respect to direction [66] or compression or dilation in the spatial patterns [59] or either clustering or anti-clustering [67].

There are lots of methods that investigate anisotropy in a defined spatial pattern. For instance, wavelet analysis [66] studies the points clustering in special directions. Redenbach *et al.* proposed a method for detecting anisotropies which are caused by compression of regular 3D point patterns [59]. Nicolis *et al.* [68] proposed a wavelet based hypothesis test using the empirical logarithm of directional scalogram as their test statistic for assessing isotropy. A more complete list of anisotropy analysis tests can be find in the work of Rajala *et al.* [6] including Ripley's function and Fry plot.

0.4.2 Ripley's function

Ripley's function evaluates the mean of pairwise distances of all points. It is a useful method to study the spatial distribution of points on a surface. The main idea of Ripley's function as is shown in figure 9 is to draw circles with different distances from a certain point and count the number of events in each circle. Ripley's k function $K(x)$ can be

calculated according to equation below.

$$K(x) = \lambda^{-1} \sum_i \sum_{j \neq i} w(l_i, l_j)^{-1} \frac{I(d_{ij} < x)}{N}, \quad (0-9)$$

where d_{ij} is the distance between the i th and j th points, λ is the density (number per unit area) of events, and $I(x)$ is the indicator function with the value of 1 if x is true and 0 otherwise. However, since the boundaries of the study area are usually arbitrary, edge effects arise because points outside the boundary are not counted in the numerator, even if they are within distance r of a point in the study area. The weight function, $w(l_i, l_j)$, provides the edge correction. It has the value of 1 when the circle centered at l_i and passing through the point l_j (i.e. with a radius of d_{ij}) is completely inside the study area. If part of the circle falls outside the study area (i.e. if d_{ij} is larger than the distance from l_i to at least one boundary), then $w(l_i, l_j)$ is the proportion of the circumference of that circle that falls in the study area. The effects of edge corrections are more important for large r because large circles are more likely to be outside the study area [69].

In practice it is easier to use linear form of Ripley's K function ($L(x) = \sqrt{\frac{K(x)}{\pi}}$) that is so called Ripley's L Function [69]. For a completely randomly distribution or Poisson point process Ripley's L function is a straight line of $F(x) = x$. In the case of clustering or dispersion the graph will deviate from this line. These definitions can be seen in figure 10.

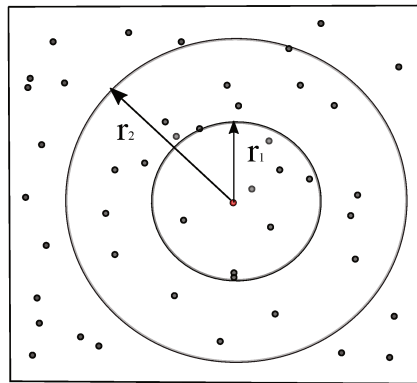


Figure 9: The main idea of Ripley's function is to count the number of points that are in distance r from center.

In the case of anisotropy, second order of Ripley's function (so called Ripley's K directional (K_{dir}) function) can be used that also takes into accounts the effect of rotation. Ripley's K_{dir} function counts the number of points in specified distance and specified angles with respect to each point. In two dimensional systems, one can assume a predefined element rotating around a center point and detecting the number of its neighbor points in specified distances and angles. After a complete rotation of 360° the radius of this element increases by a small amount like ϵ . Figure 11 shows two conical and cylindrical elements of K_{dir} function.

K_{dir} function in the element of $C_u(r, \theta)$ in direction θ and distance r can be noted by $K_{dir,u,\theta}(r)$ (see figure 11). An unbiased estimator of $K_{dir,u,\theta}(r)$ on the point process ψ is

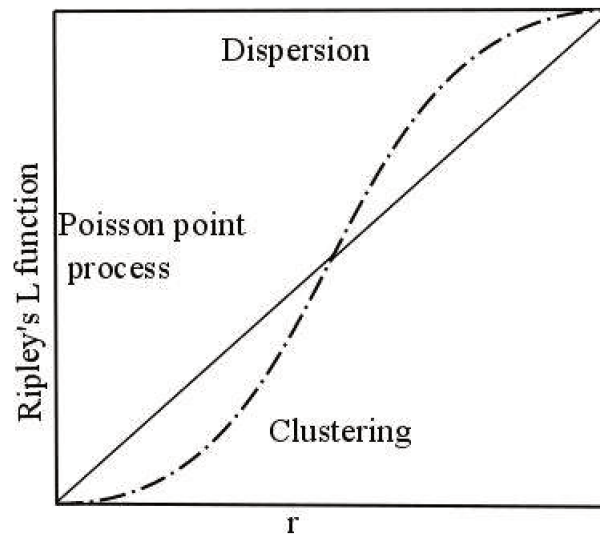


Figure 10: Ripley's L function, the straight line represents the Ripley's L function of Poisson point process. Positive and negative deviations from this line indicate dispersion and clustering of the points.

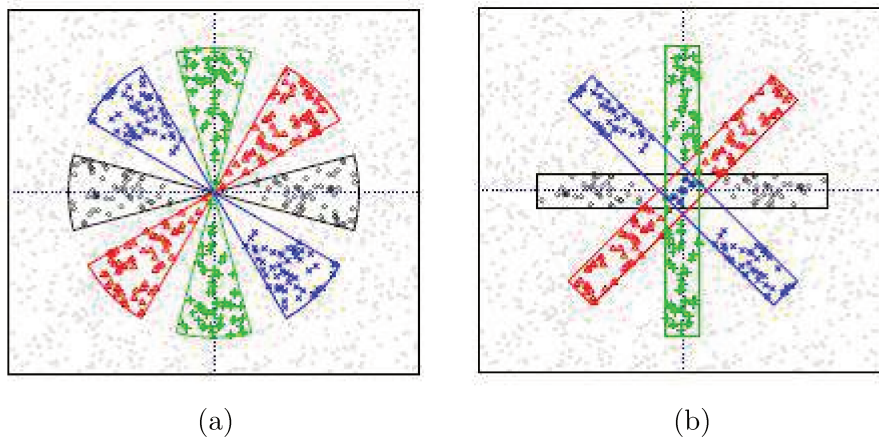


Figure 11: (a) Conical and (b) cylindrical elements for K_{dir} function. Meaning that this cone or cylinder sweeps the area around a center point and detects the number of points in the sweeping area. Then, after 360° its radius increases by a small amount like ϵ [6].

given by [59, 70]:

$$K_{dir,u,\theta}(r) = \lambda^{-2} \sum_{x \in \psi} \sum_{y \in \psi, y \neq x} \frac{I_{C_u(r,\theta)}(x-y)}{|W_x \cap W_y|}, \quad r \geq 0, \quad (0-10)$$

W_x is the translation of the window W by the vector x , and $|B|$ denotes the volume of a set $B \subset \mathbb{R}^3$.

0.4.3 Fry plot

Another tool to study and visually representative the isotropy of a point process is Fry plot. Fry [67] considers that if we plot the pairwise difference vectors $x_i - x_j$ for all point pairs in a regular point distribution, the central area around the origin will have fewer points, that indicates less pairs at short distances than long distances. For an isotropic distribution, the shape of the central vacant area will be circular, while in the case of anisotropic process it can be ellipsoidal. The clustered pattern shows a somewhat inverse structure: the central area is dense, typical for clustered processes [6]. Rajala *et al.* [7] then fitted ellipsoids to the empty space in the center of Fry plot to estimate the direction of the linear transformation in the case of geometric anisotropy. Figure 12 shows an example of Fry plot and the fitted ellipsoid in the vacant zone at origin.

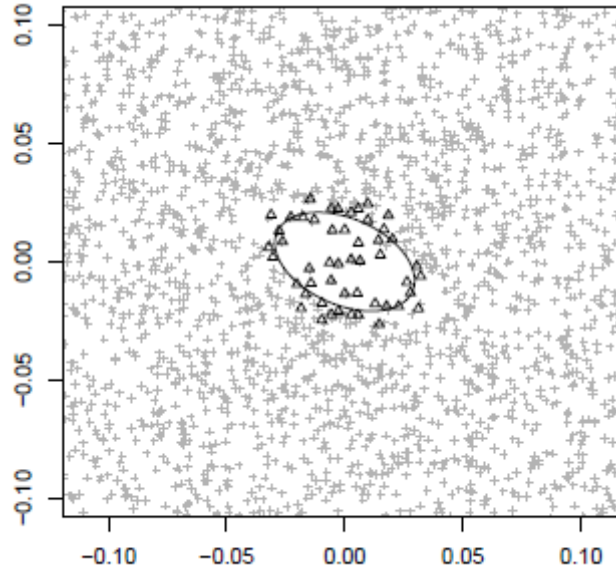


Figure 12: An example of Fry plot with fitted an ellipsoid in the vacant zone at origin. Image from [7].

The tools that are presented in this section will be used to study the spatial distribution of water droplets on the flat and textured substrates.

0.5 Droplets temporal distribution

As was mentioned above, all three latest steps of dropwise condensation: coalescence, nucleation of new small droplets, and departure of big droplets change droplets density and lead to a temporal distribution of droplets. Although in this thesis we will not study droplets temporal distribution, it is interesting to present some methods that were used before in this regard. In contrary to spatial distribution, the temporal distribution is not a random process especially for bigger droplets. It is mentioned before that most of the studies related to temporal distribution of droplets is done on the rain drops that fall on a substrate, but due to the similarity between these two processes they can be considered as good inspiration for droplets temporal distribution during dropwise condensation. Kostinski and Jameson [8] proposed a Poisson mixture process that had better estimation than a pure Poisson distribution of droplets temporal distribution. Generally, the Poisson distribution (equation (0–8)) is a function of one parameter, the mean, that is equal to the variance. There are two natural generalizations of the Poisson process in the statistical literature: a Poisson process having a time-dependent mean and a Poisson process with the mean as a random variable (the so-called “doubly stochastic Poisson process” or the “Poisson mixture process”, for short).

In the first one, mean is a time-varying but a deterministic parameter. So the number of droplets observed over time can be calculated by rewriting Poisson process (equation (0–8)) by integration of variable mean over the whole observation time T .

$$P(X = k) = \frac{\int_0^T \mu(t) dt \exp(-\int_0^T \mu(t) dt)}{k!} \quad (0-11)$$

where k is the event and μ is the average of k . In the Poisson mixture process, $\mu(t)$ is itself a random variable (unpredictable). So the whole area or time must be patched into smaller parts, in which mean $\mu(t)$ that is equal to variance (σ_k^2) is constant and therefore a distribution like $f(\mu(t))$ can be assumed for each patch. This bears in mind the concept of coherence time (τ) that is the shortest time interval in which the distribution of droplets size is constant. In this point of view there are two sources of randomness in such a process:

1. Poissonian fluctuations (σ_p^2), this is the variance of a complete Poisson process and happens at steady condensation rate, meaning that the average number of droplets per time is constant and is equal to global mean ($\mu(t) = \mu$).
2. The fluctuations in the condensation rate (σ_k^2) due to the un-predictable nature of $\mu(t)$ because the average number of droplets changes over time.

Since these sources of randomness are statistically independent, the total variance can be calculated as bellow:

$$\sigma_k^2 = \sigma_p^2 + \sigma_{\mu(t)}^2, \quad (0-12)$$

where, $\mu(t)$ can be interpreted as the mean concentration of drops per unit time, while k would be the number of drops actually observed in one unit time. They supposed μ being the global mean, global here refers to long time average comparing to the coherence timescale.

For Poisson mixture process the distribution of number of droplets during time interval $[0, T]$ is a Poisson equation (equation (0–8)) with a function of variable mean:

$$P(k) = \frac{\int_0^T \left(-\mu(t) \exp f(-\mu(t)) \right) d\mu(t)}{k!}. \quad (0-13)$$

The distribution of $P(X = k)$ depends on the shape of $f(\mu(t))$. For example if $f(\mu(t))$ is an exponential distribution, P will be a geometric distribution and for $f(\mu(t))$ as a Gamma function P will be a negative binomial distribution. These differences can be seen in figure 13. So the key point in this process is to choose the best $f(\mu(t))$ that is in agreement with the experimental results.

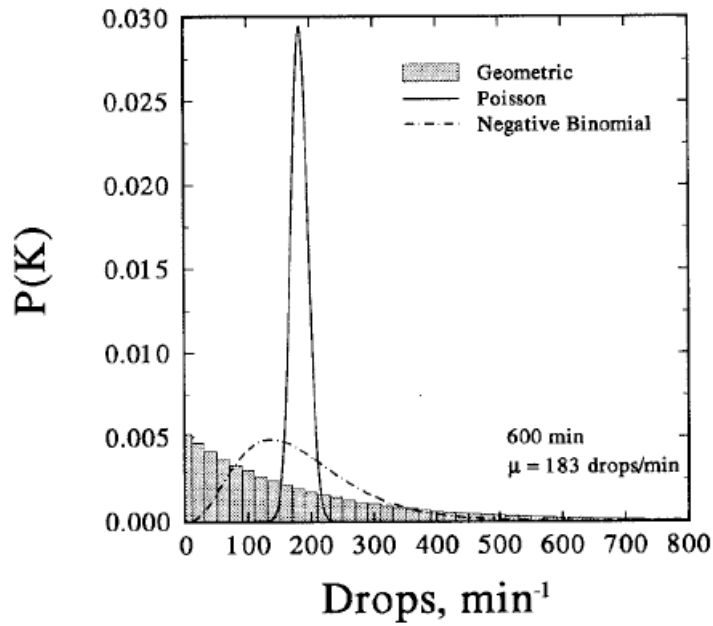


Figure 13: Comparison of three PDFs for a certain rain drops within $T = 600min$ and $\mu = 183drops/min$ [8]. The distribution of $P(X = k)$ depends on the shape of $f(\mu(t))$.

Since Kostinski considered mixed Poisson distribution in which mean is a random function and fluctuates over time, for defining $f(\mu(t))$ they needed the concept of coherence time (τ) that is the time interval in which $\mu(t)$ is constant. In order to estimate $\mu(t)$ in each patch, the counting interval t must be smaller than the coherence time τ of the patch, so that many trials can be performed. On the other hand, the full description of $f(\mu(t))$ requires that the entire observation period T be much larger than t . Hence, in order to estimate $f(\mu(t))$ with sufficient resolution and accuracy, they must satisfy

$$t \ll \tau \ll T \quad (0-14)$$

They considered $t = 10min$ in the total time $T = 900min$, and $f(\mu(t))$ as a Poisson

process in each of 90 patches. The results can be seen in figure 14. According to this figure there is a good agreement between observed data and Poisson mixture process. While, Poisson itself could not predict the phenomena.

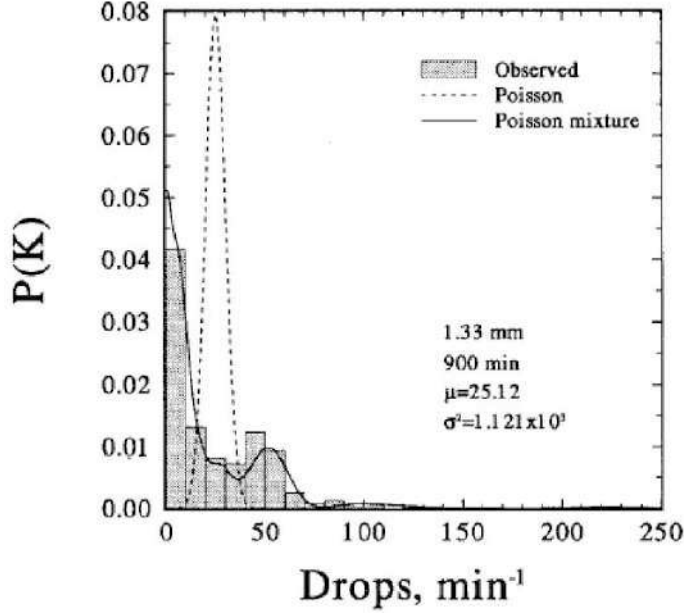


Figure 14: The PDF of a Poisson and Poisson mixture distribution for rain drops compared with real observed data over $T = 900min$ and $t = 10min$ in [8].

Damit and his team [71] used three parameters to investigate the transfer time from Poissonian distribution, for the temporal distribution of four different sizes of nanomaterials dispersed in an aerosol: distribution pair-correlation function (PCF), scaled clustering index (SCI), and coefficient of variation (CV).

They assumed the probability of finding a particle in time interval dt equal to $\frac{N}{T}dt = \bar{N}dt$. According to Poisson distribution since the particles are randomly distributed, the probability of finding two droplets on dt_1 and dt_2 is equal to:

$$P(t) = \bar{N}^2 dt_1 dt_2, \quad (0-15)$$

where dt_1 and dt_2 are separated by the time Δt . Thus if the droplets are not randomly distributed, there must be a term that shows the dependency between time intervals, that is PCF or $\eta(t)$.

$$P(t) = \bar{N}^2 dt_1 dt_2 (1 + \eta(t)) \quad (0-16)$$

This is apparent that for Poissonian process $\eta(t) = 0$. PCF shows the relevance of the probability of the particle detection in two different time zones with the distance of Δt . A simple formula that can describe this function is as below that was used by several authors [71, 49, 50]:

$$\eta(t) = \frac{\overline{N(t_0)k(t)}}{\mu^2} - 1, \quad (0-17)$$

where μ is the long-term mean over the entire period of observations and $\overline{N(t)}$ is the average number of points in time t , that is in the distance of Δt from time t_0 . In reality, the drop flux is always random and varies from moment to moment, for a statistically stationary process the average number of drops during Δt over the entire observation period T still remains constant. That is, assuming $\overline{N(t_0)}$ and $\overline{N(t)}$ are statistically independent, as they would be for a Poisson distribution, $\overline{N(t_0)k(t)} = \mu^2$ so that $\eta(t) = 0$.

$\eta(t)$ can include the amounts between $[-1, +\infty)$. A system exhibiting Poisson statistics at all temporal scales should have $\eta(t) = 0$ for all t . Likewise, for any scale with $\eta(t) = 0$, there are no correlations present on that scale, though there may be non-unity σ^2/μ^2 ratio or deviations from the Poisson relation resulting from correlations at shorter scales. Also $\eta(t) < 0$ physically suggests that the probability of detecting a particle at $t_0 + t$ given a particle at t_0 is less than the amount would be expected in a Poisson distribution, that is the negative effect of two probability in each other. Moreover $\eta(t) = -1$ states that it is impossible to have a mutual detection at $t_0 + t$ and t_0 [71].

Another widely used parameter called scaled clustering index (SCI) or the time- or volume-averaged PCF. The SCI indicates how particle detection deviates from a Poisson process over a sampling period with length of s .

$$SCI = \frac{\sigma_s^2 - \mu}{\mu^2}, \quad (0-18)$$

where σ_s^2 and μ are the variance and average of the observations and since these two parameters are equal in Poissonian distribution $SCI = 0$ in such conditions.

Coefficient of variation ($CV = \sigma^2/\mu$) practically describes how a measured concentration would change from sample to sample (for a specified sampling period) due to random fluctuations. Larsen proposed to not use this ratio because there are two problems with this parameter [71].

1. Finding a unity σ^2/μ ratio at one scale does not necessarily imply that the underlying distribution obeys Poisson statistics at all scales.
2. It is not known that what departure from a σ^2/μ ratio of unity is significant. Careful consideration may reveal that a σ^2/μ ratio of 1.2, for example, is in some cases a significant departure from a Poisson expectation and in other cases close enough to be within sampling error due to the finite nature of the data.

According to the results of Demit's study, the distribution is in relationship with the size of the particles in a solution and Poisson process is valid for nanoparticles, contrary to micro size particles and for particles bigger than $10nm$ there are some fluctuations from Poisson distribution. The same conclusion might be possible for small and big droplets, because big droplets tend to coalesce and so do not obey the Poissonian distribution rules. This was the conclusion that was made in the spatial distribution too.

Scott [72] developed the probability of having droplets in each size intervals and the probability of coalescence by the concept of Poisson distribution. He considered a situation in which droplets are distributed over space according to their sizes. So he considered

$PN(v_1, v_2, \dots, v_N, t)dv_1, dv_2, \dots, dv_N$ as the probability of finding N drops at sizes between $[v_1, v_1 + dv_1], [v_2, v_2 + dv_2], \dots, [v_N, v_N + dv_N]$ at time t and a specified volume of space. So over the whole observation time, T , the total amount of droplets can be calculated by the following integral. Dividing by $N!$ is to compensate for counting all the $N!$ physically equivalent ways of arranging the drops in order of size, $v_1 < v_2 < \dots < v_N$, and then considering both changes in the order of integration and interchanges of the variables subscripts. He emphasized that the Poisson process is a good approximation for the distribution of droplets in a small range of volume or space.

$$N_S(t) = \sum_{N=1}^{\infty} \frac{1}{N!} \int_0^{\infty} d\nu_1 \dots \int_0^{\infty} d\nu_N P_N(\nu_1, \dots, \nu_N). \quad (0-19)$$

This section was dedicated to presenting some methods that were used to describe droplets temporal distribution. It is just an introduction to this interesting subject, though for the rest of this manuscript droplets temporal distribution will not be discussed.

0.6 Droplets size distribution function

Another important parameter in a process of dropwise condensation is the droplets size distribution function at each time step. Knowing the number of droplets at each size range plays a great role in calculating total heat transfer flux. Le Fevre and Rose [73] modeled the heat transfer through a single droplet considering the effects of surface tension, conduction, and dissipation associated with mass transfer during condensation. In order to be able to determine the total heat transfer, they proposed a power law equation for the area fraction covered by droplets within a specified size range. Subsequently, by integrating the obtained surface fraction, they could calculate the total heat transfer. This also formed the initial idea for developing the size distribution function of droplets. Next, Rose [74] divided the droplets into two categories: adhering and falling. He then emphasized that their proposed model works well only for the adhering droplets and attempted to modify the heat transfer model for the falling droplets.

Drop-size distribution function ($f(r)$ for droplets smaller than r_c and $F(r)$ for bigger droplets) represents the changes in the number of droplets ($\Delta\bar{N}$) at each size interval of ($r, r + \Delta r$) per unit area (A). Therefore, considering $\Delta r \rightarrow 0$ we will have:

$$f(r) \quad \text{or} \quad F(r) = \frac{-d\bar{N}}{A.dr}. \quad (0-20)$$

The negative sign in this equation shows the opposite relation between size and number of droplets, meaning that the number of droplets decreasing by increasing their size. Lots of studies have been performed up to now for predicting $F(r)$ specially for big droplets. Most of the initial works were carried out by Rose which lead to a considerable amount of research findings in this regard. Rose and Glicksman [13] developed the size distribution function for coalescing droplets using the power law equation proposed before by Le Fevre and Rose [73]. They considered S (the total area covered by droplets with radius greater than r) as a power law function with respect to r :

$$S = 0 - \left(\frac{r}{r_{max}}\right)^\epsilon. \quad (0-21)$$

If we consider N as the number of big droplets of each generation per unit area of generation, the size distribution function proposed by Rose and Glicksman is [13]:

$$F(r) = \frac{-dN}{dr} = \frac{-1}{\pi r^2} \frac{dS}{dr} = \frac{\epsilon}{\pi r_{max}^3} \left(\frac{r}{r_{max}}\right)^{(\epsilon-3)}, \quad (0-22)$$

where ϵ is the drop-size distribution exponent and must be determined experimentally. Rose and Glicksman [13] reported $\epsilon = 0.382$ based on the theoretical evidences. Wu [12, 45] assumed $\epsilon = \frac{1}{3}$ based on the experimental works of Graham and Griffith [75] and Tanaka [58] that reported ϵ laying in the real number range [0.313-0.350]. Mei [45] also used $\epsilon = \frac{1}{3}$ based on experimental results of other researchers. The most frequently reported value for ϵ in literature is around $\frac{1}{3} = 0.33$ [75].

In fact Rose and Glicksman [13] determined the average distribution of drop size over a complete cycle as a function of fraction of available area, maximum radius of any generation, and the growth rate of a generation. In their point of view a generation of droplets consists of droplets that nucleate at the same time and grow together. This is a very successful model and has been cited in all the succeeding works. They determined the average size distribution of droplets over a complete cycle as a function of the available area fraction, maximum radius and growth rate of each generation. Maximum radius of each generation of droplets before sliding (r_{max}) can be derived by force balance between surface tension $F_\sigma = 2\sigma r_{max} \sin\theta_e (\cos\theta_r - \cos\theta_a)$ and droplet weight $F_g = (2 - 3\cos\theta_e + \cos^3\theta_e)\pi r_{max}^3 \rho_l g$ [25] and for hemisphere droplets is [76]:

$$r_{max} = \sqrt{\frac{6(\cos\theta_r - \cos\theta_a)\sin\theta_e\sigma}{\pi(2 - 3\cos\theta_e + \cos^3\theta_e)\rho_l g}}, \quad (0-23)$$

where σ is liquid surface tension, ρ_l and ρ_v are liquid and vapor density respectively, and g is the earth acceleration. θ_a and θ_r are advancing and receding contact angles and $\theta_e = \cos^{-1}(0.5\cos\theta_a + 0.5\cos\theta_r)$ is the apparent equilibrium contact angle. Equation (0-22) has a good understanding of big droplets behavior and was frequently used by many authors up to now. But when the majority of droplets are smaller than r_c , Rose model is not able to predict their size distribution very precisely. Most of the time the logarithmic version of this equation is used to describe the spatial distribution pattern of droplets:

$$\log\left(\frac{-dN}{dr} r_{max}^3\right) = \log\left(\frac{\epsilon}{\pi}\right) + (\epsilon - 3)\log\left(\frac{r}{r_{max}}\right) \quad (0-24)$$

The logarithmic scale is more preferable because the terms are dimensionless and thus easier to compare. Moreover, droplets nucleation function is normalized for size of droplets and area of fractal zone and thus the results will be independent of experimental situation.

Baojin and his colleagues [27] then developed the Rose model considering parameters such as the contact angle and its hysteresis, the nucleation site density, the fractal dimension of droplets sizes, and the maximum and minimum drop radius. Wu *et al.* [12] introduced an algorithm to generate droplets based on the Rose model and calculate the rate of heat transfer based on this algorithm.

To investigate time-series features and the percentage of surface occupied by droplets, Tanaka [57] numerically solved two equations relating to the spatial distribution of droplets

. He proposed another theory that indicates dropwise condensation is closely influenced by three dynamic characteristics: (1) drop-size distribution density, (2) substantial growth rate of drops by condensation, and (3) growth rate of drops by both condensation and coalescence [77, 57]. Abu-Orabi [47] tried to develop the Rose model for small droplets considering the effect of surface renewal parameter. This parameter describes the rate of surface cleaning by sliding of big droplets and finally lead to a complex size distribution model. His model is applicable for the adsorbing droplets at later stages when there are big droplets that slide. In his model if we neglect the effect of surface renewal that is the case at earlier stages, the model shows considerable errors.

Continuing the attempts to derive a model describing evolution of the nucleation site density during time, Vemuri and Kim [34] developed their model using the population balance concept to predict the drop-size distribution of small drops which grow mainly by direct condensation. Tianyi *et al.* [35] presented a clustering physical model to describe the state of steam molecules before condensing on the cold substrate that affects droplets size distribution. El-Adawia and Felemban [78] suggested a statistical model to describe the distribution of droplets size.

Tanasawa and Ochiai [77] made a lot of experimental and numerical investigations and presented a power law model for describing drop size distribution function. More recently Mei *et al.* [45, 79] developed a fractal model based on fractal geometry theory for describing the relation between drop size distribution function and average radius. They supposed that since the pictures taken at different scales from droplets during dropwise condensation are the same, the droplets will follow the law of fractal geometry theory. According to fractal geometry theory, in a fractal zone if we assume the size of the biggest particle equal to l_{max} made up of smaller units with size of l , the number of fractal units bigger than l is [80]:

$$N = \left(\frac{l_{max}}{l}\right)^{d_f} \quad (0-25)$$

$$d_f = \lim_{r \rightarrow 0} \frac{\log(N)}{\log\left(\frac{r_{max}}{r}\right)} \quad (0-26)$$

where d_f is the fractal dimension and is different for each of fractal patterns. For two dimensional droplets growing on a flat surface d_f is smaller than 2, while for three dimensional ones d_f is smaller than 3 [79]. Based on fractal geometry theory, the cumulative number of droplets bigger than a specified value of r on a flat surface during dropwise condensation is:

$$N = \left(\frac{r_{max}}{r}\right)^{d_f}, \quad \text{for } r_{min} < r < r_{max} \quad (0-27)$$

By differentiating from equation (0-27) with respect to r , the differential distribution function of droplets size will be:

$$f(r) = \frac{-dN}{dr} = \frac{d_f}{r_{max}} \left(\frac{r_{max}}{r}\right)^{d_f+1} \quad (0-28)$$

The negative sign indicates opposite relation between size and number of droplets. Equation (0-28) in log-log system is a straight line with slope and intercepts that are function of d_f :

$$\log\left(r_{max} \frac{-dN}{dr}\right) = \log(df) - (df + 1)\log\left(\frac{r}{r_{max}}\right) \quad (0-29)$$

To be able to derive an average model comparable with equation (0-22), this equation must be divided by the total area occupied by fractal particles. Total area of a fractal zone was calculated by Mei [45] by integrating equation (0-28) :

$$A = \int_{r_{min}}^{r_{max}} -dN\pi r^2 = \frac{\pi d_f(0 - \phi)r_{max}^2}{(2 - d_f)\phi} \quad (0-30)$$

where ϕ is the fraction of covered area by a fractal zone and is equal to:

$$\phi = \left(\frac{r_{min}}{r_{max}}\right)^{2-d_f} \quad (0-31)$$

where r_{min} is the size of the smallest viable droplets and must be calculated based on physical evidences [43]:

$$r_{min} = \frac{2\sigma T_s}{H_{fg}\rho\Delta T_t} \quad (0-32)$$

It is obvious that r_{min} is just a function of the process conditions and physical properties of liquid. Dividing equation (0-29) by equation (0-30) and next taking logarithm, we will get the average distribution function of droplets for Mei model:

$$\begin{aligned} \log(N_{ave}) &= \log\left(\frac{(2 - d_f)\phi}{\pi(0 - \phi)}\right) \\ &+ (d_f - 2)\log(r_{max}) - (d_f + 1)\log(r_{ave}) \end{aligned} \quad (0-33)$$

This equation represents a straight line with slop and intercept as functions of d_f and surface coverage(ϕ). Both of these parameters are depended on temperature difference between cold substrate and hot air. Equations (0-29) and (0-33) are differential and average Mei distribution of droplets during dropwise condensation. These two formulas are based on the fractal geometry theory and assume the droplets as fractal particles growing in a fractal zone with area equal to equation (0-30). The importance of this model is due to describing drop size distribution function by parameters that have physical meanings, such as fraction of area covered by droplets, fractal dimension of droplets pattern, and the maximum radius of droplets.

In other work, Rumaa [9] tried to develop a model based on the three concepts birth function $B(r)$, death function $D(r)$, and population density function $N(r)$. He derived these functions by the probability of coalescence between the droplets using the assumptions of homogeneity and constant probability of finding a drop over space. These three concepts were defined as below:

- $B(r)dr$ is the number of drops within the size range $(r, r + dr)$ produced by coalescences of smaller drops per unit surface area per unit time.
 - $D(r)dr$ is the number of drops raised from the size range $(r, r + dr)$ to larger size owing to coalescence per unit surface area per unit time.
 - $N(r)dr$ is the number of drops within the size range $(r, r + dr)$ per unit surface area.
- Mass balance rules force the above concepts to be in relation like:

$$B(r) - D(r) - \frac{N(r)}{\dot{t}} - \frac{dN(r)G(r)}{dr} = 0. \quad (0-34)$$

Where $G(r)$ is the growth rate of a single droplet and the last term of the left hand side of this equation relates to the number of drops per unit time and unit surface area that enter the size rang $(r, r + dr)$ due to droplets growth. \dot{t} is the revers of the sweep frequency and since dimension of $N(r)$ is $1/m^2$ and dimensions of other terms are $\frac{1}{sm^2}$, $N(r)$ must be divided by \dot{t} . Thus, the physical meaning of the third term is the number of drops within the size range $(r, r + dr)$ per unit surface area per unit time. All the above functions were defined using the concept of probability. The probability that a droplet with the size r (that is growing with rate $G(r)\Delta t$) cannot coalesce with a droplet of size x (that is growing with rate $G(x)\Delta t$) within a time interval Δt is equal to

$$P_{rx} = \exp\{-a_{rx}N(x)\Delta x\}. \quad (0-35)$$

Where a_{rx} is the area of a circle in the center of droplet r and radius $r + x$. This droplet is shown in figure 15. In this figure the shaded area represents the growth rate of big droplet after coalescence.

$$a_{rx} = 2\pi(r + x)\{G(r) + G(x)\}\Delta t. \quad (0-36)$$

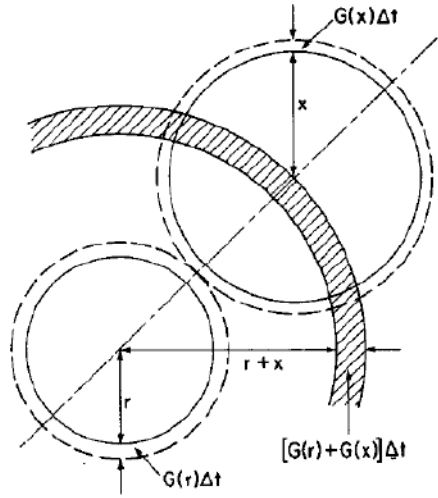


Figure 15: Coalescence model of two droplets

So, the probability that droplet of size r dose not coalesce with any droplet of any other sizes within a time interval δt is

$$P_{r1} = \exp\left\{ \sum_{x=r_{min}}^{x=r_{max}} -a_{rx}N(x)\Delta x \right\}, \quad (0-37)$$

and the probability that droplet of size r can coalesce with other droplets within a time interval Δt is

$$P_{r2} = 1 - \exp\left\{ \sum_{x=r_{min}}^{x=r_{max}} -a_{rx}N(x)\Delta x \right\}. \quad (0-38)$$

Considering these definitions and $N(r)\Delta r$ as the number of droplets in the size range $(r, r + \Delta r)$ in the unit area, death density functions can be calculated as below:

$$D(r)\Delta r = \frac{1}{\Delta t}N(r)\Delta rP_{r2}. \quad (0-39)$$

Now, for estimating birth density function, consider the situation that droplets of sizes y and z which are smaller than r join to each other and form a droplet with size r . So, for the coalescence of these two droplets equations (0-35) to (0-37) can be written for P_{y1} , P_{y2} , and a_{yz} . Then birth density function for the droplets with size r , which are the results of coalescence of droplets y with other droplets, can be calculated as below:

$$B(r)\Delta r = \frac{1}{\Delta t} \sum_{y=r_{min}}^{y=r} P_{ry}N(y)\Delta y. \quad (0-40)$$

This is important to note that the upper limit of integral is $y = r$, this means that just droplets of size $(y, y + \Delta y)$ that are smaller than r can coalesce and form a droplet in the size range $(r, r + \Delta r)$ in the unit area. P_{ry} is the probability of producing a drop in the size range $(r, r + \Delta r)$ from this y drop

$$P_{ry} = P_{y1} \frac{a_{yz}N(y)\Delta y}{\sum_{z=r_{min}}^{z=r_{max}} a_{yz}N(z)\Delta z}. \quad (0-41)$$

By solving the above equations by numerical relaxation method, Rumma [9] could get the population density function of N droplets with different sizes. The results showed that there are a minimum and a maximum in the drop size distribution function as is shown in figure 16. The minimum is when the predominant mechanism for droplet growth is direct condensation. Then by continuing the process, bigger drops coalesce and at the same time in their empty area, new small drops nucleate and grow. At this time both coalescence and diffusion are responsible for droplets growth and the number of drops reach to its maximum value.

Finally Watanabe [81] summarized the referent models that were successful in describing drop-size distribution function. Then, he used the image-processing approach to evaluate the geometric parameters, including the distribution degree and clustering coefficient of target drops having radius greater than $0.05mm$ [82].

0.7 Algorithms for simulating dropwise condensation

In order to numerically simulate dropwise condensation four main steps of the process must be taken into account: nucleation of small droplets, adsorption, coalescence and big drops departure. Therefore, the algorithm always starts with some amount of droplets that grow through a main loop consisting of the last three steps named here. There were

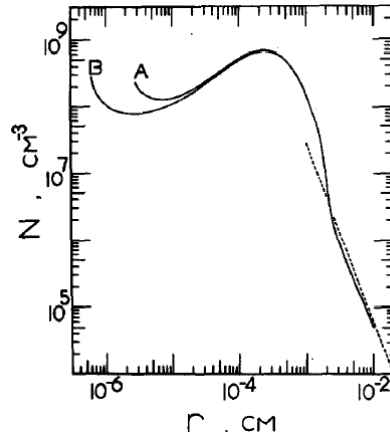


Figure 16: Drop size distribution for condensation of saturated steam at $100^{\circ}C$ with $N_s = 5 \times 10^6 cm^{-2}$. A, $\Delta T = 1^{\circ}C$; B, $\Delta T = 4^{\circ}C$. broken line, experimental data [9].

some weaknesses in the initial attempts for generating droplets by this algorithm. For example, Glicksman *et al.*[83] considered the monodispersity of the initial configuration of droplets meaning that all the initial droplets had the same size. As another example of lack of information at the very first simulating algorithms, Gose *et al.* [10] calculated the growth rate considering just the effect of heat convection through a droplet. Also, in some other articles the center point of droplets after coalescence was considered at the center of bigger droplet [11]. This classic algorithm was modified step by step but still has inaccuracy in some details. For example, the spatial distribution of droplets was not studied. Spatial distribution deals with the position of droplets on the substrate that can affect the coalescence procedure. Also the size distribution of new nucleations was not considered in these studies.

Earl *et al.* [10] proposed an algorithm to simulate the droplets formation on the flat surface, starting with 200 random points. They considered the growth rate of droplets according to equation (0-42).

$$r_{new} = \sqrt{r_{old}^2 + \frac{2a_1\Delta t}{3a_2}}, \quad a_1 = \frac{1}{r} \frac{dV}{dt}, \quad a_2 = \frac{V}{r^3}. \quad (0-42)$$

At each step two main lists were defined to check the coalescence:

1. Neighboring list for a specific droplet i : consists of the droplets that are in vicinity of this droplet. In this regard, the distance between each droplet like j with a droplet i is calculated according to equation (0-43) and if the distance is less than $2r_c$, droplet j is considered in the neighboring list of droplet i . The drops in the neighboring list have the chance to coalesce with droplet i . After coalescence, the radii of the smaller drop was set at zero and the center of the daughter drop at the center of its bigger parent.

$$D_{i,j} = \sqrt{(x_i - x_j)^2 + (y_i - y_j)^2} \quad (0-43)$$

2. Covered site list: sites on this list are covered by a drop that is centered in another site. The sites in this list are not allowed to grow any droplet before that drop slides.

The main algorithm used by Earl *et al.* [10] is shown in figure 17. The program was written in ALGOL and run on a UNIVAC-1107 digital computer. The model took into account the drops growth by coalescence, re-nucleation on the newly exposed sites and then drops removal. The theory shows that in order to account for the heat-transfer coefficients in steady-state dropwise condensation, the minimum nuclei density must be $5 \times 10^4 \text{ sites/cm}^2$. Nucleation site densities slightly larger than this minimum value have been observed by Tammann and Boehme [84], Peterson [85], McCormick and Baer [86], and Welch and Westwater [42].

Continuing the study, Andrew and Gelicksman developed a statistical method for simulating the phenomena that is somehow with the same algorithm which was mentioned in figure 17 [83]. The model was written in Fortran 77 to carry out the simulation procedure starting with 1000 random sites that were generated by the six-place random number generator. It was run on a 16 Mb ram, 50 MHz, PC. In this method the check for coalescence was done at each time step and the center of the new drop after coalescence was set at the center of bigger drop like Earl's method presented in figure 17. The coalescence check was done by assuming a square with side length of $2r$ around each drop and checking for any overlaps in these squares. This program was used to calculate heat transfer coefficient, nucleation site density, and average nuclear radius. The results of this model were compared with McCormick and West experimental results [87].

Figure 18 shows the algorithm that Burnside and Hadi [11] used to simulate dropwise condensation. Comparing the two methods of figures 17 and 18 will reveal that Burnside and Hadi used more specific method for coalescence calculations. They calculated the size of new droplet according to equation (0-44) using the summation of the volumes of the coalescing drops. While Earl's method predicts this parameter equal to the size of the bigger droplet.

$$r = \sqrt[3]{\frac{3V}{2\pi}} \quad (0-44)$$

Wu and his colleagues [12] developed a method based on fractal dimensions but for randomly distributed nucleation sites, called random fractal model. They developed the concept of probability of finding a droplet in a grid, P , which is equal to the fraction of area covered by the droplets surface to empty area. The authors suggested to divide a square with surface of unity into γ^2 smaller squares and select $P \times \gamma^2$ squares randomly as the first generation, in which $0 < P < 1$. In order to construct next generation, in each step the squares were divided into smaller squares by the coefficient of $\frac{1}{\gamma}$, where γ was the side length of the squares in each step. Then some of these small squares were randomly selected as the second generation of nucleation cells. In this method, the probability of finding a droplet in a grid is equal between all the generations. Using this algorithm, they could obtain the lifelike picture of drop distribution in dropwise condensation that is very similar with photographs of dropwise condensation as is shown in figure 19.

In each step they found the probability of finding a drop in a grid by the renormalization group method as follow.

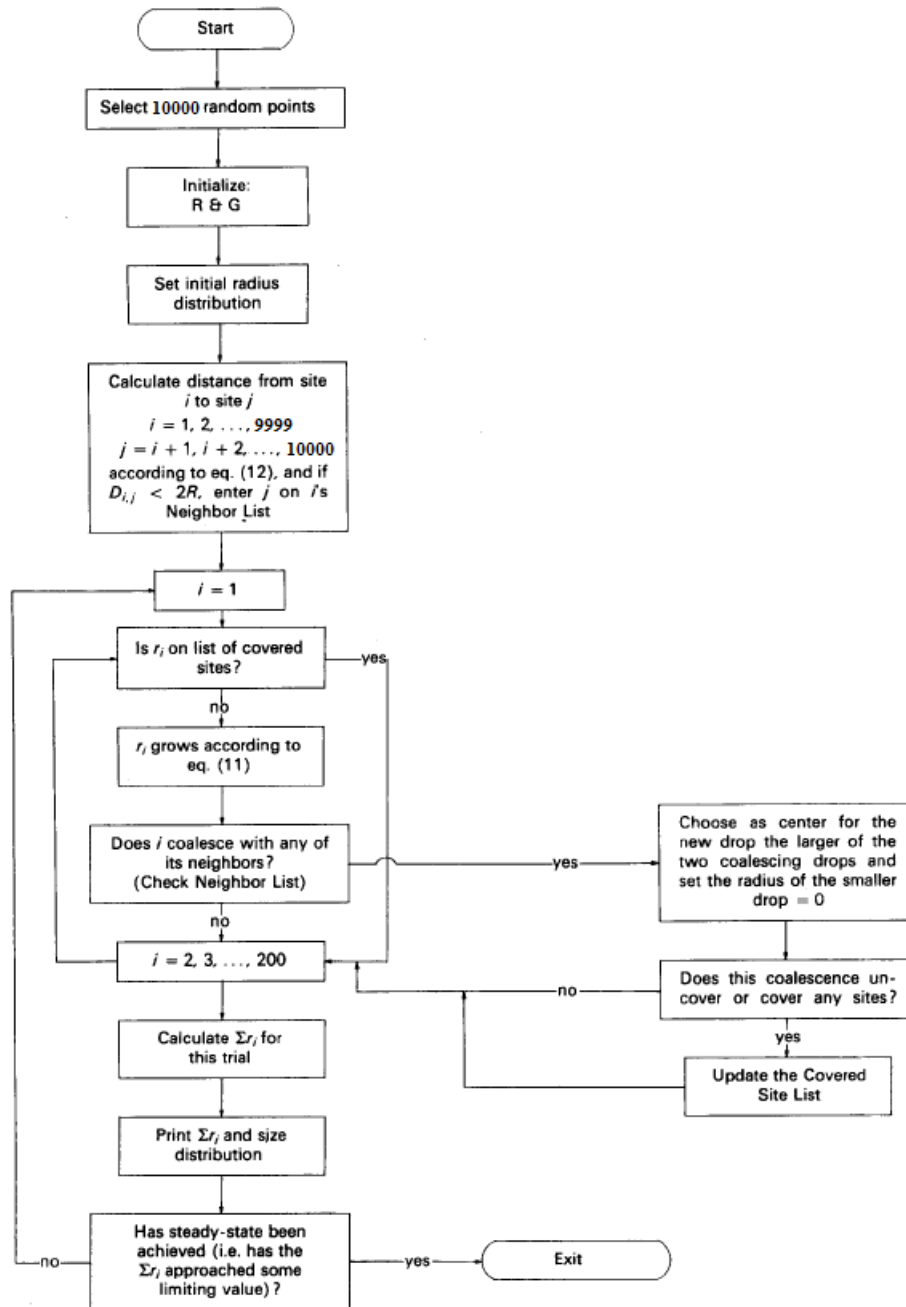


Figure 17: Flow diagram of computer simulation used by Earl *et al.* to simulate droplet growth [10]

$$P = P^4 + 4P^3(1 - P) + 4P^2(1 - P)^2 \quad (0-45)$$

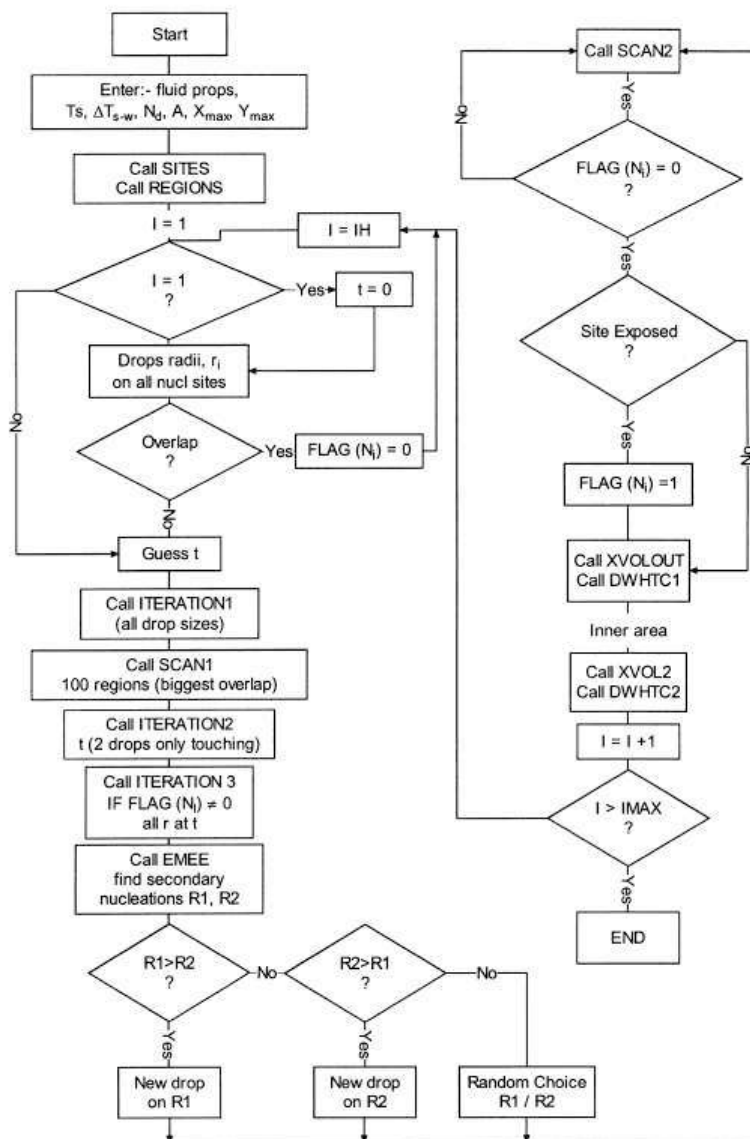


Figure 18: Flow diagram of computer simulation used by Burnside and Hadi to simulate droplet growth [11]

This equation has maximum 4 roots and only the roots which satisfied the condition $0 < P < 1$ were accepted. They also proposed a compensation factor equal to $\pi/4$ to change the small square into spheres. These calculations were proceeded in each generation until the steady state was reached, in which the difference of two radius of two following steps

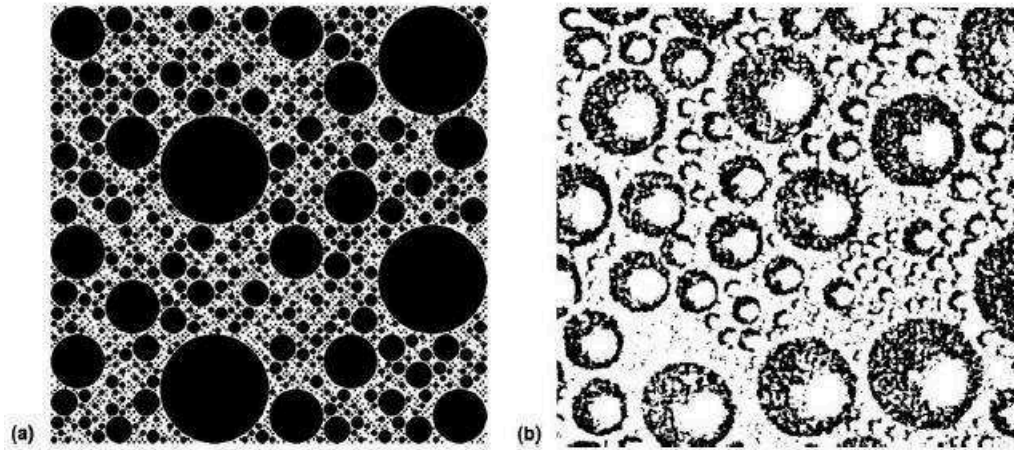


Figure 19: Comparison of drop distribution between random fractal model and photography. (a) random fractal model, (b) close-up photography of condensing surface [12]

were negligible. It was found that the values of $P = 0.55$ and $\gamma = 5.29$ have the best agreement with the experimental results of Rose and Glicksman [13].

Rose and Glicksman also considered the same P in each step. In order to estimate this parameter they used a step-by-step program like the one that was discussed in figure 17 under three different initial situations:

1. the initial drops have approximately the same size,
2. the initial drops have random radii with maximum-to-minimum radius ratio equal to 1000,
3. circles are in closed-pack and almost touching in uniform triangular array.

Three different growth functions were used, corresponding to rate of increase in radius by the powers: -0.5, -1, and -2. Their results showed that after a while all the progresses reached the same results of the actual pictures. For uniform equilateral triangular array, as is shown in figure 20 P is obtained as follow:

$$P = \frac{2\pi}{\sqrt{3}} \left(\frac{a}{s}\right)^2, \quad (0-46)$$

where a and s are the radius of circle and distance between two neighboring sites in a uniform array according to figure 20. Thus P will be calculated as the fraction of area covered by the droplets at each instance.

0.8 The aim of this study

As was mentioned before, depending on the purpose from the system either dropwise or filmwise condensation can be more preferred. The ratio of dropwise to filmwise conden-

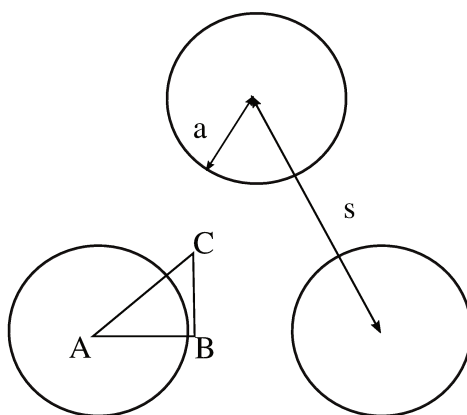


Figure 20: Determination of P (probability of finding a droplet in a grid) [13]. P can be calculated as the fraction of area covered by the droplets at each instance.

sation can be changed by using chemical coatings or by manipulating surface roughness and surface topography. Up to know, the process of dropwise condensation was mostly studied on flat surfaces [45, 83] or surfaces with coatings [34, 35]. Although, applying hydrophobic coatings will control the percentage of dropwise condensation with respect to filmwise mode, the use of chemical coatings is aimed to be limited in near future, because of their harmful effects on environment and waste waters.

The effect of surface topography was investigated as another solution for controlling droplets arrangement on the substrate by lots of authors [39, 88, 89], but there is a lack of studies dealing with presenting a model describing droplets growth on the textured surfaces. This is because of the complexity of the droplets shape on textured surfaces. Generally, on textured surfaces droplets are more elliptical than circular, because they tend to make a canal of liquid between the texturing patterns. This difference can be seen in figure 21. Figure 21 (a) shows the circular droplets growing on a flat surface, while figure 21 (b) shows the elliptical droplets growing on a pillared surface.

Another area that has not been taken into consideration is the droplets spatial distribution. As was mentioned, applying different texturing patterns can change droplets arrangement that can effectively change the droplets growth rate and even condensation regime. But there are not many studies dealing with droplets spatial distribution, although it is investigated vastly in the case of clouds and rain drops. In this study we aim to control the growth rate of water droplets on a two dimensional substrate by applying anisotropy to their spatial distribution. In fact, the growth rate of droplets is mostly due to the process of coalescence that is affected by the positioning of droplets with respect to each other or in other words their spatial distribution. In this regard, the effect of applying different texturing patterns on the spatial distribution of the droplets is going to be studied.

In this research, the process of nucleation and growth of droplets on flat and two kinds of textured surfaces (pillared and sinusoidal substrates) will be studied. In this regard, the experimental procedure is conducted on different substrates using a home-made set-up that was developed previously [90]. Also, surface characterization is done using Interferometric microscope, Scanning electron microscopy, and contact angle measurement in the case of

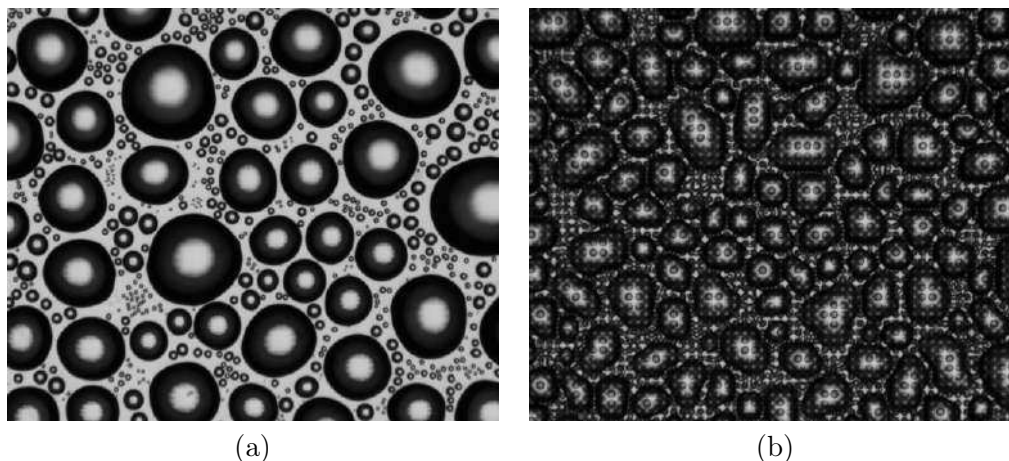


Figure 21: Differences between shape of droplets on the flat and pillared surfaces, (a) spherical droplets growing on a flat surface, (b) elliptical droplets growing on a micrometric pillared surface. The small points in image (b) are the texturing patterns.

sinusoidal substrate. The effect of sinusoidal pattern on the contact angle and average roughness of substrate is studied statistically using Factorial design.

Then, three mathematical models are developed for describing the behavior of different kinds of droplets on flat and textured surfaces.

1. a classical method that considers droplets as spherical-caps growing on a flat substrate
2. a method that considers elliptical droplets (contact angle = 90°) growing on the textured substrates
3. and a modified method that considers ellipsoidal-cap droplets (contact angle $\neq 90^\circ$) growing on the textured substrates.

Additionally, for each model a corresponding algorithm is proposed for generating droplets during computer simulation. All these algorithms start with points that are distributed uniformly on the surface. These uniform droplets then grow due to adsorption and coalescence and if they are big enough to overcome friction with substrate, they will slide and clean of the surface. The rate of growth and maximum radius of droplets before sliding are calculated based on each mathematical model named above.

In addition, a mathematical model for describing drop-size distribution function for adsorbing droplets is proposed using the method of Abou-Orabi, but by neglecting the effect of surface renewal. Therefore, this model is simpler with respect to the model of Abou-Orabi and can be used for describing size-distribution of droplets before coalescence.

0.9 Conclusion

0.9.1 English

As it was explained the main goal of this work is to study the process of dropwise condensation experimentally and numerically. The reason of choosing this topic is to investigate how texturing patterns will affect the rate of dropwise condensation and the transition from dropwise to filmwise mode. In this part at first a brief introduction to physics of dropwise condensation was presented. Then some important aspects of this process that can affect the droplets growth and heat transfer rate, such as droplets nucleation, temporal distribution and droplets size distribution function were discussed. At last, the algorithms that were used for generating droplets and predicting their behavior were introduced.

In the following, firstly the details of the experimental set-up used to study the droplets behavior and the procedure of the substrates preparation will be presented at chapter 1. Since the results of the experimental set-up will be the gray-scale images that must be segmented in order to get the information related to the size and distribution of droplets at each step, in chapter 2 the image processing method will be discussed. Then, in chapter 3 three numerical models developed for describing droplets nucleation and growth on the flat and textured substrates will be presented and finally at chapter 4 the results of these models will be validated by comparing with the experimental results from chapters 1 and 2.

0.9.2 French

Comme il a été expliqué le but principal de ce travail est d'étudier le processus de condensation par gouttelette expérimentalement et numériquement. La raison de choisir ce sujet est d'étudier comment les modèles de texturation affecteront le taux de condensation par gouttelette et la transition du mode gouttelette au mode film. Dans cette partie d'abord une brève introduction à la physique de condensation par gouttelette a été présentée. Ensuite, certains aspects importants de ce processus qui peuvent affecter la croissance des gouttelettes et le taux de transfert de chaleur, tels que la nucléation des gouttelettes, la distribution temporelle et la distribution de la taille des gouttelettes ont été discutés. Enfin, les algorithmes qui ont été utilisés pour générer des gouttelettes et prédire leur comportement ont été introduits.

Dans ce qui suit, tout d'abord les détails de la configuration expérimentale utilisée pour étudier le comportement des gouttelettes et la procédure de préparation des substrats seront présentés au chapitre 1. Puisque les résultats de la configuration expérimentale seront les images en échelle de gris qui doivent être segmentées afin d'obtenir l'information relative à la taille et à la distribution des gouttelettes à chaque étape, dans le chapitre 2 la méthode de traitement d'image sera discutée. Ensuite, dans le chapitre 3 trois modèles numériques développés pour décrire la germination et la croissance des gouttelettes sur les substrats plats et texturés seront présentés et finalement au chapitre 4 les résultats de ces modèles seront validés par comparaison avec les résultats expérimentaux des chapitres 1 et 2.

Chapter 1

Experimental Procedure

1.1 Introduction

1.1.1 French

Dans ce chapitre, nous allons d'abord expliquer le protocole expérimental utilisé pour réaliser l'acquisition des images de condensation en goutte à goutte, ainsi que les méthodes de préparation et de caractérisation des substrats. Les substrats sont les surfaces de polycarbonate sur lesquelles les gouttelettes se forment et se développent. Ces échantillons de polycarbonate sont montés sur l'installation expérimentale dans des conditions contrôlées, puis le processus commence en réduisant la température des échantillons et les gouttelettes d'eau nucléent sur les échantillons.

Comme il a été mentionné en introduction, les modifications de surface comme les prétraitements chimiques, l'application de revêtements, les changements de rugosité, etc. peuvent modifier le processus de formation et de croissance des gouttelettes. Dans cette thèse, nous visons à étudier la croissance des gouttelettes sur trois modèles physiques différents, comprenant : des motifs plats, des motifs à piliers et des motifs sinusoïdaux.

Dans ce qui suit, la configuration expérimentale sera décrite très brièvement car elle a été développée et complètement expliquée par [90]. Ensuite, le processus de préparation et de caractérisation des substrats, spécialement pour les substrats sinusoïdaux, sera étudié. Et enfin une étude statistique sur l'effet de la période et de l'amplitude des motifs sinusoïdaux sur la rugosité de surface et le mouillabilité sera présentée.

1.1.2 English

In this chapter at first the experimental apparatus that has been used to acquire the gray scale images of dropwise condensation as well as the methods for substrates preparation and characterization will be explained. Substrate here means the polycarbonate surfaces over which the droplets form and grow. These polycarbonate samples are mounted on the experimental set-up under controlled condition, then the process starts by reducing the samples temperature and water droplets begin to nucleate on the samples.

As it was mentioned in introduction, surface modifications like chemical pre-treatments, applying coatings, changes in roughness and, etc ... can change the process of droplets formation and growth. In this thesis we aim to study droplets growth on three different

physical patterns including: flat, pillared and sinusoidal patterns.

Therefore, in the following the experimental set-up will be described very briefly because it has been developed and completely explained by [90]. Then the process of substrates preparation and characterization specially for the sinusoidal substrates will be investigated. And finally a statistical study on the effect of period and amplitude of the sinusoidal patterns on the surface roughness and wettability will be presented.

1.2 Experimental set-up

The experimental set-up used in this study is the same as in [90] and consists of a closed humid chamber that is completely under control by means of PID control systems. Inside the chamber, hot and humid air is in contact with cold substrate on which the droplets are formed. Ambient air is compressed and filtered via a $0.01\mu m$ gas filter. The filtered air is then injected by means of a 250V Condor compressor in a distilled water with controlled temperature around $30^{\circ}C$. Controlling the flow rate of the filtered air and temperature of the cartridges will let the humidity be stable on 45% inside the chamber. At this situation the dew point of humid air will be around $16.5^{\circ}C$ so if the temperature of the substrate goes below this value, water droplets will appear. Substrate temperature reduces by means of two 23.4 W thermoelectric coolers (UEPT-1RE-063-050M125S, UWE Electronic) to around $12^{\circ}C$.

Formation and growth of droplets is recorded at each second by a 5Mpx gray scale video camera (MANTA G-504B, Allied Vision) mounted on a long-focal-distance adjustable lens (QIOPTIQ). This system allows spatial resolution $1.34 \pm 0.04\mu m/pixel$. The camera system is adjusted outside the humid box to avoid any damages due to contact with humid atmosphere. Figure 1.1 illustrates the top view of the experimental set up and the CCD camera used to record droplets evolution as well as schematic diagram of the whole system.

The polycarbonate substrates are washed by distilled water in order to remove any pollutants and cleaned by nitrogen gas to remove any dust and external imperfections. They are then dried for minimum 4 hours in oven with temperature of $120^{\circ}C$ to remove any water contents from the surface that can affect the droplets nucleation process. For starting the experiments, these samples will be located on the place that is marked by number 5 in figure 1.1. Then, the humid chamber that is shown by number 2 will be closed and air current will flow. After regulating humidity and temperature of air mixture, that takes around 2 hours, the substrate temperature is set at $1^{\circ}C$ below the dew point of the mixture. At this time the nucleation of small droplets will start and the CCD camera records all the process.

As was explained before, the process starts by reducing the substrate temperature to blow the dew point of the air mixture that results to nucleation of the initial droplets. Then, these small droplets start to grow by adsorbing water molecules from humid air. After a while if two or more droplets become big enough to overlap, they will merge and form a bigger droplet -called daughter droplet- in the mass center of the parents [46]. This phenomenon is called coalescence in literature. Although coalescence is a mass conservative process, the area covered by daughter droplet is lower than the summation of area covered by it's parents. This will lead to forming vacant area around daughter droplet, in which new small droplets can nucleate and grow. Both these steps will change droplets density during

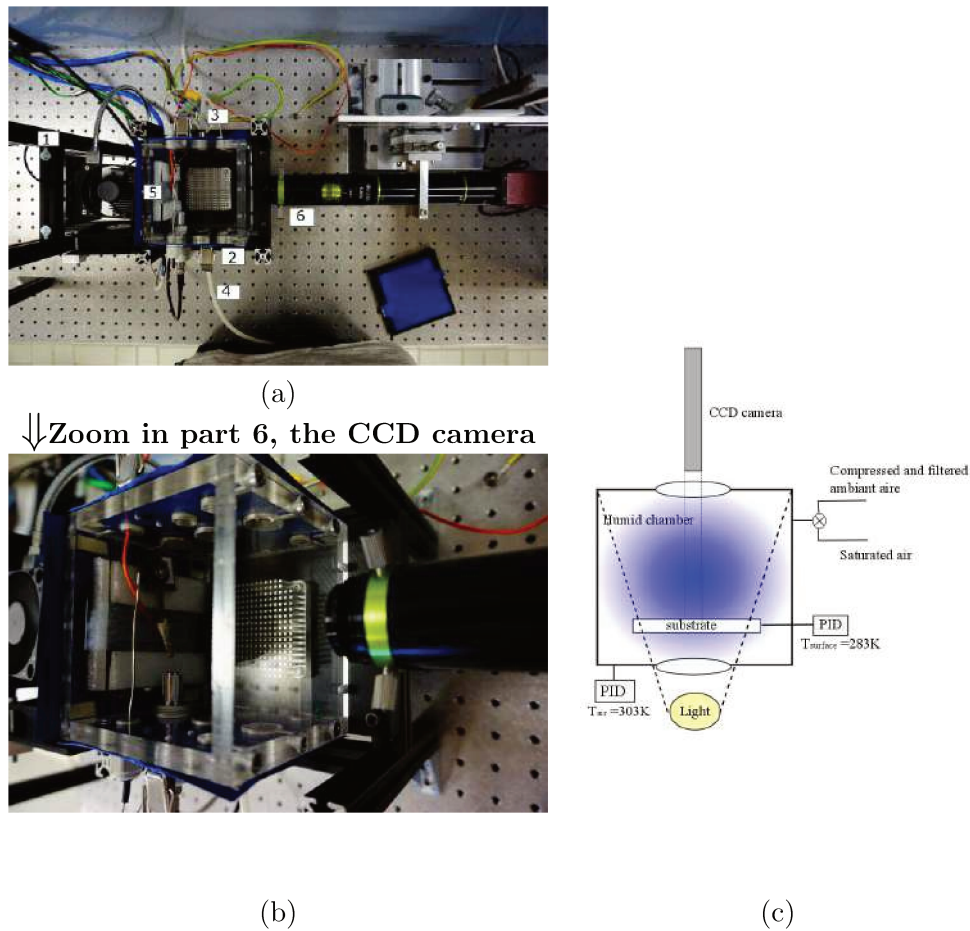


Figure 1.1: Illustration of experimental set up. (a) Top view, (b) Closer view of the humid chamber and CCD camera. The parts that are marked in (a) correspond to: 1) light for taking high quality images, 2) humid chamber, 3) gas inlet, 4) gas outlet 5) cold substrate, and 6) CCD camera, (c) schematic diagram of the whole system

time and lead to a temporal distribution [48]. Finally in the case of vertical substrates, the big droplets that can not resist the gravity force, will slide and produce more vacant area on the surface. Therefore five main steps can be considered in a process of dropwise condensation: initial nucleation, growth due to adsorption, growth due to coalescence, nucleation of new small droplets, and departure of big droplets. These steps are shown in figure 1.2. In this figure coalescence and nucleation of new droplets are shown together because they occur at the same time.

1.3 Surface preparation

The experiments are carried on a flat substrate as well as on 6 different pillared and 12 sinusoidal substrates in order to investigate the effect of surface texturing on the growth rate of droplets. These surfaces have been manufactured on metallic molds using laser

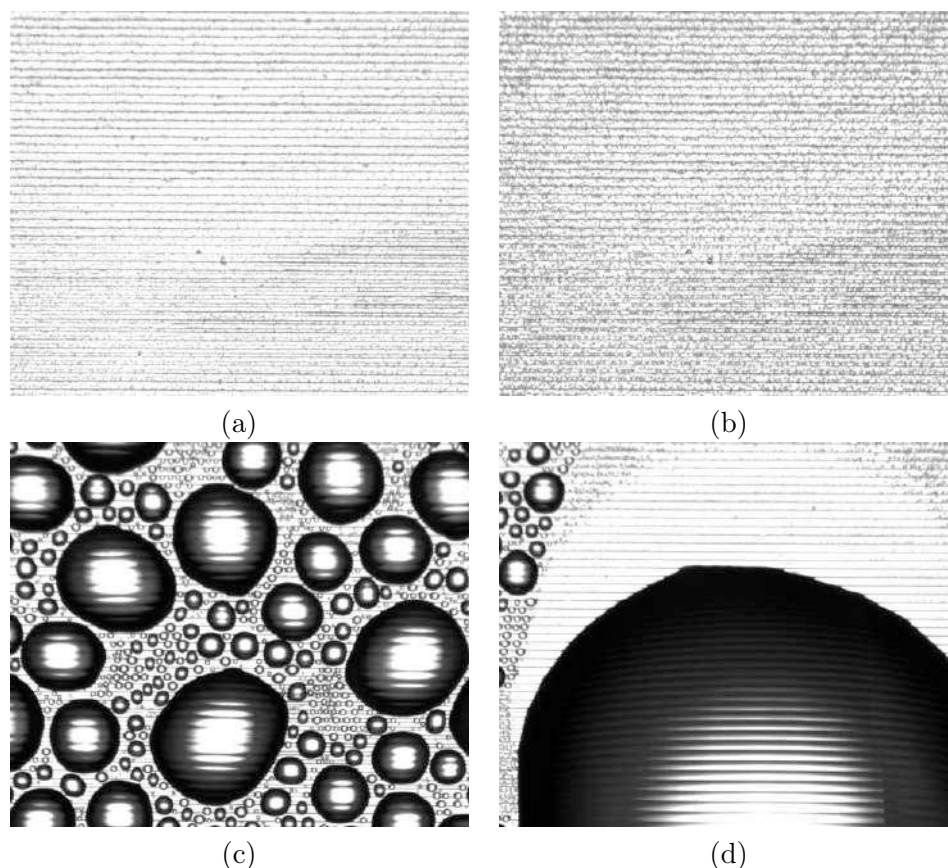


Figure 1.2: Four main steps of dropwise condensation including: (a) initial nucleation, (b) growth due to adsorption, (c) growth due to coalescence and nucleation of new small droplets, and (d) departure of big droplets.

technology. These metallic molds are then duplicated by means of an injected press machine of Sumitomo Shi Demag systec 35-200 that is illustrated in figure 1.3. The polymer used for the substrates duplication is polycarbonate that is the main component of the car light shields. Polycarbonate granulates are dried under 119.5°C during 4 hours in order to reduce their humidity content. Dried polymer granulates are fed into the machine (figure 1.3(a)) and are melted at 310°C . The metal mold (figure 1.3(b)) is warmed up to 85°C using circulating hot water to avoid thermal stress to the polymer. Molten granulates are injected into the warm mold by a screw rotating with speed of 360mm/s that provides the polymer volume flow rate of $50\text{cm}^3/\text{s}$. Inside the mold, the polymer fluid is kept under the pressure of 600 bar for 20s. The results of this process are polycarbonate samples (figure 1.3(c)) that will be used as the substrate for nucleating water droplets during the dropwise condensation experiments.

The theoretical size and distance between the pillars corresponding to each pattern are presented in table 1.1. In this table, 6 substrates are named as Configuration 1 to 6 and r_t represents the theoretical radius of pillars, d_t is the theoretical distance between the pillars, and h_t is the theoretical height of pillars, while the term theoretical means that

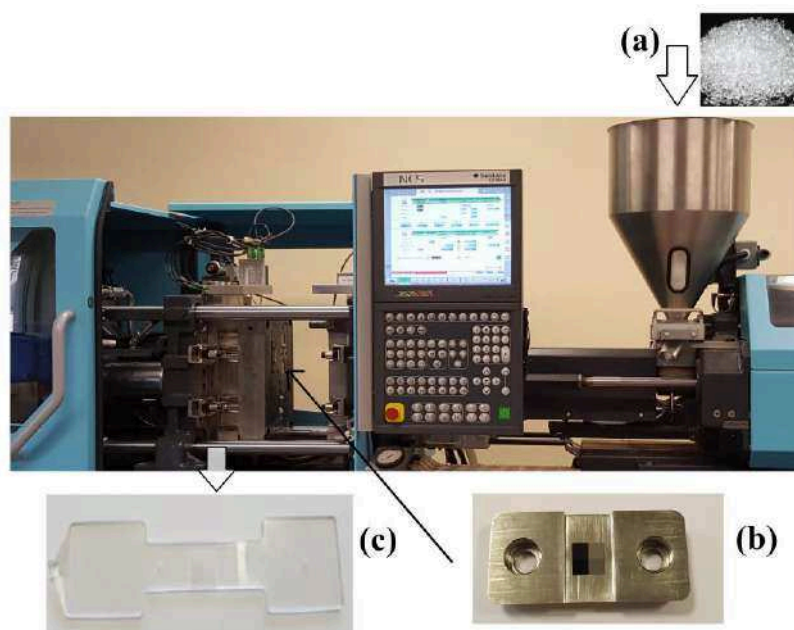


Figure 1.3: Illustration of the injection press system. (a) Polymer granulates, (b) metal mold (the small squares are the sinusoidal surfaces), (c) polymeric textured surfaces that will be used as substrates in dropwise condensation experiments.

these dimensions are the designed values for pillars and must be validated by microscopical measurements. These dimensions are illustrated in figure 1.4, also figure 1.5 shows the top point of view of these 6 pillared substrates.

Similarly, the theoretical details of the sinusoidal surfaces are shown in table 1.2. These 12 sinusoidal substrates are produced with three periods of $\lambda = 30, 60,$ and $100\mu m$ and four different heights ($a = 5, 10, 30,$ and $50\mu m$). In table 1.2 the surfaces are denoted based on their periods and amplitudes. For instance, 30-5 means the surface with $\lambda = 30\mu m$ and $a = 5\mu m$. In practice, three metallic molds each containing 4 textured area with the same periods but different heights are manufactured liked what is shown in figure 1.3(b).

6 top view examples of sinusoidal substrates can be seen in figure 1.6. These illustrations are related to surfaces with amplitude 5 and 10 μm .

1.4 Surface Characterization

This section is dedicated to characterization of the texturing patterns both on the metallic molds (section 1.4.1) and on the polycarbonate substrates (section 1.4.2) in order to verifying the accordance between the real sizes on the molds and on the samples with the designed values. Here just the results related to the metallic molds of sinusoidal substrates are presented.

Surface identification	r_t (μm)	d_t (μm)	h_t (μm)
Configuration 1	12.5	50	3
Configuration 2	12.5	125	3
Configuration 3	25	65	10
Configuration 4	25	60	10
Configuration 5	25	100	10
Configuration 6	25	150	10

Table 1.1: Size and distance between the pillars of each substrate. r_t represents the theoretical radius of pillars, d_t is the theoretical center to center distance between the pillars, and h_t is the theoretical height of pillars.

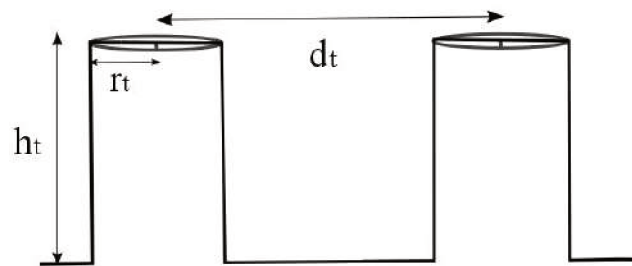


Figure 1.4: Schematic illustration of pillars dimensions that are mentioned in table 1.1.

Surface identification	λ (μm)	a (μm)	Surface identification	λ (μm)	a (μm)
30-5	30	5	60-30	60	30
30-10	30	10	60-50	60	50
30-30	30	30	100-5	100	5
30-50	30	50	100-10	100	10
60-5	60	5	100-30	100	30
60-10	60	10	100-50	100	50

Table 1.2: Characteristics of each sinusoidal surface. λ and a being the period and amplitude of the sinusoidal profiles.

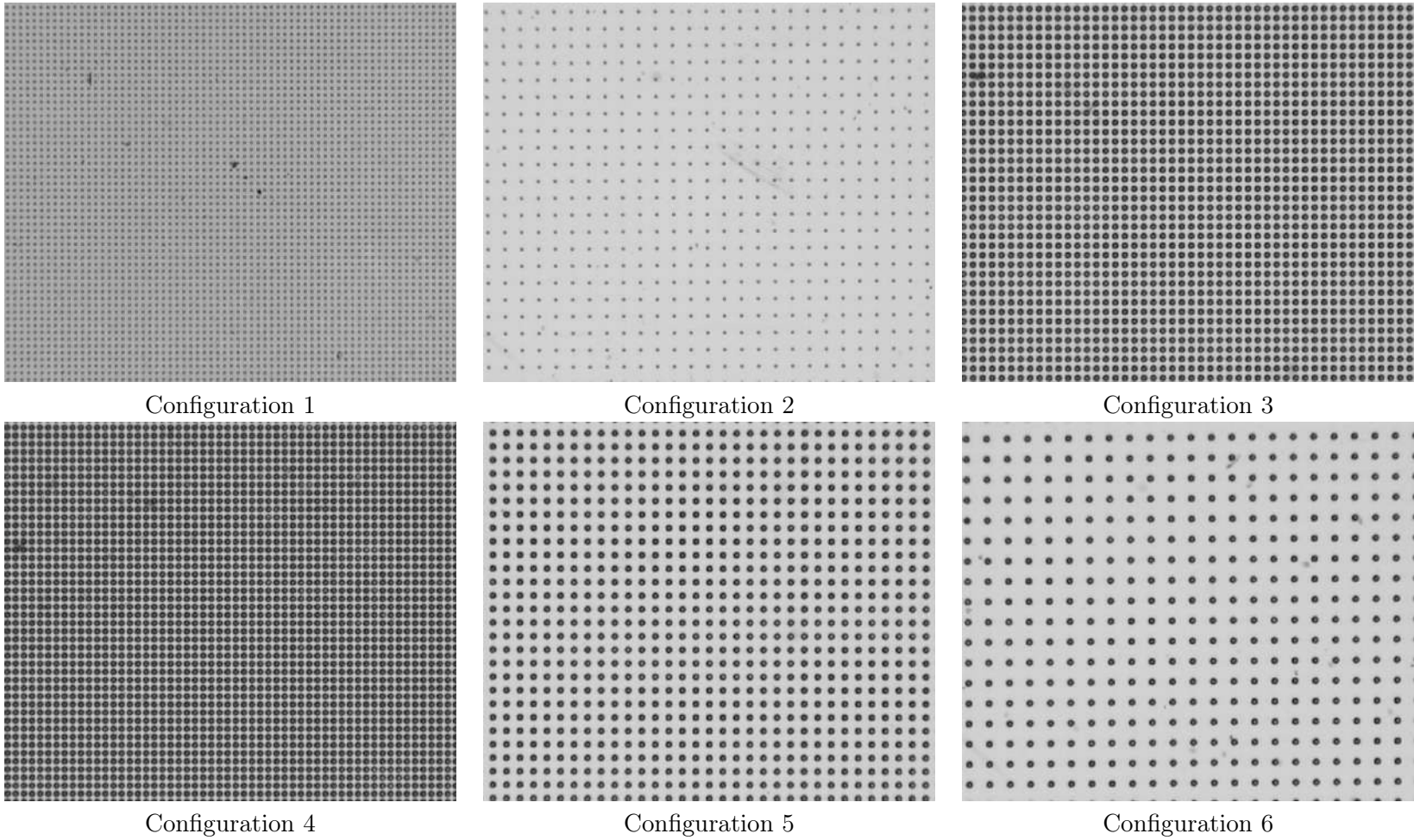


Figure 1.5: Optical microscope images of 6 polycarbonate pillared surfaces. The black points represents the pillars with radius and heights according to table 4.1. The size of the substrate in all these images is $3.2\text{mm} \times 2.7\text{mm}$.

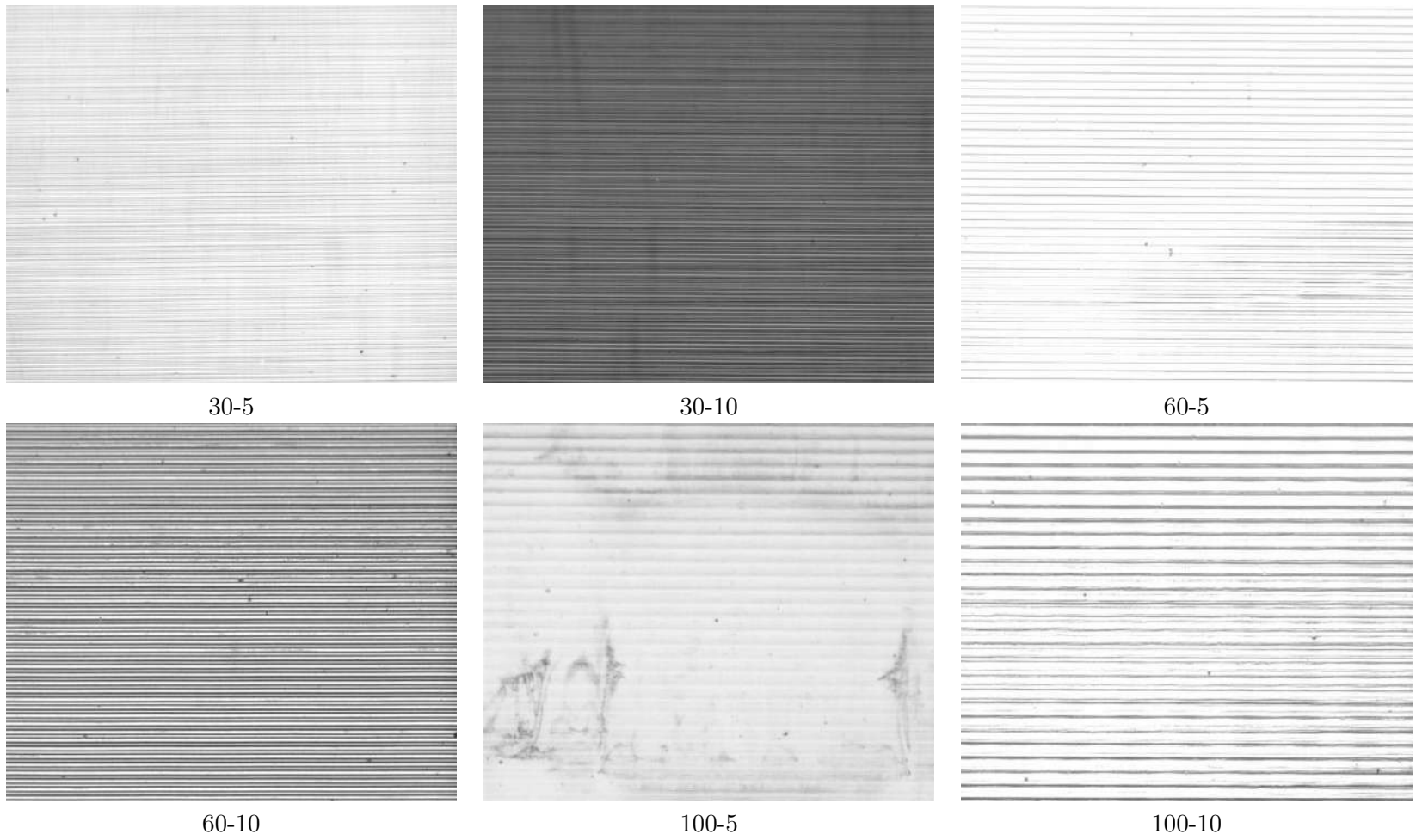


Figure 1.6: Optical microscope images of 6 examples of polycarbonate sinusoidal surfaces. The size of the substrate in all these images is $3.2\text{mm} \times 2.7\text{mm}$.

1.4.1 Surface characterization of the metallic molds

As was mentioned above, the aim of this section is to validate the results of the process of metallic molds preparation by laser technology. The importance of this section is because the polycarbonate samples that will be used as the substrates for growing water droplets, will be duplicated from these metallic molds and any defects on this part can affect the whole process of nucleation and growth of droplets. Therefore, in the following, at first the (scanning electron microscopy) SEM images of 12 sinusoidal surfaces will be presented, then the two dimensional roughness analysis will be investigated from the images captured by interferometric microscope.

Figure 1.7 illustrates the real Microscopic view of the sinusoidal surfaces taken by the SEM Oxford, X MAX microscope with magnification $311\times$. In this figure, at each row periods are the same and the amplitude of sinusoidal profiles varies, and so at each column the amplitude is constant and period changes.

In order to validate the theoretical values of table 1.2, the two dimensional roughness parameters are done by means of an interferometric microscope, Bruker gk1, using a capture CCD 640×480 pixel and magnification of $25\times$ for the period of 60 and 100 μm and $50\times$ for the period of 30 μm . The magnification for 3 surfaces with $\lambda = 30\mu m$ is different because with magnification of $25\times$, the small distance between the peaks did not let the light beams reach to the lowest level of the valleys. All the images are taken by the green light that diffuses better into the valleys with respect to the white light, but produces less precise information. Figure 1.8 shows the three dimensional microscopic images produced by interferometric microscope to measure λ and a of each sinusoidal profile. In these images, a is defined by colors. At each row from left to right a increases and the yellow color that shows the height of peak with respect to lowest point (blue color) turns into red.

One of the examples of the values of λ and a measured by the interferometric microscope is shown in figure 1.9. This figure represents the two dimensional roughness profile of the configuration 30-5. The value of Z at the right hand side of this graph represents the height of the profile and x on the top of the plot is the half of the period. Also the nanometric imperfections are visible in this graph that indicate the surface of the peaks and valleys are not perfectly flat. The same graphs are obtained for all the 12 substrates but are not illustrated here. The roughness information extracted from these graphs are shown in table 1.3.

Table 1.3 shows the roughness parameters of the 12 sinusoidal surfaces. The first three columns are as in table 1.2. The fourth column represents the mean roughness (average roughness R_a) that is the arithmetic average of the absolute values of the roughness profile ordinates. R_a is one of the most effective surface roughness parameters commonly adopted in general engineering practice. It gives a good general description of the height variations on the surface. R_q in this table represents root mean square of the roughness profile. If R_v and R_p indicate minimum valley depth and maximum peak height respectively, and $R_t = R_p - R_v$ will be the maximum amplitude of the sinusoidal profile and R_z will be the average of R_t on the surface. So, by comparing R_z and a one will be able to calculate the average error of the height of the real surface with respect to the theoretical values ($E_{ave} = \frac{R_z - a}{R_z}$). One of the sources of this error can be light reflection by the walls of the valleys. Interferometric microscope works based on the light adsorbed and light reflected

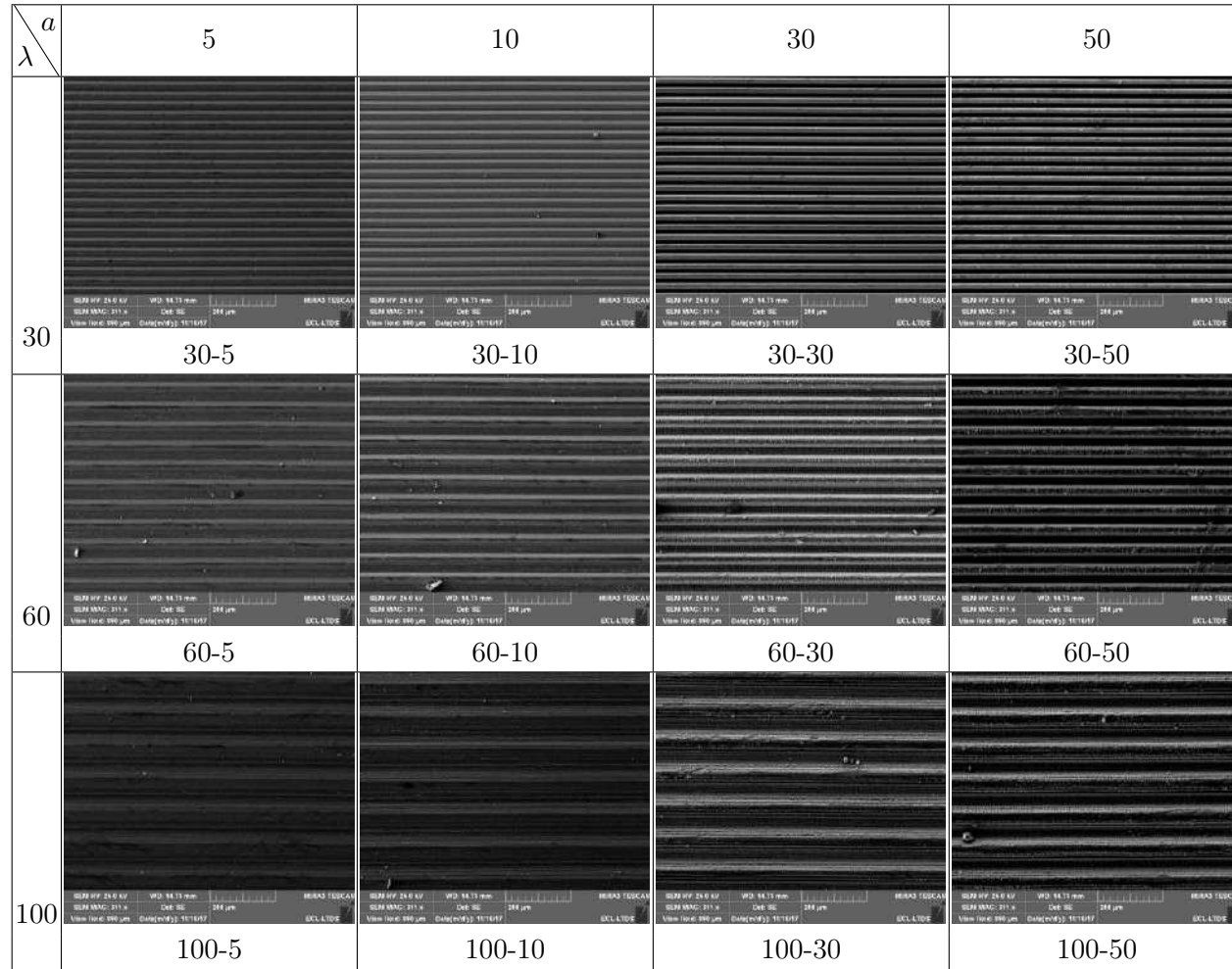


Figure 1.7: SEM microscopic images (magnification $\times 311$) of the sinusoidal surfaces. λ and a here are the period and amplitude of the sinusoidal profiles.

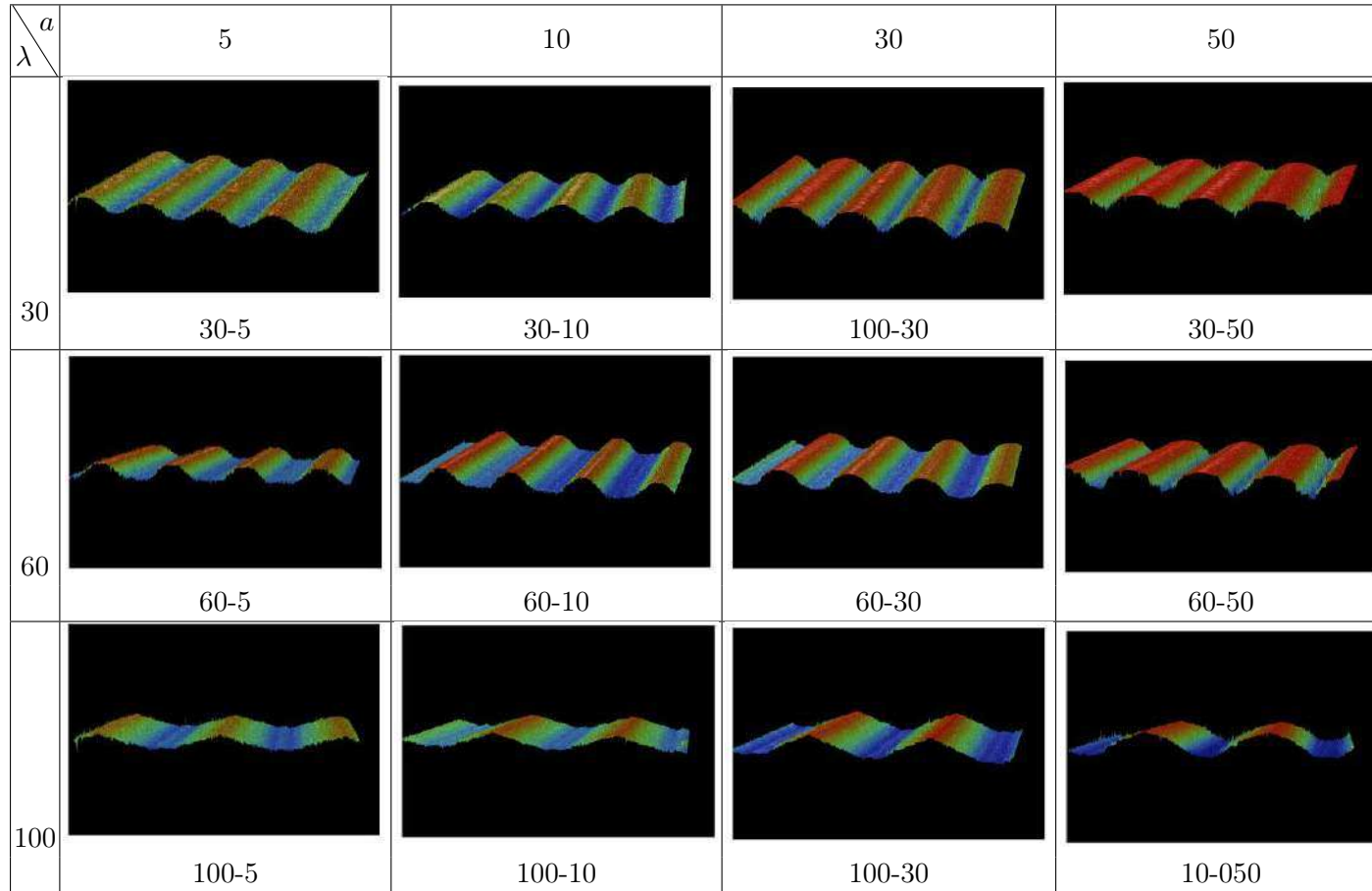


Figure 1.8: Three dimensional images produced by the interferometric microscope. λ and a represent the period and amplitude of the sinusoidal profiles.

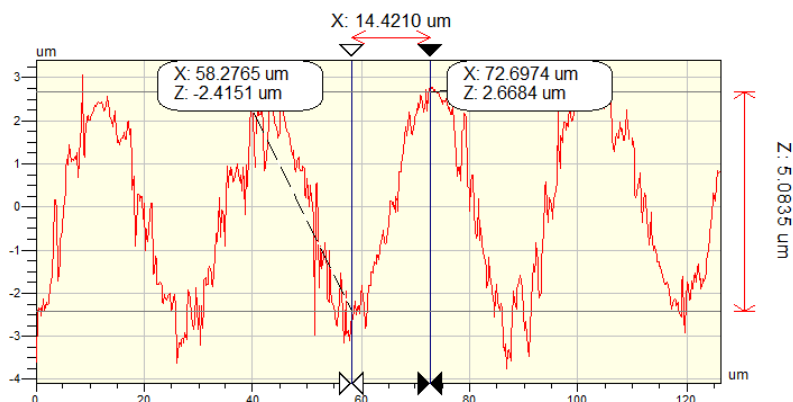


Figure 1.9: Two dimensional roughness profile of the configuration 30-5. This plot can be used to measure the roughness parameters

form the surface. So, when the period is too small or the depth of valley is too large, beams cannot reach to the bottom of the valleys and they show this error in height measurement. In the case of 30-50 there is even no results because the period is smaller than the other surfaces and we have to change the magnification of the microscope to $100\times$.

Relatively high errors in this table are because that R_z measures the difference between the highest and the lowest points on the surface. In the images of interferometric microscopy, sometimes these points are due to imperfections on the surface or light reflection. To avoid these points, a Fourier filtering is applied in order to smoothing the sinusoidal profiles. The results after this filtering process are presented in table 1.4. As was predicted the highest amount of error is related to surface with narrower grooves and deeper valleys (30-50).

1.4.2 Surface characterization of the polycarbonate samples

1.4.2.1 Scanning electron microscopy (SEM)

Figure 1.10 illustrates the SEM images taken from the polycarbonate samples of sinusoidal substrates. Since polycarbonate samples are transparent, in order to have high quality SEM images, the samples are coated by a metallic coating of gold-platinum. The coating process is done by a Sputter coater of Palaron-Range under vacuum, voltage of $1.5kV$, and electricity current of $25mA$. The coating thickness is defined by the time of coating that is 60s for the textured side and 120s for the back side. The thickness of the metallic coating applied on the textured side is finer due to preventing of any effects on the texturing patterns.

In the following, the roughness and wettability of the polycarbonate samples will be characterized. This characterizations are very important because the polycarbonate surfaces are the real substrates imposing to dropwise condensation and it is possible that despite of having acceptable texturing patterns on the metallic molds, there will be some defects that can affect the whole process of dropwise condensation. Here, we just present the microscopic measurements of the sinusoidal surfaces.

Surface identification	$\lambda(\mu m)$	$a(\mu m)$	$R_a(\mu m)$	$R_q(\mu m)$	$R_t(\mu m)$	$R_z(\mu m)$	$E_{ave}(\%)$
30-5	30	5	1.66	1.87	10.70	9.47	89
30-10	30	10	3.14	3.50	18.50	16.37	64
30-30	30	30	9.28	10.54	47.04	45.43	51
30-50	30	50	9.24	11.30	68.55	59.18	18
60-5	60	5	1.76	1.94	9.20	8.80	76
60-10	60	10	3.32	3.67	15.60	14.62	46
60-30	60	30	11.52	12.34	52.66	43.50	45
60-50	60	50	19.20	21.20	77.81	71.91	44
100-5	100	5	1.39	1.61	9.76	9.43	83
100-10	100	10	2.59	3.02	18.21	15.42	54
100-30	100	30	7.95	9.00	36.37	33.98	13
100-50	100	50	13.95	15.20	52.08	49.49	-1

Table 1.3: Roughness parameters of each sinusoidal surface on the metallic molds. $\lambda(\mu m)$ and $a(\mu m)$ denote the period and amplitude of the sinusoidal profiles respectively, R_a is the average roughness, while $R_t = R_p - R_v$ is the maximum amplitude of the sinusoidal profile and R_z is the average of R_t on the surface. R_q in this table represents root mean square of the roughness profile and finally, E_{ave} here is the average error between R_z and a .

Surface identification	$\lambda(\mu m)$	$a(\mu m)$	$R_a(\mu m)$	$R_q(\mu m)$	$R_t(\mu m)$	$R_z(\mu m)$	$E_{ave}(\%)$
30-5	30	5	1.53	1.71	5.58	5.49	10
30-10	30	10	2.92	3.29	10.81	10.78	8
30-30	30	30	8	9.24	31.56	31.30	4
30-50	30	50	6.16	7.23	33.19	32.50	-35
60-5	60	5	1.60	1.75	5.09	5.06	2
60-10	60	10	2.90	3.25	10.90	10.87	9
60-30	60	30	10.29	11.19	35.96	35.83	20
60-50	60	50	16.07	18.15	54.96	54.59	10
100-5	100	5	1.28	1.47	5.07	5.05	1
100-10	100	10	2.38	2.77	9.81	9.74	-3
100-30	100	30	7.25	8.22	27.23	27.13	-10
100-50	100	50	12.69	13.90	41.55	41.48	-17

Table 1.4: Roughness parameters of each sinusoidal surface on the metallic molds using Fourier filter in order to avoid the highest and the lowest points that are not the real peaks and valleys. $\lambda(\mu m)$ and $a(\mu m)$ denote the period and amplitude of the sinusoidal profiles respectively, R_a is the average roughness, while $R_t = R_p - R_v$ is the maximum amplitude of the sinusoidal profile and R_z is the average of R_t on the surface. R_q in this table represents root mean square of the roughness profile and finally, E_{ave} here is the average error between R_z and a .

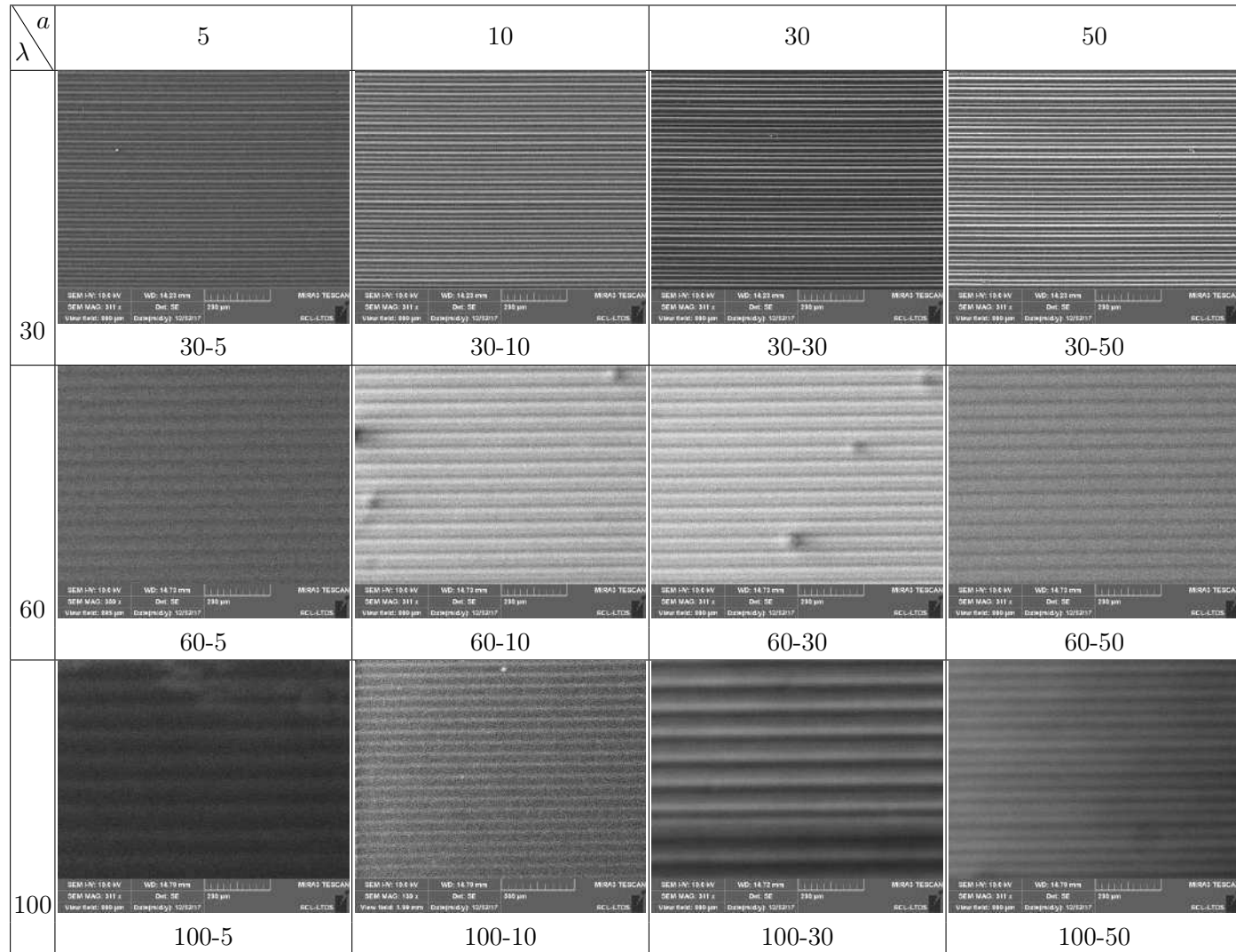


Figure 1.10: SEM microscopic images of the sinusoidal surfaces on polycarbonate samples. λ and a here are the period and amplitude of the sinusoidal profiles.

configuration of surface	$r_p(\mu m)$	$D_p(\mu m)$	$H_p(\mu m)$	$R_a(\mu m)$
configuration 1	12.5	50	3	0.31
configuration 2	12.5	125	3	0.09
configuration 3	25	60	10	0.31
configuration 4	25	65	10	0.19
configuration 5	25	100	10	0.17
configuration 6	25	150	10	0.10

Table 1.5: Roughness parameters of each pillared surface.

1.4.2.2 Roughness measurements

A Veeco optical microscope with magnification of $50\times$ is used in order to validate the theoretical size of the texturing patterns that were presented in tables 1.1 and 1.2 as well as calculating the roughness parameters. Figure 1.11 illustrates the three dimensional schematic of the 6 pillared substrates. The graphs related to the sinusoidal substrates are avoided here because of their similarity with figure 1.8.

Figures 1.12 and 1.13 show the two dimensional roughness profile of the six pillared substrates. At each graph, the two cursors measure the distance between a pair of specific points in the directions of $X - Z$ on the substrate. In figure 1.12, X measures the distance between two pillars centers. This value is shown in table 1.1 by D_t . Figure 1.13 is a closer point of view to measure the radius and height of pillars on each substrate. X and Z can be compared with the values of r_t and h_t in table 1.1 respectively.

According to these images there is an acceptable accordance between sizes and distances of the pillars and the theoretical data presented in table 1.1, but the pillars are not perfectly cylindrical as was assumed in the simulation algorithm. It can be clearly seen that the top heads of pillars in all configurations are rounded and dome-shaped. the same calculations are made for the sinusoidal substrates.

Tables 1.5 and 1.6 show the roughness parameter (R_a) of the pillared and sinusoidal substrates respectively. The detail of the measurements is presented in table 1.6. The average roughness parameter R_z in this table is smoothen by means of the Fourier transform in order to remove the noises. According to this table, by reducing the period and increasing the amplitude, the difference between actual and theoretic values of amplitude on the samples increases. Meaning that for $\lambda = 30\mu m$ and $a = 30$ and $50\mu m$, the difference between R_z and a is much more significant. This shows that during the injection process the molten polymer could not enter completely in the valleys that are narrower and deeper. On the other hand, the patterns with amplitudes of $a = 30$ and $50\mu m$ are not perfectly duplicated on the polycarbonate samples. It can be seen that for example, for configurations 30-30 and 30-50 the R_z is equal to 14.21 and 10.75 μm that is really far from the design values. The same problem happens for configurations 60-30, 60-50, 100-30, and 100-50. Therefore, we will not consider these 6 substrates neither in dropwise condensation experiments nor in simulation algorithms.

Comparing the amounts of R_a in tables 1.6 and 1.5 reveals that the pillared substrates studied here are much less rougher than the sinusoidal substrates. There the Cassie-Baxter droplets are more expected.

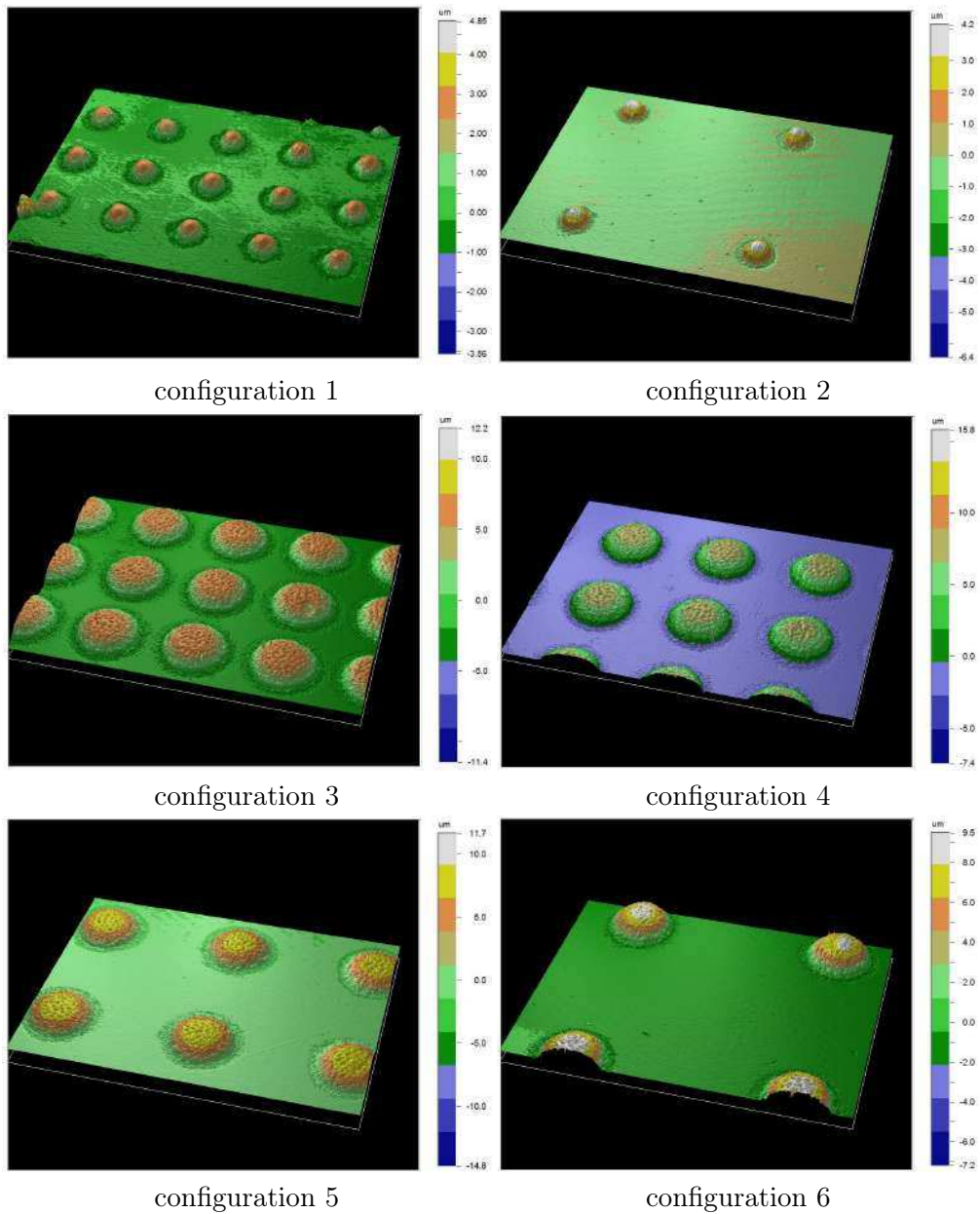


Figure 1.11: Three dimensional microscopic illustration of 6 pillared substrates with $50\times$ magnification. The colored bar on the right hand side of each image measures the height of the pillars. Meaning that each color on this bar corresponds to a value on μm , so for measuring the height of each pillar it is enough to find the value corresponds with the color of it's top head.

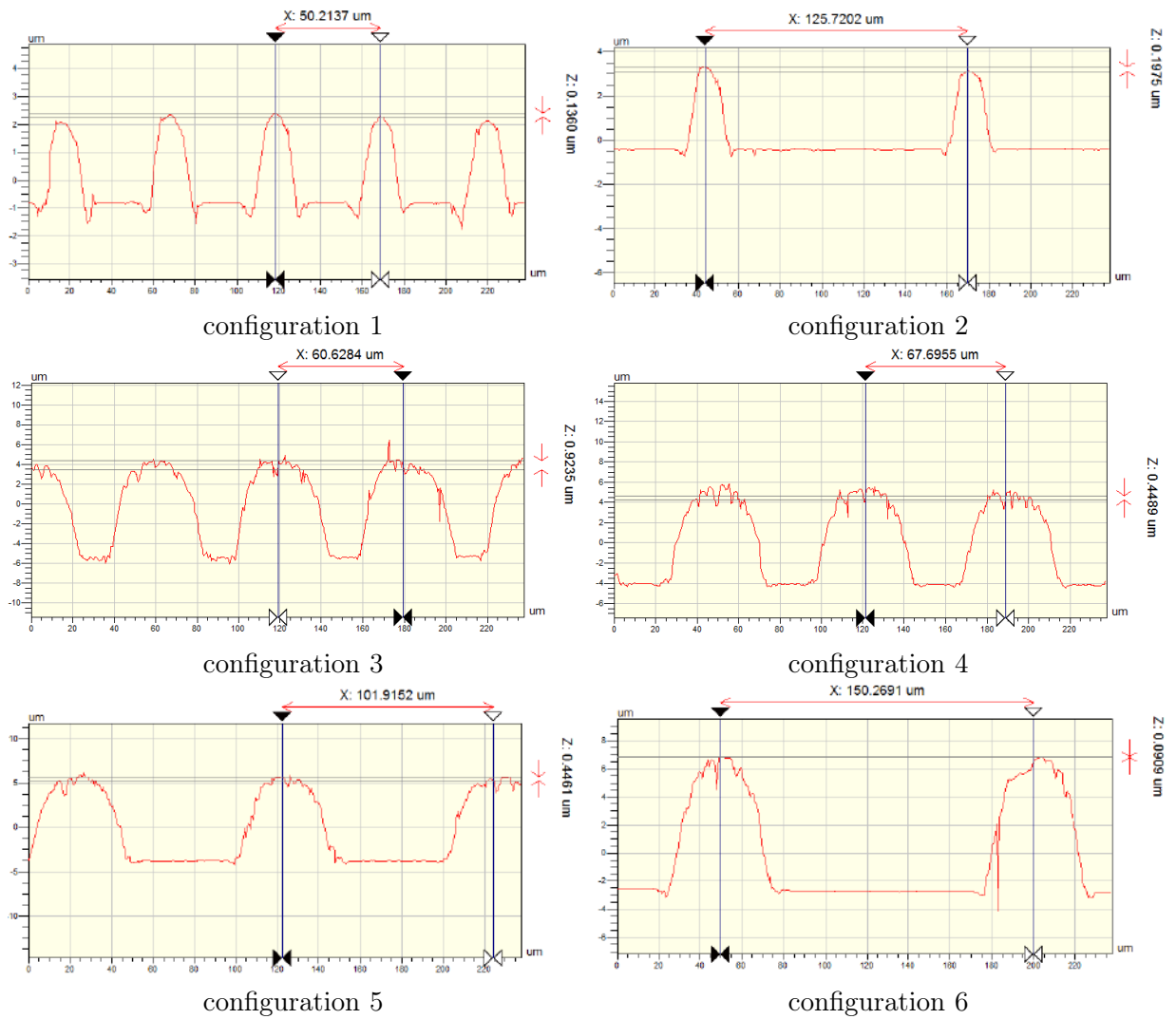


Figure 1.12: Illustration of two dimensional roughness profile of the six pillared substrates. At each graph, X is the distance between the pillars.

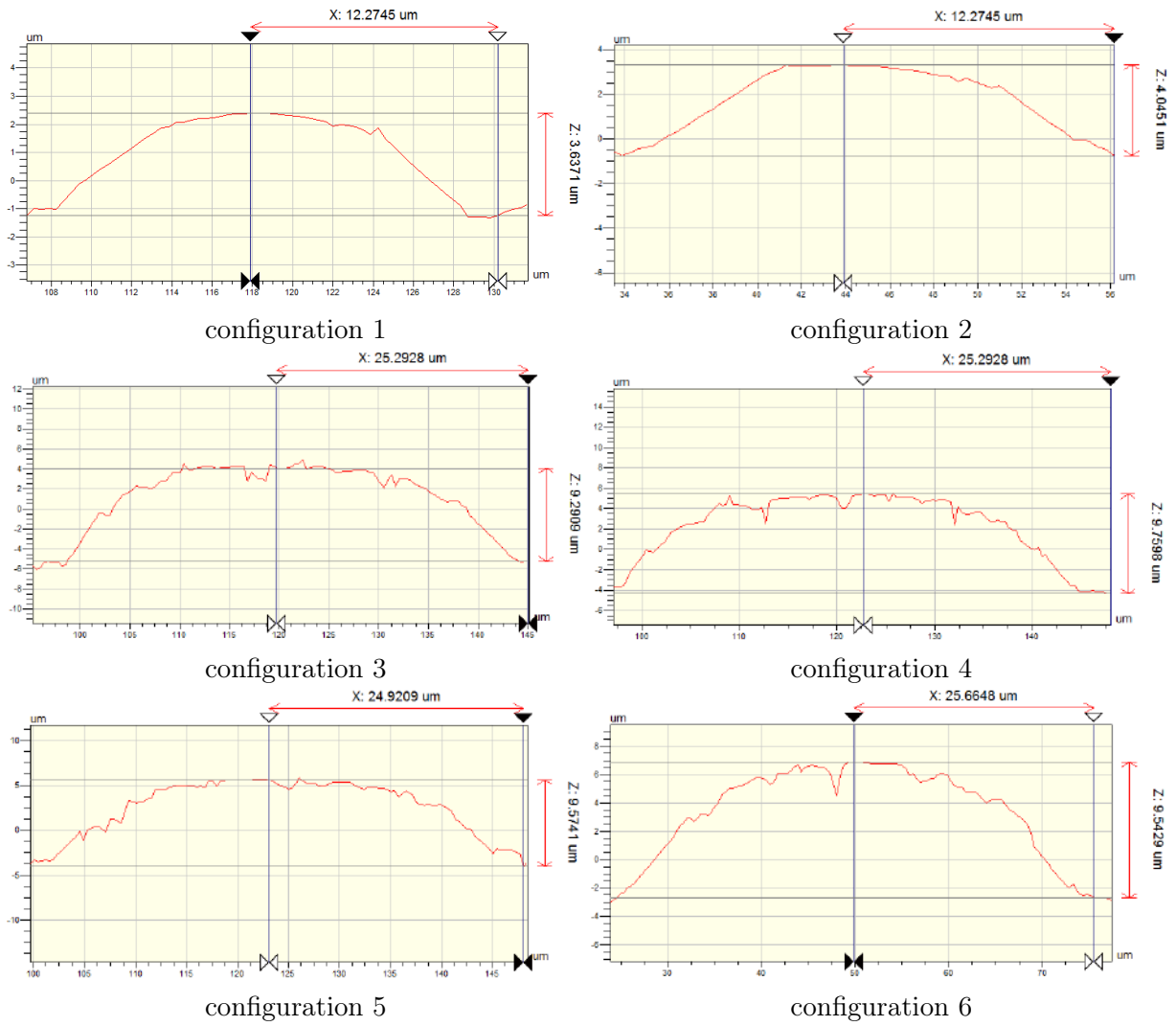


Figure 1.13: Illustration of two dimensional roughness profile of the six pillared substrates. At each graph, X and Z represent the radius and height of the pillars, respectively.

Surface identification	$\lambda(\mu m)$	$a(\mu m)$	$R_a(\mu m)$	$R_q(\mu m)$	$R_t(\mu m)$	$R_z(\mu m)$	$E_{ave}(\%)$
30-5	30	5	1.07	1.21	3.77	3.74	-25.20
30-10	30	10	2.37	2.57	7.71	7.67	-23.30
30-30	30	30	3.56	3.85	11.09	14.21	-52.63
30-50	30	50	3.42	3.74	10.85	10.75	-78.50
60-5	60	5	1.45	1.62	5.19	5.16	3.20
60-10	60	10	2.77	3.14	10.09	10.05	0.50
60-30	60	30	7.79	8.55	25.91	25.74	-14.20
60-50	60	50	7.38	8.16	25.54	25.44	-49.12
100-5	100	5	1.24	1.41	4.46	4.45	-11.00
10010	100	10	2.34	2.71	8.97	8.93	-10.70
100-30	100	30	5.79	6.93	26.79	26.65	-11.17
100-50	100	50	9.49	11.00	39.67	39.28	-21.44

Table 1.6: Roughness parameters of each sinusoidal surface on polycarbonate samples using Fourier filter in order to avoid the highest and the lowest points that are not the real peaks and valleys. $\lambda(\mu m)$ and $a(\mu m)$ denote the period and amplitude of the sinusoidal profiles respectively, while $R_t = R_p - R_v$ will be the maximum amplitude of the sinusoidal profile and R_z will be the average of R_t on the surface. R_q in this table represents root mean square of the roughness profile and finally, E_{ave} here is the average error between R_z and a .

1.4.2.3 Contact angle

Contact angles of water droplets (θ) on the sinusoidal texturing are measured by a DSA30 set-up made by KRUSS. The main part of this set-up is illustrated in figure 1.14. As shown in this image, the polymeric sample is placed on the substrate support emphasized by (a). The sample is cleaned before, by distilled water and dried by Nitrogen in order to remove any contamination. On the syringe shown in (b) water droplets with volume $1\mu l$ with speed of $150\mu l/min$ are formed at room temperature through a needle with diameter of $500\mu m$. Parts (c) and (d) in this figure show the light source and CCD camera that takes images of droplets sited on the substrate. Images are taken at each second until 20s. Before starting taking the images, droplets are allowed to be well situated on the substrate for 10s.

This process is repeated nine times (three times on three samples of each substrate. In order to measure θ_a and θ_r (advancing and receding contact angles), another $7\mu l$ of water is added to the droplets with speed of $10\mu l/min$, and then the adsorbing part is started with the same speed until the droplet is adsorbed completely.

The values of contact angle (θ), advancing contact angle (θ_a) and receding contact angle (θ_r) on the pillared substrates are indicated in table 1.7. Also, the average of left and right contact angle on each sinusoidal pattern is presented in table 1.8. Corresponding droplets images are presented in figure 1.15. The contact angle on the flat surface with the same materials is measured as 93.8° .

According to table 1.8 and figure 1.15 the micro grooves improved hydrophobicity behavior of the surfaces. The difference between θ is more significant between textures with different amplitudes with respect to surfaces with different periods. Meaning that in figure 1.15 at each row from left to right θ shows noticeable improvement, while at

configuration of surface	$r_p(\mu m)$	$D_p(\mu m)$	$H_p(\mu m)$	$\theta(^{\circ})$	$\theta_a(^{\circ})$	$\theta_r(^{\circ})$
configuration 1	12.5	50	3	100.2	100.0	44.1
configuration 2	12.5	125	3	97.0	99.6	54.2
configuration 3	25	60	10	102.4	101.8	41.1
configuration 4	25	65	10	105	101.8	41.1
configuration 5	25	100	10	106	106.6	54.0
configuration 6	25	150	10	84.5	98.3	62.4

Table 1.7: Contact angle of droplets on pillared surfaces.

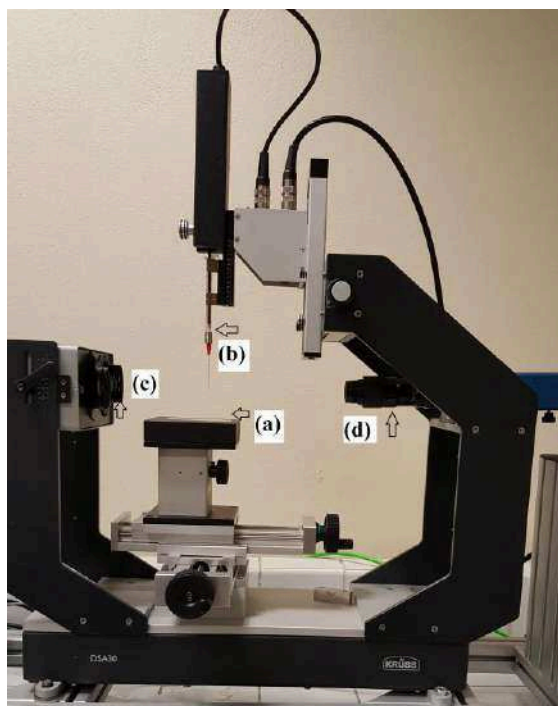


Figure 1.14: Illustration of contact angle measurement set-up. (a) the substrate support, (b) the syringe for injection water droplets on the substrate, (c) light source, and (d) the CCD camera that acquires images of droplets sited on the substrate.

Surface identification	$\lambda(\mu m)$	$a(\mu m)$	θ°	Surface identification	$\lambda(\mu m)$	$a(\mu m)$	θ°
30-5	30	5	104.6	60-30	60	30	137.5
30-10	30	10	118.6	60-50	60	50	141.3
30-30	30	30	128.5	100-5	100	5	94.3
30-50	30	50	128.1	10010	100	10	99.2
60-5	60	5	99.9	100-30	100	30	132.6
60-10	60	10	115.0	100-50	100	50	132.7

Table 1.8: Average contact angle on each sinusoidal substrate.

Run order	$\lambda(\mu m)$	$a(\mu m)$	θ°	Run order	$\lambda(\mu m)$	$a(\mu m)$	θ°
1	60	10	115.57	15	30	5	103.02
2	100	50	131.10	16	30	50	127.71
3	30	10	108.87	17	30	10	125.22
4	100	5	92.91	18	30	50	137.78
5	60	10	116.81	19	60	5	99.23
6	100	10	95.36	20	100	10	107.02
7	30	50	118.72	21	100	50	134.55
8	100	50	132.00	22	60	50	142.86
9	60	10	113.09	23	100	5	95.08
10	60	5	100.72	24	100	10	103.32
11	60	50	138.38	25	30	5	95.00
12	30	5	104.95	26	100	5	95.0
13	30	10	122.53	27	60	5	99.50
14	60	50	142.65				

Table 1.9: θ experiments table designed by FFD.

each column from up to down that period is changing θ remains almost constant. In this period range, by increasing the amplitude of the sinusoidal surface, droplets tend to form the Cassie state and stay on top of the peaks. Comparing the two tables refT 1-61 and 1.8 show that the contact angles on the pillared substrates are close to 90° , while on the sinusoidal substrates contact angles are much bigger than 90° .

1.5 Statistical analysis of sinusoidal surface characteristics

In this section the effects of period and amplitude of the sinusoidal profiles on the contact angle of water droplets (θ) and two dimensional roughness (R_a) are statistically studied using the method of full factorial design (FFD) considering significance level $\alpha = 0.05$. FFD is a powerful method of design of experiments (DOE) that enables to analysis the results of the experiments by considering the effect of all known and unknown errors. Also this method is used for interpreting the effect of several parameters on a specified factor, by running the minimum number of experiments required.

In this study we used the FFD by Minitab 18 to analysis the effect of two parameters (period (λ) and amplitude (a)) on the average contact angle of water droplets (θ) and average roughness (R_a) of the sinusoidal substrates. The experiments are designed at 3 levels of $\lambda = 30, 60, 100\mu m$ and 3 levels of $a = 5, 10, 50\mu m$ according to tables 1.9 and 1.10.

Contact angle measurement on each substrate is repeated 9 times to have the more precise results. In this regard, the experiments must be done by the order presented in tables 1.9 and 1.10 that are completely randomly (based on Gaussian rule) and are proposed by FFD. The random order of experiments enables to reduce the effect of unknown errors by distributing them between all the experiments.

According to [91] the effect model for a FFD can be written as:

$$y = \beta_0 + \beta_1x_1 + \beta_2x_2 + \beta_{12}x_1x_2, \quad (1- 1)$$

where y is the response, β_i are the regression coefficients, and x_i are the independent variables [92]. This method of FFD changes k independent variables in n levels (between

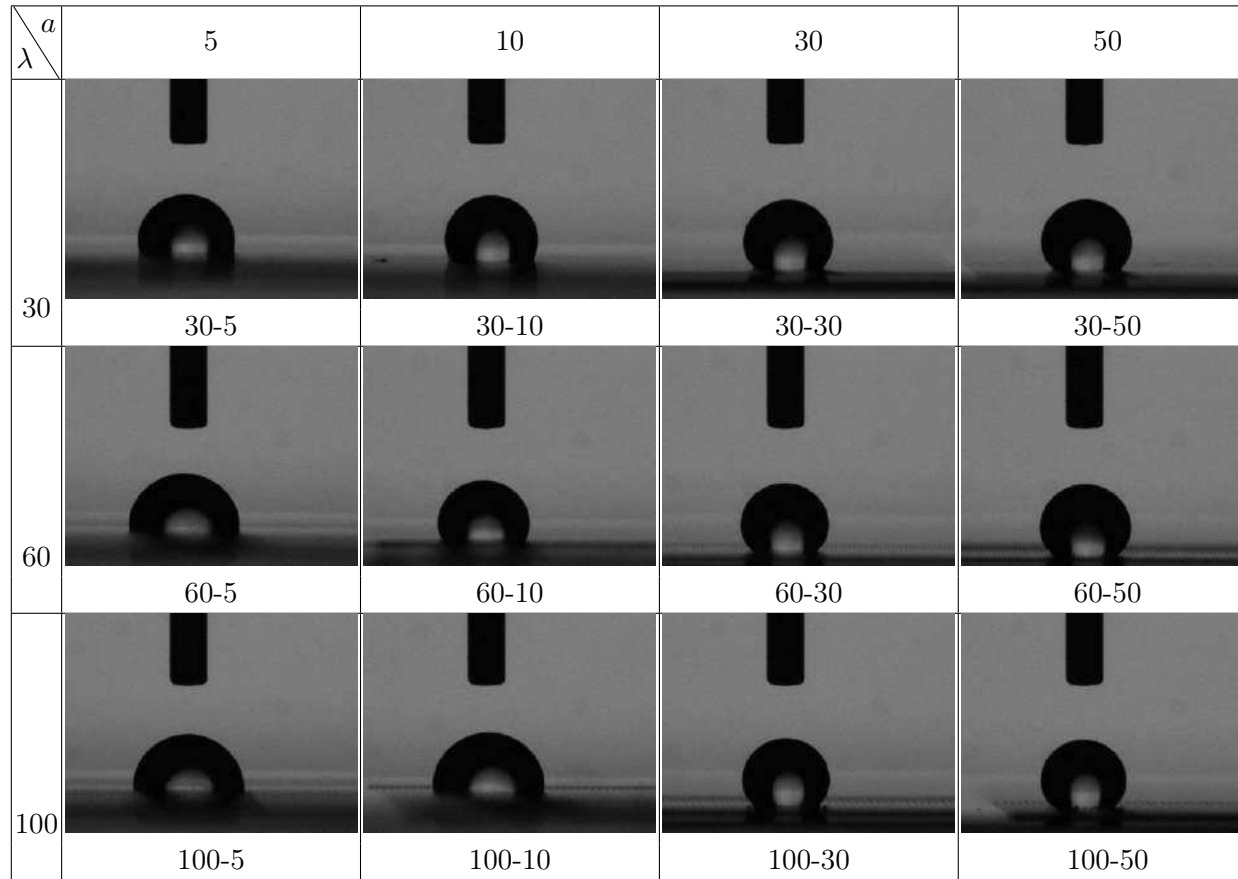


Figure 1.15: Contact angle of droplets on sinusoidal surfaces. λ and a being the period and amplitude of the sinusoidal profiles. In this images the sinusoidal profiles are perpendicular to the base lines of the droplets.

Run order	$\lambda(\mu m)$	$a(\mu m)$	$R_a(\mu m)$
1	60	50	7.38
2	30	50	3.42
3	30	5	1.07
4	60	5	1.45
5	60	10	2.77
6	100	50	9.49
7	100	10	2.34
8	100	5	1.24
9	30	10	2.37

Table 1.10: R_a experiments table designed by FFD.

their minimum and maximum) and fits the coefficients of regression model to study the effect of each independent variable on the response. The regression models fitted by FFD to describe the effect of λ and a as independent variables on θ and R_a as responses are as follow:

$$\theta = 8.76 - 0.1320\lambda + 0.6751a, \quad (1-2)$$

$$R_a = -0.83 + 0.0286\lambda + 0.1164a, \quad (1-3)$$

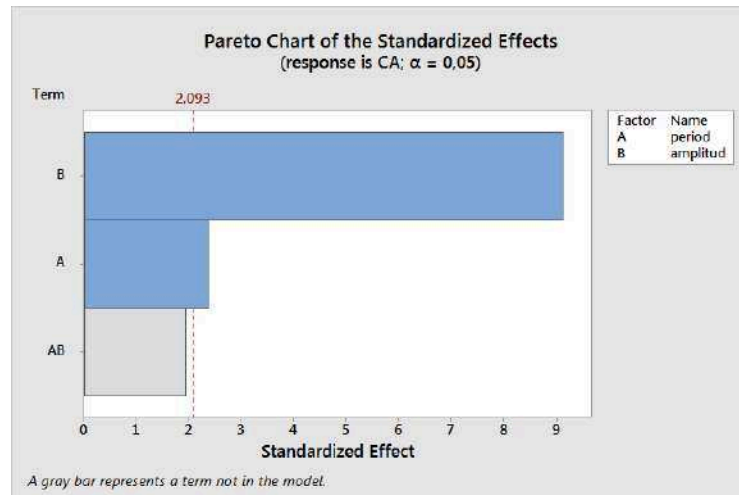
with $R^2 = 86.08\%$ and $R^2 = 80.13\%$ for θ and R_a respectively. This shows that the data are close enough to the regression line, because for a satisfactory fitting $R^2 > 80\%$. Apparently, the effect of a on both θ and R_a is much more significant than λ . This is what has been expected from figure 1.15. By comparing the values of β_i in equation (1-3), we can claim that λ does not have any specific effect on roughness in the range of our study. For concluding more precisely, one will need the Pareto charts and ANOVA tables of the two regression model.

The Pareto charts of the effects of λ and a on θ and R_a are presented in figure 1.16. The Pareto chart shows the absolute values of the standardized effects from the largest effect to the smallest effect. The standardized effects are t -statistics that test the null hypothesis saying that the effect of independent variable on the response is 0. The Pareto chart also plots a reference line to indicate which effects are statistically significant. The reference line usually is calculated based on the Lenth's pseudo-standard error (PSE). The red dashed line of the Pareto chart is drawn at the margin of error (ME), which is:

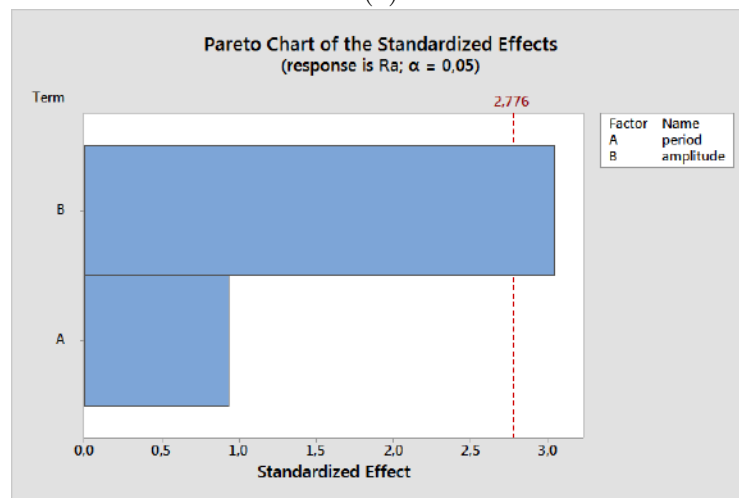
$$ME = t \times PSE \quad (1-4)$$

where $t = 1 - \alpha/2$ quantifier of a t -distribution with degrees of freedom equal to the number of effects / 3. Figure 1.16(a) illustrates that both of the parameters A (period) and B (amplitude) have statistically significant effect on θ because both of them pass from the reference line but the effect of amplitude is much more than the effect of period. This is what is apparent in figure 1.15 and regression equation 1-2 also. In the pareto chart AB indicates the effect of the two parameters at the same time.

The Pareto chart of the effective parameters on R_a , as was predicted by regression equation (equation (1-2)), confirms the evident fact that the period is not statistically effective on the surface roughness, while the effect of amplitude is really important.



(a)



(b)

Figure 1.16: Pareto charts of the effects of λ and a on (a) θ and (b) R_a

These claims can be confirmed by studying the Analysis Of VAriance (ANOVA table). ANOVA is used to determine whether there are any statistically significant differences between the means of several independent groups. The ANOVA compares the means between the groups and determines whether any of those means are statistically significantly different from each other. In DOE, ANOVA is used to detect the importance of each parameter on the result of the experiments.

Tables 1.11 and 1.12 indicate the ANOVA table for studying the importance of effect of λ and a on θ and R_a respectively. According to table 1.11 although the two parameters are statistically significant, because their $P - value$ is less than $\alpha = 0.05$, the effect of period with $P - value = 0.04$ is not as noticeable as amplitude with $P - value = 0$. Table 1.12 indicates that $P - value$ of amplitude is inferior to the confidence level, so this parameter statistically has important effect on R_a , while period with $P - value = 0.155$ that is far bigger than α cannot affect roughness in the range of this study.

Source	Degree of freedom	Adj SS	Adj MS	F-value	P-value
Regression	2	4964.1	2482.08	37.58	0.000
Period	1	317.1	317.07	4.8	0.040
Amplitude	1	4402.8	4402.82	66.66	0.000
Error	21	1387.0	66.05		
Total	23	6351.2			

Table 1.11: ANOVA table for studying the importance of effect of λ and a on θ for significance level $\alpha = 0.05$.

Figures 1.17 and 1.18 show the residual error analysis of θ and R_a . Residuals are estimates of experimental error obtained by subtracting the observed responses from the predicted responses. The residual analysis is a way to study how the errors affect the test results. These patterns are useful for knowing if there is some unknown parameter that affects the experiments, for example any failure in the set-up that increases by the time. Therefore, it is desirable that the standardized residual errors distribute randomly (based on Gaussian rule) and not far from the normality and also the fitted residuals do not obey any special pattern. This will show that there is no any unusual parameter that influences on the experiments. The normal probability plot and histogram in figures 1.17 and 1.18 show that the residual errors obey the normal distribution and can be said that they are distributed randomly. On the other hand, fitted residual plots in these figures indicate that the distributions of residual errors do not follow any special pattern and can be said that is randomly distributed. These evidences show that the results of the regression models

Source	Degree of freedom	Adj SS	Adj MS	F-value	P-value
Regression	2	55.542	24.771	12.10	0.008
Period	1	6.068	6.068	2.64	0.155
Amplitude	1	49.475	49.475	21.56	0.004
Error	6	13.769	2.295		
Total	8	69.311			

Table 1.12: ANOVA table for studying the importance of effect of λ and a on R_a for significance level $\alpha = 0.05$.

and FFD analysis are trustful.

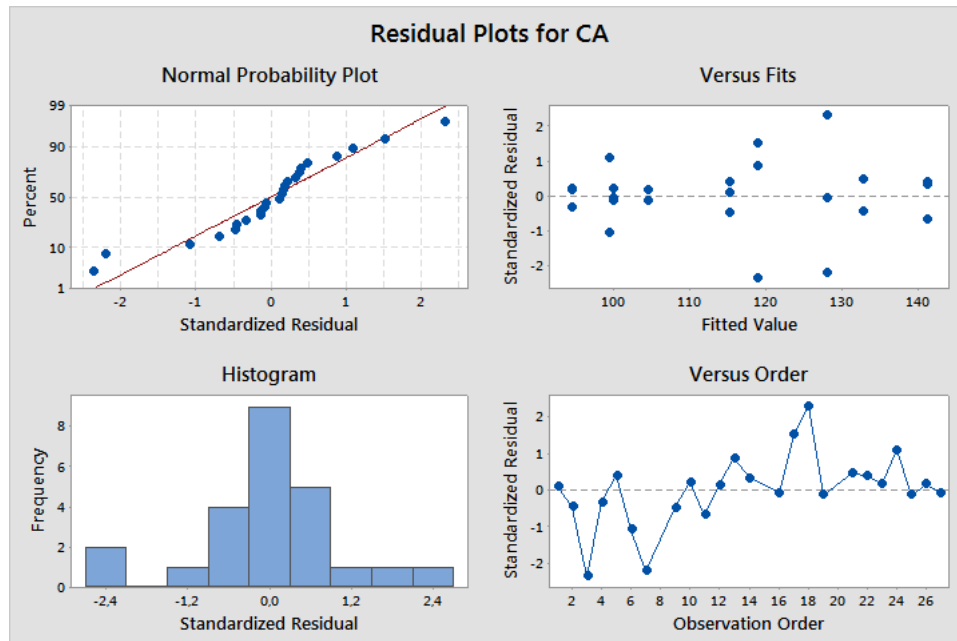


Figure 1.17: Residual plots of θ at $\alpha = 0.05$.

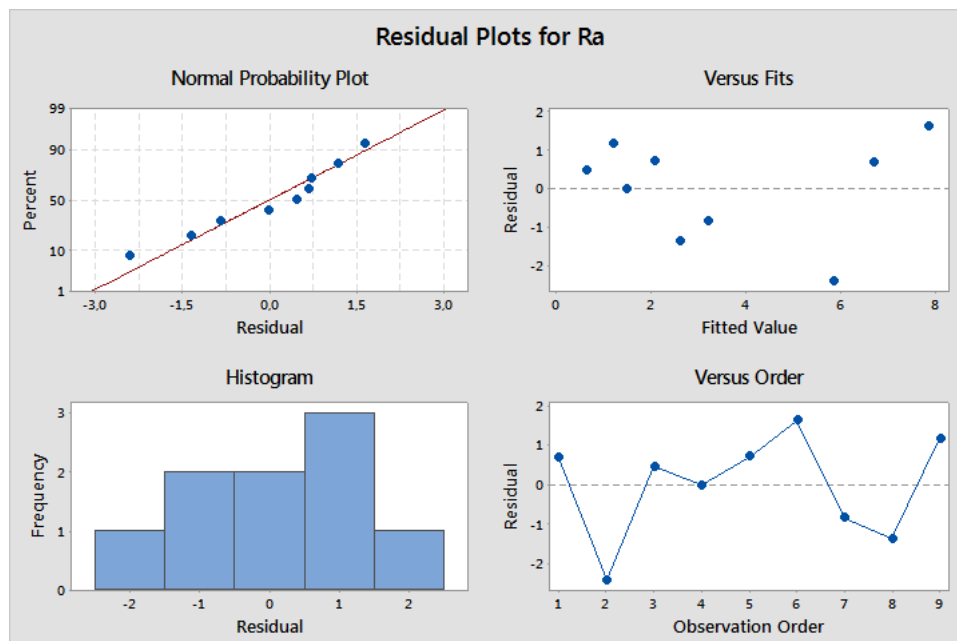


Figure 1.18: Residual plots of R_a at $\alpha = 0.05$.

1.6 Conclusion

1.6.1 English

The experimental procedure for studying the behavior of water droplets on different texturing patterns, was explained in this chapter. At first the preparation of polycarbonate substrates by polymer injection press was presented. During this process the metallic molds textured using laser technology were duplicated by melted polycarbonate. Then these samples were used as the substrate for condensation procedure on the experimental set-up described in section 1.2.

Also, some characterizing tests were done on both the metallic mold and the polycarbonate samples of the sinusoidal patterns including two dimensional roughness profile studied by interferometric microscope, real microscopic view of the sinusoidal profiles captured by scanning electron microscopy (SEM) and surface wettability using contact angle measurements. According to the results of contact angle measurement test, by changing the sinusoidal parameters even the contact angle as much as 140° is accessible.

The effect of sinusoidal profiles period and amplitude on both average roughness and average contact angle was studied statistically. These statistical studies showed that the effect of the amplitude of the sinusoidal profile is much more important than the effect of period on both of the parameters.

1.6.2 French

La procédure expérimentale pour étudier le comportement des gouttelettes d'eau sur différents modèles de textures a été expliquée dans ce chapitre. Dans un premier temps, la préparation de substrats en polycarbonate par presse à injection de polymères a été présentée. Au cours de ce processus, les moules métalliques texturés en utilisant la technologie laser ont été dupliqués par du polycarbonate fondu. Ensuite, ces échantillons ont été utilisés comme substrats pour la procédure de condensation sur la manipulation expérimentale décrite dans la section 1.2.

En outre, certains tests de caractérisation ont été effectués sur les échantillons de moules métalliques et de polycarbonate des profils sinusoïdaux, notamment : profil de rugosité bidimensionnel étudié par microscope interférométrique, vue microscopique réelle des surfaces sinusoïdales captées par microscopie électronique à balayage (MEB) et mesures d'angle de contact. Selon les résultats du test de mesure de l'angle de contact, en changeant les paramètres des sinusoïdes, même il est possible d'atteindre des valeurs d'angle de contact jusqu'à 140° .

L'effet de la période et de l'amplitude des profils sinusoïdaux sur la rugosité moyenne et l'angle de contact moyen ont été étudiés statistiquement. Ces études statistiques ont montré que l'effet de l'amplitude du profil sinusoïdal est beaucoup plus important que l'effet de la période sur ces deux paramètres.

Chapter 2

Image processing method

2.1 Introduction

2.1.1 French

Jusqu'à présent, l'appareil expérimental utilisé pour capturer des images du processus de condensation par gouttelette ainsi que la préparation et la caractérisation des substrats ont été expliqués. Dans l'étape suivante, les images d'échelle de gris prises par la caméra CCD doivent être binarisées afin d'extraire les informations relatives à la densité, la taille et la distribution spatiale et temporelle des gouttelettes.

En ce qui concerne la condensation par gouttelette sur les substrats plats et sinusoïdaux, la binarisation n'est pas très compliquée car comme on peut le voir sur la figure 2.1 (a) et (b) les gouttelettes se distinguent facilement du substrat. Mais, sur les substrats à piliers, puisque les piliers sont vraiment similaires aux gouttelettes, une technique plus élaborée est nécessaire. Comme on peut le voir clairement, les gouttelettes de la figure 2.2 (b) et (c) ne sont pas facilement détectables à partir des piliers nus qui sont montrés dans la figure 2.2 (a). La technique, qui est développée ici, caractérise et sépare les piliers des gouttelettes, puis applique 4 techniques différentes pour binariser les images en fonction de la gamme de tailles de gouttelettes .

Puisque les gouttelettes sur les substrats plats et sinusoïdaux sont plus facilement détectables que sur les substrats à piliers, nous avons utilisé la même méthode pour les deux premiers types de substrats, puis nous avons développé une autre méthode de segmentation des images de substrats à piliers. Ainsi, ce chapitre est divisé en deux sections principales : développer une méthode pour les images de binarisation de substrats plats et sinusoïdaux et dans la partie suivante, présenter un algorithme plus complet pour les images de binarisation des substrats à piliers.

2.1.2 English

So far, the experimental apparatus used for capturing images of the process of dropwise condensation as well as substrates preparation and characterization have been explained. In the next step, the gray scale images acquired by CCD camera have to be segmented in order to extract the information related to density, size, and spatial and temporal distribution of the droplets.

Most of the time, the image processing algorithms are divided into three main steps: pre-processing, segmentation and reconstruction:

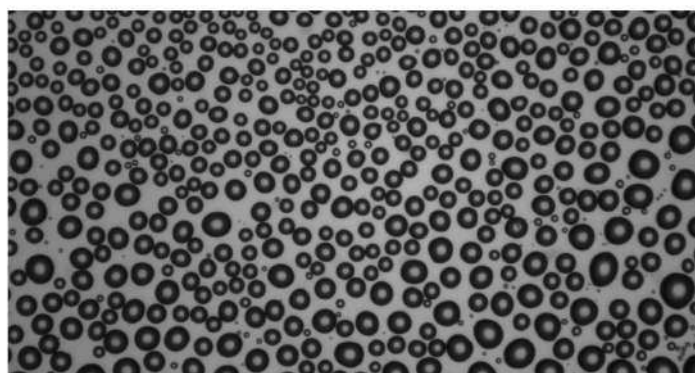
Preprocessing The preprocessing or pretreatment step aims at improving contrast and removing noise in order to facilitate the segmentation step. Regarding dropwise condensation images, the low contrast as well as inhomogeneity of small droplets are the main sources of problems for segmentation.

Segmentation The droplet segmentation step consists of isolating droplets from the background and then separating overlapping drops. The corresponding algorithms can be classified into three groups: the ones based on the shape analysis, the ones based on the edge analysis, and the ones based on the intensity analysis. The algorithms based on the shape analysis consider droplets as circles with dark edges and bright centers. These drops can be detected by using circle detection methods like the Hough transform [93] and its improvements, such as the normal-line Hough transform [94] and the coherent circle Hough transform [95]. However, these methods are only efficient for spherical droplets. The algorithms based on the edge analysis use images generated by an edge detection method [96]. For this purpose, the Canny method seems to be the most convenient since although it is more sensitive to noise with respect to other methods, it provides more connected contours. Then, the contour discontinuities that represent multiple overlapping droplets are detected. Such points are called breakpoints, that can be detected by means of several techniques, either by rotating the edge curves [97] or by analyzing their curvature [98, 99]. The main drawback of these techniques is the noise sensitivity, which necessitates to smooth the edge curvatures. A way to limit the noise sensitivity of measurements is to use an adaptive curvature [100]. Finally, the algorithms based on an intensity analysis use the gray-level intensities as a drop presence indicator. These intensities can be used directly like the PIV methods [101] using a dynamic thresholding and watershed [102] or indirectly like the appearance-based approaches using an isolated drop to select the same appearance drops [103]. These methods can be combined through a tree of decision to improve the detection quality [104]. For instance, the PIV methods are particularly efficient for isolated drops while the watershed method works well for overlapping ones. However, this combination requires a long computational time.

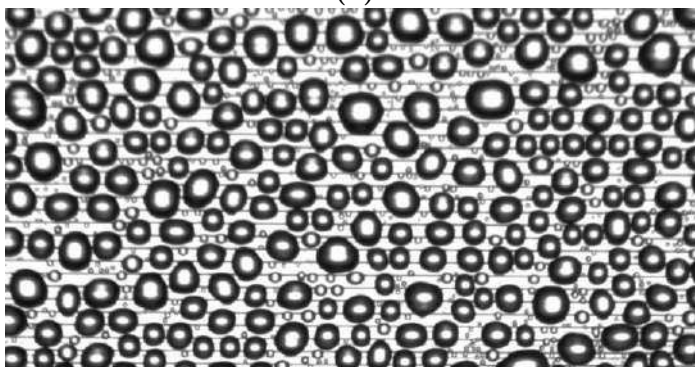
Reconstruction The drop reconstruction step consists of reconstructing missing parts of drops by determining their radius and their centers. These methods can be divided into four main groups: the ones based on ellipse fitting, based on the geometrical analysis, based on the morphological analysis and the ones using drop inner boundaries. The ellipse fitting methods consist of recognizing ellipse-like shapes in the image. For this purpose, least-squares fitting methods [105] or k -means methods [106] are used. However, these methods work only on ellipsoidal droplets. The geometrical methods aim at determining whether two arcs belong to the same drops by means of either correlation coefficients [97] or applying convexity criteria directly to the contour image [107] or to the polygonal approximation image [108]. The main drawback of these methods is the use of deterministic parameters. The morphological techniques use the morphological reconstruction principle. For this purpose, overlapping drops are reduced to independent characteristic areas before being reconstructed, but the percentage of overlapping droplets must not be too high. Different techniques can be used in this regard: successive erosion [109, 110], skeletonization and shrinking [111] or the watershed technique applied to a distance map [112]. More recently Gavet and Pinoli [113] developed their algorithm based on skeletonization, distance

map and watershed technique for detecting the cornea endothelial cells. After all, a final technique is applied in order to complete missing parts of droplets by using drops inner boundaries [104]. This last method necessitates high inner boundaries quality.

As was explained, the experiments are conducted on three kinds of substrates with flat, pillared and sinusoidal texturing patterns. Regarding dropwise condensation on the flat and sinusoidal substrates, binarization is not very complicated because as it can be seen in figure 2.1(a) and (b) the droplets are easily distinguishable from substrate. But, on the pillared substrates, since the pillars are really similar to the droplets, a more complicated technique is needed. As can be clearly seen, the droplets in figure 2.2(b) and (c) are not easily detectable from the bare pillars that are shown in figure 2.2(a). The technique, that is developed here, characterizes and separates the pillars from the droplets, then applies 4 different techniques depending on the size range of droplets to binarize the images.



(a)



(b)

Figure 2.1: Droplets on the (a) flat and (b) sinusoidal substrates are distinguishable from the substrates. Due to similarity between the images on the flat and sinusoidal substrates, the same segmentation algorithm is used for the images of these two kinds of substrates.

Since the droplets on the flat and sinusoidal substrates are more easily detectable than on the pillared substrates, we used the same method for the two first kinds of substrates and then we developed another method for segmentation the images of pillared substrates. So, this chapter is divided into two main sections: developing a method for binarization images of flat and sinusoidal substrates and in the next part, presenting a more complete algorithm for binarization images of the pillared substrates.

2.2 Image processing technique for the droplets on flat and sinusoidal surfaces

In the following the method that is used to binarize gray-scale images taken of droplets nucleation and growth on the flat and sinusoidal surfaces is presented.

2.2.1 Preprocessing

As was mentioned above, due to the low contrast and inhomogeneity of small droplets, the preprocessing step is required for images on all the surfaces. The Laplacian operator can be used in this regard, because it depends on the curvature instead of the gray level intensity and so it is robust with respect to contrast. The Laplacian filtering subtracts the pixel intensity of each droplets center point from the average of its neighborhood:

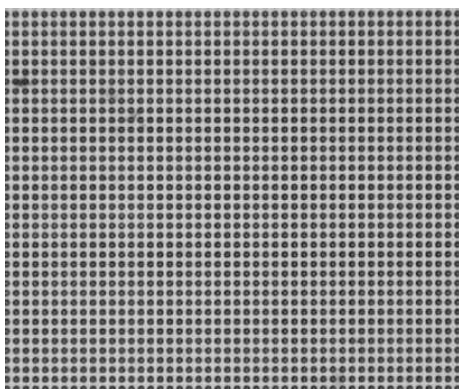
$$f(x, y) = \frac{I(x-1, y) + I(x, y-1) + I(x+1, y) + I(x, y+1)}{4} - I(x, y). \quad (2-1)$$

The Laplacian of an image highlights regions of rapid intensity change and is therefore often used for edge detection. The effect of Laplacian is illustrated in figure 2.3. It can be seen that in the filtered image, the contour of droplets is more visible and the gray level intensity of the small droplets is also improved with respect to the original image.

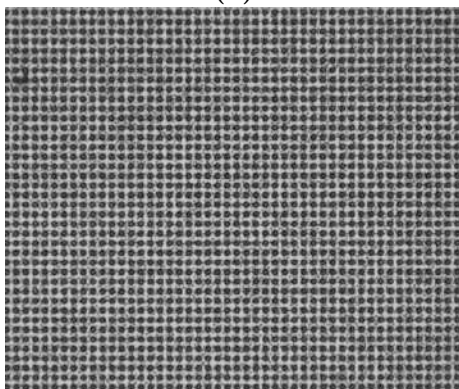
2.2.2 Segmentation

The first step of image segmentation is to isolate the droplets from the substrate. The main goal is to prepare black and white images, in which the white pixels belong to the droplets on the black substrate. For this reason, one can compare the value of each pixel with a thresholding value. The amounts inferior the thresholding value will convert to 0 (black pixels) and the amounts superior the thresholding value will convert to 1 (white pixels). Therefore, the objective of this step is how to define the thresholding value.

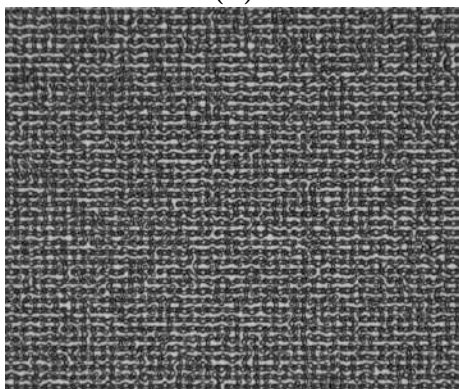
In this regard we used the adaptive integral image method. An integral image (also known as a summed-area table) is a tool that can be used when the goal is to compute the sum of a function from pixels to real numbers $f(x,y)$ (like pixel intensity) over a rectangular region of the image [114]. For instance, this method has been applied in texture mapping [115], face detection in images [116], and stereo correspondence [117]. In this method the intensity of each pixel $I(x, y)$ is equal to the sum of all the pixels above and to the left of (x, y) , inclusive:



(a)



(b)



(c)

Figure 2.2: (a) A pillared surface without droplets. (b) Adsorbing and (c) coalescing droplets on the same pillared substrate. The droplets are not easily detectable from the pillars so a more complicated image processing technique is required.

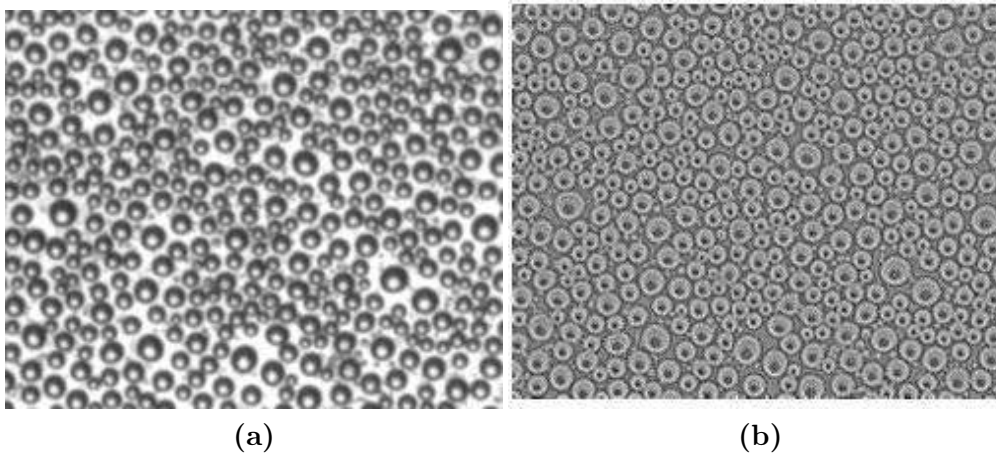


Figure 2.3: Image pretreatment by Laplacian filtering. (a) Original image, (b) filtered image

$$\begin{bmatrix} 0 & 1 & 0 \\ 1 & -4 & 1 \\ 0 & 1 & 0 \end{bmatrix}$$

therefore,

$$I(x, y) = f(x, y) + I(x - 1, y) + I(x, y - 1) - I(x - 1, y - 1). \quad (2- 2)$$

So, the intensity over the rectangle drawn on the left right (x_1, y_1) and right below (x_2, y_2) side of the pixel (x, y) , $f(x, y)$ is:

$$\sum_{x=x_2}^{x_2} \sum_{y=y_2}^{y_2} f(x, y) = I(x_2, y_2) - I(x - 1, y_2) - I(x_2, y - 1) + I(x_1 - 1, y_1 - 1). \quad (2- 3)$$

Then using the method of Sauvola [118, 119], one will be able to calculate the value of thresholding (t). The idea behind the method of Sauvola is to vary the threshold over the image, based on the local mean (m) and local standard deviation (σ), computed in a small neighbourhood of each pixel. We used the rectangles of integral image method as the neighbourhood of each pixel.

$$t(x, y) = m(x, y) \left[1 + k \left(\frac{\sigma(x, y)}{R} - 1 \right) \right], \quad (2- 4)$$

where k is a parameter equal to 0.34 and R is the dynamic range of standard deviation (here 128). Considering a rectangle with length size w around the point (x, y) , m and σ can be calculated as:

$$m(x, y) = \frac{1}{w^2} \sum_{i=x-w/2}^{x+w/2} \sum_{j=y-w/2}^{y+w/2} f(i, j), \quad (2- 5)$$

$$\sigma^2(x, y) = \frac{1}{w^2} \sum_{i=x-w/2}^{x+w/2} \sum_{j=y-w/2}^{y+w/2} f^2(i, j) - m^2(x, y). \quad (2-6)$$

Applying the summed-area method and using operator I_2 for the double sum of equation (2-6), we will have:

$$m(x, y) = \frac{1}{w^2} [I(x_2, y_2) - I(x_2, y_1 - 1) - I(x_1 - 1, y_2) + I(x_1 - 1, y_1 - 1)], \quad (2-7)$$

$$\sigma^2(x, y) = \frac{1}{w^2} [I_2(x_2, y_2) - I_2(x_2, y_1 - 1) - I_2(x_1 - 1, y_2) + I_2(x_1 - 1, y_1 - 1)] - m^2(x, y), \quad (2-8)$$

2.2.3 Reconstruction

The method that is used here to reconstruction the overlapping droplets is watershed. Watershed is a morphological method for gray scale image segmentation and reconstruction [120, 121]. In this method, the image is partitioned into different regions so called basins, that are related to the local minimums. These local minima are considered as holes filled with water. When the water fills two basins, they overflow and connect, so a dam is inserted at their meeting point. These dams form the watersheds.

In order to separate the connecting droplets, at first the distance map is used that highlights the pixels inside a droplet that are farthest with respect to substrate. Figure 2.4(a) illustrates a binarized image before reconstruction. In this figure the overlapping droplets are simply visible. The distance map and surface partitioned with watershed technique are shown in figure 2.4(b) and (c). Figure 2.4(d) represents the results of reconstruction.

Therefore, by applying the three steps mentioned here we are able to binarize the gray scale images taken from droplets on flat and sinusoidal substrates. The results of this algorithm on the flat substrate is shown in figure 2.5. As was mentioned above, image processing for droplets growing on pillared substrates depends on the size of droplets because of their similarity as well as their connections with pillars. In this part, the technique used for binarization images taken from pillared surfaces will be discussed.

2.3 Image processing technique for the droplets on pillared surface

In the case of pillared surfaces, the texturing patterns do not let the directly use of the technique presented in section 2.2, although they are adapted to different drop shapes and image conditions. Indeed, pillars have the same properties as drops, they have dark edges and bright centers. Moreover, when the drop shape becomes irregularly connected over the pillars, the previous methods are not able to separate them and recognize each droplet. Thus, the goal of this section is to find a way to detect drops and pillars separately, in order to analyze drop characteristics evolution on the surface.

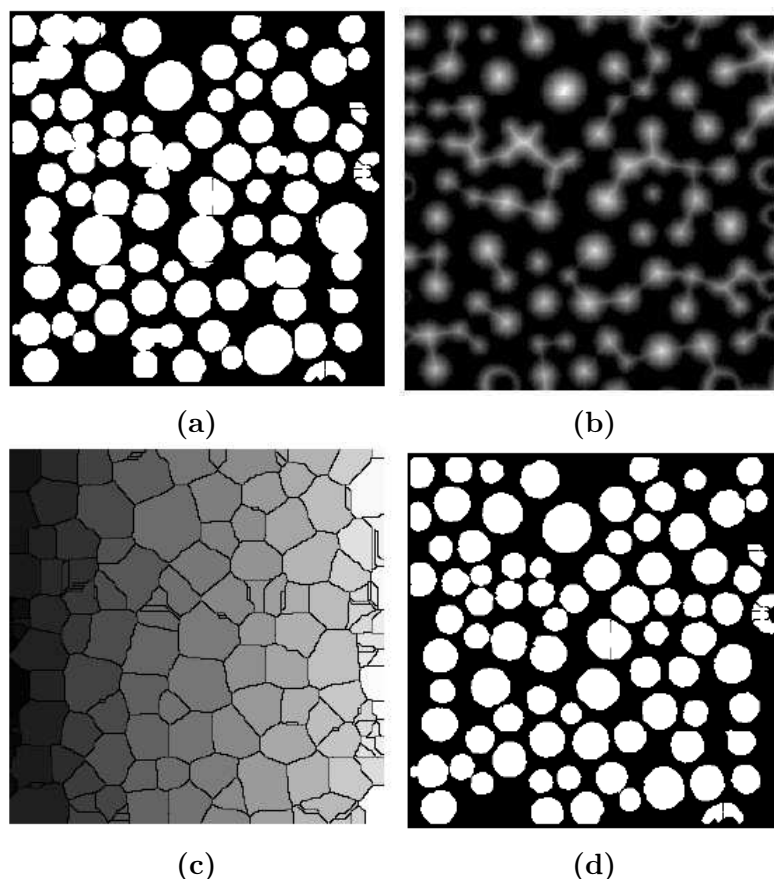


Figure 2.4: Reconstruction step. (a) Binarized image before reconstruction, (b) Distance map, (c) Watershed partitioned image, (d) Binarized image after reconstruction

An image processing algorithm is developed to segment the drops and to analyze their characteristics evolution during dropwise condensation. This algorithm consists of three main steps as shown in figure 2.6. The pillar characterization step aims at isolating pillars in the first image, in order to remove them from the rest of the images. The goal of the second step is to divide the image set into four groups: very small drops, small drops, medium drops and big drops. The first two groups refer to the droplets growth by adsorption. The third group corresponds to the coalescence step and the last one corresponds to the steady state where the changes in size and number of droplets are negligible. After categorization, the corresponding image processing algorithm is applied to each group. It is worth pointing out here that the stability on drops sizes and density comes from the balance between coalescence and nucleation of new droplets. In coalescence the droplets grow rapidly but since they join their density decreases, on the other hand in the bare area produced during coalescence new small droplets can grow that can increase the drops density but they reduce the average radius. The opposition between these two phenomenons will lead to a stable pattern in the graphs of droplets size and density.

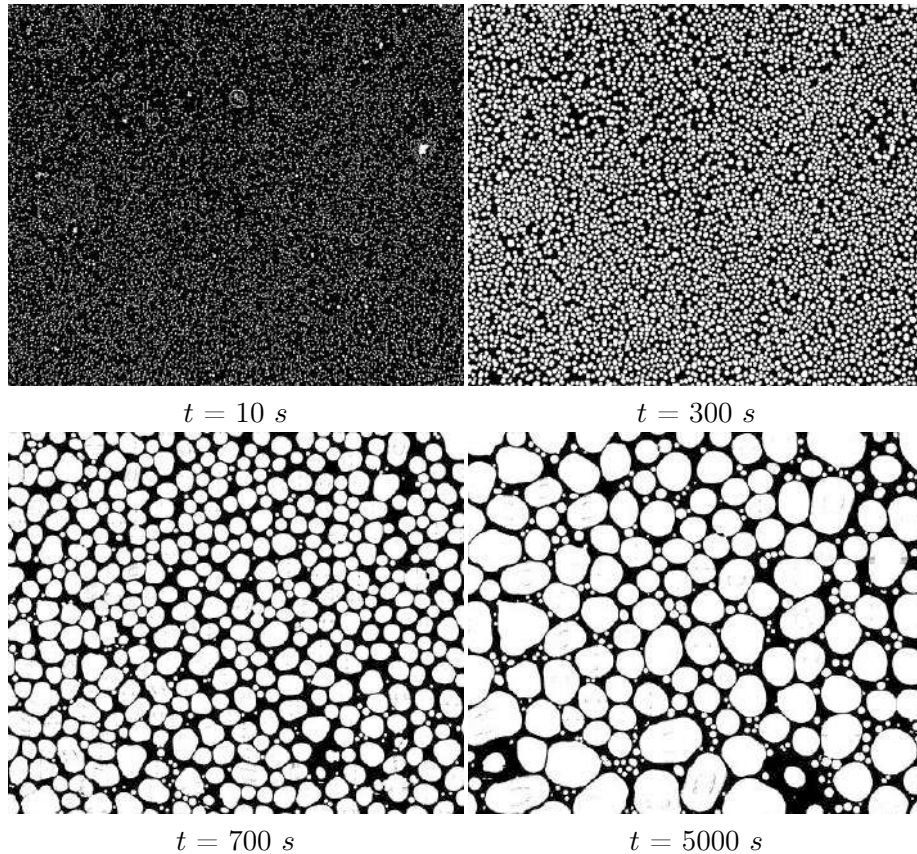


Figure 2.5: The segmented images of droplets growing on the flat substrate at different time steps ($t = 10$, 300 , 700 , 5000 s). These time steps correspond to initial nucleation, adsorption, coalescence, and steady state steps.

2.3.1 Pillar characterization

The goal of this step is to isolate pillars from background in order to remove them in images to be able to detect the droplets. In fact, pillars can entail mis-measurement because of their similar properties to drops. As the images are taken without shifting, pillars are at the same locations on all of the images. So, for the purpose of pillar elimination, the first image of a considering set of experiments is used because the drop presence can be neglected. The algorithm is detailed in figure 2.7.

As pillars are circular, the circle Hough transform is the most adapted technique. Moreover, an approximation of pillar radius is known based on table 1.1. It is important to consider a quite narrow range for Hough transform radius around pillars size, in order to get accurate results and a low computational time. To improve again the algorithm performances, the Hough transform is used [95].

By means of this method, some artefacts are detected too as shown in figure 2.7 (b). As they don't have the same size as pillars, a technique to solve this problem is to consider the distribution of circle radius and to remove the ones with an aberrant radius, as shown in figure 2.7 (c) and (d). Thus, the circle radius must be inside the band $[\mu - \sigma; \mu + \sigma]$ to

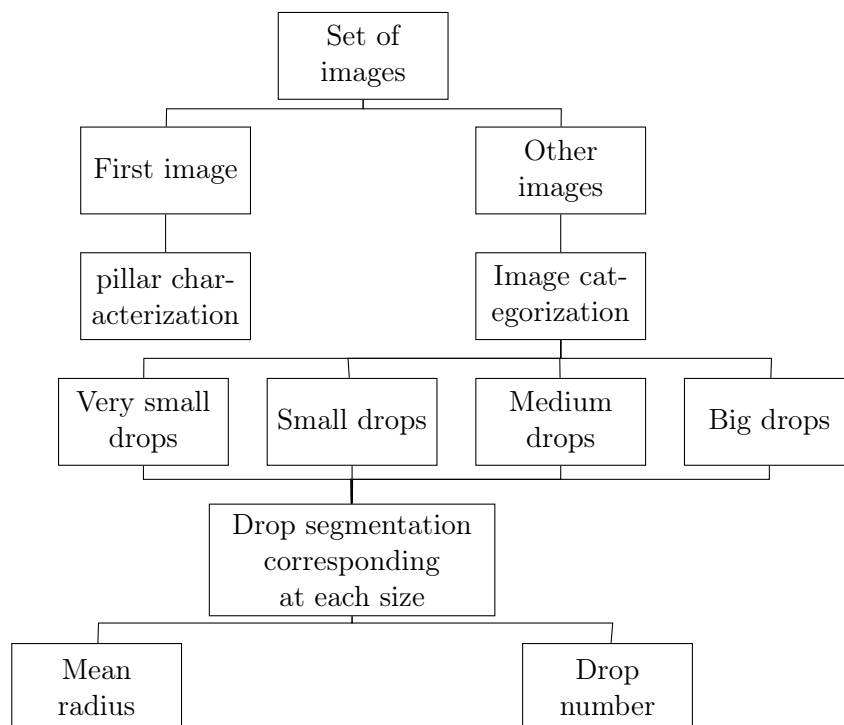


Figure 2.6: Schematic diagram of the image processing algorithm on pillared substrate

be considered as pillars, where μ and σ are the average and the standard deviation of the radius distribution.

At the same time, a manual pillar recognition test is led, as shown in figure 2.7 (e). This secondary method enables to confirm the position of pillars and to validate the calculated radius. This is necessary because, if the radius of a certain circle is much smaller than the real radius of pillars (from table 1.1), the circle will be considered as a droplet instead of a pillar.

Figure 2.7 (f) shows that pillars from the Hough transform are slightly smaller than the real ones, that can be explained by their blurred boundaries. Consequently, the circles from the Hough transform must be enlarged. In order to quantify the correct radius, the equivalent circle radius is calculated by means of the manual measurements. This equivalent radius refers to the radius of the circle with the same center as the one from the Hough transform but covering both the Hough transform circle and the manual measured circle, as shown in figure 2.8. In our case, pillar radius must be enlarged from four-pixel wide.

All in all, the image with the pillars radius calculated from the Hough transform is firstly generated, then this image is dilated by a disk structuring element whose radius corresponds to circle enlargement found previously and finally, the binary image of the pillars is extracted. The final results show visually good approximation of the pillar location and size.

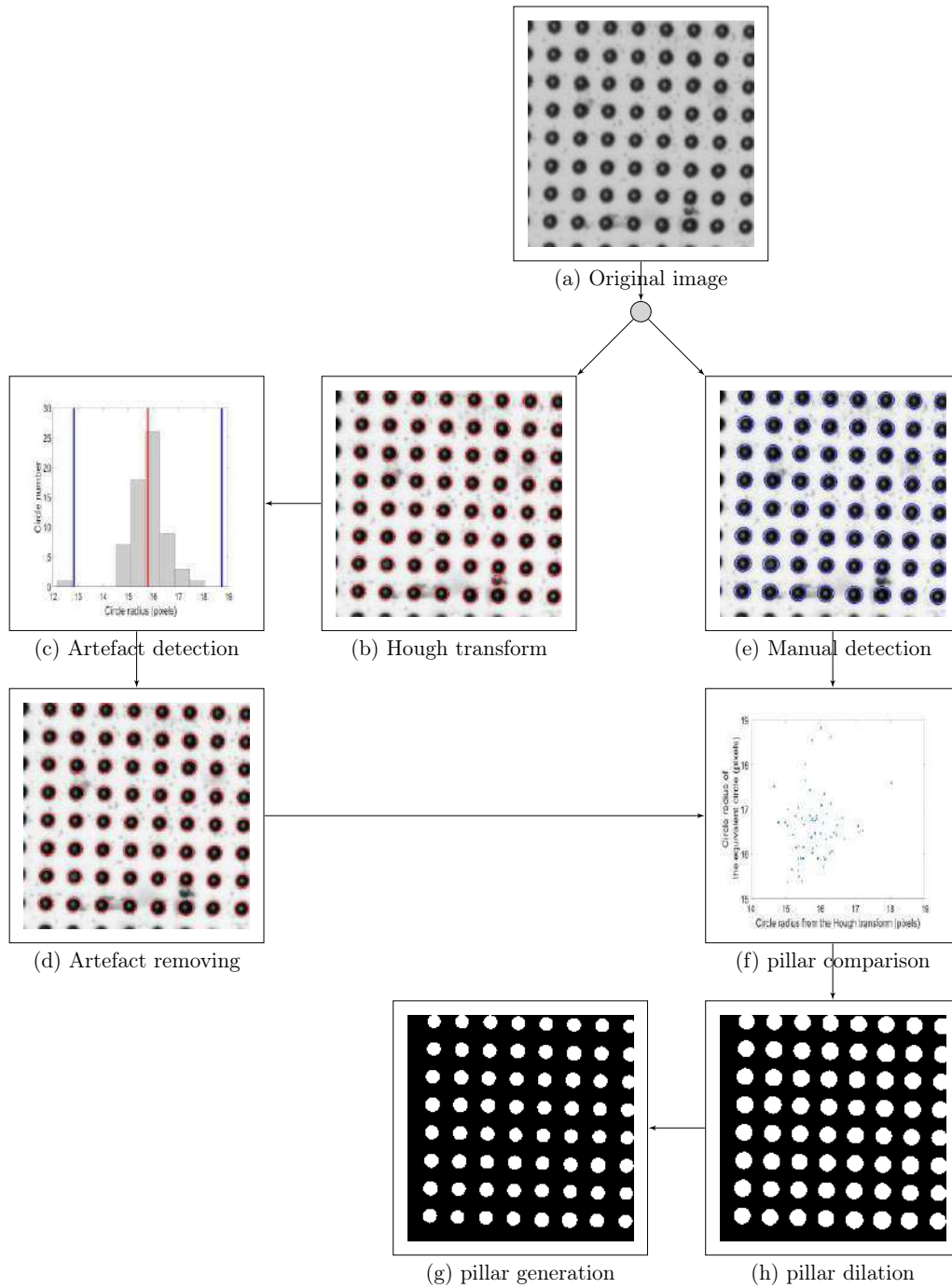


Figure 2.7: Algorithm for pillar characterization

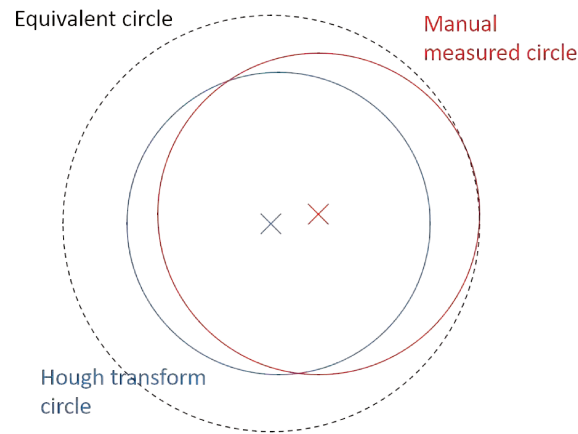


Figure 2.8: Equivalent circle determination

2.3.2 Image categorization

As mentioned previously, there are four kinds of drops: very small, small, medium and big drops. It is important to distinguish these groups because the drop identification algorithm will be adapted to each kinds of drops. Two main categorization methods exist: the ones based on the intensity distribution [122] and the ones based on the pattern distribution [123, 124]. As the image categorization needs to be very fast, the study of intensity histograms is preferred in our case.

Ten percent of images have been chosen regularly, since the time step between images is equal to 1 s, 10% of images means the images have been taken after each 10 s. The corresponding gray-tone histograms of each studied image is determined. As shown in figure 2.9, the number of major peaks in histograms vary as a function of time. Four types of the gray-tone histograms with 3, 2, 1 and again 2 peaks are shown in figure 2.10. This variation represents the different droplets sizes. Thus, the ranges of each size group of droplets are characterized:

- Very small droplets: histogram with three major peaks, corresponding to the background, the drop edge and the drop center.
- Small drops: after a while when the histogram of gray tone turns into bimodal diagram, the majority of droplets are called small droplets that grow mainly due to adsorption. With respect to the former stage here the peak related to the background disappeared because drops tend to cover entirely the sample.
- Medium droplets: in the third stage, drops start to coalesce and their centers become larger with the same intensity as background. Therefore, the gray tone histogram will turn to a unimodal diagram.
- Big droplets: finally, when the droplets are big enough to reach the steady state condition, the gray tone histogram will have two peaks again, that refer to the drop edges and centers.

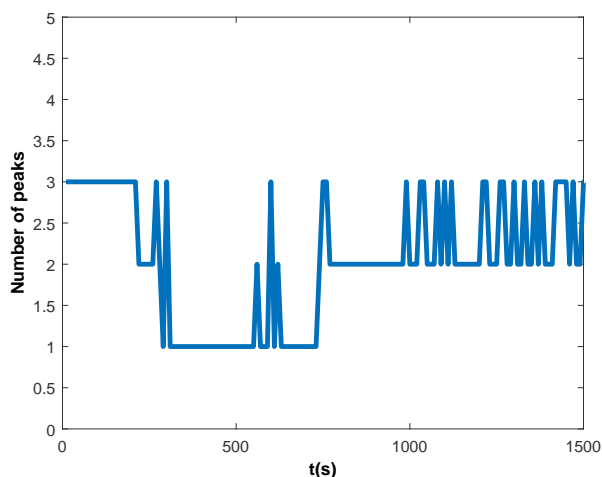


Figure 2.9: The changes in number of the major peaks in gray-tone histograms on time. Since the size of droplets is changing, the gray-tone histograms shows different number of peaks at different time steps. Based on the number of these peaks we can categorize the droplets in the four categories: very small, small, medium, and big droplets.

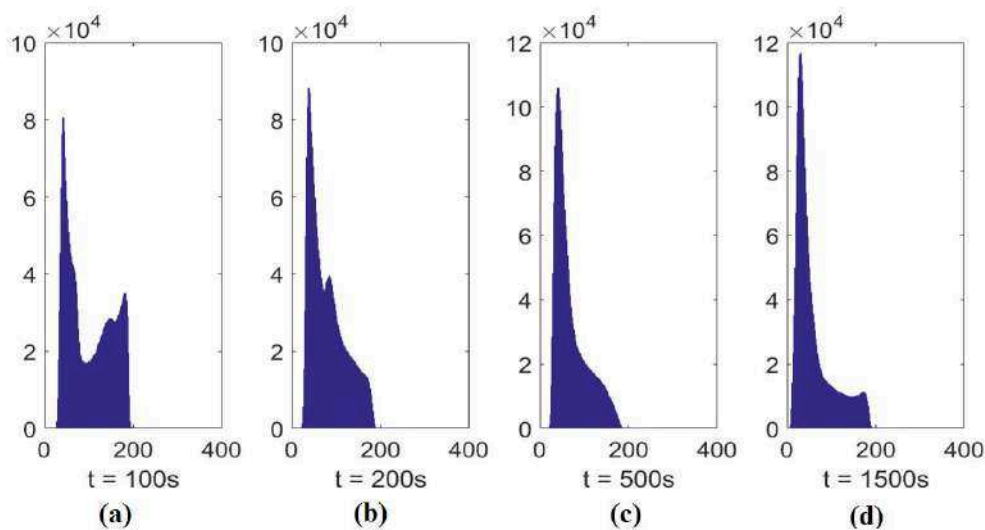


Figure 2.10: Intensity histogram of (a) very small droplets at $t = 100 s$, (b) small droplets at $t = 200 s$, (c) medium droplets at $t = 500 s$ and (d) big droplets drops at $t = 1500 s$.

2.3.3 Drop identification

This last part of the algorithm consists of identifying drops in each image in order to determine the evolution of drop characteristics such as size, density and spatial distribution.

Very small drops refer to the small elements between pillars (figure 2.11). The idea of this algorithm is to segment drops by means of correct thresholding values, as

shown in figure 2.12.

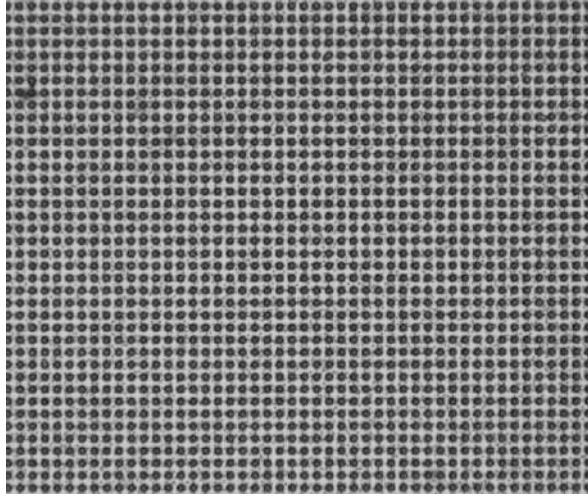


Figure 2.11: Image of very small drops on a pillared surface.

The very small droplets spread the gray tone histogram towards darker area, because generally they are darker than the substrate. Therefore, the superposition point between these two histograms can be used as thresholding value for figure 2.12 (a). But since there are lots of superposition points between these two histograms along the vertical axis, the thresholding value can be calculated by finding the superposition point with the maximum value. Figure 2.12 (g) represents the difference between these two histograms and the zero values in this graph shows the superposition points. So, the first zero point after the peak corresponds to the maximum superposition point or the thresholding value. This value then used for thresholding the images containing very small drops as is shown in figure 2.12 (h). At last each region is labeled according to figure 2.12 (i). Therefore, the number of regions corresponds to the drop number N , that enables to determine the mean drop radius R_{avg} from the total region area A :

$$R_{avg} = \sqrt{\frac{A_{tot}}{N\pi}}. \quad (2-9)$$

Small drops are presented as small circular elements which are smaller than the pillars in the images (figure 2.13). Since, at this step, droplets are perfectly circular, they can be recognized by means of the Hough transform as shown in figure 2.14 (b).

Then, as shown in figure 2.14 (c), the circles corresponding to pillars are removed by comparing the position of circle centers between the considered image and the first image of the set. The binary image obtained here (figure 2.14 (d)) gives the total area A_{tot} of drops. To get the number of drops, the overlapping drops need to be separated. For this purpose, the distance map is performed on the binary images by means of the Euclidean distance (figure 2.14 (e)) and the watershed operation is applied to this distance map (figure 2.14 (f)). A labeling step enables to get the number of the droplets and finally, the equation 2-9 gives the mean radius of drops.

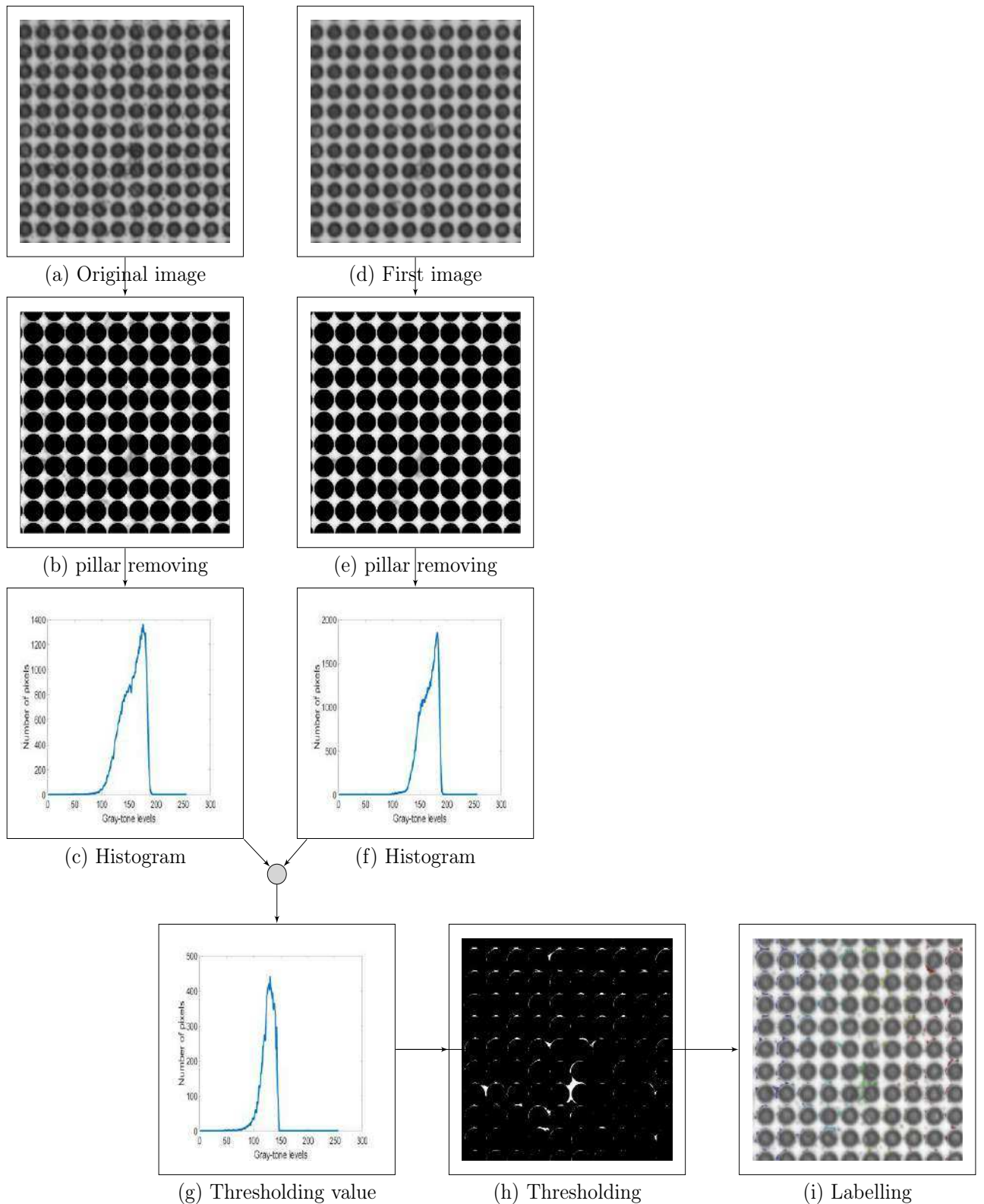


Figure 2.12: Algorithm for very small drops.

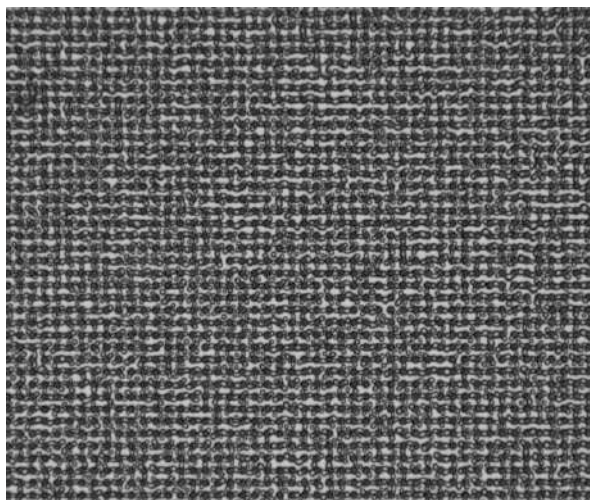


Figure 2.13: Image of small drops on a pillared surface.

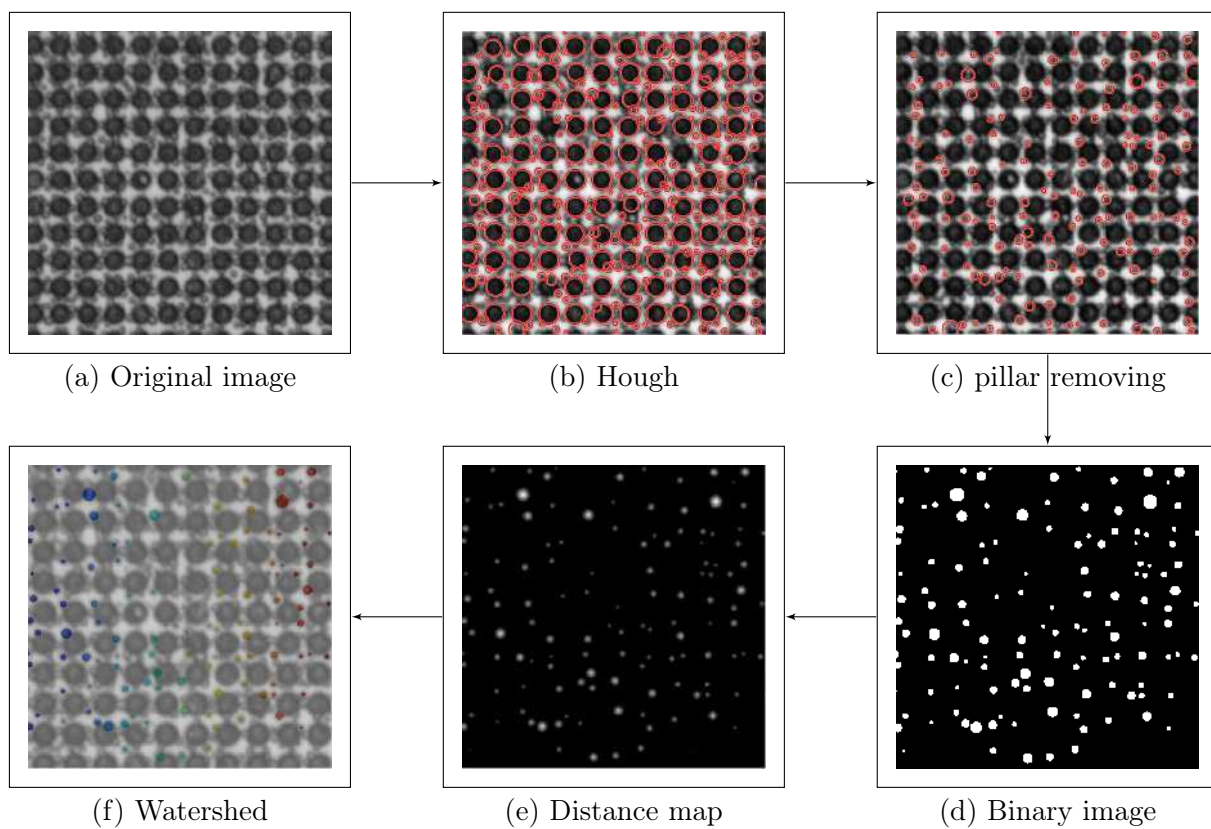


Figure 2.14: Algorithm for small drops.

Medium drops form a continuous cluster around pillars and drop centers look like background regions (figure 2.15). Therefore, the centers of drops must be determined by means of some criteria based on both geometry and intensity (figure 2.16).



Figure 2.15: Image of medium drops on a pillared image.

In this regard, the original images are firstly thresholded by means of Otsu's method as is shown in figure 2.16 (b). The problem here is that white area represents both droplets center and substrate. In order to recognizing droplets center, two techniques are applied to sufficiently large white regions. The droplets central zones are either more convex than substrate or are less homogeneous in intensity. Convexity here means the if we connect each two points inside a curve their connecting line does not cut the curve. By that definition, the bright zones with convexity rate of over 4 % (figure 2.16 (d)) or with low rate of gradient magnitude are considered as the drops centers (figure 2.16 (c)). The limited rate of gradient magnitude corresponds to $4/5$ of the mean gradient magnitude of the neighborhoods. Finally, the binarization of images of the droplets as in figure 2.16 (f) are made by applying the watershed method.

Big drops are characterized by the fact that they cover entirely several pillars as shown in figure 2.17. For binarizing images containing big droplets, shrinking and gradient properties are used as is shown in figure 2.18.

Firstly, the images are thresholded by the Otsu's method as shown in figure 2.18 (b). Then, in figure 2.18 (c) the black parts are shrunk in order to get their skeletons around the white regions which correspond to either the drops centers or the background. As was explained for the medium drops, the average of gradient magnitude is calculated on the white regions according to figure 2.18 (d). Then, the distribution of this value is divided into two groups by means of the histogram specification in which the median between the two main peaks gives the criterion value (figure 2.18 (e)).

However, when several white regions belong to the same drop, the watershed operation can't be applied directly. To solve this problem, the white regions are dilated and overlaid with the pillar image. Thus, the white regions which belong to the same drop are connected. A test on convexity enables to reconstruct each drop center (figure 2.18 (g)). Finally, a

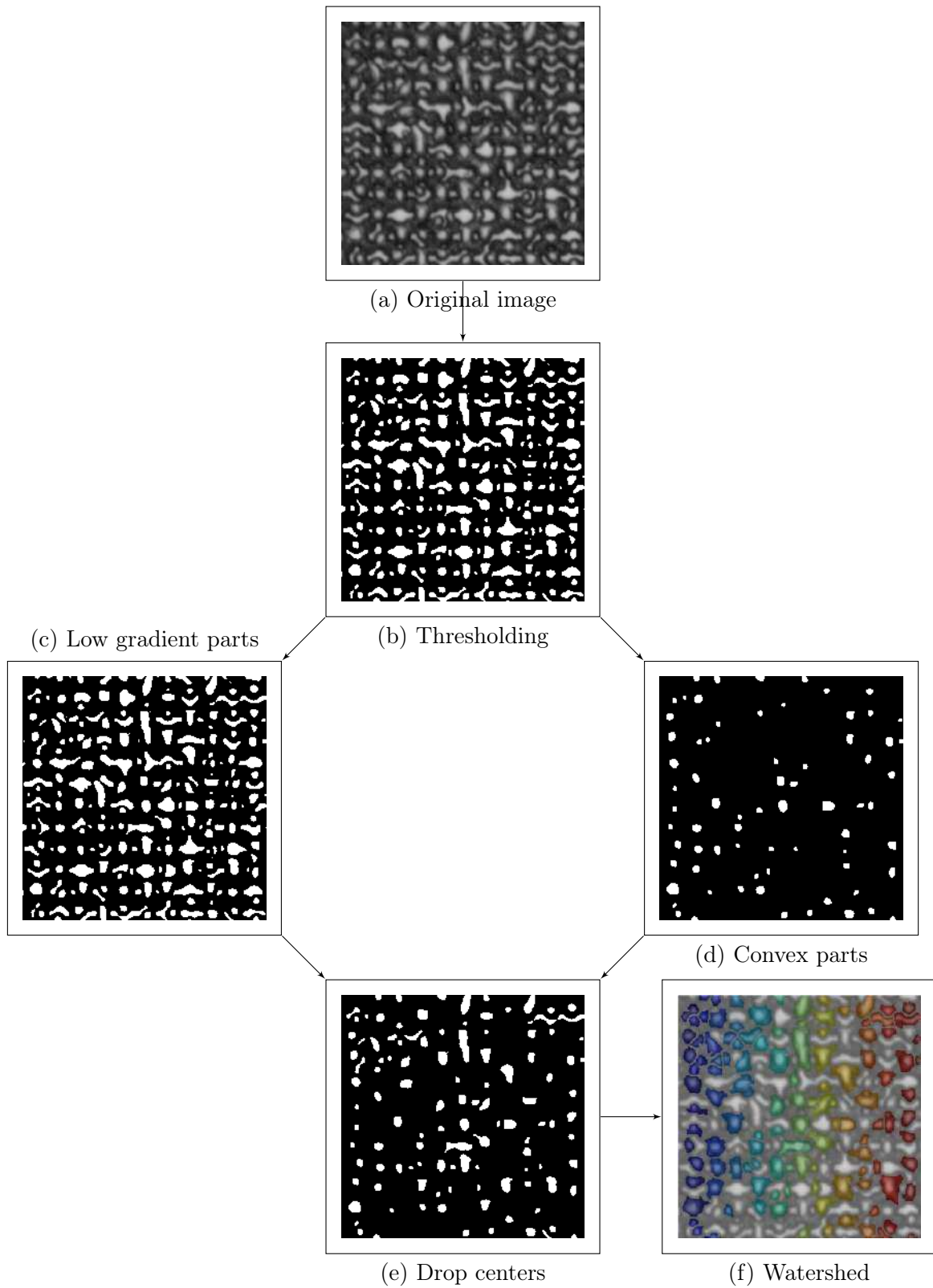


Figure 2.16: Algorithm for medium drops.

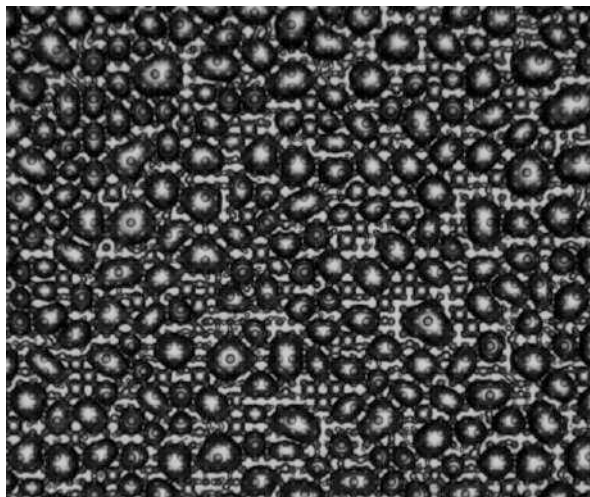


Figure 2.17: Image of big drops on a pillared image.

watershed technique is used to detect each drop region (figure 2.18 (h)), that enables to get the drops number and mean radius.

2.3.4 Algorithm verification

In order to measure quantitatively the performance of this algorithm, the drops are divided into four groups according to their presence in the initial configuration and their detection by the algorithm:

- The true positive drops (TP) which are detected by the algorithm and are present in the initial image.
- The false positive drops (FP) which are detected by the algorithm but are not present in the initial image.
- The false negative drops (FN) which are not detected by the algorithm but are present in the initial image.
- The true negative drops (TN) which are not detected by the algorithm and are not present in the original image.

The idea of these parameters is visualized in figure 2.19. In this figure we consider the parts of droplet that are or are not detected, but it can be generalized for the number of droplets that are detected compared to the numbered that exist really in the images. In this figure, the blue solid circle represents the real droplets captured in the original image and the red dashed circle is the droplet detected by the image processing algorithm. Therefore, TP represents the part of the real droplet that is detected by the algorithm, FP is the part detected falsely by the algorithm, FN shows the part which is not detected by the algorithm but presents in the initial image, and TN is the part that is not detected by the algorithm and dose not present in the original image.

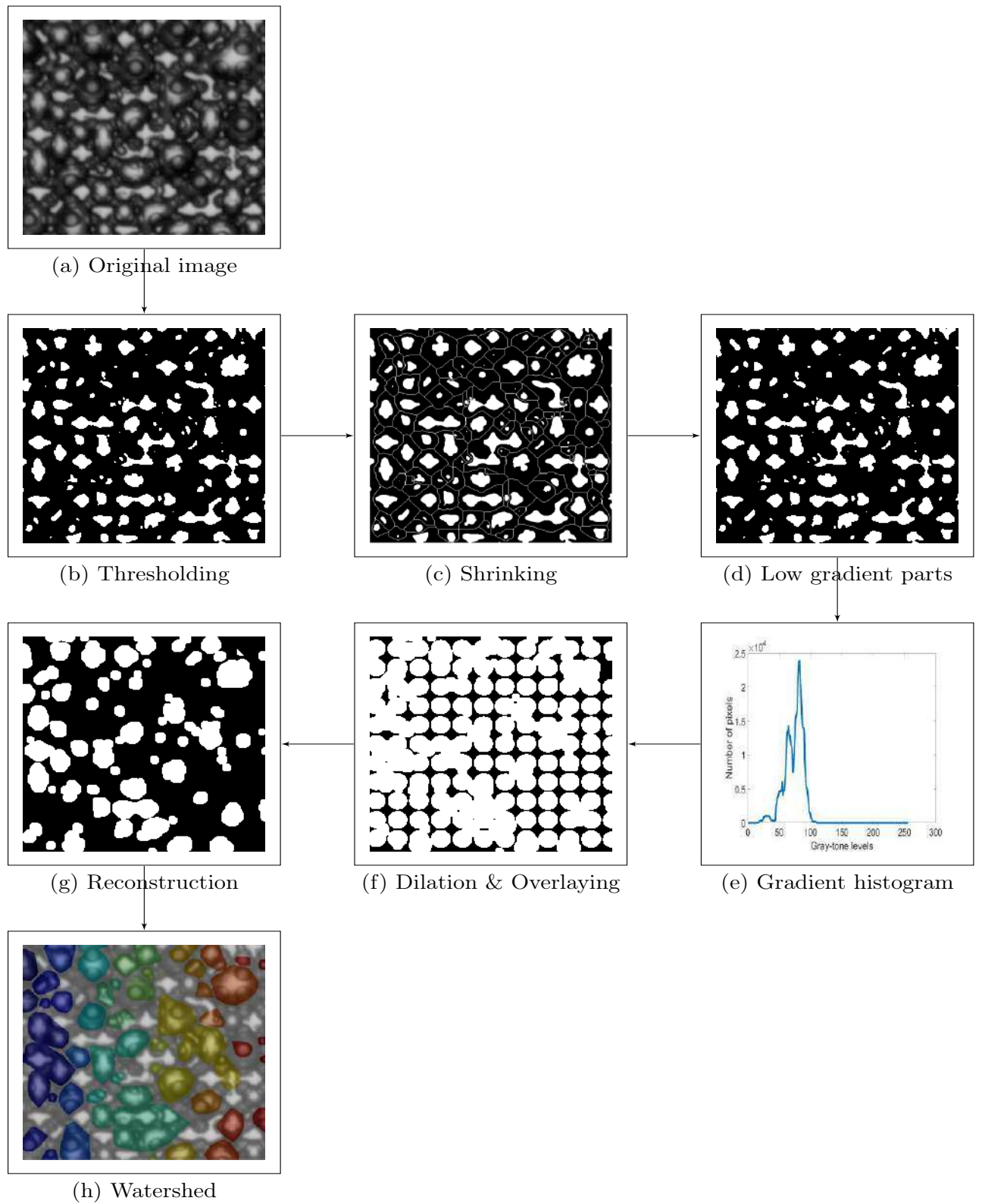


Figure 2.18: Algorithm for big drops.

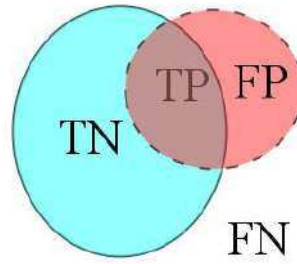


Figure 2.19: Schematic diagram of parameters using for algorithm validation. The blue solid circle represents the real droplets captured in the original image and the red dashed circle is the droplet detected by the image processing algorithm. Therefore, TP represents the part of the real droplet that is detected by the algorithm, FP is the part detected falsely by the algorithm, FN shows the part which is not detected by the algorithm but presents in the initial image, and TN is the part that is not detected by the algorithm and dose not present in the original image.

The number of drops which belong to each groups enables to estimate the precision (PR) and the recall (RC) of the algorithm:

$$PR = \frac{TP}{TP + FP}, \quad (2-10)$$

$$RC = \frac{TP}{TP + FN}. \quad (2-11)$$

A high value of PR indicates that detected drops are present in the original image and there can be other drops which are not detected by the algorithm. On the contrary, a high value of RC indicates that the algorithm detects almost all drops, but it also detects some drops, which do not exist in the original image. Thus, these both measurements suffer from a lack of accuracy. In fact, neither FN nor FP are preferred for an accurate algorithm. That's why, a more robust measurement of the algorithm accuracy so-called F -measure (FM) is used [125]:

$$FM = \frac{2}{1/PR + 1/RC}. \quad (2-12)$$

In order to evaluate the FM of this algorithm, the drops are manually detected in a sub-sampling of images and are compared with those detected by means of the algorithm. Table 2.1 shows the evolution of the F -measure as a function of the considered image set and the drop size.

The low values obtained for small drops can be explained by the fact that drops are not really circular because they are adjacent to pillars. Despite these mis-measurements, Table 2.1 shows that this algorithm is very accurate, especially for large drops. Thus, the pillar pattern has an influence on the algorithm accuracy.

Drop size	FM
Very small	-
Small	5 %
Medium	71 %
Big	87 %

Table 2.1: Performance parameters of the algorithm for several image sets

2.4 Conclusion

2.4.1 English

As the results of the experimental set-up introduced at the previous chapter are the gray-scale images of water droplets growing on different substrates, in this chapter the methods that was used to segment these images were presented. The aim of image segmentation was to extract the information related to droplets size evolution, droplets density, and spatial distribution.

In the case of flat and sinusoidal substrates, segmentation is not very complicated because the droplets are detectable from the substrate. While on the pillared substrates, since the coalescing drops are really similar to the pillars and the segmentation needs a more complicated technique. Regarding the flat and sinusoidal substrate a simple method consisting of three steps were developed: pretreatment, segmentation and reconstruction. For the pillared substrates, at first the pillars are characterized and separated from the substrate. Then, the droplets are divided into four main categories based on their size and similarity to the pillars and for each group an adequate technique of segmentation was developed. At the end, the validity of this method was verified manually using the F -measure test.

2.4.2 French

Comme les résultats du montage expérimental présenté au chapitre précédent sont les images en échelle de gris des gouttelettes d'eau qui se développent sur différents substrats, les méthodes utilisées pour segmenter ces images ont été présentées dans ce chapitre. Le but de la segmentation de l'image était d'extraire l'information liée à l'évolution de la taille des gouttelettes, à la densité des gouttelettes et à la distribution spatiale.

Dans le cas de substrats plats et sinusoidaux, la segmentation n'est pas très compliquée car les gouttelettes sont détectables à partir du substrat. Alors que sur les substrats à piliers, puisque les gouttes coalescentes sont vraiment similaires aux piliers, la segmentation nécessite une technique plus élaborée. En ce qui concerne le substrat plat et sinusoidal, une méthode simple consiste en trois étapes: prétraitement, segmentation et reconstruction. Pour les substrats à piliers, ceux-ci sont d'abord caractérisés et séparés du substrat. Ensuite, les gouttelettes sont divisées en quatre catégories principales en fonction de leur taille et de leur similarité avec les piliers et pour chaque groupe une technique de segmentation adéquate a été développée. À la fin, la validité de cette méthode a été vérifiée manuellement en utilisant le test de mesure F .

Chapter 3

Modeling and simulation

3.1 Introduction

3.1.1 French

Le processus de condensation par gouttelet démarre par la nucléation de très petites gouttelettes tout autour du substrat. Ces petites gouttelettes commencent alors à adsorber les molécules d'eau de leur environnement et à croître lentement. Au bout d'un certain temps, si deux ou plusieurs gouttelettes deviennent assez grosses pour se toucher, elles formeront une plus grosse gouttelette appelée gouttelette fille au centre de masse des parents. La croissance par coalescence est plus rapide que l'adsorption, mais la surface totale couverte par les gouttelettes diminue. La zone couverte par la gouttelette fille est en effet plus petite que la somme de la superficie couverte par ses parents. Dans cette nouvelle zone dénudée, d'autres petites gouttelettes peuvent germer et se développer de la même manière. Les gouttelettes qui se développent en raison de la coalescence et de l'adsorption peuvent devenir très grosses et lourdes, ne pouvant plus résister à la force de gravité et glisser et produire une zone plus libre pour produire de nouvelles petites gouttelettes. Par conséquent, quatre étapes principales peuvent être considérées dans un processus de condensation par gouttelet :

1. nucléation initiale,
2. croissance par l'adsorption,
3. croissance par la coalescence et nucléation de nouvelles petites gouttelettes,
4. départ de grosses gouttelettes.

Le taux de croissance et les changements dans la densité des gouttelettes au cours de ces cinq étapes dépendent à la fois de la forme des gouttelettes et de la topographie de la surface. En effet, tout changement de la morphologie de la surface et des propriétés chimiques modifiera le comportement des gouttelettes d'eau sur la surface. Par exemple, l'utilisation de revêtements chimiques et de nano-revêtements modifie l'aptitude au mouillage du substrat et conduit à un comportement hydrophile, hydrophobe et même super-hydrophobe. La même situation peut se produire en changeant la topographie de surface, comme ce qui a été expliqué dans la section 1.4.2, table 1.8. Dans ce tableau, il a été revendiqué qu'en

faisant des motifs sinusoïdaux sur le substrat en polycarbonate, l'angle de contact de l'eau sur la surface change. La figure 3.1 montre qu'en ajoutant des motifs de textures sur une surface, la forme des gouttelettes peut changer de sphérique à ellipsoïdale.

Par conséquent, afin de modéliser la nucléation et la croissance des gouttelettes, il faut choisir un modèle approprié qui correspond à la forme des gouttelettes et aux caractéristiques du substrat. Dans ce chapitre, trois modèles numériques pour générer les gouttelettes sur des substrats plats et texturés sont présentés. Chaque modèle itère à travers une boucle principale jusqu'à ce que la condition d'état stable soit satisfaite. Dans un premier temps, nous présentons le modèle de gouttelettes sur une surface plane qui considère les gouttelettes comme des calottes sphériques sur le substrat. Ce modèle peut simuler le comportement des gouttelettes pour un large éventail de mouillabilité. Ensuite, pour modéliser la croissance des gouttelettes sur des substrats texturés, deux autres modèles seront développés pour considérer les gouttelettes comme des ellipsoïdes et des calottes ellipsoïdales (nous les avons appelés semi-ellipsoïdes). La différence entre ces deux modèles est l'angle de contact des gouttelettes d'eau. En d'autres termes, lorsque le modèle est développé sur la base de l'hypothèse de gouttelettes ellipsoïdales, il suppose l'angle de contact des gouttelettes à 90° . Un modèle plus compliqué mais complet doit considérer les gouttelettes de forme elliptique et leurs angles de contact sur le substrat. Ce modèle est développé en considérant les gouttelettes comme des chapeaux ellipsoïdaux et sera présenté à la fin de ce chapitre. Après avoir présenté chaque modèle, il y aura une sous-section qui explique l'algorithme de simulation de la condensation par gouttelette basé sur le modèle actuel sur la texturation correspondante.

De plus, un autre paramètre important appelé la fonction de distribution de tailles des gouttes sera introduit. Cette fonction mesure la densité des gouttelettes dans la gamme de taille spécifiée $r_i - r_{i+1}$. Bien que la fonction de densité de gouttes pour les gouttelettes adsorbantes et coalescentes soit calculée auparavant, nous présentons ici une formule plus simple pour calculer cette fonction dans le cas des gouttelettes adsorbantes.

Dans le prochain chapitre (chapitre 4) tous ces modèles seront validés en comparant avec des résultats expérimentaux extraits des images d'échelle de gris acquises par la configuration expliquée au chapitre 1.

3.1.2 English

The process of dropwise condensation commences by nucleation of very small droplets all around the substrate. These small droplets then start to adsorb water molecules from their environment and grow slowly. After a while, if two or more droplets become big enough to touch, they will coalesce and form a bigger droplet -called daughter droplet- at the mass center of the parents [46]. During coalescence the rate of growth is faster than adsorption, but the total area covered by droplets reduces. This is because the area covered by daughter droplet is smaller than the summation of areas covered by its parents. In this new bare area, other small droplets can nucleate and grow in the same way. The droplets growing due to coalescence and adsorption can become so big and heavy that they can not resist to the gravity force any more, slide down and produce more vacant areas to grow new small droplets. Therefore, four main steps can be considered in a process of dropwise condensation:

1. initial nucleation,

2. growth due to adsorption,
3. growth due to coalescence and nucleation of new small droplets,
4. departure of big droplets.

The growth rate and changes in density of droplets during these five steps depend on both droplets shape and surface topography. This is because any changes in the surface topography and chemical properties will change water droplets behavior on the surface. For instance, using chemical and nano-coatings will change wettability of the substrate and lead to a hydrophilic, hydrophobic and even super hydrophobic behavior. The same situation can happen by changing surface topography, like what has been explained in section 1.4.2, table 1.8. In this table it has been claimed that by making sinusoidal patterns on the polycarbonate substrate, water contact angle on the surface changes. Figure 3.1 shows that by adding texturing patterns on a surface, the shape of droplets can change from spherical to ellipsoidal.

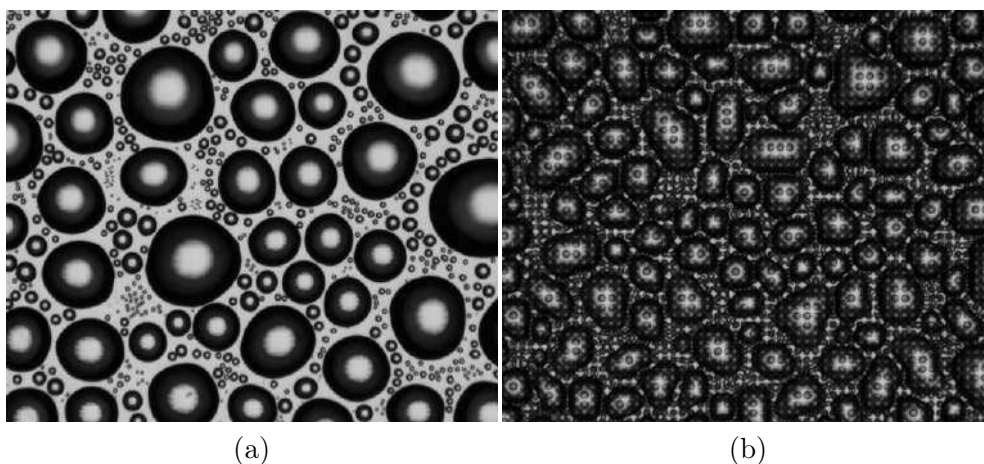


Figure 3.1: (a) Spherical droplets on a flat substrate, (b) ellipsoidal droplets on a textured substrate.

Therefore, in order to model nucleation and growth of droplets, one has to choose a suitable model that corresponds to the shape of droplets and substrate features. In this chapter three numerical models for generating the droplets on flat and textured substrates are presented. Each models iterates through a main loop until the steady state condition satisfied. At first, the model of droplets on flat surface is presented that considers the droplets as spherical-caps on the substrate. This model can simulate droplets behavior for a wide range of wettability. Then, for modeling droplets growth on textured substrates, two other models will be developed that consider the droplets as ellipsoids and ellipsoidal caps (we named them semi-ellipsoids). The difference between these two models is the contact angle of water droplets. In other words, when the model is developed based on the assumption of ellipsoidal droplets, it assumes the contact angle of droplets 90° . A more complicated but complete model should consider both droplets' elliptical shape and their contact angles on the substrate. This model is developed by considering the droplets

as semi-ellipsoids and will be presented later in the current chapter. After presenting each model, there will be a subsection that explains the algorithm for simulating dropwise condensation based on the current model on its corresponding texturing pattern.

Moreover, another important parameter called drop-size density function will be developed for adsorbing droplets at earlier stages. This function measures the density of droplets that are in specified size range $r_i - r_{i+1}$. Though, drop-size distribution function for adsorbing and coalescing droplets are calculated before, here we will modify the model for adsorbing droplets so that it can have better answers at earlier stages when there is no sliding droplet.

In the next chapter (chapter 4) all these models will be validated by comparing with experimental results that are extracted from the gray scale images acquired by the set-up explained at chapter 1.

3.2 Model that considers droplets as spherical-caps

In this part, the model that describes droplets nucleation and growth on flat surfaces will be explained. In this model, droplets are assumed as spherical-caps that have the same radius along with X and Y axis ($r_x = r_y$), but different radius at the Z direction (r_z). If we consider $r_z = r_x = r_y$, then the spherical-cap will turn into a hemi-sphere with contact angle of $\theta = 90^\circ$. A spherical cap as is shown in figure 3.2 is a part of a sphere with radius r_1 that is cut by a plain with distance h from the center of the sphere. Lets consider the radius of the spherical cap equal to r_2 and its contact angle θ . If the cutting plain passes from the center of the sphere ($h = 0$) then, the spherical cap will turn into a hemi-sphere with radius $r_2 = r_1$ and contact angle $\theta = 90^\circ$. Therefore, when the contact angle of water droplets is not 90° , we can consider them as the spherical-caps. In the following the model of dropwise condensation based on spherical cap assumption as well as the simulation algorithm that is developed based on this model will be presented.

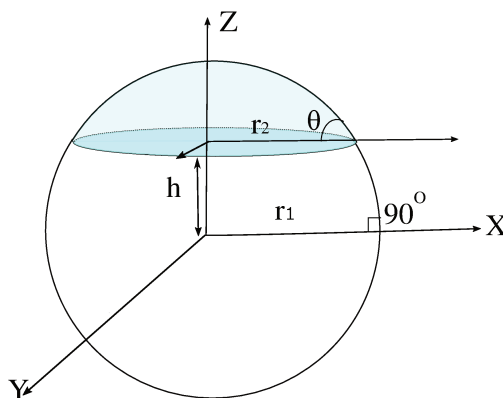


Figure 3.2: A spherical cap is a part of a sphere that is cut by a plain with distance h from the center of sphere and its contact angle with surface is not equal to 90° .

3.2.1 Initial nucleation

Figure 3.3 represents initial configuration of real droplets during the experiments and their corresponding Ripley's L function. As was explained in introduction, Ripley's function can be applied as a useful tool for investigating droplets spatial distribution. The blue line in this graph represents completely randomly distributed droplets that follow the Poisson point process (equation (0–8)). The accordance between the two graphs indicates that the distribution of initial droplets on flat substrate is completely random and can be simulated by a Poisson point process.

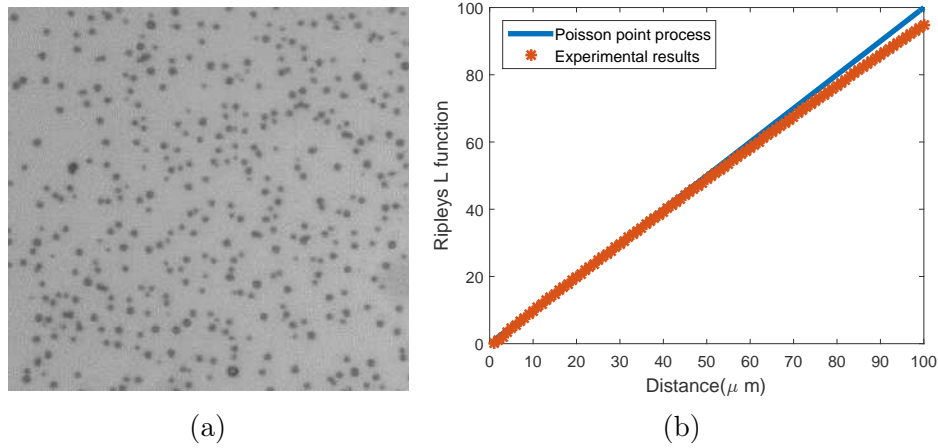


Figure 3.3: (a) Nucleation of the initial droplets that is completely randomly based on Poisson point process. (b) Ripley's L function corresponding to this image is the same as Ripley's L function of Poisson point process ($F(x) = x$).

3.2.2 Adsorption

As it is said before, the first step in dropwise condensation is the nucleation of small droplets that can be considered completely randomly on the flat surface. Lots of droplets with variable sizes can form in this step but just the ones with radius bigger than a minimum value can grow and the rest will evaporate and disappear. So, r_{min} is the minimum size for droplets that are able to grow and the droplets smaller than this radius are assumed to disappear [27, 83].

$$r_{min} = \frac{2\sigma T_{sat}}{H_{fg}\rho(\Delta T_t)}. \quad (3-1)$$

In this equation, σ is water surface tension, H_{fg} is the latent heat of condensation, ρ is water density, T_{sat} represents the saturated temperature of humid air and ΔT_t is total temperature gradient that is the main driving force for adsorption. ΔT_t is equal to wall temperature and T_{sat} (in the case of condensation from pure vapor, for condensation from humid gas one must consider dew point instead of saturated temperature) gradient ($\Delta T_{w-sat} = T_w - T_{sat}$) minus temperature gradient due to droplet's curvature (ΔT_{CD}) [10]:

$$\Delta T_t = \Delta T_{w-sat} - \Delta T_{CD}, \quad (3-2)$$

ΔT_{CD} being the temperature difference due to droplet's curvature, which is the temperature drop of a curved surface with respect to a planar surface. This temperature difference can be calculated by equation (3-3):

$$\Delta T_{CD} = \frac{2\sigma T_{sat}}{H_{fg}\rho r}, \quad (3-3)$$

where r represents the radius of droplets. Total heat transfer is equal to ΔT_t divided by the sum of heat resistances between hot air and cold substrate including convection resistance between droplet and its surroundings ($R_{Convection} = \frac{1}{2\pi r^2 h_i (1 - \cos\theta_a)}$) and conduction through the droplet itself ($R_{Conduction} = \frac{\theta_a}{K_w \pi r \sin\theta_a}$) [126]. These resistances can be seen in figure 3.4.

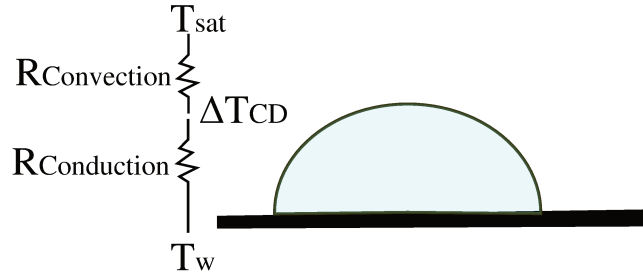


Figure 3.4: There are two main heat transfer resistances through a droplet: conduction resistance ($R_{Conduction}$) and convection resistance ($R_{Convection}$).

So, total heat resistance will be:

$$R = \frac{1}{2\pi r^2 h_i (1 - \cos\theta_a)} + \frac{\theta_a}{4K_w \pi r \sin\theta_a}, \quad (3-4)$$

where K_w is water thermal conductivity, θ_a advancing contact angle, and h_i is the interfacial heat transfer coefficient that will be discussed in section 3.2.2.1. Combining equations (3-1) to (3-4) the total heat transfer can be calculated as

$$q = \frac{\Delta T_{sat-wall} - \frac{2T_{sat}\sigma}{H_{fg}\rho r}}{\frac{1}{2\pi r^2 h_i (1 - \cos\theta_a)} + \frac{\theta_a}{4K_w \pi r \sin\theta_a}}. \quad (3-5)$$

On the other hand, heat of condensation is equal to the mass of condensate multiple by the latent heat of condensation:

$$q = \rho_l H_{fg} \pi r^2 (1 - \cos\theta)^2 (2 + \cos\theta) \frac{dr}{dt}, \quad (3-6)$$

this is because the volume of the spherical cap illustrated at figure 3.2 is equal to [127]:

$$V = \frac{\pi r^3}{3}(1 - \cos\theta)^2(2 + \cos\theta). \quad (3-7)$$

By equaling equations (3-5) and (3-6), the size of droplets of next generation can be calculated according to Euler method for solving ordinary differential equations:

$$r_k = r_{k-1} + G, \quad G = \frac{dr}{dt} = \frac{C_1(1 - \frac{r_{min}}{r})}{C_2 + C_3 r} \quad (3-8)$$

where k represents each generation of droplets and $C_1 = \frac{1}{(1 - \cos\theta)^2(2 + \cos\theta)} \frac{\Delta T_{sw}}{\rho H_{fg}}$, $C_2 = \frac{1}{2h_i(1 - \cos\theta_a)}$, and $C_3 = \frac{\theta_a}{4K_w \sin\theta_a}$.

3.2.2.1 Heat transfer coefficient

Generally in condensation study, heat transfer coefficient is considered as the interfacial heat transfer coefficient which can be calculated from:

$$h_i = \frac{2\alpha}{2 - \alpha} \sqrt{M/(2\pi \dot{R} T_{sat})} \frac{H_{fg}^2}{T_{sat} v_g}. \quad (3-9)$$

v_g here is specific volume of gas phase, H_{fg} latent heat of condensation, M is molecular weight of water and \dot{R} is the gas universal constant. α is known as accommodation coefficient or condensation coefficient that is assumed to be equal to evaporation coefficient [128]. This parameter represents the fraction of vapor molecules that will be captured by the liquid droplet [126]. Tansawa [128] summarized the experimental and theoretical works that have been done to estimate the value of α , but he confessed that he can not judge which theory is more reasonable. According to him a wide range of experimental values between [0.006-1] have been presented for α by lots of authors. Hatamiya and Tanaka [129] reported condensation coefficient of water vapor between (0.2-0.6), the most probable value being 0.4 from the experimental results of the dropwise condensation of low-pressure steam. Fujikawa and Maerefat [130] stated that condensation coefficient of a poly-atomic fluid should be significantly smaller than 1 because the rotational motion of molecules is constrained. While Stylianou and Rose [131] and Rose [132] suggested that, if the polyatomicity of water molecules is taken into account, the reported values of α should be corrected to the amounts near 1 [128]. In most of the references α is assumed as unity in the absence of non-condensable gases, that concerns condensation from saturated steam. Bansal *et al.* [133] considered the accommodation coefficient equal to 1 for temperature difference of [0.4°C – 2°C] with respect to the saturated temperature. Mareka and Straub [134] extensively analyzed the evaporation and condensation coefficients of water, considering the effect of pressure, temperature and surface renewal rate. Regarding dropwise condensation from humid air Shaofei *et al.* [135] reported that the condensation coefficient equal to 0.001 gives better answers.

Equation (3-9) comes from the definition $q = \dot{m} H_{fg}$ where \dot{m} represents the net rate of condensations and is equal to the difference between the maximum flux of the vapor molecules impinging on the surface and the emission from the liquid [128]

$$\dot{m} = \frac{2\alpha}{2 - \alpha} \frac{P_v - P_i}{\sqrt{2\pi \dot{R} T_v}}. \quad (3-10)$$

P_v and P_i are vapor pressure and saturated pressure at uniform temperature T_i of liquid, and T_v is vapor temperature. Then from Clausius-Clapeyron relation:

$$\frac{P_v - P_i}{T_v - T_i} = \frac{\rho H_{fg}}{T_v}, \quad (3-11)$$

Which results in:

$$\dot{m} = \frac{2\alpha}{2 - \alpha} \frac{H_{fg}}{\sqrt{2\pi R}} \frac{\rho_v (T_v - T_i)}{T_v^{3/2}}. \quad (3-12)$$

Consequently,

$$q = \dot{m} H_{fg} = \frac{2\alpha}{2 - \alpha} \frac{H_{fg}^2}{\sqrt{2\pi R}} \frac{\rho_v (T_v - T_i)}{T_v^{3/2}} = h_i (T_v - T_i). \quad (3-13)$$

Therefore,

$$h_i = \frac{2\alpha}{2 - \alpha} \frac{H_{fg}^2 \rho_v}{\sqrt{2\pi R T_v^3}}. \quad (3-14)$$

Suspended droplets

Considering the suspended droplets or homogeneous dropwise condensation (droplets nucleate as a mixture with the gas and not on a substrate), there is another approach to calculate h_i that considers hydrodynamic of the process. In these approaches at first the dimensionless heat transfer number known as Nusselt number (Nu) is calculated based on hydrodynamic of the process, and then h_i is calculated based on its relation with Nu :

$$Nu = \frac{h_i L}{K}. \quad (3-15)$$

K here is thermal conductivity of fluid. L is the characteristic length of heat transfer through the system. There are some definitions for L but it really depends on the geometry of the system.

When a sphere with temperature T_s is immersed in a fluid with temperature T_∞ , a boundary layer develops along the curved surface [136]. The boundary layer thickness d_t at each point like P of the sphere is a function of φ that is the angle of the point with respect to the lowest point of the sphere, so as is shown in figure 3.5 $\varphi = 0$ at the bottom of the sphere. As the angle φ increases, the thickness of the boundary layer increases and the local Nusselt number decreases. Merk and Prins [137] obtained an integral solution by assuming the momentum and thermal boundary layer thicknesses are identical and they proposed that average Nusselt number for free convection over a sphere is

$$Nu = C Ra_D^{1/4}, \quad (3-16)$$

where $Ra = Pr \times Gr$ and C is a function of Pr and for $Pr = 0.7$, C is equal to 0.5. Pr defined as the ratio of momentum diffusivity (ν) to thermal diffusivity (α).

$$Pr = \frac{\nu}{\alpha} = \frac{\mu/\rho}{k/(\rho c_p)} = \frac{\mu c_p}{k}, \quad (3-17)$$

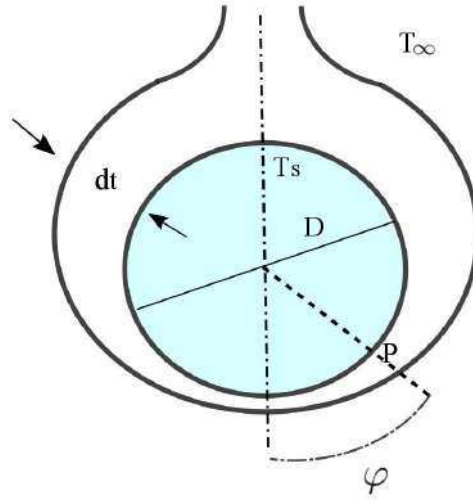


Figure 3.5: Thickness of boundary layer d_t at each point P of a sphere with temperature T_s that is immersed in a fluid of temperature T_∞ depends on the angle between P and the bottom of the sphere φ .

where μ and ρ are dynamic viscosity and heat capacity of air. Gr represents Grashof number that is the ratio of the buoyancy to viscous force acting on a fluid. Grashof number frequently arises in the study of situations involving natural convection and is analogous to the Reynolds number in force convection.

$$Gr = \frac{g\beta(T_s - T_\infty)L^3}{\nu^2}, \quad (3-18)$$

β is the coefficient of thermal expansion and is equal to approximately $1/T_\infty$ for ideal gases.

Although the integral solution can yield results all the way to the top where $\varphi = 180^\circ$ and $Nu_\varphi = 0$, the result beyond $\varphi = 165^\circ$ is no longer applicable because boundary layer separation occurred.

Some modifications are reported to Nu depending on different experiments. Amato and Tien [136] proposed a laminar free convection correlation for Nu regarding sphere emerged in liquid fluid that have viscosity bigger than air and for $10 < Nu < 90$ and $3 \times 10^5 < Gr$. $Pr < 8 \times 10^8$

$$Nu = 2 + 0.5 \times Ra^{0.25}, \quad (3-19)$$

They also reported around 13 correlations for Nu under different situations.

3.2.3 Coalescence

The droplets grow continuously at the rate G according to equation (3-8). When two droplets (the so-called parents) become big enough to touch, they will merge and form a

bigger one named daughter drop. This means that if the Euclidean distance between two droplets ($L_{i,j}$) with sizes r_i and r_j becomes less than $r_i + r_j$, then they will coalesce and form a bigger droplet in the mass center of the original drops with size r that is given by:

$$r = \sqrt[D]{r_i^D + r_j^D}, \quad (3-20)$$

where D is the droplets dimension. $L_{i,j}$ is the Euclidean distance between two droplets center. For two dimensional substrate ($d = 2$), $L_{i,j}$ is:

$$L_{i,j} = \sqrt{(x_i - x_j)^2 + (y_i - y_j)^2} : \quad (3-21)$$

and for three dimensional substrate ($d = 3$) is:

$$L_{i,j} = \sqrt{(x_i - x_j)^2 + (y_i - y_j)^2 + (z_i - z_j)^2}. \quad (3-22)$$

Coalescence is generally described by the dimension of drops (D) and dimension of substrate (d) while $D \geq d$ [138]. D and d must be determined by the process, for example in the formation of dew on the cobweb three dimensional drops form on one dimensional thread. In this case $d = 1$ and $D = 3$ or in the case of formation of hemispheric droplets on the plate $d = 2$ and $D = 3$ as well. It is worth to point out here that there are two different situations depending on d and D [138].

1. If $D = d$: in such situation after a while a single droplet will form that can extent across the entire system. This is the concept of gelation or percolation. For example in the reaction of silans and water in acidic or basic solution, droplets of silan hydroxide grow in 3 dimension ($d = 3$ and $D = 3$) and after a while gelation occurs and the whole solution turns into a unique droplet.
2. If $D > d$: in this case there is no gelation in a finite time and the process continues in the same manner as low-density colloidal aggregation, in which particles can merge but do not form a unique big particle. This is the case of dropwise condensation on the flat surface ($d = 2$ and $D = 3$). The droplets grow and coalesce but the whole system will never unite.

The center point of the daughter droplet after coalescence can be considered at the mass center of its parents:

$$\begin{aligned} x &= \frac{r_i^3 \cdot x_i + r_j^3 \cdot x_j}{r_i^3 + r_j^3}, \\ y &= \frac{r_i^3 \cdot y_i + r_j^3 \cdot y_j}{r_i^3 + r_j^3}, \\ z &= \frac{r_i^3 \cdot z_i + r_j^3 \cdot z_j}{r_i^3 + r_j^3}. \end{aligned} \quad (3-23)$$

On the flat surface $z_i = z_j = 0$, meaning that droplets are dispersed on two dimensional substrate. Sometimes coalescence is the combination of more than two droplets (multiple

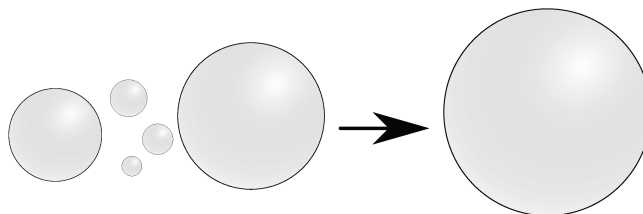


Figure 3.6: Multiple coalescence: two big droplets adsorb each other and swallow the small droplets in their between.

coalescence). This happens especially when two big droplet adsorb each other and there are some small droplets in the space between them. This effect can be seen in figure 3.6.

The effect of multiple coalescence is considered in the simulating algorithm that will be presented at the end of this section.

3.2.4 Nucleation of new droplets

As was mentioned before, nucleation of new drops in the vacant area produced during coalescence occurs continuously along the process. Number and size of new droplets can be calculated based on probability density function (PDF) of droplets during condensation process (figure 3.7). In this figure horizontal axis represents the average droplets size (r_{ave}). This figure shows that at first there is a unimodal distribution due to Poisson point process (see figure 3.3) with the peak concentrated on small droplets with size of $6 \mu m$. The mean of PDF then will move towards bigger values due to droplets growth, and after a while another peak around small droplets will appear again. In this step, PDF will turn into a bimodal shape. The second peak relates to nucleation of new small droplets in the vacant area of substrate and stays on this point until the end of process. This peak presents in the area near the size of initial small droplets and shows that the average size of new small droplets nucleating at each step is near the size of initial droplets. At latest steps although there are big droplets that are the results of coalescence, since their number is much less than the number of new small droplet that nucleate in the vacancies, PDF shows just one peak near $6 \mu m$.

Therefore, the size of new small droplets will be around the size of the first generation of droplets. Regarding the number of droplets that must be added at each iteration, we assumed that density of new droplets with respect to free area on the surface is also equal to the density of initial droplets. It is worth pointing out here that, since the density is based on the free area presenting at each step on the substrate, the number of new small droplets varies at each iteration.

$$N = \text{density of initial droplets} \times [\text{surface area} - \Sigma(\text{area of all of the already-existing drops})]. \quad (3-24)$$

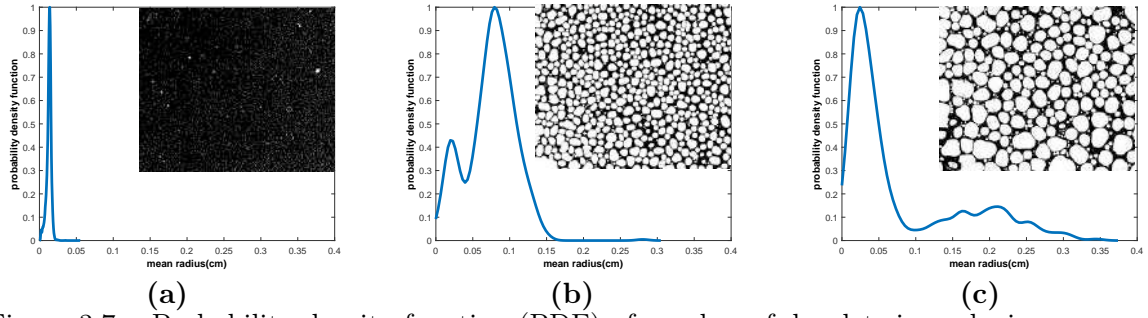


Figure 3.7: Probability density function (PDF) of number of droplets in each size range at three time steps: (a) $t = 200s$, (b) $t = 2500s$, (c) $t = 5000s$.

3.2.5 Departure of big droplets

The droplets continue growing until their weight becomes bigger than the adhesive force with the surface, that according to [139] comes from surface roughness and contact angle hysteresis. When droplets become heavy enough to overcome the adhesive force, they will slide and clean off the droplets that are in their path. The check for departure can be done by comparing the gravity force and adhesive force affecting to each droplet. The gravity force for a droplet with advancing and receding contact angles θ_a and θ_r is [36, 25]:

$$F_g = \frac{(2 - 3\cos\theta + \cos^3\theta)\pi r_{max}^3 \rho g}{3}. \quad (3-25)$$

The adhesive force with the surface can be assumed as the surface tension force [36, 25]:

$$F_\sigma = 2\sigma r_{max} \sin\theta (\cos\theta_r - \cos\theta_a). \quad (3-26)$$

θ here is the apparent equilibrium contact angle and is equal to $\cos^{-1}(0.5\cos\theta_a + 0.5\cos\theta_r)$. r_{max} that is the maximum radius of each generation of droplets before sliding can be calculated by equaling the equations (3-25) and (3-26) as [5, 25]:

$$r_{max} = \sqrt{\frac{6(\cos\theta_r - \cos\theta_a)\sin\theta\sigma}{\pi(2 - 3\cos\theta + \cos^3\theta)\rho g}}, \quad (3-27)$$

3.2.6 Drop-size distribution function

An interesting parameter in dropwise condensation is the drop-size distribution function. This parameter is the key factor in the study of heat transfer of dropwise condensation [12]. This is because the heat transfer flux of the small and big droplets are not the same and the

total heat transfer is the sum of the heat fluxes of these two groups. Therefore, knowing the number or density of droplets at each size range is very important. If we consider two rates of growth for droplets (by adsorption and by coalescence), we can divide the droplets into two groups: the ones growing by adsorption and the ones growing by the two mechanisms. So, there must be a slight limit radius between these two groups so-called the critical radius (r_c). Therefore, we can consider that the droplets that are smaller than r_c grow by adsorbing water molecules from humid air (adsorbing droplets) and the droplets that are bigger than r_c grow mainly by coalescence (coalescing droplets). It is worth pointing out here that coalescing droplets grow also by adsorption, but since the growth rate due to coalescence is much bigger than adsorption they are called coalescing droplets.

Abu-Orabi [47] proposed the critical radius (r_c) as the half-spacing between active sites on the substrate. By this definition, r_c can be calculated as follows, where N is the number of droplets and L is the side length of the square substrate: :

$$r_c = \sqrt{\frac{L^2}{4N}}. \quad (3-28)$$

Drop-size distribution function ($f(r)$ for adsorbing droplets and $F(r)$ for coalescing droplets) represents the average number of droplets at each size interval of ($r_i, r_i + \Delta r$) per unit area (A) [13]:

$$f(r) \quad \text{or} \quad F(r) = \frac{-N}{A \cdot \Delta r}. \quad (3-29)$$

The negative sign in this equation shows the opposite relation between size and number of droplets, meaning that the number of droplets is decreasing when their size is increasing. As was explained in introduction, Rose and Glicksman [13] were the first ones who developed the size distribution function ($F(r)$) for coalescing droplets. They determined the average size distribution of droplets over a complete cycle as a function of the available area fraction, maximum radius and growth rate of each generation. They considered α (the fraction of total area covered by droplets with radius greater than r) as a power law function with respect to r :

$$\alpha = 1 - \left(\frac{r}{r_{max}} \right)^\epsilon. \quad (3-30)$$

If we consider N as the number of coalescing droplets of each generation per unit area of generation, the size distribution function proposed by Rose and Glicksman is [13]:

$$F(r) = \frac{-1}{\pi r^2} \frac{d\alpha}{dr} = \frac{\epsilon}{\pi r_{max}^3} \left(\frac{r}{r_{max}} \right)^{(\epsilon-3)}, \quad (3-31)$$

where ϵ is the drop-size distribution exponent and must be determined experimentally. The most frequent value reported for ϵ is near $\frac{1}{3} = 0.33$ [75, 45]. r_{max} is the maximum radius of each generation of droplets before sliding and can be calculated using equation (3-27).

Abu-Orabi [47] tried to develop the size distribution function for small droplets considering the effect of surface renewal parameter. This parameter describes the rate of surface cleaning by sliding of big droplets and finally lead to a complex size distribution model. In his model at first, the mass balance of adsorption process is written in order to drive

the growth rate of small droplets at initial stages. Then the Rose model is used as the boundary condition at $r = r_c$ to develop a precise model for describing size distribution of small droplets. But the formula that he derived is relatively huge and complicated with respect to Rose model. If we consider the initial stages of the process, where there are not yet coalescing and falling drops, surface renewal parameter can be neglected and a simpler model will be derived. But by neglecting this effect his model does not give very good answers for the small droplets. So in this section, we will modify the model of Abu-Orabi for the adsorbing droplets at earlier stages before sliding the first droplet.

Small droplets grow by adsorbing water molecules from vapor phase. So, we can assume f_1 as the number of droplets entering to $(r_i, r_i + \Delta r)$ due to adsorption at time step Δt per unit surface area, G_1 as the growth rate of these droplets and A as the total surface area. Respectively f_2 will be the number of droplets leaving the interval at Δt per unit area and G_2 the growth rate of leaving droplets. Since droplets growth due to adsorption is a mass conservative process, the number of droplets entering each interval is equal to the number of droplets leaving it:

$$Af_1G_1\frac{\Delta t}{\Delta r} = Af_2G_2\frac{\Delta t}{\Delta r}. \quad (3-32)$$

Here we assume that at earlier stages, there are not yet very big droplets who slide and clean off the surface. Dividing equation (3-32) by $A.\Delta t$ and assuming $\Delta r \rightarrow 0$ we will have:

$$\frac{d(fG)}{dr} = 0, \quad (3-33)$$

which results in:

$$f\frac{d(G)}{dr} + G\frac{d(f)}{dr} = 0. \quad (3-34)$$

$G = dr/dt$ is the rate of growth due to adsorption and can be calculated using equation (3-8). Differentiating of equation (3-8) will lead to:

$$\frac{dG}{dr} = C_1\frac{(C_2r^2 + C_3r) - (r - r_{min})(2C_2r + C_3)}{(C_2r^2 + C_3r)^2}, \quad (3-35)$$

substituting equations (3-8) and (3-35) in equation (3-34) will lead to:

$$-\frac{df}{f} = \frac{1}{(r - r_{min})}\frac{(C_2r^2 + C_3r) - (r - r_{min})(2C_2r + C_3)}{(C_2r^2 + C_3r)}dr. \quad (3-36)$$

Simplified form of equation (3-36) is:

$$-\frac{df}{f} = \left[\frac{1}{(r - r_{min})} - \frac{(2C_2r + C_3)}{(C_2r^2 + C_3r)} \right]dr. \quad (3-37)$$

Integration of equation (3-37) between (r, r_c) by partial fractions method, f will be calculated as:

$$f = C\frac{(C_2r^2 + C_3r)}{r - r_{min}}, \quad (3-38)$$

where C is the constant of integral. f here is the result of integral and represents total number of droplets between (r, r_c) per unit surface area and unit radius regardless of their generation. While in Rose model, equation (3–31), F is the number of droplets of each generation per unit area of generation and unit radius. There are two differences between these two definitions:

1. Number of droplets of each generation is not equal to the number of droplets at each size range, unless we made two assumptions:
 - The droplets are growing by adsorption and not by coalescence, this assumption is correct at earlier stages when we are dealing with droplets smaller than critical radius that are growing just by adsorption.
 - All the droplets of a specified generation have been nucleated with the same radius. The assumption of mono-dispersity of each generation is not correct, because we know that droplets can nucleate with different radius around r_{min} . But by assuming a small standard deviation, we can consider that the mean radius of all the initial droplets is r_{min} .
2. In the Rose model F is per area of generation, while in the model of Abu-Orabi f is per surface area.

Therefore, we need to make a correction for the surface in equation 3–38. The correction can be made by multiplying by the coefficient $\frac{\text{surface area}}{\text{area of droplets generation}} = \frac{L^2}{\pi r_i^2}$, L being the length of substrate and r_i being the radius of generation i .

Now for calculating the value of C , we can assume that at $r = r_c$, size density function of adsorbing and coalescing droplets are the same $f(r) = F(r)$. Substituting $f(r)$ from equation (3–38) and $F(r)$ from equation (3–31), we will have:

$$C = \frac{\epsilon}{\pi r_{max}^3} \left(\frac{r_c}{r_{max}} \right)^{(\epsilon-3)} \frac{r_c - r_{min}}{C_2 r_c^2 + C_3 r_c}. \quad (3-39)$$

Substituting equation (3–39) in equation (3–38) will results in:

$$f = \frac{\epsilon}{\pi r_{max}^3} \left(\frac{r_c}{r_{max}} \right)^{(\epsilon-3)} \frac{r_c - r_{min}}{r - r_{min}} \frac{C_2 r^2 + C_3 r}{C_2 r_c^2 + C_3 r_c}. \quad (3-40)$$

Equation (3–40) indicates the size distribution function for droplets smaller than r_c , who grow mainly due to adsorption.

3.2.7 Algorithm for generating circular droplets on flat substrates

Figure 3.8 represents the simulation algorithm designed based on the model developed for nucleation and growth of droplets in the form of spherical-caps on the flat substrate. At first 13479 random droplets with density of $N_t = 1.29 \times 10^8 m^{-2}$ are distributed completely randomly according to the Poisson point process method. This amount is chosen based on the one set of experiment that has been done. Each droplet then grows through a main loop which consists of three parts.

- Nucleation of new droplets: New small droplets with the size and density calculated according to the method described in section 3.2.4 are added at each step. After addition of these new droplets their overlaps with already-existing droplets is checked through an inner loop. It is important to locate the new small droplets in the vacant area between already-existing droplets. We did this process inside an inner loop, during which the Euclidean distance between the new drops and already-existing droplets is calculated and if it is smaller than the radius of the already-existing droplet, then they will coalesce and the small drop will be eliminated.
- Adsorption: In this part, all the droplets grow with the process explained in section 3.2.2 and the rate of G according to equation (3–8).
- Coalescence: The check for coalescence is done according to section 3.2.3 at each iteration. It is worth pointing out here that in order to take into account the multiple coalescence, after each coalescence the distance between daughter droplet with all the already-existing drops is checked in an inner loop and if one of the already-existing droplets is inside the area of the daughter drop they will merge.
- Departure of big droplets: At the end of each step there is a check for departure of big droplets that cannot resist against gravity force based on the method explained at section 3.2.5, by comparing size of each droplet with r_{max} from equation (3–14). The heavy droplets, that are bigger than r_{max} , will slide and clean off other droplets in their path and reproduce more vacant area to grow new small droplets. In this work the algorithm is stopped before sliding the first droplet.

At the end of the main loop there is a check for steady state, meaning that the difference between the size of droplets at iteration k and the size of droplets at iteration $k - 1$ is calculated and if the difference is smaller than a pre-specified error (that is considered 10^{-7}), then the loop will stop.

The model is run for five different T_w and four different initial densities (N_D) in order to investigate the effective parameters in controlling droplets growth in dropwise condensation.

3.3 Model that considers droplets as ellipsoids

The model describing up to now is based on the assumption of spherical-caps growing on a flat substrate. But speaking of a textured substrate, some modifications will be needed in the presented model. Firstly, on textured substrates droplets can grow and touch in a three dimensional configuration. So z in equation (3–23) will not be 0 anymore. In addition, coalescence in all three planes $X - Y$, $X - Z$, and $Y - Z$ must be considered. Secondly, on textured surfaces droplets usually tend to form more ellipsoidal shape than spherical, depending on the size of surface texturing patterns with respect to the size of droplets. For texturing patterns at the same size or bigger than the droplets, the fact that droplets are limited by surface topography and are not free to slide on the substrate makes them prefer to form ellipsoidal shape along the surface pattern. Moreover, droplets tend to form a canal of liquid between surface imperfections, that can be another reason of forming the ellipsoidal shape. Also, sometimes when the texturing patterns are very smaller than

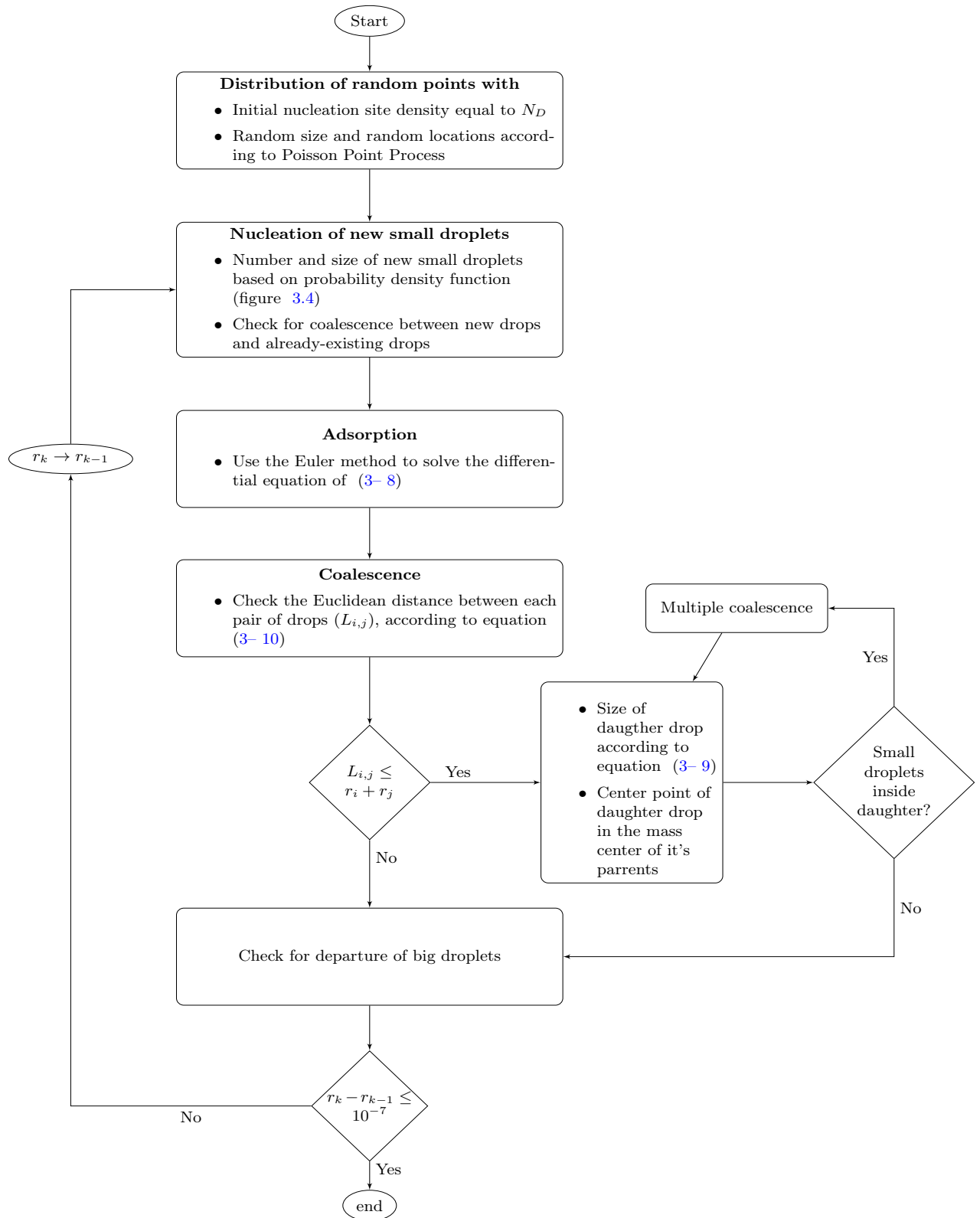


Figure 3.8: Schematic diagram of the simulation algorithm for generating circular droplets on flat substrate

the size of droplets there are more elliptical droplets than the circular ones. This can be because that the texturing usually affects surface roughness and again prevent droplets from free sliding. But, we must not neglect that in the case of very big drops that are able to slide from the substrate, the texturing patterns can not affect their circular shape. This effect can be seen in figure 3.9 that shows, the big droplets that are huge enough to not be influenced by surface micro texturing, tend to present more spherical shape to occupy less space due to the effect of their surface tension. This effect can be seen in figure 3.9. All in all, ellipsoidal shape of droplets as well as texturing configuration will change the growth rate due to both adsorption and coalescence in the last algorithm.

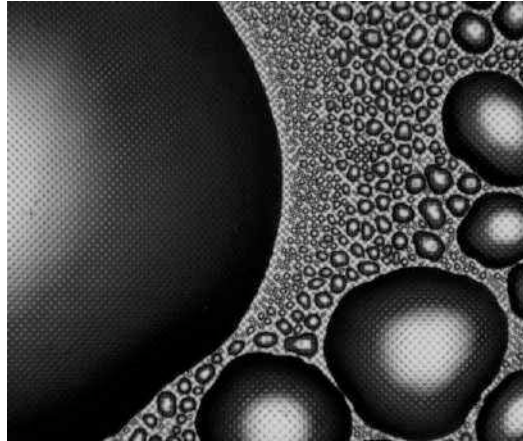


Figure 3.9: Comparison between the shape of small and big droplets on a pillared substrate. Small droplets tend to form more elliptical shapes due to adhesion with surface texturing, while big droplets present more spherical shapes in order to occupy less surface. The size of the image is $3.3mm \times 2.7mm$.

In this part, a mathematical approach for modeling ellipsoidal droplets will be developed and then the algorithm that can simulate droplets nucleation and growth based on this model will be presented. In the next step this approach will be modified by considering the contact angle of ellipsoidal droplets on the surface.

3.3.1 Adsorption

For a spherical droplet, the size in all the directions is the same and equal to radius r . This kind of droplets with related equation can be seen in figure 3.10 (a). Figure 3.10 (b) shows an ellipsoidal droplet with its major diameters a , b , and c in the directions of X , Y , and Z , respectively. We will consider $b = e.a$ and $c = f.a$, where e and f are the ratios between Y -direction and Z -direction radius of ellipsoid with respect to its X -direction radius.

The growth rate due to adsorption for spherical cap droplets is presented in equation (3–8). If we consider r as the equivalent radius of an ellipsoidal and define it as the radius of the sphere having the same volume as the ellipse, then we will have:

$$r^3 = a.b.c. \quad (3-41)$$

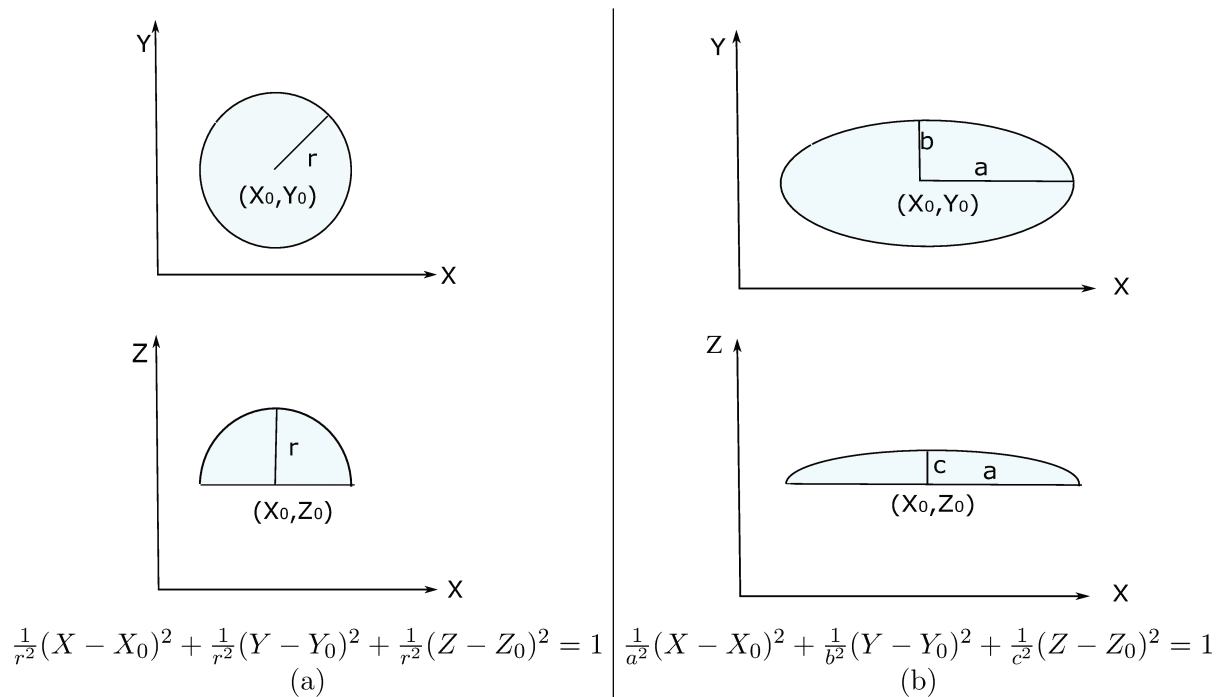


Figure 3.10: Schematic of (a) spherical droplets and (b) ellipsoidal droplets in two planes (X-Y) and (X-Z) and their corresponding equations.

Considering $b = e.a$ and $c = f.a$:

$$3r^2 \frac{dr}{dt} = \left(\frac{3e}{f^2}\right) c^2 \frac{dc}{dt}, \quad (3-42)$$

and thus,

$$\frac{dc}{dt} = \left(\frac{f^2 \cdot r^2}{e \cdot c^2}\right) c^2 \frac{dr}{dt}, \quad (3-43)$$

where $\frac{dr}{dt}$ can be calculated using the method of Euler in solving ordinary differential equations (3-8), considering $\theta = 90^\circ$. Then, since $\frac{da}{dt} = \frac{1}{f} \cdot \frac{dc}{dt}$ and $\frac{db}{dt} = \frac{e}{f} \cdot \frac{dc}{dt}$, it is possible to calculate the growth rate of an ellipsoidal droplet due to adsorption in all three dimensions:

$$\begin{aligned} a_k &= a_{k-1} + \frac{da}{dt}, \\ b_k &= b_{k-1} + \frac{db}{dt}, \\ c_k &= c_{k-1} + \frac{dc}{dt}. \end{aligned} \quad (3-44)$$

k here represents the drops generation.

3.3.2 Coalescence

The coalescence of ellipsoidal droplets growing on three dimensional pillared substrate is different from the procedure explained in section 3.2.3 in 3 points of view:

- Check for coalescence: ellipsoidal droplets can touch in different directions and check for coalescence is not anymore possible by comparing the Euclidean distance between their center points with the sum of their radius. On the other hand, three dimensional coalescence can occur, because of the three dimensional configuration of droplets on textured substrate.
- Growth rate due to coalescence: ellipsoidal droplets will have different growth rate with respect to circular ones.
- Position of daughter droplet: the center point of daughter droplets after coalescence are no longer at the mass centers of the parents. This is because if one of the parents is in touch with a pillar, they tend to stay in touch till the end of process.

3.3.2.1 Checking for coalescence

Ellipsoidal droplets can touch in different ways. According to figure 3.11 (a), if the droplets are spherical, the condition for their coalescence can be studied by measuring the Euclidean distance between their center points. If the Euclidean distance between the center points goes beyond the summation of their radius, they will merge and form the daughter droplet. In contrary, there are many ways for approaching two ellipsoidal droplets. Two ellipsoids can touch in the directions of $a_1 - a_2$, $b_1 - b_2$, $a_1 - b_2$, or even in the directions not corresponding to parameters a and b . So, the best way for studying the condition of coalescence between two ellipsoids is verifying the existence of their intersection that is shown in figure 3.11 (b).

In this regard, at first the equation of intersection of the two ellipsoids must be derived and then the conditions under which this equation has at least one real root must be investigated. Since for three dimensional ellipsoids calculating the equation of intersection will be complicated, here the intersection of their two dimensional projected images on each plane X - Y , X - Z , and Y - Z will be studied. The projected images of the two ellipsoids will be two ellipses at each planes as is shown in figure 3.12. In this figure the ellipses that are the results of the projection of the two ellipsoids on the plane $X - Y$ are shown by black. Therefore, the calculations will reduce to calculating the intersection of two ellipses, but in three planes.

at X - Y plane:

$$\left\{ \begin{array}{l} \frac{1}{a_1}(X_1 - X_0) + \frac{1}{b_1}(Y_1 - Y_0) = 1, \\ \frac{1}{a_2}(X_2 - X_0) + \frac{1}{b_2}(Y_2 - Y_0) = 1, \end{array} \right. \quad \begin{array}{l} (3-45) \\ (3-46) \end{array}$$

at X - Z plane:

$$\left\{ \begin{array}{l} \frac{1}{a_1}(X_1 - X_0) + \frac{1}{c_1}(Z_1 - Z_0) = 1, \\ \frac{1}{a_2}(X_2 - X_0) + \frac{1}{c_2}(Z_2 - Z_0) = 1, \end{array} \right. \quad \begin{array}{l} (3-47) \\ (3-48) \end{array}$$

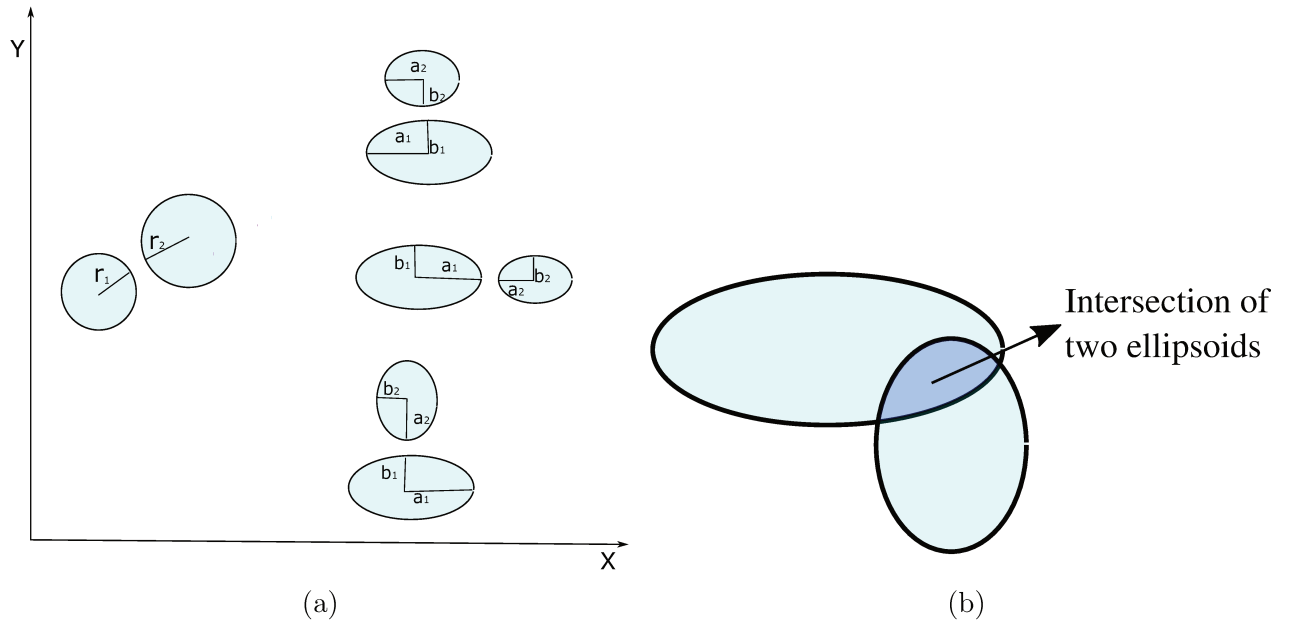


Figure 3.11: (a) The difference between approaching two spherical droplets *v.s* two ellipsoidal droplets, (b) intersection of two touching ellipsoidal droplets.

at Y - Z plane:

$$\left\{ \begin{array}{l} \frac{1}{b_1}(Y_1 - Y_0) + \frac{1}{c_1}(Z_1 - Z_0) = 1, \\ \frac{1}{b_2}(Y_2 - Y_0) + \frac{1}{c_2}(Z_2 - Z_0) = 1, \end{array} \right. \quad (3-49)$$

$$\left\{ \begin{array}{l} \frac{1}{b_1}(Y_1 - Y_0) + \frac{1}{c_1}(Z_1 - Z_0) = 1, \\ \frac{1}{b_2}(Y_2 - Y_0) + \frac{1}{c_2}(Z_2 - Z_0) = 1, \end{array} \right. \quad (3-50)$$

But according to figure 3.12, there might be the droplets that are not really in contact, while their projected images superimpose in some planes. For avoiding this problem and reducing calculation time as well, before checking for intersection of the ellipses of projected images, the three dimensional Euclidean distance between two ellipsoids (equation (3-22)) must be compared with the summation of their bigger radius. If the Euclidean distance is inferior than the summation of maximum sizes, then the intersection will be calculated.

For calculating the intersection between two ellipses, one has to solve the system of equations of two ellipses, considering the point of $(0,0)$ at the center of the first ellipse. So, the equation of the first ellipse will reduce to equation (3-51).

$$\left\{ \begin{array}{l} A_1 X + Y = R_1, \\ A_2(X - X_0) + (Y - Y_0) = R_2 \end{array} \right. \quad (3-51)$$

$$\left\{ \begin{array}{l} A_1 X + Y = R_1, \\ A_2(X - X_0) + (Y - Y_0) = R_2 \end{array} \right. \quad (3-52)$$

where $A_1 = \frac{b_1^2}{a_1^2}$ and $R_1 = b_1^2$, $A_2 = \frac{b_2^2}{a_2^2}$, and $R_2 = b_2^2$. Subtracting equation (3-52) from equation (3-51) gives:

$$A_2(X - X_0)^2 - A_1 X^2 + (Y - Y_0) - Y^2 = R_2 - R_1, \quad (3-53)$$

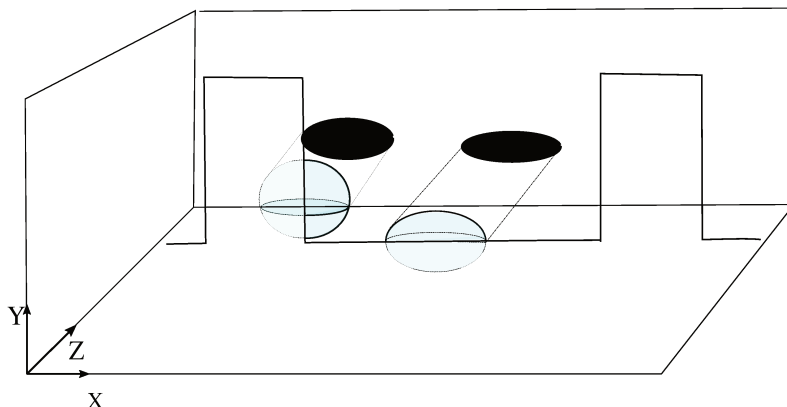


Figure 3.12: Two ellipsoidal droplets approaching on the space between two pillars. For checking coalescence between these two droplets we can verify the existence of intersection between their projected images on each planes X - Y , X - Z and Y - Z . But, this calculation is done if the three dimensional Euclidean distance between the ellipsoids is inferior than the summation of their maximum sizes.

$$Y^2 = A_3^2 X^4 + B_3 X^2 + C_3 + 4A_3 B_3 X^3 + 2A_3 C_3 X^2 + 2B_3 C_3 X, \quad (3-54)$$

where $A_3 = \frac{A_2 - A_1}{2Y_0}$, $B_3 = \frac{-2A_2 X_0}{2Y_0}$, $C_3 = \frac{R_1 - R_2 + A_2 X_0^2 + Y_0^2}{2Y_0^2}$.

Substituting equation (3-54) in equation (3-51), will results in:

$$A_4 X^4 + B_4 X^3 + C_4 X^2 + D_4 X + E_4 = 0, \quad (3-55)$$

where $A_4 = A_3^2$, $B_4 = 2A_3 B_3$, $C_4 = A_1 + B_3^2 + 2A_3 C_3$, $D_4 = 2B_3 C_3$, $E_4 = C_3^2 - R_1$. Two ellipses have intersection if and only if equation (3-55) has at least one real root. This means that if equation (3-55) has at least one real root, the two ellipses have a real intersection, meaning that two droplets are in touch at plane X - Y and coalescence will occur. As was mentioned before on textured surfaces, the droplets are distributed on three dimensional space, consequently coalescence can occur in all three dimensions, but solving the system of equations (3-51) and (3-52) for the intersection of 3 dimensional ellipsoids is very complicated. Therefore, for checking coalescence in three dimensional space, we can solve the same system of equations but in three planes (X - Y , X - Z , and Z - Y).

3.3.2.2 Growth rate due to coalescence

After the criterion for coalescence is satisfied, the next step is to calculate the size and position of the daughter droplet. The growth rate due to coalescence can be calculated based on the assumption that coalescence is a mass conservative process. Meaning that during this process the total amount of liquid will not change. For spherical cap droplets the mass conservative assumption will give equation (3-20), where r indicates the radius of daughter droplet resulting from coalescence of droplets i and j . If we consider that the

volume of daughter droplet is equal to the total volume of liquid present in the coalescence of two ellipsoidal droplets i and j , then we will have:

$$volume = \left(\frac{2\pi}{3}\right)(a.b.c) = \left(\frac{2\pi}{3}\right)(a_i.b_i.c_i + a_j.b_j.c_j), \quad (3-56)$$

therefore, we will have 1 equation and 3 unknown parameters (a , b , and c). For solving this equation we will need two assumptions. From analogy with equation (3-20) for spherical cap droplets, we can assume a and b of daughter drop as:

$$\begin{aligned} a &= \sqrt[3]{a_i^3 + a_j^3}, \\ b &= \sqrt[3]{b_i^3 + b_j^3}. \end{aligned} \quad (3-57)$$

Then c can be calculated from equation (3-56) and then e and f can be calculated from $e = b/a$ and $f = c/a$.

3.3.2.3 Position of daughter droplet

In the process of coalescence for hemispherical droplets, the center point of daughter drop is at the mass center of its parents according to equation (3-23). For ellipsoidal droplets the mass center of droplets will change into:

$$\begin{aligned} x &= \frac{(a_i.b_i.c_i).x_i + (a_j.b_j.c_j).x_j}{a_i.b_i.c_i + a_j.b_j.c_j}, \\ y &= \frac{(a_i.b_i.c_i).y_i + (a_j.b_j.c_j).y_j}{a_i.b_i.c_i + a_j.b_j.c_j}, \\ z &= \frac{(a_i.b_i.c_i).z_i + (a_j.b_j.c_j).z_j}{a_i.b_i.c_i + a_j.b_j.c_j}. \end{aligned} \quad (3-58)$$

The study on real images from pillared surfaces shows that if a droplet touches a pillar, they will stay in touch till the end of process. This effect can be seen in figure 3.13. In this figure, if we follow each droplet that is in touch with a pillar, we will see that it will stay adhered to this pillar. This fact will add another condition to the coalescence process that is:

If one of the parents is in touch with a pillar, the center point of daughter drop will not be in mass center of the parents any more.

So there will be two situations after coalescence for center of daughter droplets:

- If both parents or non of them already touch the pillars: center point of daughter will be the same as in equations (3-58).
- If just one of the parents already touches at least one pillar: center point of daughter will be at the center of the parent that is in touch with the pillars.

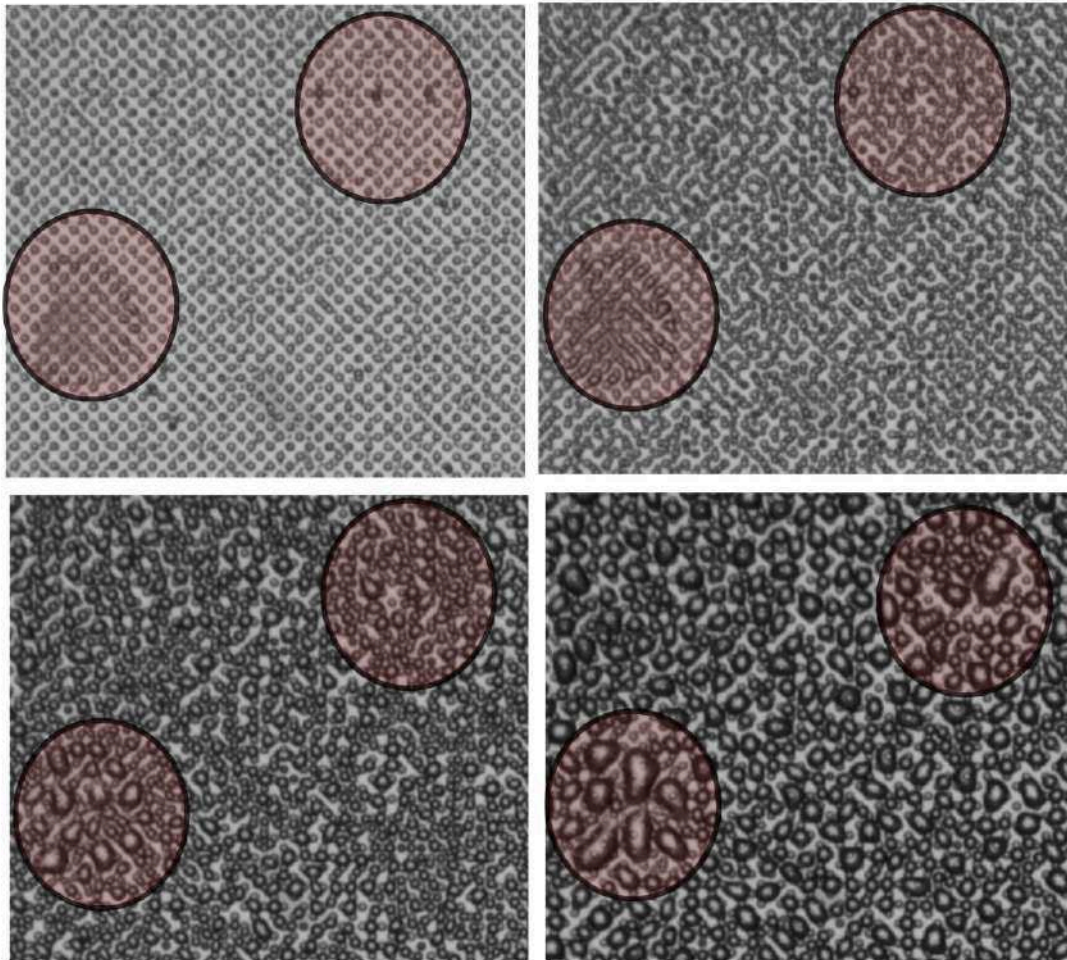


Figure 3.13: Images of the real droplets growing on a pillared substrate at $t = 100, 200, 400, 800$. Two example zones are highlighted in these images that consist of droplets in touch with pillars. It can be seen that if a droplet touches a pillar, they will stay in touch till the end of process.

3.3.3 Algorithm for generating ellipsoidal droplets on pillared substrates

The algorithm for simulating nucleation and growth of droplets on pillared surfaces is presented in figure 3.14. The first step is to simulate the pillars as cylinders with the specified patterns that are presented in table 1.1. This table represents 6 different configurations of pillars on the substrates during the experimental procedure. Then, the random ellipses with the same densities as are extracted from the binarized images are distributed on the three dimensional pillared substrate. For the 6 pillars configurations mentioned here, the droplets initial density is between $10^{12} - 10^{13} m^{-2}$ with the equivalent radius around $5\mu m$. This is important to mention here that, the density of droplets depends also on the bare area that is imposed for droplets formation. On the textured substrate, the surface area for the initial droplets is more than the area of flat substrates because the texturing patterns introduce more free area that must be taken into account.

Since on a textured surface the droplets can locate at different positions with respect to texturing, there will be a three dimensional configuration of droplets that can approach in the directions of X , Y , or Z . On a uniform pillared surface the height of each droplet can be calculated by measuring the spatial distance between its center point and the pillars in its vicinity (D):

- If $D > r_{pillar}$: the droplet nucleates on the substrate, $z = 0$.
- If $D < r_{pillar}$: the droplet nucleates on the top of the pillars, $z = z_{pillar}$.
- If $D = r_{pillar}$: the droplet nucleates on the side of the pillars, $0 < z < z_{pillar}$.

r_{pillar} here is the radius of a pillar. The sizes of each ellipse are considered as a (radius along axis X), $b = e.a$ (radius along axis Y) and $c = f.a$ (radius along axis Z), where e and f are the random numbers based on Poisson point process. The small ellipses also nucleate in the vacant area of substrate at each iteration. Then, all these ellipses grow by adsorbing water molecules from humid air according to the process explained at section 3.3.1. At each iteration there is a check for recognizing the droplets that stick to at least one pillar. This is because as was mentioned in section 3.3.3, if one of the parent droplets is in contact with a pillar, the location of daughter droplet after coalescence will be at its center point. Also, the experiments show that droplets bigger than $3\mu l$ will slide from the top of the pillars, so in the algorithm the volume of each droplet is calculated at each iteration and if it is more than $3\mu l$, then the height of droplet (z) will be put at zero. In the next step, the ellipsoidal droplets that are in touch in each of the planes $X - Y$, $X - Z$, or $Y - Z$ are detected by verification the real root of their intersection equation according to the method proposed in section 3.3.2.1. These droplets will merge and the size and center point of daughter droplet is calculated according to sections 3.3.2.2 and 3.3.2.3 respectively. Then, as was explained in section 3.2.5, if a droplet becomes big enough to overcome the surface tension, it will slide and clean off all the droplets on its path and expose strip area to nucleate new small droplets. It is worth pointing out here that, since the very big droplets are more circular than ellipsoidal (figure 3.9), equation (3-27) that is developed originally for spherical droplets can be used for verifying droplets departure in this model also. At the end, the difference between the mean radius of droplets with the mean radius of the droplets in the former iteration is calculated and if it is negligible (less than $10^{-7}m$) the program will stop iterating.

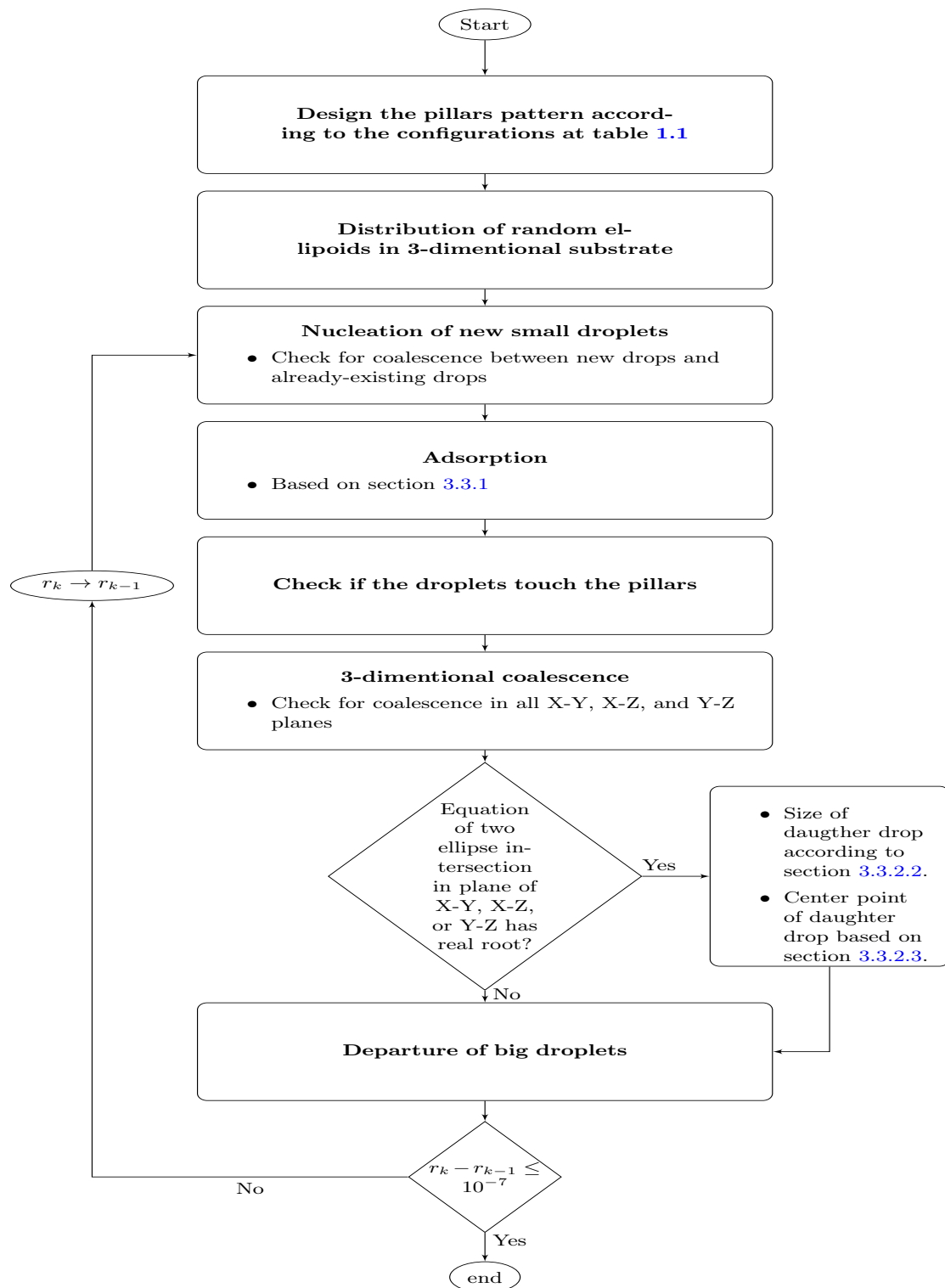


Figure 3.14: Schematic diagram of the simulation algorithm for generating ellipsoidal droplets on pillared substrate

3.4 Model that considers droplets as semi-ellipsoids

In this section a general modeling for droplets on patterned substrates is proposed based on the semi-ellipsoid approach. An ellipsoid (figure 3.15 (a)) is a surface that may be obtained from a sphere by deforming it by means of directional scaling, or more generally, of an affinity transformation. The contact angle of a hemi-ellipsoid with horizontal surface is $\theta = 90^\circ$. But when we cut the head of an ellipsoid with contact angle $\theta \neq 90^\circ$, we will have a semi-ellipsoid (figure 3.15 (b)).

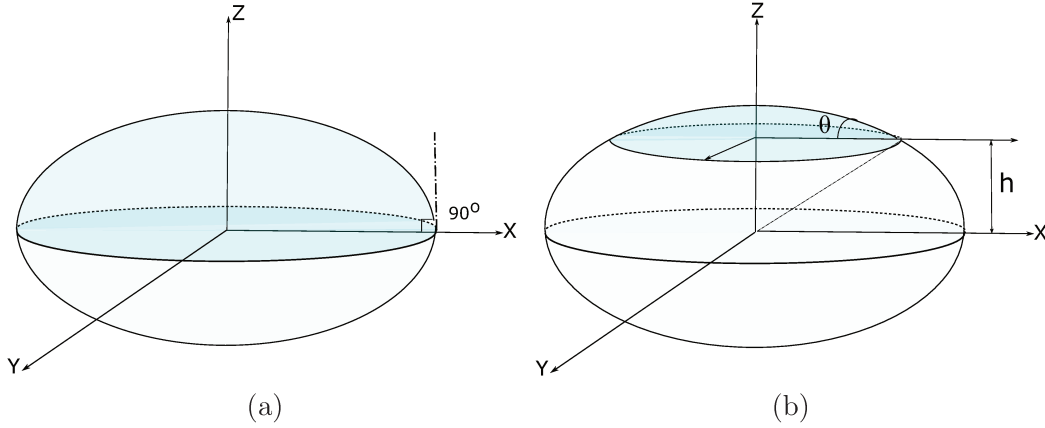


Figure 3.15: (a) An ellipsoid (contact angle with surface is 90°), (b) a semi-ellipsoid (contact angle with surface is θ). On theory we consider that the semi-ellipsoid is cut from the head of an ellipsoid.

Since the droplets on textured substrates are ellipsoid shape but with contact angle $\theta \neq 90^\circ$, a general method for modeling their growth rate is developed by considering them as semi-ellipsoids. In this regard we will consider the semi-ellipsoidal droplets as the caps that are cut off from a bigger ellipsoid. Since we know the sizes of the droplets (a, b, c) and θ , we must find the radius of the big ellipsoid that the droplets are considered to be cut from (A, B, C).

If we consider the equation of the semi-ellipsoid and big ellipse as $\frac{1}{a^2}X^2 + \frac{1}{b^2}Y^2 + \frac{1}{c^2}Z^2 = 1$ and $\frac{1}{A^2}X^2 + \frac{1}{B^2}Y^2 + \frac{1}{C^2}Z^2 = 1$ respectively, (figure 3.16), and the contact angle of the semi-ellipsoid with horizon θ and the angle between center and semi-ellipsoid as γ , the equation of the line tangent to the big ellipsoid at point P can be defined from:

$$\frac{1}{A^2}X^2 + \frac{1}{C^2}Z^2 = 1, \quad (3-59)$$

rearranging for X will give:

$$C^2X^2 + A^2Z^2 - A^2C^2 = 0 \quad (3-60)$$

and so

$$\frac{dZ}{dX} = \frac{-C^2X}{A^2Z}. \quad (3-61)$$

So the slop and the equation of the tangent line will be:

$$m = \frac{-C^2 a}{A^2 h}, \quad (3-62)$$

and

$$\frac{aX}{A^2} + \frac{hZ}{C^2} = 1. \quad (3-63)$$

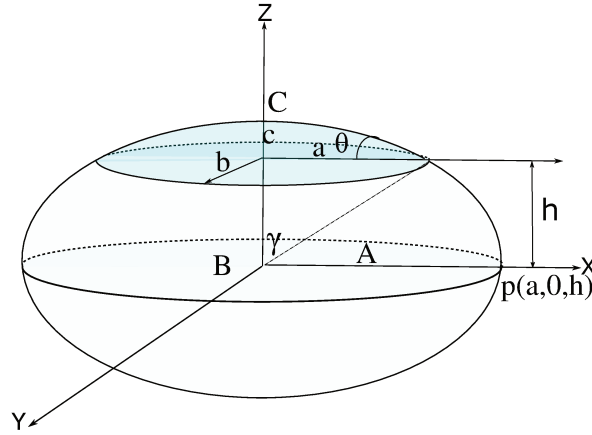


Figure 3.16: Semi-ellipsoid with contact angle θ is cut of from a bigger ellipsoid by angle γ and height h .

This line will cross the vertical axis at $\hat{Z} = \frac{C^2}{h}$. On the other hand we know that the contact angle of the droplet on the surface is θ and we have $\tan(\pi - \theta) = \hat{Z}/a$. By equaling these two equations:

$$\frac{C^2}{h} = a \tan(\pi - \theta) = -a \tan(\theta), \quad (3-64)$$

$$\frac{C^2}{C - c} = -a \tan(\theta), \quad (3-65)$$

rearranging for C :

$$C^2 + a \tan(\theta) C - a c \tan(\theta). \quad (3-66)$$

Equation (3-59) is a quadratic equation with respect to C . The roots of this equation will be easily find equal to:

$$C = \frac{-a \tan(\theta) \pm \sqrt{a^2 \tan(\theta)^2 + 4 a c \tan(\theta)}}{2}. \quad (3-67)$$

This is the height of the big ellipsoid at Z direction. Then h will be:

$$h = C - c, \quad (3-68)$$

and

$$\gamma = \tan^{-1}(a/h). \quad (3-69)$$

Now we can calculate A and B also. Considering two dimensional equation of ellipsoid in plane $X - Z$ will have:

$$\frac{X^2}{A^2} + \frac{Z^2}{C^2} = 1, \quad (3-70)$$

at point P we have $X = a$ and $Z = h$, therefore:

$$\frac{a^2}{A^2} + \frac{h^2}{C^2} = 1, \quad (3-71)$$

which will results in:

$$A = \frac{a}{\sqrt{1 - \frac{h^2}{C^2}}}. \quad (3-72)$$

The same approach will be used to calculate the relation between B and b on the plane $Y - Z$:

$$B = \frac{b}{\sqrt{1 - \frac{h^2}{C^2}}}. \quad (3-73)$$

3.4.1 Adsorption of semi-ellipsoidal droplets

Now that we have A, B, C the calculations are much easier because the surface and volume of the big ellipsoid can be calculated as:

$$S = 2\pi \left[\frac{A^p B^p + A^p C^p + B^p C^p}{3} \right]^{1/p} \quad p = 1.6075, \quad (3-74)$$

$$V = (2/3)\pi ABC \quad (3-75)$$

Considering $B = A.E$, and $C = A.F$, where E, F are the ratios between ellipsoids radius, we will have:

$$S = 2\pi \left[C^{2p} \frac{E^p}{F^{2p}} + \frac{1}{F^{2p}} + \frac{E^p}{F^p} \right]^{1/p}, \quad (3-76)$$

$$S = 2\pi C^2 \left[\frac{E^p}{F^{2p}} + \frac{1}{F^{2p}} + \frac{E^p}{F^p} \right]^{1/p}, \quad (3-77)$$

Considering:

$$s_1 = 2\pi \left[\frac{E^p}{F^{2p}} + \frac{1}{F^{2p}} + \frac{E^p}{F^p} \right]^{1/p}, \quad (3-78)$$

will result in:

$$S = 2\pi s_1 C^2, \quad (3-79)$$

So we can easily calculate $\frac{dS}{dC}$ and $\frac{dV}{dC}$:

$$\frac{dS}{dC} = 4\pi s_1 C, \quad (3-80)$$

and

$$\frac{dV}{dC} = 2\pi \frac{E}{F^2} C^2. \quad (3-81)$$

So we can consider the temperature gradient due to convection as:

$$\Delta T_{conv} = \frac{q}{h_i S} = \frac{q}{2\pi s_1 h_i C^2}, \quad (3-82)$$

h_i is the free convection coefficient and can be calculated based on section 3.2.2.1 and the temperature gradient due to conduction through the droplet as:

$$\Delta T_{cond} = \frac{q}{K_w \frac{dS}{dC}} = \frac{q}{4\pi s_1 K_w C}. \quad (3-83)$$

The temperature drop due to surface curvature can be calculated from the surface tension force. If we increase the droplets radius C by an amount dC , we must perform the extra work $dW = \sigma dS - \Delta P dV$, where dS is the change in surface area and dV is the change in volume. In equilibrium, where the contraction forces must balance the pressure forces, there should be nothing to gain or lose and [140]:

$$\sigma dS - P dV = 0. \quad (3-84)$$

Substituting dS and dV from equations (3-80) and (3-81), will result in:

$$4\pi s_1 C \sigma = \Delta P 2\pi \frac{E}{F^2} C^2, \quad (3-85)$$

and then:

$$\Delta p = \frac{2s_1 \sigma F^2}{C E}. \quad (3-86)$$

This parameter for a hemisphere droplets is $\Delta p = \frac{2\sigma}{r}$. Considering linear approximation between p and T_{sat} will give:

$$\Delta T = \Delta P \frac{dT_{sat}}{dp} = \frac{2s_1 \sigma F^2}{C E} \frac{dT_{sat}}{dp}. \quad (3-87)$$

From Clausius-Clapeyron approximation:

$$\frac{dT_{sat}}{dp} = \frac{T_{sat} \Delta(V)}{\Delta H_{condensation}} = \frac{T_{sat} \Delta(V)}{\rho H_{fg} \Delta(V)} = \frac{T_{sat}}{\rho H_{fg}}. \quad (3-88)$$

Combining equations (3-85) till (3-88) will give the temperature drop due to surface curvature:

$$\Delta T_c = \frac{2s_1 \sigma F^2}{C E} \frac{T_{sat}}{\rho H_{fg}}. \quad (3-89)$$

Now we can calculate the big ellipse growth rate due to adsorption by equaling the temperature gradients:

$$\Delta T_{total} = \Delta T_c + \Delta T_{conv} + \Delta T_{cond}, \quad (3-90)$$

which results in :

$$\Delta T_{total} = \frac{2s_1\sigma F^2}{C} \frac{T_{sat}}{E} \frac{1}{\rho H_{fg}} + \frac{q}{2\pi s_1 h_i C^2} + \frac{q}{4\pi s_1 K_w C}, \quad (3-91)$$

and

$$\Delta T_{total} = \frac{C_{min}}{C} \frac{F^2}{E} \frac{T_{sat}}{\rho H_{fg}} + \frac{q}{2\pi s_1 h_i C^2} + \frac{q}{4\pi s_1 K_w C}, \quad (3-92)$$

where:

$$C_{min} = \frac{2s_1\sigma T_{sat} F^2}{\rho H_{fg} E} \quad (3-93)$$

and q in equation (3-92) is the heat of condensation and can be calculated as:

$$q = \rho H_{fg} \frac{dV}{dt} = \rho H_{fg} \frac{dV}{dC} \frac{dC}{dt}. \quad (3-94)$$

Substituting $\frac{dV}{dC}$ from equation (3-81), we will be able to calculate q as a function of $\frac{dC}{dt}$:

$$q = \rho H_{fg} \frac{dV}{dt} = 2\pi\rho H_{fg} \frac{E}{F^2} C^2 \frac{dC}{dt}. \quad (3-95)$$

Substituting equation (3-95) in equation (3-92) and rearranging for $\frac{dC}{dt}$ will give:

$$\frac{dC}{dt} = \frac{A_1(1 - \frac{C}{C_{min}})}{A_2 + A_3 C}, \quad (3-96)$$

where $A_1 = \frac{\Delta T_{total} F^2}{\rho H_{fg} E}$, $A_2 = \frac{1}{h_i S}$, and $A_3 = \frac{1}{2K_w S}$. Then $dA = dC/F$ and $dB = EdA$, $\frac{dC}{dt}$ in this equation represents the growth rate due to adsorption of the big ellipsoid. For the small semi-ellipsoid, we can use the relations between a, b, c and A, B, C from equations (3-67), (3-72), and (3-73). By differentiating these equations we can calculate $\frac{da}{dt}$, $\frac{db}{dt}$, and $\frac{dC}{dt}$ as a function of $\frac{dC}{dt}$. From equation (3-72) and knowing $h = a/\tan(\gamma)$, we will have:

$$\frac{da}{dt} = s_2 \frac{C}{a} \frac{dC}{dt}, \quad (3-97)$$

where $s_2 = \frac{1}{F^2(1 + \frac{1}{F^2 \tan^2(\gamma)})}$. The same approach for $\frac{db}{dt}$ from equation (3-73) will result in:

$$\frac{db}{dt} = s_3 \frac{C}{b} \frac{dC}{dt}, \quad (3-98)$$

where $s_3 = \frac{E^2}{F^2(1 + \frac{E^2}{e^2 F^2 \tan^2(\gamma)})}$ and:

$$\frac{dc}{dt} = \frac{1}{s_4} \frac{dC}{dt}, \quad (3-99)$$

where $s_4 = 1 + \frac{1}{F \tan(\gamma)}$. Equations (3-97), (3-96), and (3-99) represent the growth rate of a semi-ellipsoidal droplet on 3 directions.

3.4.2 Coalescence of semi-ellipsoidal droplets

Calculating the growth rate due to coalescence is done based on mass balance law. Mining that if two semi-ellipsoidal droplets (so-called parents) merge and form a bigger semi-ellipsoidal droplet (daughter) total mass of water during this process is constant. So we can say mass or volume of daughter drop is equal to summation of mass or volume of its parents. Again, we do all the calculations for the big ellipse and then calculate the growth rate of the small semi-ellipsoid from the relation between their sizes. Therefore, the volume of daughter is:

$$V_{daughter} = V_{parent1} + V_{parent2} = (2/3)\pi[A_1B_1C_1 + A_2B_2C_2] \quad (3-100)$$

On the other hand:

$$V_{daughter} = (2/3)\pi \frac{E}{F^2} C^3 \quad (3-101)$$

Equaling these two equations will give the radius of daughter droplet C :

$$C = \sqrt[3]{1.5V_{daughter} \frac{F^2}{E\pi}}. \quad (3-102)$$

Then we have $A = \frac{C}{F}$ and $B = EA$. Here we consider that E and F of the daughter are the mean of these values for parents. Now for the small semi-ellipsoidal droplet, combining equation (3-72) and $h = \frac{a}{\tan(\gamma)}$ gives:

$$a = \sqrt{\frac{A^4}{C^2 + \frac{A^2}{\tan(\gamma)^2}}}, \quad (3-103)$$

So

$$c = C - h = C - \frac{a}{\tan(\gamma)}, \quad (3-104)$$

and

$$b = \frac{B}{C^2} \sqrt{C^2 - h^2}. \quad (3-105)$$

The last three equations represent the size of semi-ellipsoidal droplets after coalescence.

3.4.3 Sliding of big droplets and equivalent radius

If we consider the equivalent radius (r_{eq}) of the semi-ellipsoidal droplets, the radius of a spherical cap that has the same volume and the same contact angle with horizon as the semi-ellipsoidal droplets, the volume of the spherical cap will be:

$$V = \frac{\pi r_{eq}^3}{3} (2 - 3\cos(\theta) + \cos(\theta)^3), \quad (3-106)$$

So

$$r_{eq} = \sqrt[3]{\frac{3V}{\pi(2 - 3\cos(\theta) + \cos(\theta)^3)}}, \quad (3-107)$$

while V is equal to the volume of semi-ellipsoid, that is the volume of a big ellipsoid with equation $\frac{1}{A^2}X^2 + \frac{1}{B^2}Y^2 + \frac{1}{C^2}Z^2 = 1$ cut off by a horizontal plane with equation $Z = h$. The volume of this semi-ellipsoid is :

$$V = ABC \frac{\pi}{3} \left[\frac{h^3}{C} - 3\frac{h}{C} + 2 \right]. \quad (3-108)$$

All the results will be presented based on r_{eq} calculated by substituting equation (3-108) into equation (3-107). Another importance of r_{eq} is that we can check for sliding the very big droplets by comparing r_{eq} with r_{max} that is derived for spherical cap in literature [25]:

$$r_{max} = \sqrt{\frac{6(\cos\theta_r - \cos\theta_a)\sin\theta\sigma}{\pi(2 - 3\cos\theta + \cos^3\theta)\rho g}}. \quad (3-109)$$

θ here is the apparent equilibrium contact angle and is equal to $\cos^{-1}(0.5\cos\theta_a + 0.5\cos\theta_r)$. r_{max} is the maximum radius of each generation of droplets before sliding.

3.4.4 Surface area

As was mentioned before, the density and growth rate of droplets is in direct relationship with bare area imposed to droplets formation and growth. The surface area on which the droplets are growing, has a very important effect on the growth pattern of average radius, because if it is not correctly calculated, it will affect the rate of coalescence and as a result the nucleation rate of new small droplets. In the case of sinusoidal substrates with period λ and amplitude a (figure 3.17), the surfaces equation will be:

$$Y = \frac{a}{2} \sin\left(\frac{2\Pi}{\lambda}x\right), \quad (3-110)$$

For calculating the total surface area it will be enough to multiple the arc length by the length of the substrate (L), that will give the surface of one sinusoidal canal. Then by multiplying this amount by total number of canals on the surface we can calculate total surface area that is imposed for droplets growth.

$$A = L \times \text{Arc length} \times \text{number of canals}. \quad (3-111)$$

Surface identification	period ($\lambda(\mu m)$)	amplitude ($a(\mu m)$)
30-5	30	5
30-10	30	10
60-5	60	5
60-10	60	10
100-5	100	5
100-10	100	10

Table 3.1: period and amplitude of the sinusoidal patterns.

where the arc length will be:

$$\text{Arc length} = \int_a^b \sqrt{1 + \left(\frac{dy}{dx}\right)^2} dx = \int_0^\lambda \sqrt{1 + \frac{\pi^2 a^2}{P^2} \cos^2\left(\frac{2\Pi}{\lambda}x\right)^2} dx \quad (3-112)$$

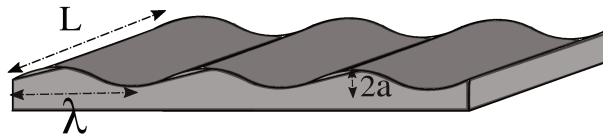


Figure 3.17: Sinusoidal surface parameters.

P and a are the characteristics of the sinusoidal profiles and in this study are chosen according to table 3.1, that represents the surfaces that are used in condensation experiments

3.4.5 Algorithm for generating semi-ellipsoidal droplets on sinusoidal substrates

Figure 3.18 shows the algorithm used for simulating nucleation and growth of semi-ellipsoidal droplets on sinusoidal substrates. This algorithm is similar to the algorithm for simulating ellipsoidal droplets on pillared substrates (figure 3.14). At first, the program starts by three dimensional distribution of semi-ellipsoidal droplets that their locations along axis X and Y are completely randomly, we can show them by x and y , but their height (z) depends on the amplitude of the sinusoidal pattern at their x and y . Contact angle of semi-ellipsoidal droplets are also defined based on the data from table 1.8. At the main loop, nucleation of new small droplets is done with the same density of initial droplets but with respect to the bare area of each iteration. Then, the growth rate of each droplet due to adsorption is calculated according to the method introduced at section 3.4.1. Experiments show that droplets bigger than $3\mu l$ will slide form the sinusoidal pattern, so in the algorithm the volume of each droplet is calculated at each iteration and if it is more than $3\mu l$, then the height of droplet (z) will put at zero. Check for coalescence will be exactly the same as for ellipsoidal droplets presented at section 3.3.2.1, but the rate of growth after coalescence will be calculated according to section 3.4.2. Then departure of very big droplets from the surface is considered as explained in section 3.4.3 by comparing

their r_{equ} with the maximum radius of a drop that can resist the gravity force. Finally, steady state test is done by comparing the difference between two following average radius and a pre-specified error in order to either stop or continuing the loop.

Choosing time step in all the three algorithms presented here (figures 3.8, 3.14, and 3.18) is very important, obviously the smaller time steps need considerable calculating time, on the other hand very big time steps will cause to the loss of some data regarding the droplets growth and nucleation of new small droplets. In all three algorithms we choose time step of $10^{-4}s$ for calculating the growth rate due to adsorption in order to have more accurate answers of Euler method and we collect the information for comparing with experimental results at each 10s. The programs were written in matlab and were run on a 2 cores PC with Intel Xeon CPU E5-2630 (2.40GHz), with 20gb ram and it took around 3 hours till completing in around 500 steps.

3.5 Conclusion

3.5.1 English

Three numerical models were developed in order to explain droplets behavior on flat and textured substrates. The differences between the behavior of droplets on the flat and textured substrates is due to their different geometries. On the flat substrates we can assume droplets with the same radius along X and Y directions, while on textured substrates there is usually tendency to have larger radius along the direction of texturing patterns. For this reason, three models have been developed here:

- Spherical-caps model, that is more adapted in the case of flat substrates,
- Ellipsoidal model, that is more preferred on the textured substrates with contact angle $\theta = 90^\circ$,
- Semi-ellipsoidal model, for droplets growing on the textured substrates with contact angle $\theta \neq 90^\circ$.

3.5.2 French

Trois modèles analytiques ont été développés afin d'expliquer le comportement des gouttelettes sur des substrats plats et texturés. Les différences entre le comportement des gouttelettes sur les substrats plats et texturés sont dues à leurs géométries différentes. Sur les substrats plats, nous pouvons supposer des gouttelettes de même rayon suivant les directions X et Y , alors que sur les substrats texturés, il y a généralement tendance à avoir un rayon plus grand dans le sens des textures. Pour cette raison, trois modèles ont été développés ici:

- Modèle à calottes sphériques, plus adapté dans le cas de substrats plats,
- Modèle ellipsoïdal, plus préféré sur les substrats texturés avec angle de contact $\theta = 90^\circ$,
- Semi-ellipsoïde, sur les substrats texturés avec angle de contact $\theta \neq 90^\circ$.

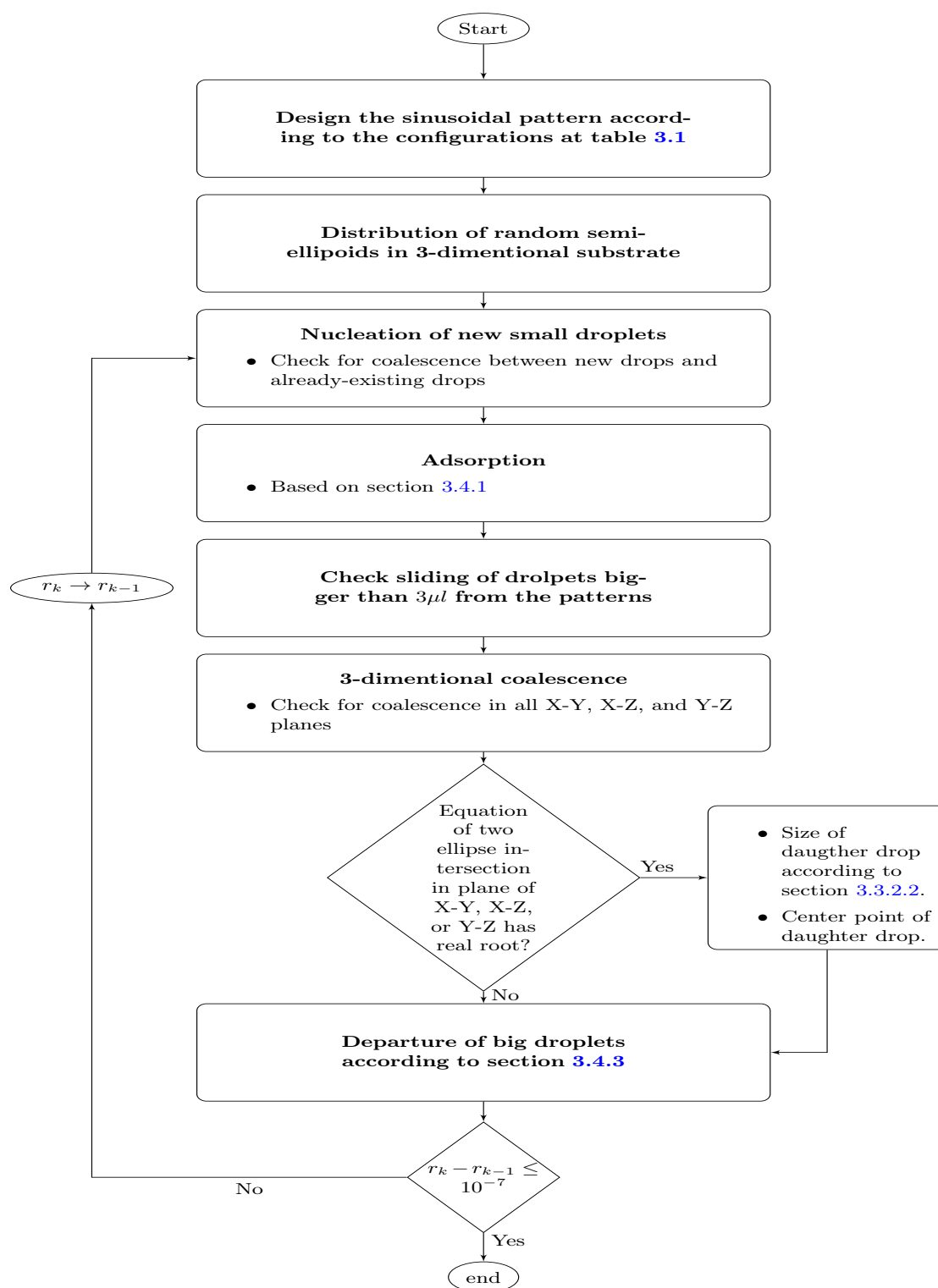


Figure 3.18: Schematic diagram of the simulation algorithm for generating semi-ellipsoidal droplets on sinusoidal substrates.

Chapter 4

Results and discussion

4.1 Summary

4.1.1 French

Dans ce chapitre, les résultats des trois modèles mathématiques et leurs algorithmes correspondants décrits au chapitre 3 seront présentés. La validation de chaque modèle sera vérifiée en comparant ses résultats pour le taux de croissance des gouttelettes, la densité des gouttelettes et les gouttelettes spatiales avec des résultats expérimentaux.

4.1.2 English

In this chapter the results of the three mathematical models and their corresponding algorithms proposed in chapter 3 will be presented. The validation of each model will be verified by comparing its results for droplets growth rate, droplets density, and droplets spatial distribution with experimental results.

4.2 Results of the spherical-cap model on flat substrates

As was mentioned before, the droplets behavior on flat surfaces usually is the same as hemi-spheres (contact angle = 90°) or in the more general cases the spherical-caps that present contact angles $\neq 90^\circ$. Therefore, the model presented in section 3.2 is used for simulating the droplets behavior on the non-textured polycarbonate substrate.

In this part at first, the validity of the simulating model will be verified by comparing its results with the experimental data. Then, the droplets spatial distribution will be studied using Ripley's L function. And at the end, the effect of wall temperature (T_w) and initial nucleation density (N_D) will be discussed on the percentage of surface covered by water droplets at steady state phase.

4.2.1 Droplets growth procedure

The results of the simulation algorithm is compared with binarized images of the real droplets in figure 4.1. It can be seen that, in both series of images by increasing the size of droplets, their number decreases. Four main steps of dropwise condensation including

nucleation of initial droplets, growth due to adsorption, growth due to coalescence, and steady state are emphasized in this figure.

The first two steps will result in rapid changes in the size and density of droplets, while at the end of the coalescence step the rates of changes are slower. This is due to the effect of nucleation of new small droplets in the vacant area produced during coalescence step. As was explained, during coalescence the parent droplets join to each other to form a bigger drop (daughter drop). Although the total volume of two coalescing drops does not change during this process, their total area reduces and daughter drop occupies smaller surface area with respect to its parents. This will lead to producing vacant areas around the daughter drops that are potential to grow new small droplets. These small droplets reduce the average radius and increase droplets density, so they smoothen the rate of changes in both of the graphs at the end of the coalescence step.

Moreover, due to forming vacant area between the droplets, the rate of coalescence reduces at later stages, because the distance between droplets is larger with respect to the initial stages. On the other hand, the droplets are bigger and the friction factor with substrate resists against coalescence. In addition, very big droplets transfer lower heat flux between cold surface and hot vapor and as a result will decrease the rate of droplets growth [83]. Therefore, in final stages there is higher amount of vacancies on the substrate that are ready to grow new small droplets and the rate of coalescence of already-existing droplets reduces. Finally, all these effects will lead to a constant mean radius and nucleation density function.

These effects can be seen in figure 4.2 that represents the comparison between computer simulation results (black dashed lines) with the results from the experiments (blue solid lines) for droplets average radius and nucleation density. In these graphs the first vertical lines indicate the time that almost the rate of changes in radius and density are lowered (due to opposite effects of coalescence and nucleation of new droplets) and the second lines are the starting time of the steady state step. This figure shows acceptable accordance between simulation results and measured data from binarized experimental images. It can be seen that the assumption of circular droplets is not far from the reality specially at earlier stages, but at steady state when the droplets are very big and cannot slide freely to form a perfectly circular shape, the two graphs are not exactly the same. In the other words, since the average contact angle for experimental droplets is 88° we assume that the droplets are spherical-caps and perfectly circular. At the earlier stages, this assumption works well, but when droplets grow due to coalescence, the friction force between droplet and substrate makes it harder to slide on the surface and form the perfectly circular shape. Therefore, the small difference between graphs of experiments and simulation can be because of this effect.

Three main periods of droplets growth can be recognized in this figure:

- (1) Nucleation and adsorption phase: at first very small droplets nucleate all around the substrate over and over again and start to grow by adsorbing water molecules from humid air. In this phase the changes in both of the graphs are very significant. The droplets in this phase are smaller than critical radius (r_c) and are referred to as "adsorbing droplets" in some literature.
- (2) Coalescence phase: following phase (1), if droplets become big enough (bigger than r_c) to touch each other, they will merge and form bigger droplets. The result of this

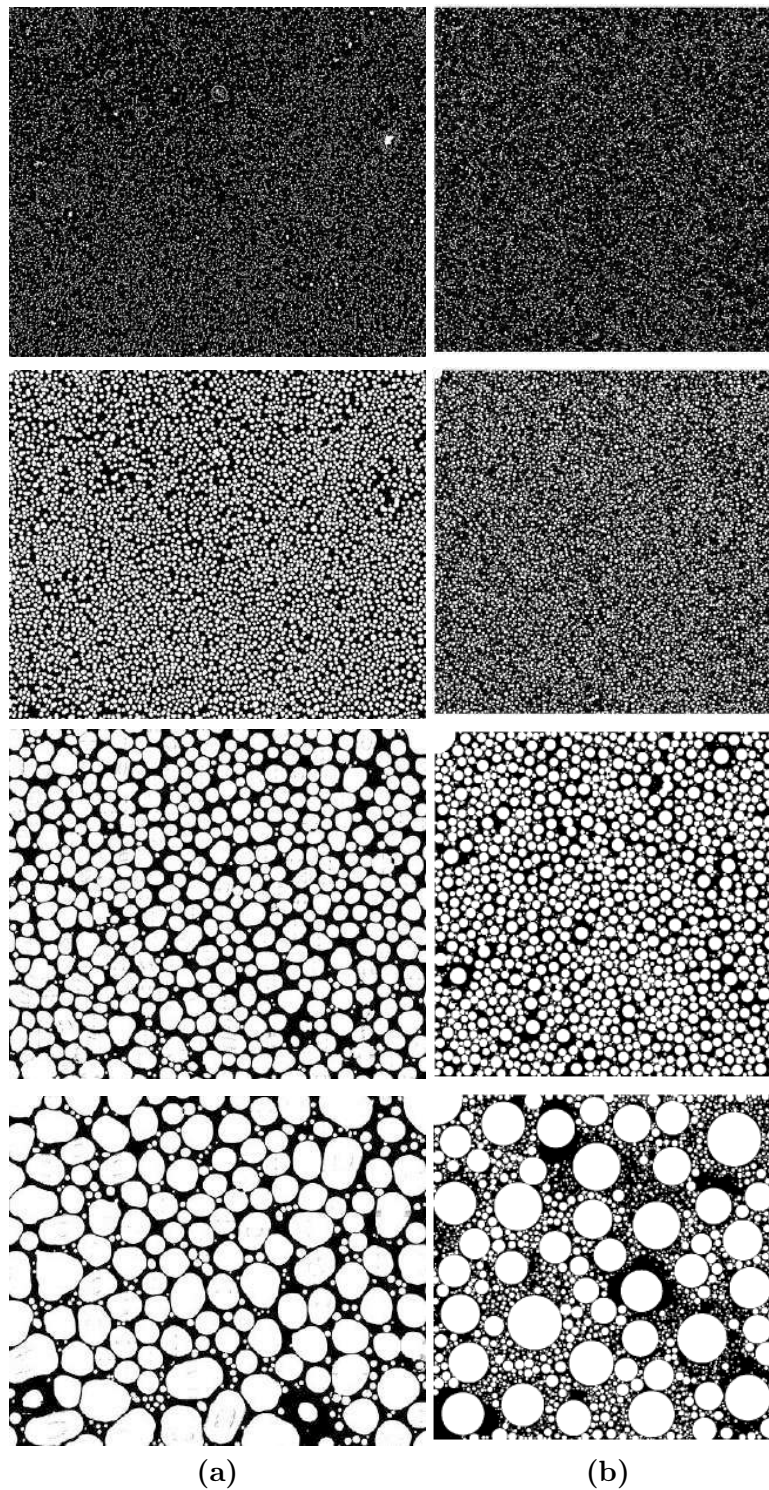


Figure 4.1: The evolution of the droplets during dropwise condensation at different time steps ($t = 10$ s (initial nucleation) , 100 s (growth due to adsorption), 700 s (growth due to coalescence), 5000 s (steady state)). (a) Binarized images of experimental results, (b) Results from simulation algorithm.

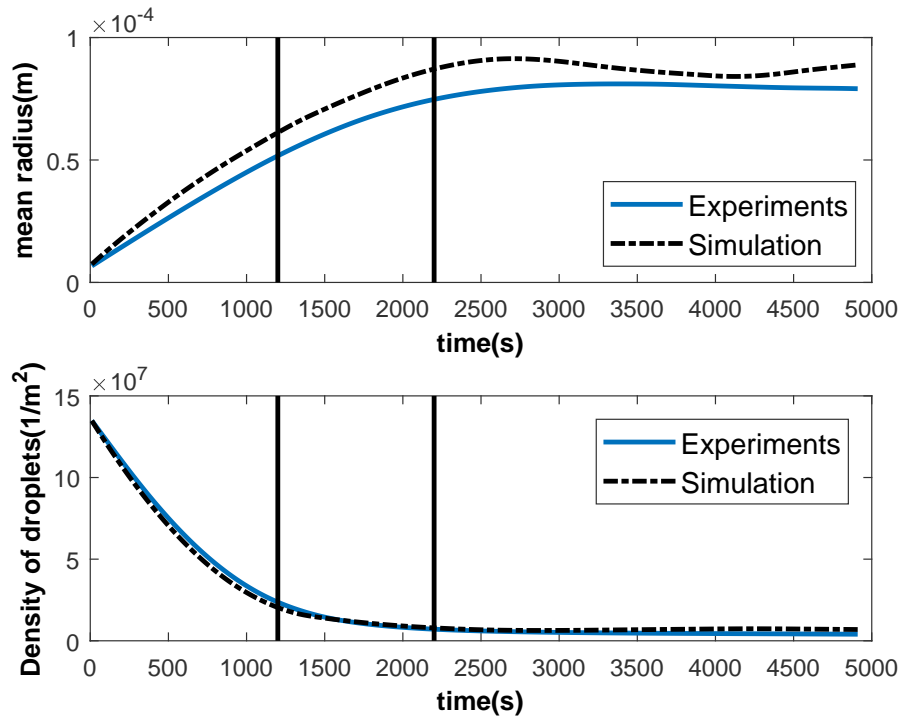


Figure 4.2: Changes in (a) droplet size and (b) droplets density during process time for simulation and experiments. The first vertical lines indicate the time that almost the rate of changes in radius and density are lowered (due to opposite effects of coalescence and nucleation of new droplets) and the second lines are the starting time of the steady state step.

phenomenon is the reduction in the number of droplets, but increase in their size and total vacant area on the substrate. In the vacant area produced by coalescence, new small droplets can nucleate and grow which increases the number, but decreases the average size of droplets. In this phase the rate of changes are less than phase (1).

- (3) Steady state phase: after a while, these contrary effects of coalescence and nucleation of new droplets will lead to an approximately constant pattern in graphs of droplets size and density. Also the droplets bigger than r_{max} (equation (3-27)) will roll off from the surface and clean the smaller droplets on their path which will introduce more vacancies for nucleation of new small droplets. This step called "steady state" situation, during which the temporal changes are negligible.

4.2.2 Droplets spatial distribution

Since before steady state the nucleation density changes rapidly, it will lead to changes in spatial distribution of droplets. In this regard, Ripley's L function method which counts the number of drops in specified distances from center of substrate can be considered as

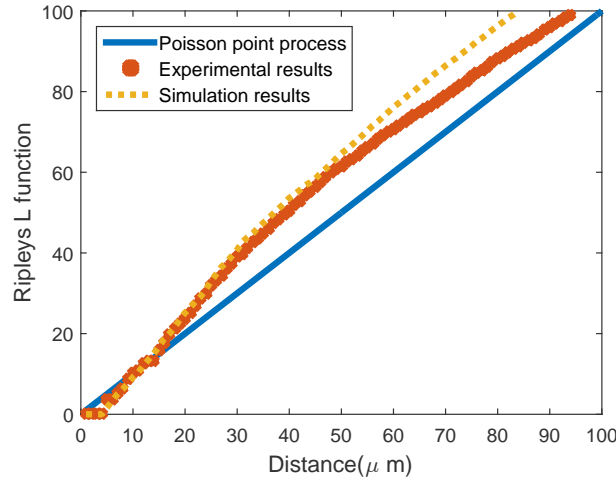


Figure 4.3: Comparison between Ripley's L functions of droplets at steady state relevant to the Poisson point process, experiments and simulation

a useful tool to evaluate the simulation method (figure 4.3). It can be seen that there is a visible similarity between Ripley's L function of simulation results and experimental data. The blue straight line represents Ripley's L function of the Poisson point process dealing with completely randomly distributed points. Any positive and negative deviation from this line indicates dispersion and coalescence, respectively. The accordance between the graphs of experimental and simulation results indicates that the program could predict spatial distribution of droplets very well.

In the Ripley's L function of both experimental and simulation results, a minimum distance of around $6 \mu m$ appears between droplets that represents the size of the smallest droplets existing on the surface. This indicates that there is no pair of droplets that can get closer than $6 \mu m$ unless they coalesce. This is the concept of Matern hard core process that prevents two points to approach to each other closer than a specified distance. Therefore, one can claim that this is the nature of coalescence that changes droplets distribution from Poisson point process to hard core point process.

4.2.3 Effect of wall temperature

In this section the effect of wall temperature on some process parameters will be discussed. By calculating the average convection coefficient (h_{ave} that is the average of h_i for all droplets) and total heat flux (q) from equations 3-9 and 3-5 at each step, we will be able to discuss the effect of T_w on the percentage of area occupied by droplets (ϕ) since these three parameters are related by:

$$\frac{q}{A} = h_{ave} \phi \Delta T_t, \quad (4-1)$$

In equation 4-1, A is the total area and $\phi = 100 \times \frac{A_{droplets}}{A}$, when $A_{droplets}$ is total area covered by droplets. h_{ave} depends strongly on the droplets size. According to figure 4.4 for small droplets near $10 \mu m$, h_{ave} is near $300000 W/m^2.K$ and it decreases to a

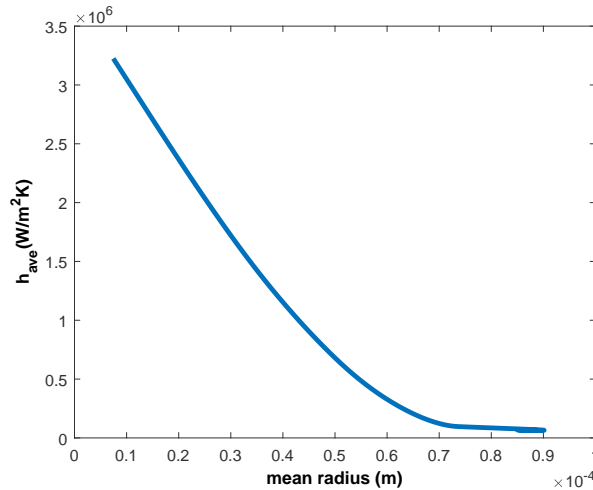


Figure 4.4: Average heat transfer coefficient v.s average size of droplets

constant value around $10000 W/m^2.K$ for droplets bigger than $90 \mu m$. This is why q during dropwise condensation is much higher than in filmwise condensation. When condensation occurs with small droplets, h_{ave} corresponds to very high values, by increasing droplets size, overall h_{ave} reduces and when droplets are big enough to wet the surface it goes down to less than one tenth of its initial value.

Average radius is related to T_w by the minimum droplets radius (r_{min}). By increasing T_w (decreasing total temperature difference) r_{min} increases continuously. Generally, there are many sites that are potential to grow droplets of different sizes. By decreasing temperature difference between substrate and air saturated temperature, the driving force for nucleation of small droplets reduces and as a result small sites become inactive. In figure 4.5 it can be seen that the size of small active sites increased from $24 nm$ to near $34 nm$ by increasing T_w from $274K$ to $303K$. By increasing r_{min} , the rate of adsorption decreases at earlier stages according to equation 3–8, but in the later stages mean radius becomes bigger and bigger and the effect r_{min} becomes negligible. So T_w affects the size and number of small droplets at earlier stages, but is not able to change these parameters for big droplets. Since h_{ave} is a function of both nucleation density and mean radius, changes in T_w will result in the same h_{ave} at later stages.

All in all it can be concluded that by increasing T_w , h_{ave} does not change very significantly because although r_{min} increases, mean radius does not change in later stages. On the other hand, by increasing T_w , the heat transfer driving force (ΔT_t) decreases, which will lead to a noticeable decrease in q . Both of these effects are presented in figure 4.6.

So, according to equation 4–1, by decreasing ΔT_t , q decreases when h_{ave} is almost constant, which will result in almost constant pattern in the graph of ϕ too. Although in the earlier stages, in experiments with higher T_w the number of small nucleation sites with huge capacity of h_{ave} are lower than experiments with colder substrate, after a while the rate of adsorption and coalescence are the same for all T_w , which will result in the same ϕ between all the substrates. In figure 4.7, the changes in ϕ at different T_w is illustrated. As was said before, at the beginning small percentage of area is covered by liquid droplets

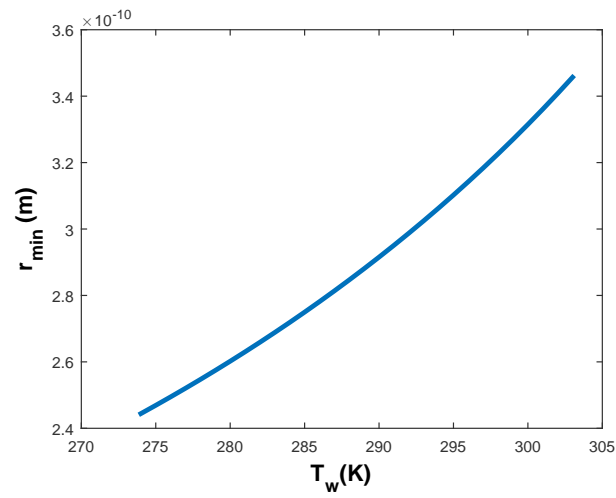


Figure 4.5: Minimum size of droplets that are able to grow v.s wall temperature

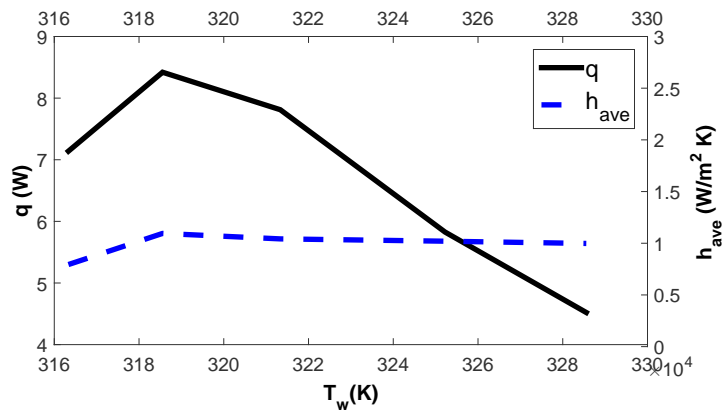


Figure 4.6: Evolution of average heat transfer coefficient and total heat flux v.s wall temperature

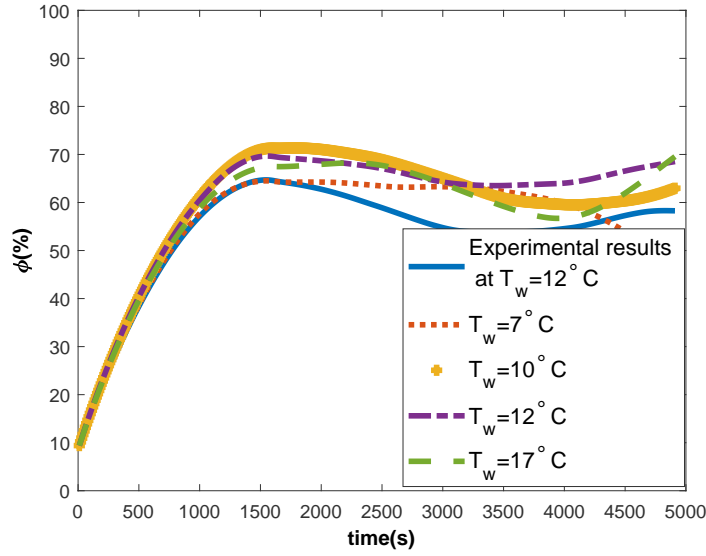


Figure 4.7: Percentage of surface coverage at different times.

but after a while coalescing drops start to cover substrate surface very rapidly. Continuing the process when coalescing drops become bigger, free area appears around them, which reduces the rate of coalescence but is potential to grow new small droplets. After this step, the fraction of area covered by water reaches it's stable value. These results are supported by experiments as is shown in figure 4.7. At first the initial droplets cover just around 2% of the substrate but after steady state ϕ reaches to near 70% for all T_w .

As was mentioned before, the main goal of this study is to increase illumination efficiency in car light shield by changing small dispersed droplets into big uniform ones and even into a film of liquid. The graphs presented up to here indicate that by changing in T_w , ϕ does not change very significantly. The next parameter that is going to be discussed is N_D .

4.2.4 Effect of initial nucleation site density

In this section the results of simulation were examined for four different droplets densities around the experimental value 4.9×10^7 , 9.7×10^7 , 1.29×10^8 , $2.4 \times 10^8 m^{-2}$ in order to investigate the effect of this parameter on the regime change from dropwise to filmwise condensation.

Generally, when the process starts with denser substrate the rate of coalescence at first is higher, while the rate of adsorption is not different from substrates with lower densities. Droplets in denser substrate are closer together and can coalesce faster but after a while a vacant area appears around each droplet due to coalescence. In this free area new small droplets will nucleate rapidly, that will lower the mean radius and increase nucleation density. This effect is indicated in figure 4.8 (a) and (b). According to these two plots, in all of the numerical simulations the initial size of droplets are the same. But after a while, the surfaces with higher value of N_D are covered by smaller droplets at each step.

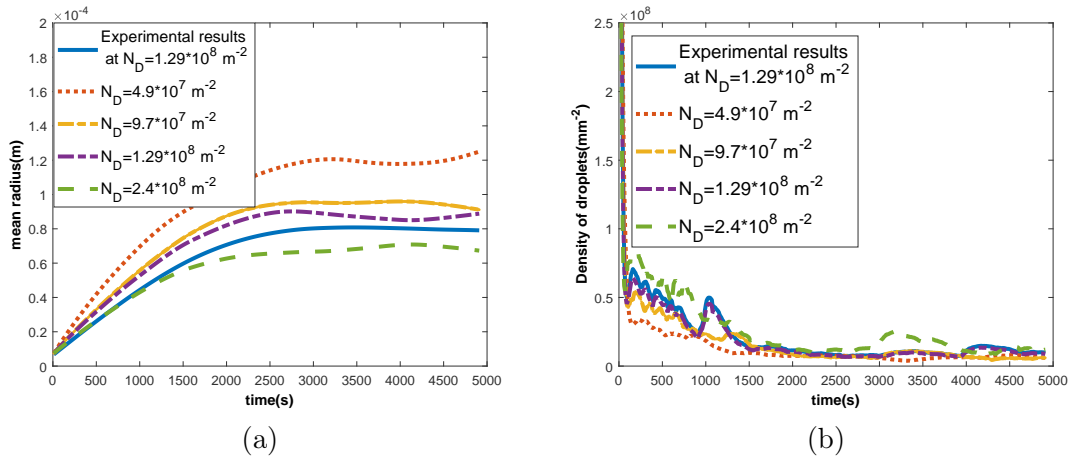


Figure 4.8: (a) Droplets size and (b) droplets densities during progress time for different initial nucleation site densities

Also, the density of the droplets on the surfaces with higher N_D are higher with respect to the surfaces with smaller N_D . In the process with more initial droplets, the rate of coalescence and production of free area is higher, that will lead to lower ϕ at later stages. If one does not consider the effect of nucleation of new small droplets at each step, both of these graphs will show opposite results.

According to figure 4.9, although the amount of droplets at the beginning is different, at steady state the percentage of surface covered with water droplets is around 20% lower for substrate with $N_D = 2.4 \times 10^8 \text{ m}^{-2}$ than substrate with $N_D = 4.9 \times 10^7 \text{ m}^{-2}$. This difference also can give us the clue to study the droplets positioning on the surface besides N_D . Meaning that it is possible to increase ϕ by manipulating the position of droplets on the surface as well as their number. The arrangement of droplets on the surface will be studied by changing surface topography in the next step of our investigation.

4.2.5 Drop-size distribution function

Another interesting parameter in studying dropwise condensation is the drop-size distribution function that pretenses the number of droplets at each size range per unit area. In section 3.2.6, the model of Abu-Orabi for the drop-size distribution function of adsorbing droplets was modified in two points of view:

- the surface area was corrected based on the surface area used by Rose [13] for coalescing droplets,
- and the periodic surface renewal was neglected. Because surface renewal happens after coalescence when there are very big droplets that can not resist the force of gravity.

Therefore, the model developed in equation (3–39) can represent the size distribution function for adsorbing droplets at earlier stages of dropwise condensation when there is

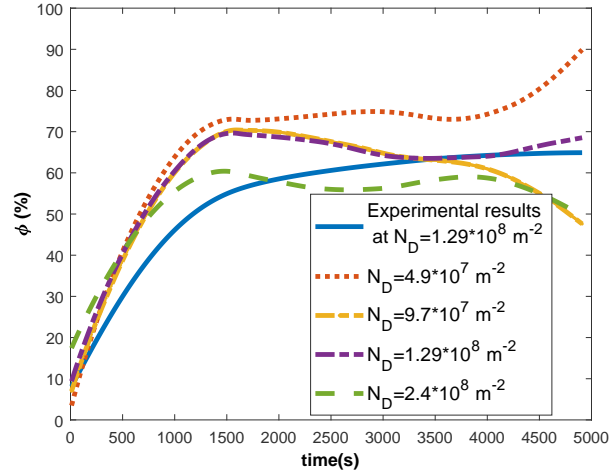


Figure 4.9: Surface coverage for different nucleation site densities v.s time

not yet any sliding droplet. For the sake of the simplicity in presenting the results, we will call this model as empirical model.

Since the most well-known model for drop-size distribution function in the literature is the model of Rose (that was developed originally for coalescing drops), here we are going to compare our experimental results with three models:

- the model of Rose (equation (3–31)) [13] for coalescing droplets,
- the model of Abu-Orabi [47] for adsorbing droplets at latest stages,
- the empirical model (equation (3–38)) for adsorbing droplets at earlier stages,

In order to compare the results of the three models with experimental data, six different time steps ($t = 10, 30, 50, 100, 300, 500$ s) are chosen. At the first three time steps the main growth rate is due to adsorption, while the last three time steps the main procedure is the coalescence. This might be taken into account here that due to the resolution of the CCD camera we are able to see the droplets bigger than around $5\mu\text{m}$, while the size of the adsorbing droplets is between $0.001 - 10\mu\text{m}$. So, we do not have the images of the very small adsorbing droplets and at all the time steps mentioned above there are also some coalescing drops.

In figures 4.10 and 4.11 the images of the real droplets at adsorption and coalescence phase as well as their corresponding size distribution functions are presented. In these graphs the black points represent the experimental data, solid blue line indicates the model of Abu-Orabi, the green stars belong to the model of Rose and the red dashed line shows the empirical model. In order to better visualization, the graphs are presented in the logarithmic scale.

These figures show that Rose model is able to describe the size distribution of coalescing droplets very well, but for small droplets the empirical model gives better answers. r_c in these graphs comes from equation (3–28) and defines the limit between small and big

droplets. Here r_c is around $12\mu m$. The model of Rose is known to have precise answers for droplets in the range $10 - 100\mu m$ and this is what can be clearly seen in figures 4.10 and 4.11. For droplets smaller than $10\mu m$ the predictions of Rose model are about ten times smaller than the real values. In contrast, the empirical model fits the size distribution of small droplets very well, but it shows deviations for big droplets.

The deviation of the model of Abu-Orabi from the experimental data is because that here we do not consider the effect of surface renewal. In fact, these graphs represent the time steps before sliding the first big droplet. Moreover, in the model of Abu-Orabi f is the number of droplets at specified size ranges per unit area of substrate, while in the model of Rose F is the number of droplets of each generation per unit area of generation. Since we used the model of Rose as the boundary condition at $r = r_c$, we have to consider this difference. Without modifying the unit area, the empirical model and the model of Abu-Orabi give the same answers in the absence of surface renewal.

As is expected, comparing the two figures 4.10 and 4.11 shows that when the majority of droplets are bigger than r_c , the model of rose is able to describe the size distribution very well. But still for small droplets nucleating at the area between the big droplets, empirical model is an acceptable model.

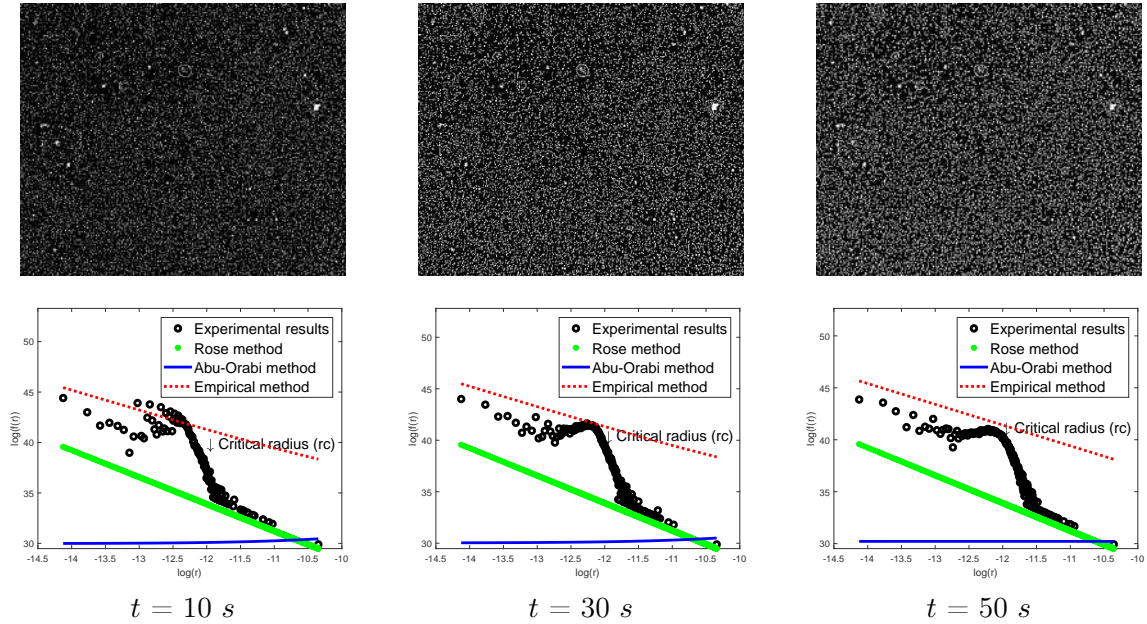


Figure 4.10: The results of the three models (Rose, Abu-Orabi and empirical models) versus experimental data at different time intervals of adsorption step ($t = 10, 30, 50\text{ s}$). The empirical and the Rose models are able to predict the size distribution function of adsorbing and coalescing droplets respectively, while the model of Abu-Orabi is far from the experimental data at earlier stages.

Figures 4.12 and 4.13 show the size distribution functions calculated based on the simulation data started with four different initial nucleation densities ($N_D = 4.97 \times 10^7, 9.7 \times 10^7, 1.29 \times 10^8, 2.4 \times 10^8 m^{-2}$) and four substrate temperatures ($T_w = 7, 10, 12, 17^\circ C$), re-

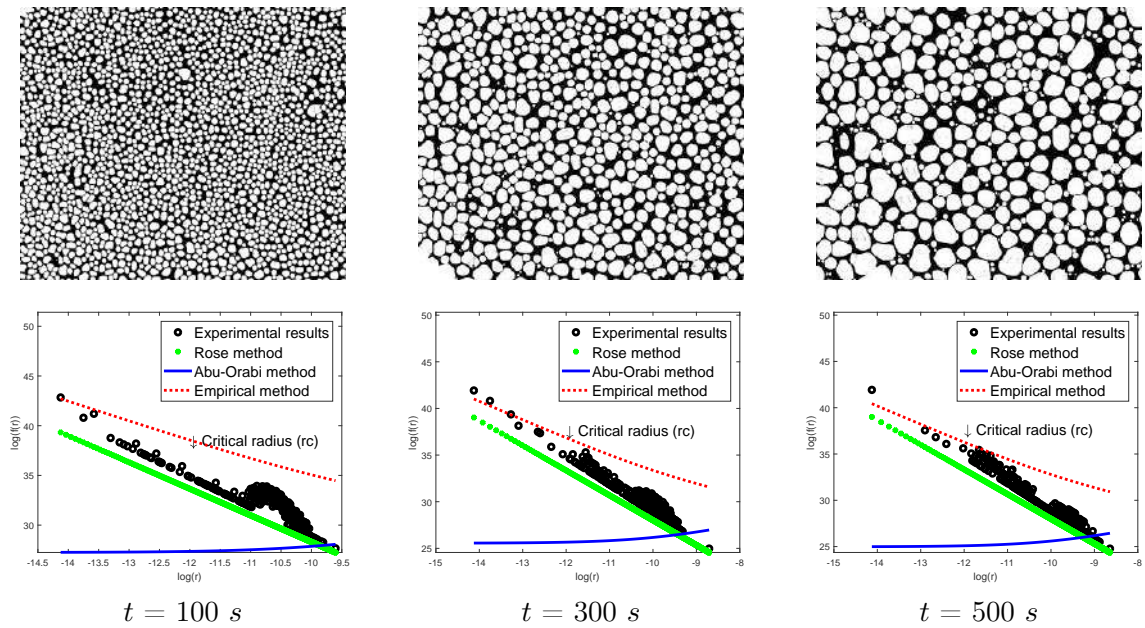


Figure 4.11: The results of the three models (Rose, Abu-Orabi and empirical models) versus experimental data at different time intervals of adsorption step ($t = 100, 300, 500$ s). The empirical and the Rose models are able to predict the size distribution function of adsorbing and coalescing droplets respectively, while the model of Abu-Orabi is far from the experimental data at earlier stages.

spectively. The aim of these graphs is to show if the empirical model describes the size distribution function of small droplets under different conditions.

The same patterns as in the figures 4.10 and 4.11 can be seen here. The size distribution is between two extreme limits calculated by the empirical and Rose models. At first that the majority of droplets are growing by adsorption, the size distribution function lies on the line of empirical model. Then by appearing coalescence the size distribution function changes slightly towards the line of the Rose model. This pattern is the same under the four different initial nucleation densities and four substrate temperatures.

This section was dedicated to the results of the empirical model developed in section 3.2.6 to describe the size distribution function of small droplets at earlier stages were presented. This model is developed by applying the modifications for surface area to the model of Abu-Orabi and by neglecting the surface renewal term. According to the graphs presented in this section, this modified model presents acceptable results for both experimental and simulation droplets. Also the model was successfully examined at four different initial nucleation densities as well as four different substrate temperatures. As was mentioned above, the most important error in this study comes from the resolution of the camera. We are able to visualize the droplets as small as $5 \times \mu m$, while according to equation (3-1) the size of smallest droplets is around $0.001 \mu m$. This will limit our model for studying density function of very small droplets. On the other hand, the method of image processing eliminates some droplets even with considerable sizes from binarized

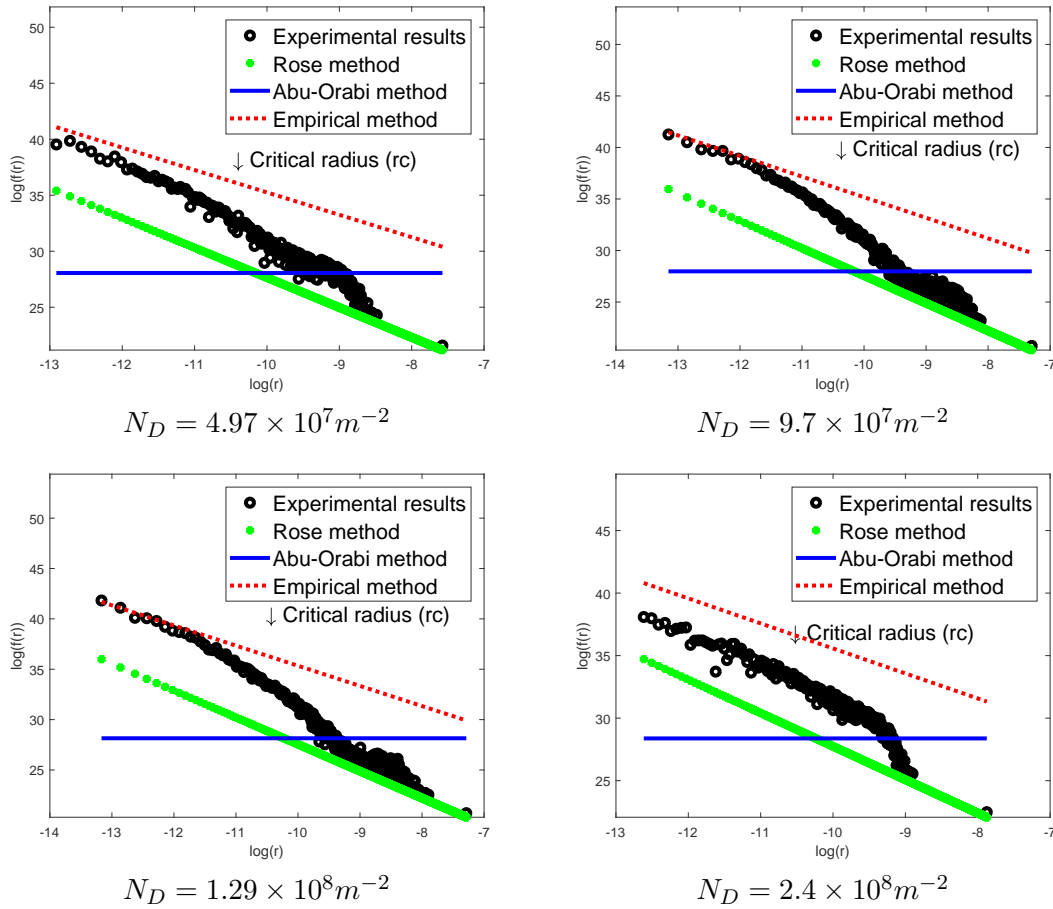


Figure 4.12: The results of the three models (Rose, Abu-Orabi and empirical models) versus simulation data at $t = 10s$ for 4 different initial nucleation densities.

images that will lead to error in analyzing the size and density function. But since these kind of droplets will appear at the following images, we can neglect this error.

4.3 Results of the ellipsoidal model on pillared substrates

In this section we will discuss the results of the second model that is applied on the pillared substrates. This is because firstly, as was illustrated in figure 3.1, the droplets tend to form more elliptical shape than circular on the textured substrates and secondly the contact angle of water droplets in the pillared patterns is close to 90° . So, the model that was developed in section 3.3 is used to study droplets behavior on pillared substrates.

The gray scale images of all six substrates at $t = 1800s$ are presented in figure 4.14. Comparison between these images and data from table 1.1 reveals that when the pillars are smaller, the final droplets are bigger and their shape is fairly far from being circular. This is because on the surfaces with smaller pillars, the droplets that are growing on the top of a specified pillar, reach the size of the pillar in earlier stages. So, they can cover

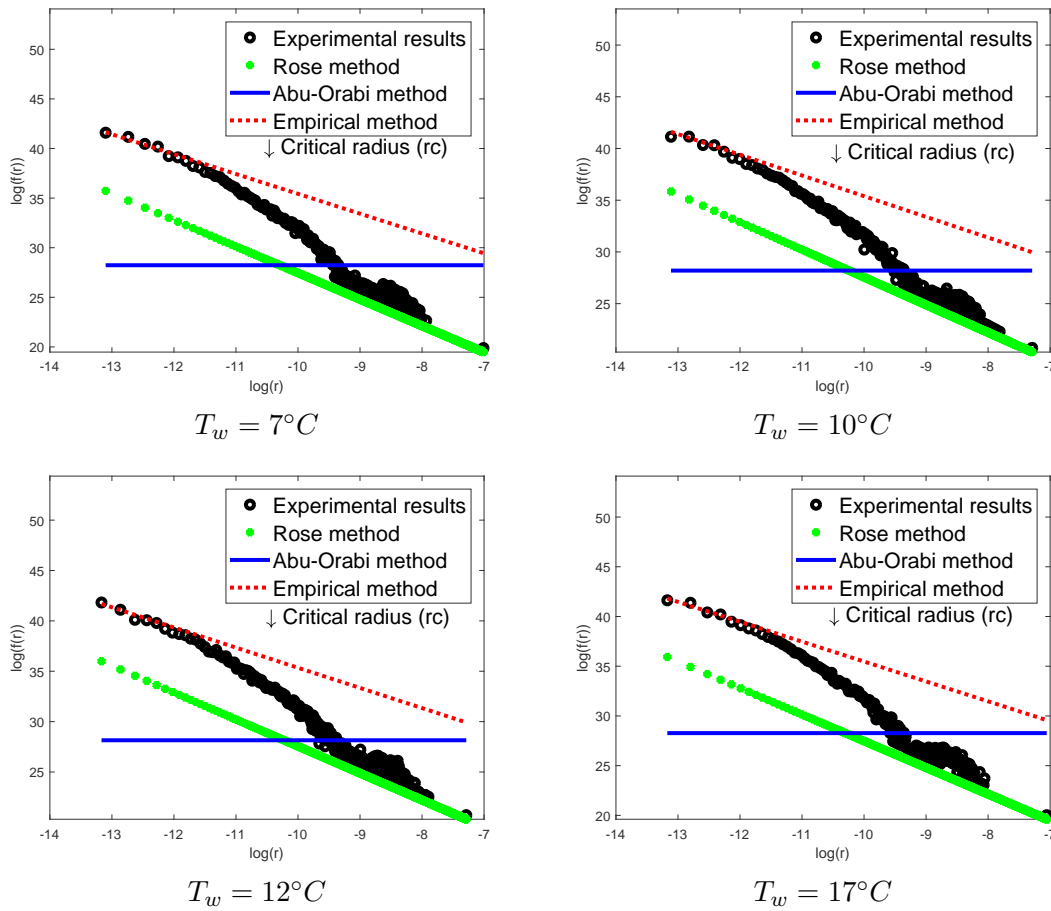


Figure 4.13: The results of the three models (Rose, Abu-Orabi and empirical models) versus simulation data at $t = 10s$ for 4 different substrate temperature.

the pillar sooner and can join the other droplets that were positioned on the other pillars. Consequently, the droplets can cover several pillars sooner and form a huge area covered by liquid. While, when pillars are bigger, it takes quite long time for droplets to become big enough to slide from pillar and coalesce with other droplets. By comparing the water droplets on surfaces of configurations 1 and 2 with the surfaces of configurations 3 and 4, one can conclude that when more percentage of substrate is occupied by pillars, the resulting droplets are smaller and consequently more circular. Also in substrates with configurations 3, 4, 5, and 6 that the height of pillars are $10\mu m$, the droplets are less dispersed and are mostly connected between two pillars, while in the first 2 surfaces that the height of pillars is $3\mu m$ the droplets lie on the area of several droplets.

Figures 4.15 and 4.16 show the comparison between growth rate and changes in droplets density predicted by the proposed model and real droplets on the six different configurations of pillars. All these graphs show that the ellipsoidal-droplet model can predict real droplets behavior on the pillared surface very well. At first, in all the surfaces very small droplets start to nucleate between and on the top of the pillars. Since the radius

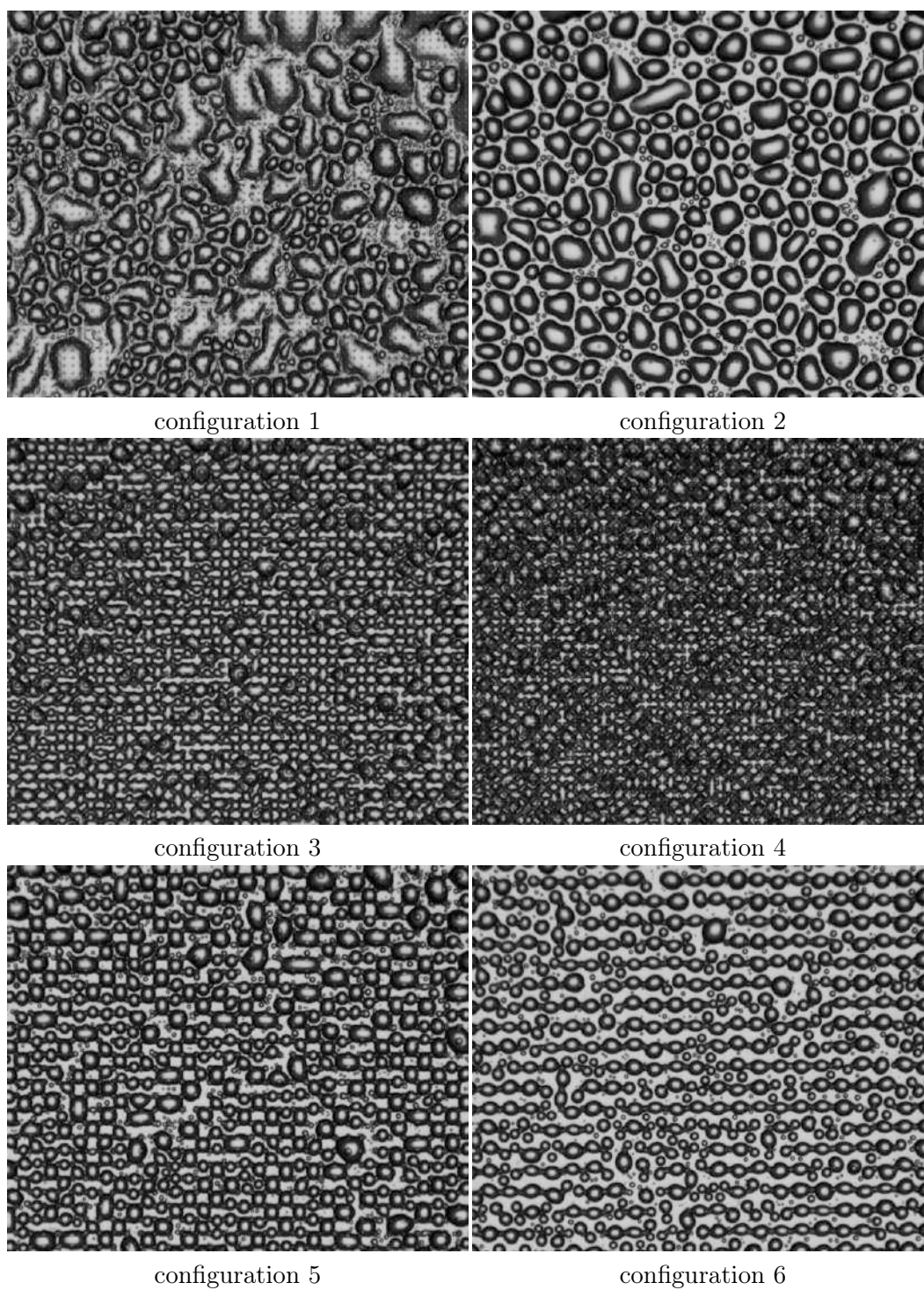


Figure 4.14: Illustration of 6 pillared surfaces after 1800s. The size of the substrate at each image is $3.3\text{mm} \times 2.7\text{mm}$.

of the pillars are fairly bigger than the radius of the initial droplets, we can assume that there is not considerably preference on top of the pillars for growing very small droplets. According to these graphs, surface with configuration 1, 3, 4, and 6 that introduce more surface area, are more potential to nucleate initial droplets.

The same pattern in all the surfaces can be considered after this step: all the droplets grow by adsorbing water molecules, if they touch they will coalesce and form bigger droplets and introduce more bare area to nucleate new small droplets. As was expected, the first two surfaces that have pillars with smaller radius, grow bigger droplets, but reached the steady state situation later.

The mean and standard deviation of errors of the proposed model for different configurations of pillars are presented in table 4.1. In this table mean relative error is calculated as:

$$e = 100 \times \frac{F_{experimental} - F_{model}}{F_{experimental}}, \quad (4-2)$$

where $F_{experimental}$ is the amount of value calculated based on gray scale images of real droplets and F_{model} is the amount predicted by the simulation model. According to this table, the mean relative error for density of droplets on all of the substrates is $10.00\% \pm 0.68\%$, while the model is more accurate for predicting droplets radius with mean relative error of $2.28\% \pm 0.42\%$. The error in this model can come from different sources:

- Firstly, the assumption of the ellipsoidal droplets is not very accurate although it is more precise than the spherical droplets. For example, according to table 4.1 the highest error for nucleation density is reported for surface configuration 1, and taking a look at figure 4.14 reveals that the droplets on this surface have more irregular shapes than the other surfaces.
- Secondly, the assumption of analogy between ellipsoidal droplets and spherical droplets in calculating the rate of growth due to coalescence, can be another source of error of the model.
- Thirdly, the difference between r_t , H_t , and D_t between simulated and real pillars can affect the results also.
- Fourthly, this model does not consider the effect of water contact angle on the surface.

But, the highest inaccuracy comes from the method of image processing. As was mentioned before, the data related to the size and density of real droplets are extracted from the gray scale images. On the gray scale images taken from the real droplets, the droplets have the same appearance as the pillars specially when they are in the same size ranges. Both of them are circles with bright centers and dark borders. Moreover, in the later stages the droplets are connected and it is difficult to count their exact number. The image processing method that is explained in chapter 2 is able to recognize these droplets from the pillars and also is able to separate connected droplets, but we assume that the relatively high error for density of droplets comes mostly from this problem. This can be claimed by comparing the data from table 4.1 and radius of bigger droplets from figure

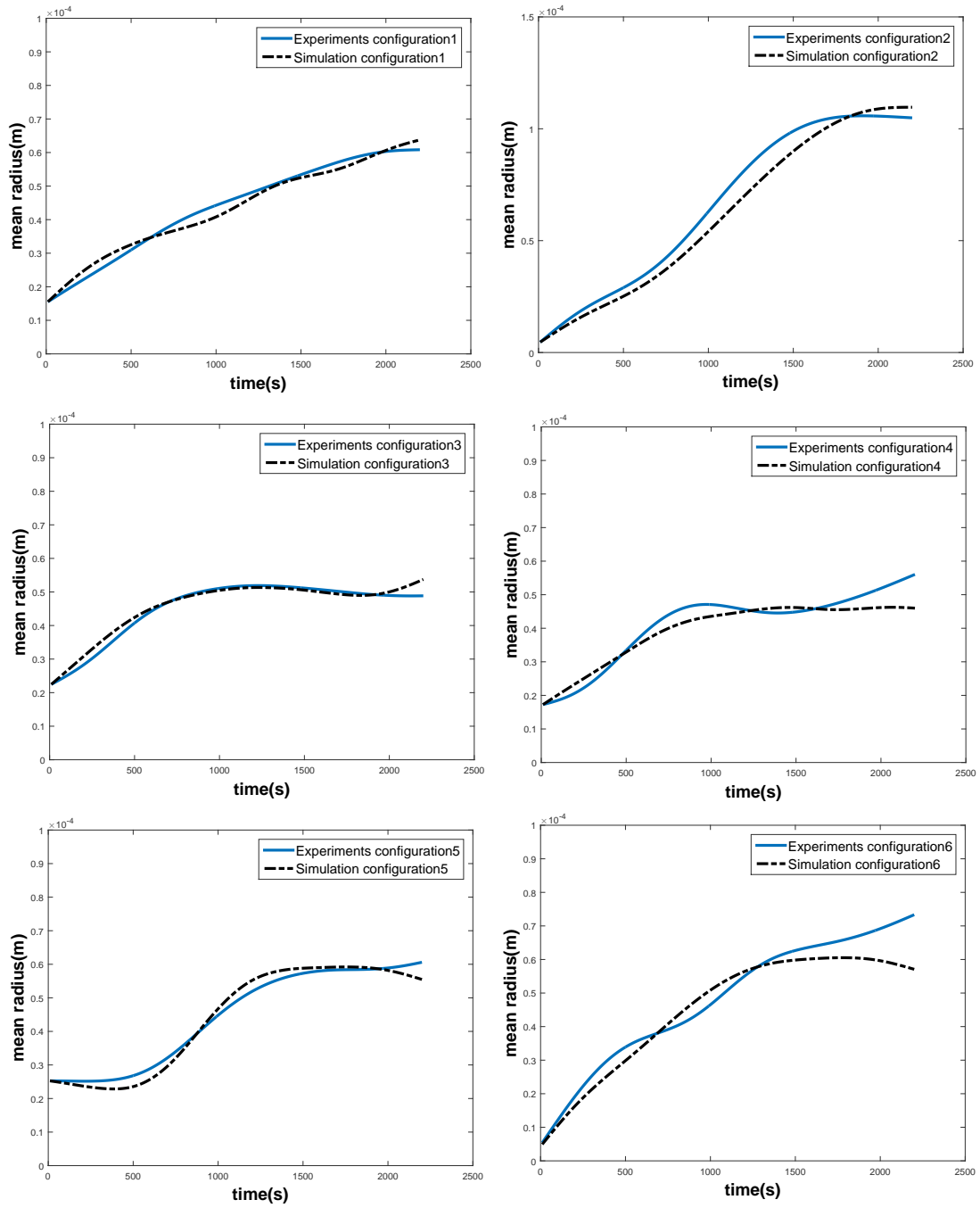


Figure 4.15: Comparison between growth rate of experimental and simulation droplets on 6 different pillared surfaces.

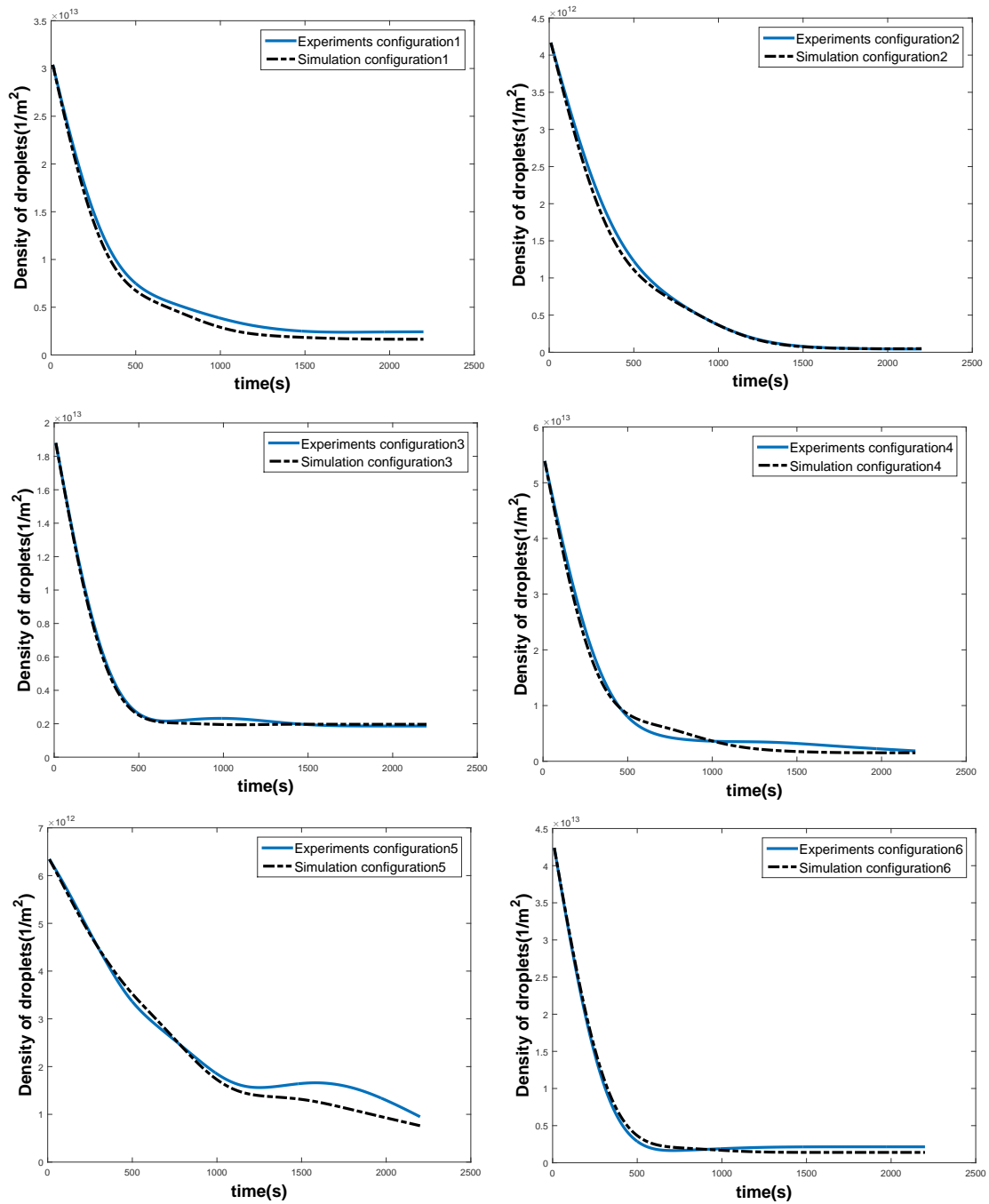


Figure 4.16: Comparing the changes in droplets density between experimental and simulation droplets on 6 different pillared surfaces.

configuration of pillars	Mean error of density (%)	Mean error of radius (%)
configuration 1	21.28	-0.62
configuration 2	3.55	9.26
configuration 3	3.01	-2.01
configuration 4	13.14	0.18
configuration 5	11.33	1.80
configuration 6	7.7	5.04
Mean	10.00 ± 0.68	2.28 ± 0.42

Table 4.1: The mean and standard deviation of errors of the model for different configurations of pillars.

4.14. Surfaces with configuration 1, 4 and 5 that represents higher percentage of error for droplets density, contain droplets with the size of twice the pillars, while for surface with configuration 2 that the mean error for droplets density is just 3% the droplets are about eight times greater than the pillars and are easily separable from pillars in image processing algorithm. But, this might not be neglected that all these sources of errors lead to an average of error of about 10% for droplets density and 2% for droplets size, so it can be claimed that the ellipsoidal model has a good approximation of the process of dropwise condensation on textured surfaces.

4.4 Results of the semi-ellipsoidal model on sinusoidal substrates

4.4.1 Droplets growth procedure

As was mentioned in section 4.3, ellipsoidal model gives better predictions for the droplets growing on the textured substrates. But in this method the effect of contact angle is neglected. Semi-ellipsoidal model takes into account both elliptical shape and contact angle effect. In the current section, the results of this model will be discussed.

Figures 4.17 to 4.19 illustrate the experimental droplets growing on 6 sinusoidal substrates at three stages: adsorption, coalescence, and steady state. The spatial distribution at these three series of images is not the same:

- adsorption stage: initial very small droplets that grow due to adsorption at earlier stages, are very smaller with respect to the surface texturing sizes. Therefore, the sinusoidal pattern can not affect adsorbing droplets spatial distribution and they are distributed completely randomly (figure 4.17).
- coalescence step: at this stage, the bigger droplets appear that are the result of merging smaller droplets. The coalescing drops are more or less at the same size of the sinusoidal canals, so they follow the sinusoidal pattern and are not randomly distributed anymore. Figure 4.18 shows that coalescing droplets obey the substrate pattern especially in the cases of smaller periods or bigger amplitudes of the sinusoidal canals.

Configuration of surface	Total surface area(m^2)	Initial droplets density (m^{-2})
30-5	$1.5304 * 10^{-5}$	$5.5 * 10^8$
30-10	$2.3158 * 10^{-5}$	$7.8 * 10^8$
60-5	$1.5030 * 10^{-5}$	$8.4 * 10^8$
60-10	$3.1233 * 10^{-5}$	$8.7 * 10^8$
100-5	$1.4870 * 10^{-5}$	$4.4 * 10^8$
100-10	$1.4713 * 10^{-5}$	$5.6 * 10^8$

Table 4.2: Comparison between total surface area and density of the initial droplets on 6 configurations of sinusoidal patterns.

- steady state: at the latest stages, the droplets become relatively bigger than the sinusoidal patterns and as a result, the texturing cannot affect anymore drops spatial distribution.

Figures 4.20 and 4.21 compare the changes in size and density of real droplets with the droplets that are simulated by the semi-ellipsoidal method presented in section 3.4 on 6 configurations of sinusoidal substrates. These two figures indicate acceptable accordance between the results of semi-ellipsoidal model and experimental data. The mean errors of the model, calculated based on equation (4-2), for droplets growth rate is about 2% and for droplets nucleation density about 30%.

Although on all of the substrates the size of initial droplets are the same, their density varies from one texturing pattern to another. This is because, each texturing pattern introduces different amount of bare area to nucleation of small droplets. In other words, since the total surface area of each substrate is different, the number of droplets that can nucleate on different substrates are not the same. Table 4.2 shows the area of sinusoidal substrates calculated by equation (3-111) and the initial nucleation density on each substrate. The values of total area calculated in this table depend on the period and amplitude of the sinusoidal patterns. It must be taken into account that, although the number of droplets on the patterns with more surface area is higher, this does not mean that the droplets density is higher also, because the density is defined as $\frac{\text{Number}}{\text{area}}$. Therefore, by increasing the denominator of a fraction, its' value decreases. So, increasing the surface area, increases the number of droplets present on the substrate, but this does not mean that density of droplets increases too.

As was explained before, the main goal of representing semi-ellipsoidal model was to describe droplets growth on textured substrates that are different from the ones growing on flat ones. Therefore in order to validate the application of this model, figures 4.22 and 4.23 compare the results of the semi-ellipsoidal model with the results of spherical-cap model that was presented in section 3.2. In these two figures the dot lines indicate spherical-cap model and the waves in the patterns of this model is due to sliding very big droplets and surface renewal.

As can be seen in figure 4.22 the changes in droplets radius at earlier stages is more significant in spherical-cap model with respect to semi-ellipsoidal model and experimental results. This is because spherical-cap model considers the droplets as circles on the $X - Y$ plane, which have the same growth rate along the directions X and Y . In other words, spherical-cap droplets grow freely on the $X - Y$ plane and their rate of growth is limited

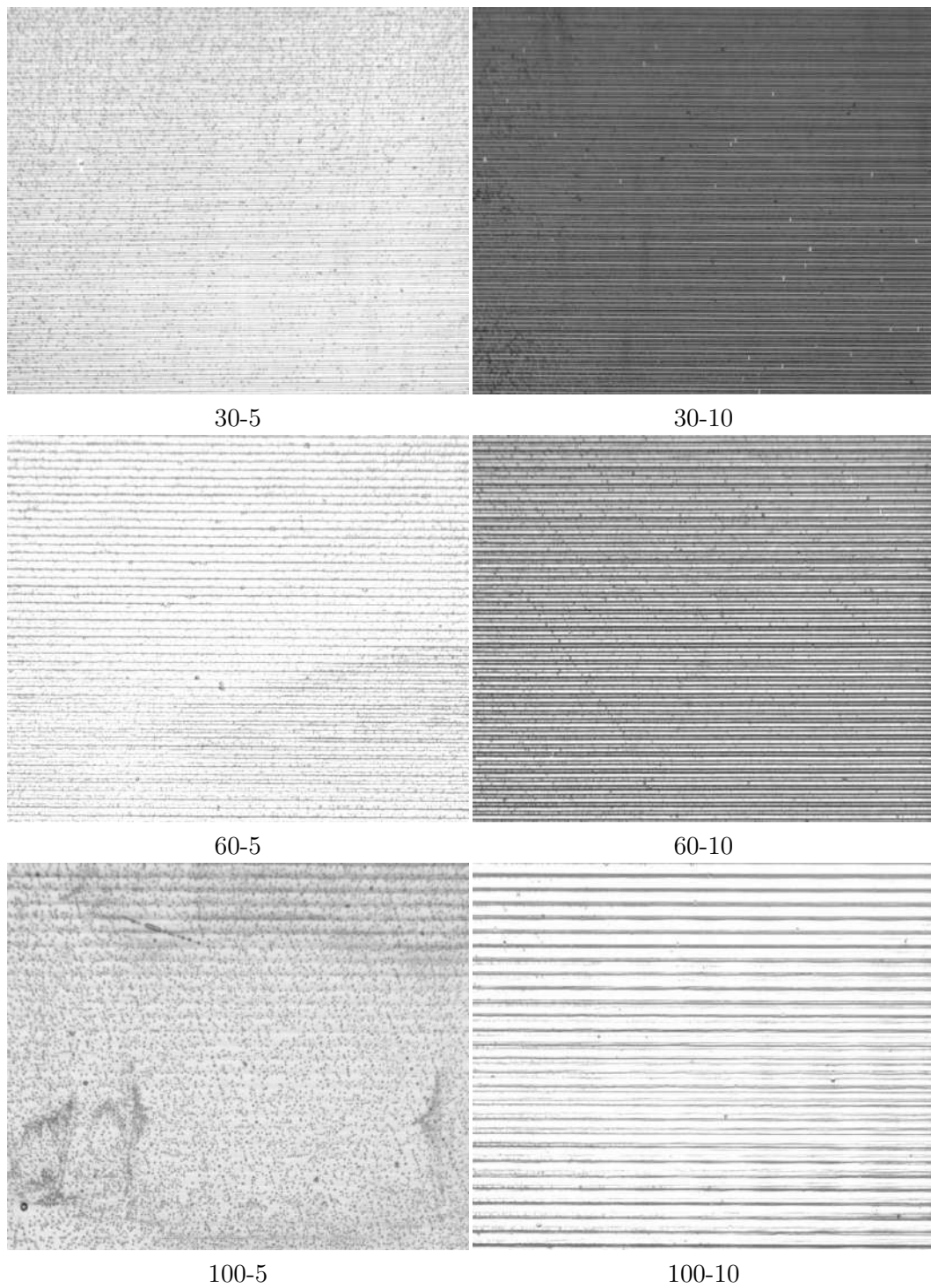


Figure 4.17: Illustration of 6 sinusoidal surfaces at adsorption stage (around $t = 10s$).

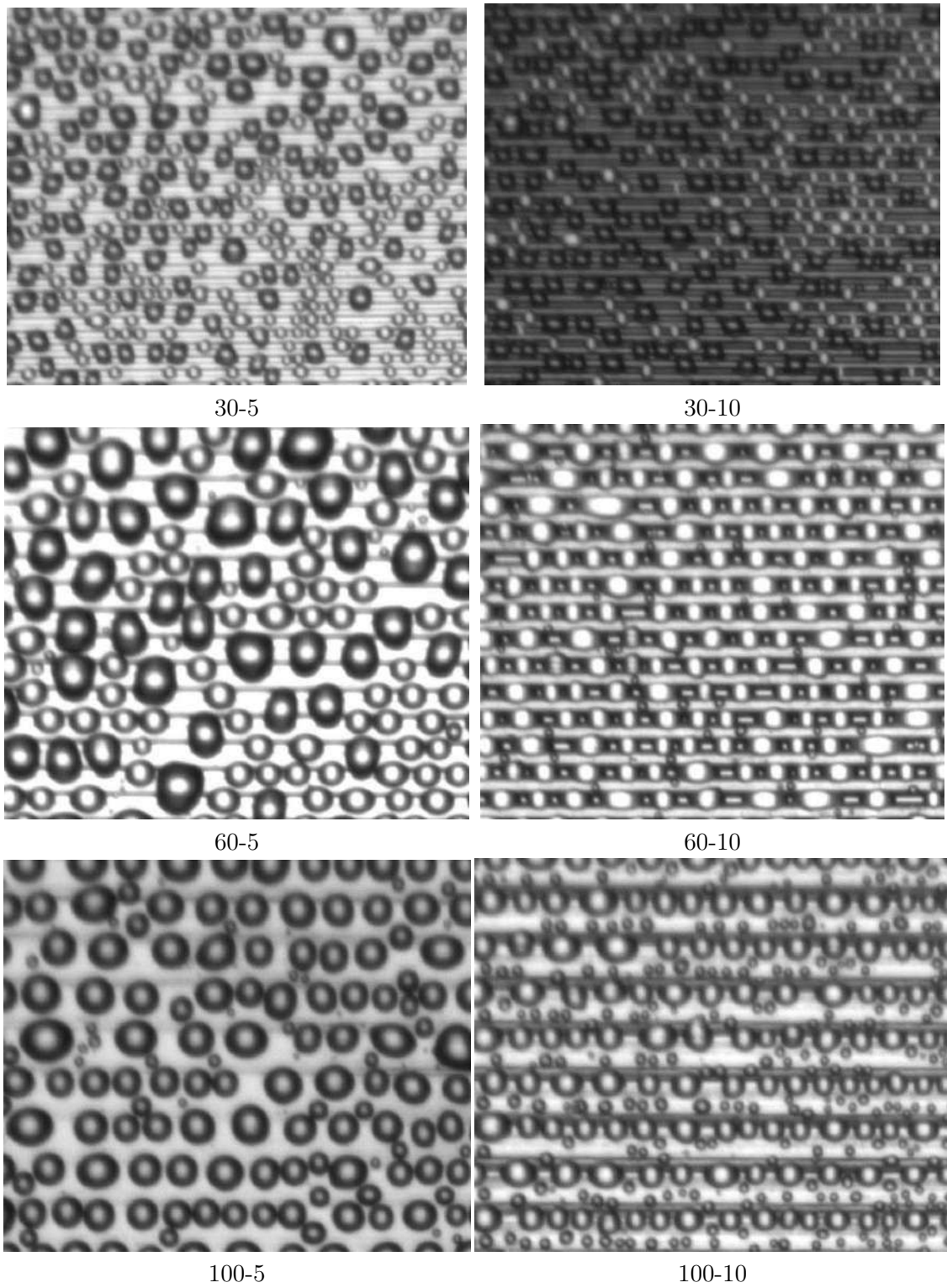


Figure 4.18: Illustration of 6 sinusoidal surfaces at coalescence stage (around $t = 1800s$).

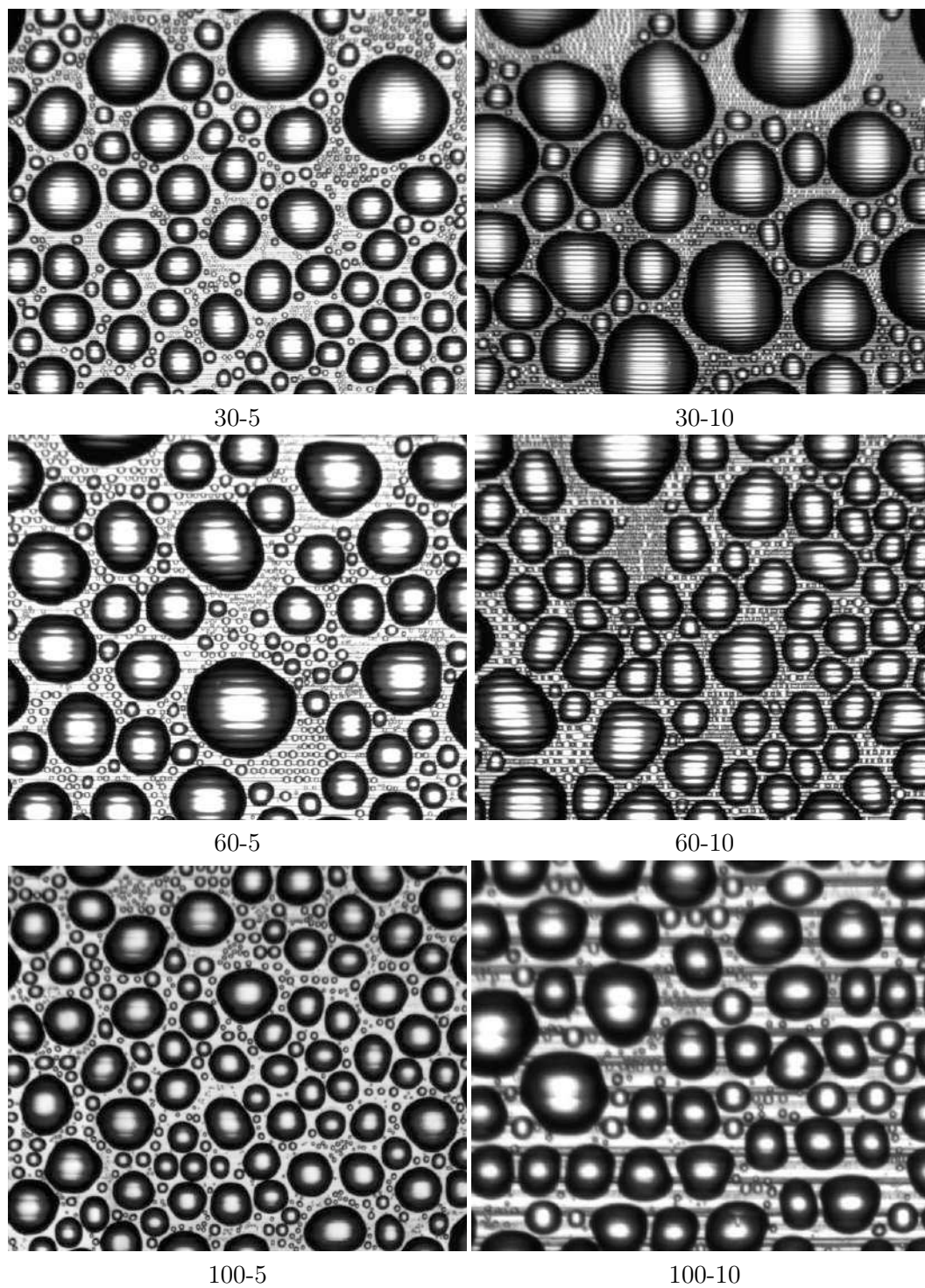


Figure 4.19: Illustration of 6 sinusoidal surfaces at steady state (around $t = 8000s$).

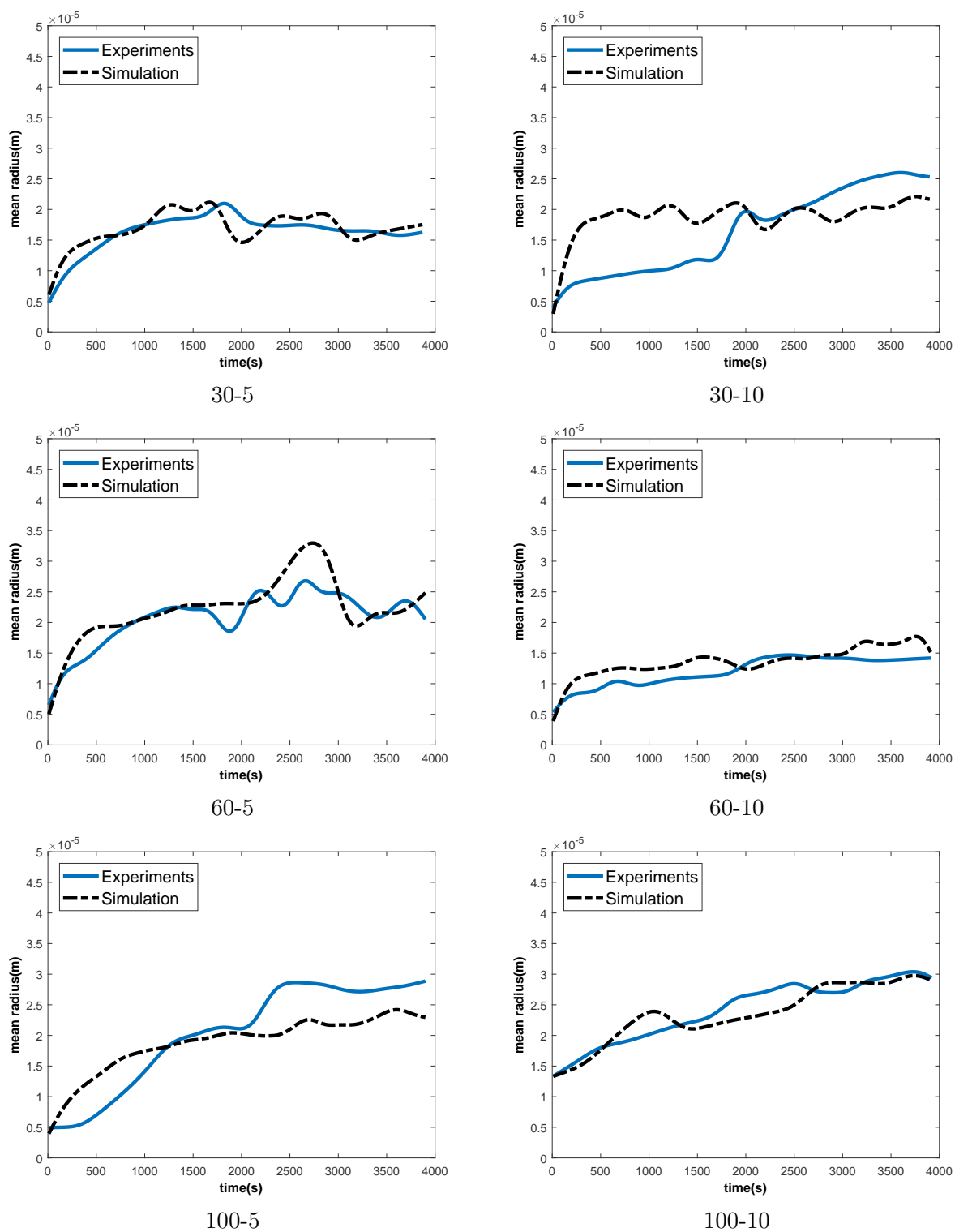


Figure 4.20: Comparison between growth rate of experimental and simulation droplets on 6 different sinusoidal surfaces

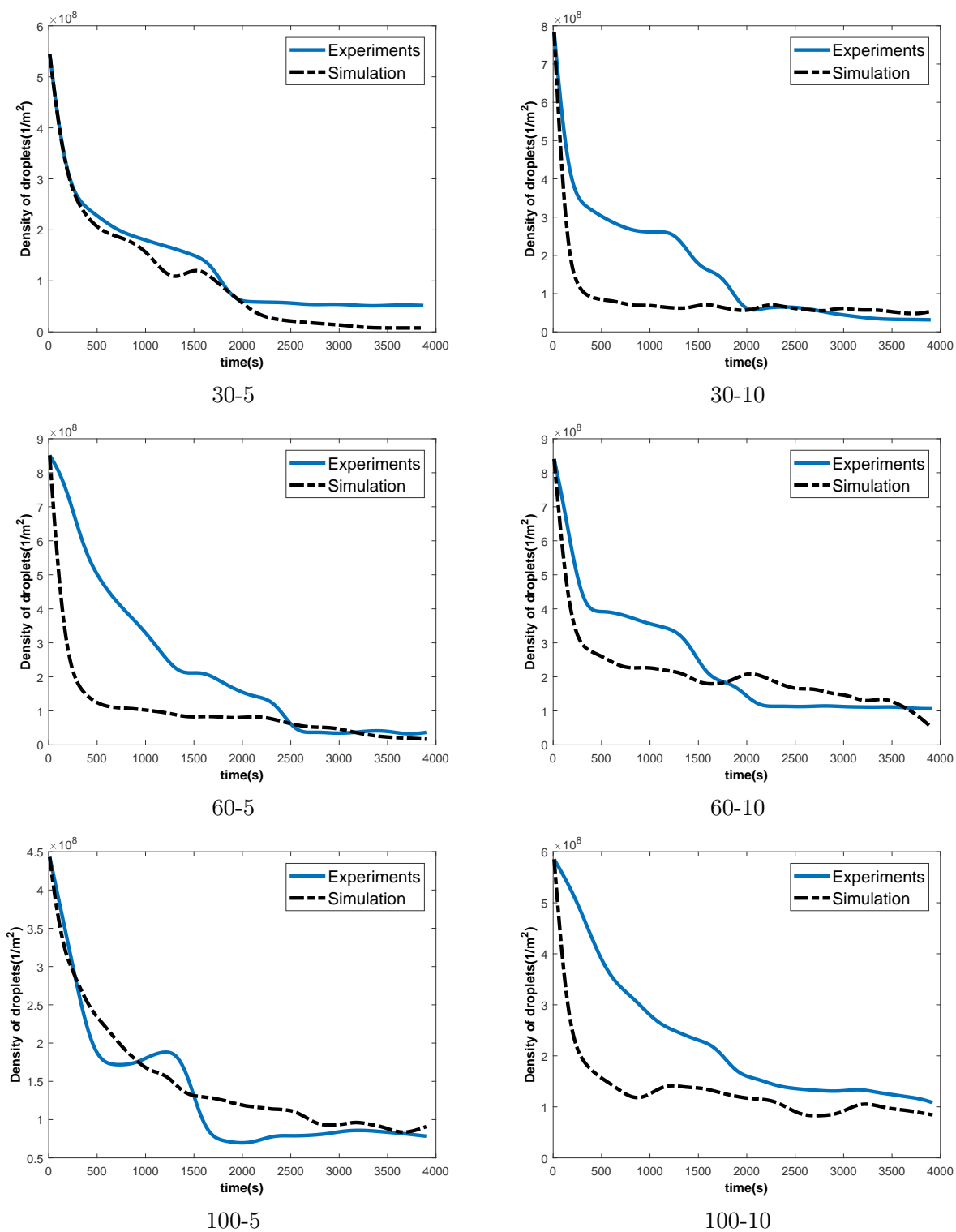


Figure 4.21: Comparison between density of experimental and simulation droplets on 6 different sinusoidal surfaces

neither by direction nor by substrate pattern. In contrast, the semi-ellipsoidal droplets model is able to show the limitation in the growth rate along Y direction that is due to sinusoidal patterns on substrate.

The difference in the growth rate of spherical-cap and semi-ellipsoidal droplets at earlier stage will change the growth rate at later stages also. This is because when the earlier droplets are bigger, coalescence starts sooner and as a result bigger droplets can be formed on the substrate. On the other hand, when two droplets coalesce, although their total volume does not change, their occupied area reduces and some vacant area forms in their vicinity on which new small droplets can nucleate. This phenomenon will result in reducing average radius of droplets, but increasing in droplets density.

The effective parameter on the drops growth rate after coalescence is the total surface area, that can provide more vacancies for nucleation of new droplets. As was explained sooner, when there are more vacant area on the substrate, more small droplets can nucleate at each iteration. Therefore, for example, on the substrate of configuration 30-10 that introduces the highest value for the total surface area reported in table 1.2, the average size of droplets predicted by spherical-cap model is less than semi-ellipsoidal model. Meaning that, the spherical-cap model generates bigger droplets than semi-ellipsoidal model, so coalescence occurs sooner and more vacant area are produced at each iteration. Moreover there is enough vacant area on the substrate for nucleation new small droplets. Therefore, at each step higher number of smaller droplets is predicted by the spherical-cap model that increases droplets density, but reduces the average radius.

The same procedure happens on the substrates configuration 30-5, 60-5, 60-10, 100-5, and 100-10. But, here the total surface areas are not big enough to produce desirable amount of small droplets at each iteration. So, big droplets produced by spherical-cap model occupy the whole surface and slide rapidly. Therefore, bigger droplets sizes are predicted by spherical-cap model and also sliding procedure can be seen in both of the graphs.

4.4.2 Droplets spatial distribution

Studying the droplets spatial distribution on the substrate can be a good way to control their growth rate because: firstly, the positioning of droplets with respect to each other has a direct impact on the coalescence process and secondly, by applying different texturing patterns, we are in fact changing drops spatial distribution. Therefore, in this section the effect of sinusoidal patterns on the droplets spatial distribution will be studied.

As was mentioned before, Fry plot is a useful tool to visualize anisotropy in the points spatial distribution. Fry plot shows the pairwise difference vectors between each two points and in the case of regular and isotropic distributions, a circular vacant area can be seen at the origin. In the case of Poisson point process no vacant area appears at the origin of Fry plot and in fact the Fry plot will be uniformly distributed [141]. If this vacant area illustrates the elliptical shape, this means that the points are clustered towards special direction and the spatial distribution is not isotropic anymore.

Figure 4.24 shows the Fry plot of 6 sinusoidal substrates during coalescing step at $t = 1800s$. This can be clearly seen in this figure that the pairwise distances between droplets are lined along some horizontal lines with distances more or less equal to the sinusoidal patterns periods. This observation confirms that coalescing droplets are distributed along

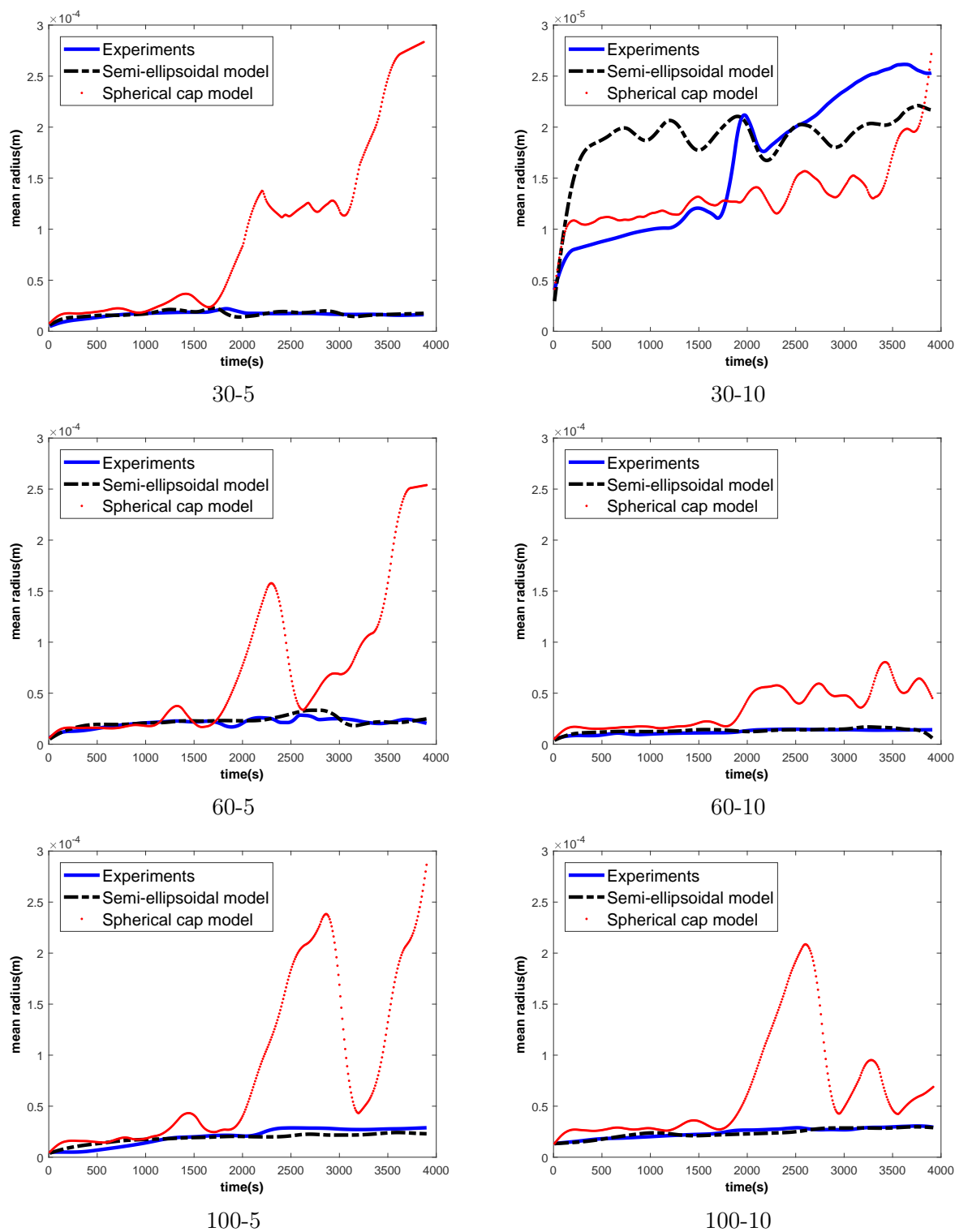


Figure 4.22: The evolution of droplets size measured by spherical-cap model and ellipsoidal cap model on 6 different sinusoidal surfaces compared to experimental results

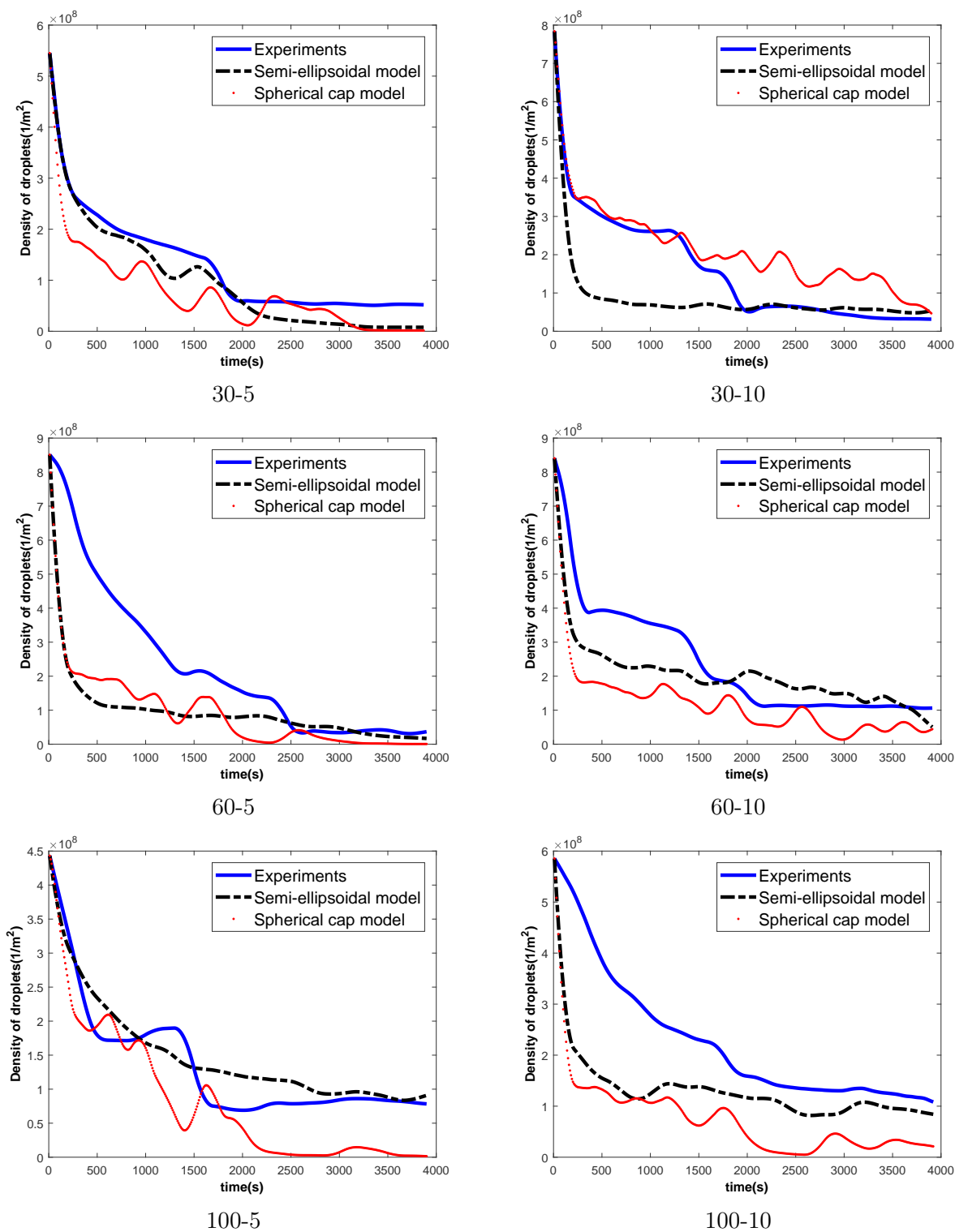


Figure 4.23: The evolution of droplets density measured by spherical-cap model and ellipsoidal cap model on 6 different sinusoidal surfaces compared to experimental results

the sinusoidal pattern (figure 4.24) and the distance between their center points along X axis is much less than along Y axis.

For better visualization the vacant zone around the origin these plots are zoomed out in figure 4.25. The minimum horizontal distance between each pair of droplets in these images is near $r_{ave} = 50\mu m$ that is two times bigger than the average radius of droplets at this stage $t = 1800s$. The minimum vertical distance must be around sinusoidal pattern period. This is why the orientation of elliptical vacant area at the origin of each plot is vertical for configurations 30-5, 30-10, 60-5, and 60-10 ($P < r_{ave}$) and horizontal for configurations 100-5 and 100-10 ($P > r_{ave}$). This is the concept of anisotropy that is imposed to droplets spatial distribution by making texturing patterns on the substrate. In the case of configuration 100-5, since the period of sinusoidal pattern is large, while its amplitude is small, it is closer to flat surface and the vacant zone at the origin of its Fry plot is closer to a circular pattern of isotropic distributions.

As was mentioned before, Ripley's K_{dir} function is an useful tool for studying spatial distribution of point over a surface or volume, when we assume the points are distributed anisotropic. Figure 4.26 shows the Ripley's K_{dir} function in a polar system as a function of r and θ . This function will show if the droplets are distributed uniformly or directionally-dependent. Meaning that, using Ripley's K_{dir} function allows to investigate if the droplets prefer to distribute in special directions or spots.

In all graphs correspond to all the 6 configurations, 4 peaks appear. This shows that the number of droplets in vicinity of each specified point is maximum on the horizontal line that passes from the point and two other through horizontal lines over and under the point. In other words, Ripley's K_{dir} function is maximum at $\theta = 0, \pi/2, \pi,$ and $3\pi/4$. This confirms the sinusoidal distribution of droplets that follow the sinusoidal pattern of the substrate.

4.5 Conclusion

4.5.1 English

In this chapter the results of the three numerical models for describing water droplets behavior on flat and textured substrates were discussed. A brief summery of what has been presented in this chapter is as below:

1. Results of the spherical-caps model:
 - Good agreement between model predictions and experimental data for the rate of growth and changes in droplets density.
 - Accordance between spatial distribution of simulated and real droplets.
 - Small droplets are distributed according to Poisson point process, while after adsorption the spatial distribution changes to Matern hard core II.
 - Substrate temperature T_w has no significant effect on the percentage of surface coverage ϕ , while by increasing the initial droplets density N_D , ϕ decreases. This is because of higher rate of coalescence and introducing more bare areas on the surface.

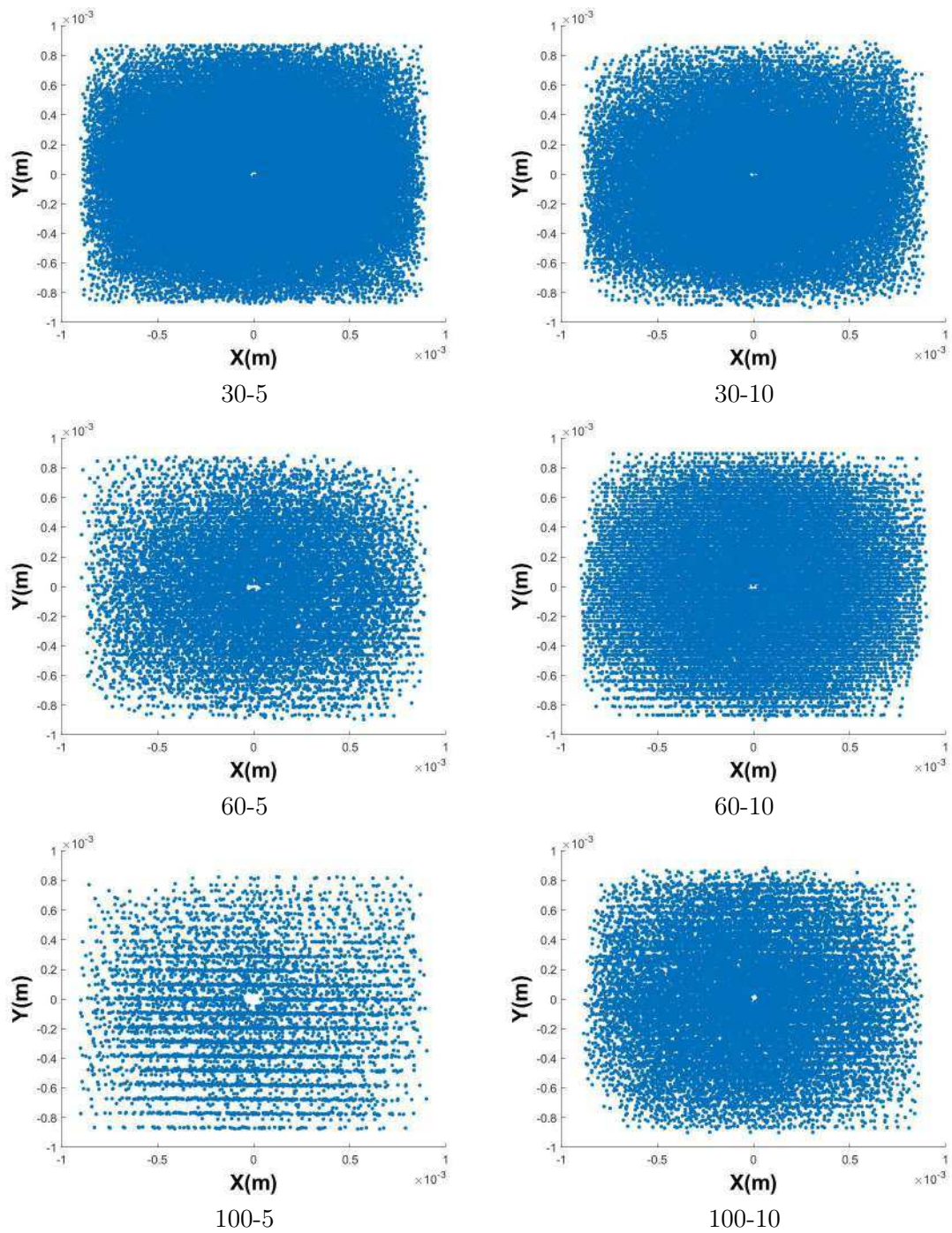


Figure 4.24: Fry plot of droplets spatial distribution on sinusoidal substrates at $t = 1800s$.

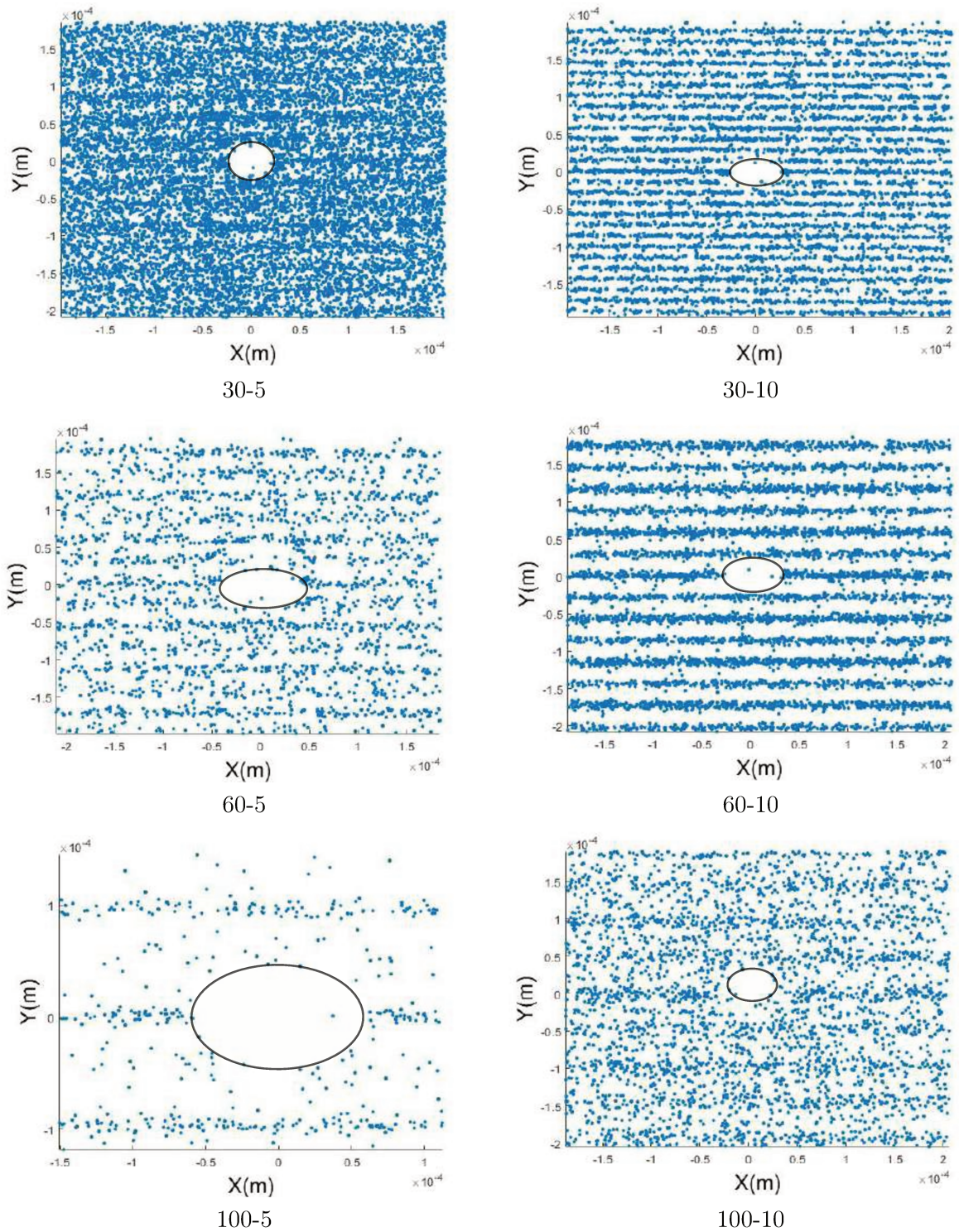


Figure 4.25: Zoomed on the origin of Fry plot of droplets spatial distribution on sinusoidal substrates.

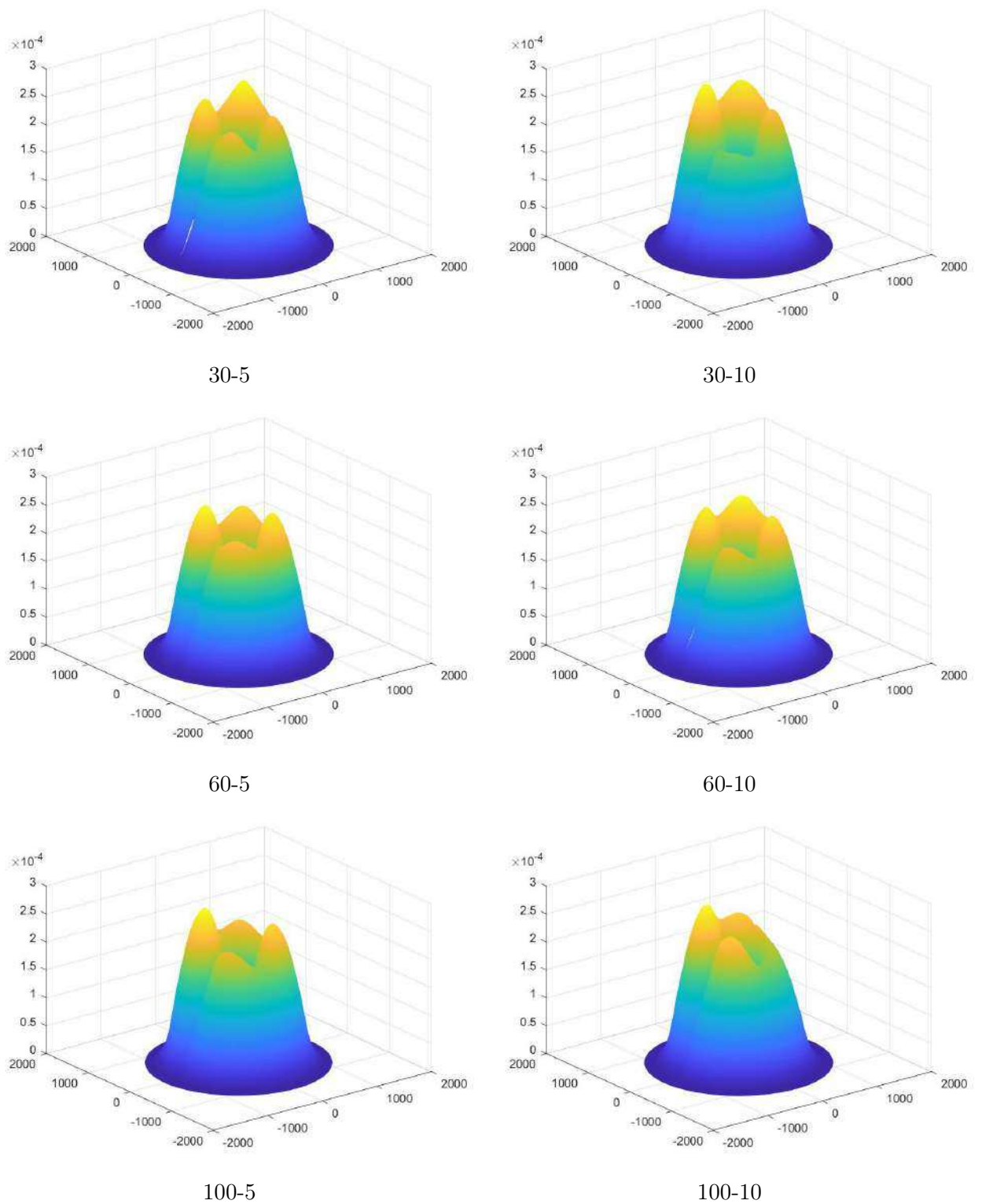


Figure 4.26: Ripley's K_{dir} function of droplets spatial distribution on sinusoidal substrates

- The empirical model for droplets size distribution function represents a good understanding of size distribution of adsorbing droplets. According to the graphs presented here, the size distribution function of droplets at earlier stages lies between the empirical model (for adsorbing droplets) and the model of Rose (for coalescing droplets).
- The behavior of the empirical model was examined at four different initial nucleation site densities and four substrate temperatures. All the presented graphs validate that the empirical model is able to describe the size distribution function of adsorbing droplets at earlier stages (before sliding the first droplet).

2. Results of the ellipsoidal model:

- The results of this model are compared with real data from 6 different configurations of pillars.
- The mean relative error of the model for droplets density is $10.00\% \pm 0.68\%$, while it proposes more accurate results for predicting droplets radius with the mean error of $2.28\% \pm 0.42\%$.
- The main source of error is recognized as the similarity between the droplets appearance and pillars on images taken from real droplets, which makes it difficult to identify the exact number of droplets.

3. Results of the semi-ellipsoidal model:

- The results of this model is compared with real data from 6 different sinusoidal patterns.
- More accurate results with respect to spherical-cap model on the textured substrates are obtained.
- The mean relative error of the model for droplets growth rate is about 2% and for droplets nucleation density about 30%.
- The vacant area at the origin of Fry plot of droplets distribution on the sinusoidal substrate is in the form of an ellipse that shows the directional anisotropy in droplets distribution.
- The minimum horizontal distance between each pair of droplets in Fry plot is near $r_{ave} = 50\mu m$ that is two times bigger that the average radius of droplets at this stage $t = 1800s$. The minimum vertical distance must be around sinusoidal pattern period.
- According to Ripley's K_{dir} function of droplets in 6 sinusoidal substrates, the coalescing drops obey the sinusoidal pattern, while very small droplets are distributed according to Poisson point process.

4.5.2 French

Dans ce chapitre, les résultats des trois modèles de simulation numérique pour décrire le comportement des gouttelettes d'eau ont été discutés. Les résultats sont les suivants:

1. Résultats du modèle de calottes sphériques :

- Bon accord entre les prédictions du modèle et les données expérimentales pour le taux de croissance et les changements dans la densité des gouttelettes.
- Conformité entre la distribution spatiale des gouttelettes simulées et réelles.
- Les petites gouttelettes sont distribuées selon le processus ponctuel de Poisson, tandis qu'après l'adsorption, la distribution spatiale change en Matern hardcore II.
- La température du substrat T_w n'a pas d'effet significatif sur le pourcentage de couverture de surface ϕ , alors qu'en augmentant la densité initiale des gouttelettes N_D , ϕ diminue. Ceci est dû au taux de coalescence plus élevé et à l'introduction de plus d'espaces vides sur la surface.
- Le modèle empirique de la fonction de distribution de la taille des gouttelettes présente une bonne compréhension de la distribution de taille des gouttelettes adsorbantes. Selon les graphiques présentés ici, la fonction de distribution de tailles des gouttelettes au début du processus se situe entre le modèle empirique (pour les gouttelettes de l'adsorption) et le modèle de Rose (pour les gouttelettes de coalescentes).
- Le comportement du modèle empirique a été examiné à quatre densités de nucléation initiales et à quatre températures de substrat. Tous les graphes présentés valident que le modèle empirique est capable de décrire la fonction de distribution de tailles des gouttelettes adsorbantes en début du processus (avant de faire glisser la première gouttelette).

2. Résultats du modèle ellipsoïdal :

- Les résultats de ce modèle sont comparés aux données réelles de 6 configurations différentes de piliers.
- L'erreur relative moyenne du modèle pour la densité des gouttelettes est $10.00\% \pm 0.68\%$, alors qu'elle propose des résultats plus précis pour prédire le rayon des gouttelettes avec l'erreur moyenne de $2.28\% \pm 0.42\%$.
- La principale source d'erreur est la similarité entre l'apparence des gouttelettes et les piliers sur les images prises à partir de vraies gouttelettes, ce qui rend difficile l'identification du nombre exact de gouttelettes.

3. Résultats du modèle semi-ellipsoïdal :

- Les résultats de ce modèle sont comparés aux données réelles de 6 modèles sinusoidaux différents.
- Les résultats sont plus précis en ce qui concerne le modèle à calotte sphérique sur les substrats texturés.
- L'erreur relative moyenne du modèle pour le taux de croissance des gouttelettes est d'environ 2% et pour la densité de nucléation des gouttelettes d'environ 30%.
- La zone vacante à l'origine de la distribution des diagrammes de Fry sur le substrat sinusoidal se présente sous la forme d'une ellipse qui montre l'anisotropie directionnelle dans la distribution des gouttelettes.

- La distance horizontale minimale entre chaque paire de gouttelettes dans le diagramme de Fry est proche de $r_{ave} = 50\mu m$ qui est deux fois plus grande que le rayon moyen des gouttelettes à ce stade $t = 1800s$. La distance verticale minimale doit être autour de la période du modèle sinusoïdal.
- Selon la fonction K_{dir} de Ripley des gouttelettes sur les 6 substrats sinusoïdaux, les gouttes coalescentes obéissent au motif sinusoïdal, alors que de très petites gouttelettes sont distribuées selon le processus ponctuel de Poisson.

General conclusion

An experimental and numerical study on the process of dropwise condensation on three kinds of substrates, flat, pillared and, sinusoidal has been conducted. The polycarbonate samples were textured by duplicating the metallic molds on which different texturing patterns were formed using laser technology. Interferometric microscope was used in order to study the two-dimensional roughness profiles of both metallic molds and polycarbonate substrates of the sinusoidal texturing patterns. The real images of both surfaces were taken by a scanning electron microscopy (SEM) system that shows the well textured substrates that are ready to be used in the process. Then, the wettability of the polycarbonate samples with sinusoidal patterns was measured, using a contact angle measurement system and the statistical study was performed for investigating the effect of period and amplitude of the sinusoidal patterns on the contact angle and average roughness. These statistical studies show that the effect of the amplitude of the sinusoidal profile is much more important than the effect of period on both of the parameters and by changing the sinusoidal amplitude even the contact angle as much as 140° is accessible.

In the next step, the polycarbonate samples were inserted on the condensation set-up. During the experiments, the temperature of the polycarbonate samples was reduced to near $17^\circ C$, that is lower than the dew point of the mixture of humid air that is in contact with the sample ($T = 30^\circ C, H = 40\%$). As a result, water droplets start to nucleate all around the samples and grow by adsorbing water molecules from humid air and by coalescence. A high resolution CCD camera records this process at time intervals of 1s. The gray scale images taken by this CCD camera were segmented in order to extract the information related to droplets radius, density and spatial distribution.

For the sake of image processing on the flat and sinusoidal substrates, a simple method consists of pre-treatment, segmentation and recognition was applied. But regarding the images of droplets on pillared substrates, the similarity between the droplets and pillars make the image processing more complicated. Therefore, a robust image processing algorithm has been developed for drop recognition on the pillared surfaces. This algorithm combines the geometrical, optical and topological information of the images to segment the droplets. It is capable of segmenting drops with a large range of radius. Indeed, by means of an histogram analysis, it estimates the drop size, divides the drops in four main size range and uses a corresponding algorithm adapted to each size range. A manual verification of drop detection ability of the present algorithm comparing to real images is conducted to verify the algorithm accuracy. The F -measure enables to quantify the accuracy of the detection that shows this algorithm has a high accuracy for drops with a radius over $50\mu m$.

Finally, three numerical models were developed to describe the droplets behavior on flat and textured substrates. The results of each algorithm was verified by comparison

with the data extracted from the gray scale images. For each numerical model the relevant algorithm was introduced that is able to simulate droplets nucleation and growth through a process of dropwise condensation.

At first, a traditional model was explained that considers the droplets as spherical-caps. This model is more adapted for droplets that are growing on flat substrates. The predictions of the proposed model for the evolution of droplets size and density were in good agreement with the experimental results. Also the spatial distribution estimated by model was the same as the real droplets according to Ripley's L function method. Meaning that, at primary steps that very small droplets are about to nucleate, they are dispersed according to Poisson point process, but when they starts to grow by coalescence, their distribution will change to Matern II hard core process. This is because of the nature of coalescence, that does not let two droplets approach closer than the summation of their radii unless they coalesce. The simulated droplets obey exactly the same distribution as the real droplets as well. Also, the effect of substrate temperature (T_w) and initial nucleation density (N_D) on the average heat transfer coefficient and percentage of surface coverage (ϕ) was investigated. It was shown that although T_w does not affect ϕ , N_D was able to decrease it. This bears in mind the idea of controlling the rate of condensation by changing the arrangement of droplets on the surface. Moreover, in this study a new model for describing drop-size distribution function of small droplets at earlier stages is introduced. This model is derived by writing the mass balance for small droplets entering the size rang ($r_i, r_i + \Delta r$), and considering the Rose model as the boundary condition at $r = r_c$. The results show acceptable accordance with experimental and computer simulation data at four different N_D s and four T_w s.

Comparison the gray scale images taken from flat and textured substrates relieves that on textured substrates droplets are far from circular shape. This is because water droplets can be easily canalized between the texturing patterns and form more elliptical shapes. The first effort for modeling droplets with elliptical shapes lead to the second model explained here. This model considers the droplets as ellipsoidal balls that can approach in a three-dimensional configuration and was applied on the droplets growing on pillared substrates. According to this model, ellipsoidal droplets nucleate all around the substrate with three radius a , b , and c along the axes X , Y , and Z respectively. Then, these droplets start to grow due to adsorption and coalescence on three dimensions and they can even cover several pillars at final stages. The proposed model is applied to six different pillared surfaces and its mean error is calculated on all the surfaces of about 10% for droplets density and 2% for droplets size. The main source of error is recognized as the similarity between the droplets appearance and pillars on images taken from real droplets that makes it difficult to identify the exact number of droplets. Moreover, this model does not consider the effect of water contact angle on the surface. But, it can be claimed that the proposed model has a good understanding of droplets growth on pillared substrates.

The third model takes into account both the elliptical shape of droplets on textured substrates and the effect of contact angle of water droplets. This model considers the droplets as semi-ellipsoids that are in fact a partial hat that is cut off from a real ellipsoid. So, by knowing the contact angle of the elliptical droplet on the substrate, one will be able to calculate its rate of growth due to adsorption and coalescence. Check for coalescence is done by verifying the existence of a real intersection between the projected equations of the two ellipsoids on each of planes $X - Y$, $X - Z$, and $Y - Z$. The results of this

model are well fitted by the experimental results. Also, the distribution of the droplets on sinusoidal patterns was studied using Ripley's K_{dir} function as well as Fry plot method. As was expected, although adsorbing and very big droplets do not follow the texturing pattern, the coalescing drops were formed more likely the same as the sinusoidal pattern. This shows that by making texturing patterns on the substrates, we will be able to change droplets spatial distribution and more importantly their growth rate.

Conclusion générale

Une étude expérimentale et numérique sur le processus de condensation par gouttelette sur trois types de substrats, plats, avec les piliers et sinusoïdaux a été réalisée. Les échantillons de polycarbonate ont été texturés par réplcation à partir des moules métalliques sur lesquels différents motifs de texturation ont été formés en utilisant la technologie laser. Un microscope interférométrique a été utilisé afin d'étudier les profils de rugosité bidimensionnels à la fois des moules métalliques et des substrats polycarbonate sur les textures de forme sinusoïdale. Les images réelles de ces deux surfaces ont été prises par un système de microscopie électronique à balayage (MEB) qui montre les substrats texturés qui sont prêts à être utilisés dans le processus. Ensuite, la mouillabilité des échantillons de polycarbonate avec des profils sinusoïdaux a été mesurée en utilisant un système de mesure d'angle de contact et une étude statistique a été réalisée pour étudier l'effet de la période et de l'amplitude des profils sinusoïdaux sur l'angle de contact et la rugosité moyenne. Ces études statistiques montrent que l'effet de l'amplitude du profil sinusoïdal est beaucoup plus important que l'effet de période sur les deux paramètres et en changeant l'amplitude sinusoïdale l'angle de contact peut atteindre 140° .

A l'étape suivante, les échantillons de polycarbonate ont été insérés dans l'installation de condensation. Au cours des expériences, la température des échantillons de polycarbonate a été ramenée à près de $17^\circ C$, ce qui est inférieur au point de rosée du mélange d'air humide qui est en contact avec l'échantillon ($T = 30^\circ C, H = 40\%$). En conséquence, les gouttelettes d'eau commencent à nucléer tout autour des échantillons et se développent en adsorbant les molécules d'eau de l'air humide ainsi que par coalescence. Une caméra CCD haute résolution enregistre ce processus à des intervalles de temps de $1s$. Les images à échelle de gris prises par cette caméra CCD ont été segmentées afin d'extraire l'information relative au rayon des gouttelettes, à la densité et à la distribution spatiale.

Pour le traitement de l'image sur les substrats plats et sinusoïdaux, une méthode simple consistant en un prétraitement, une segmentation et une reconnaissance a été appliquée. En ce qui concerne les images de gouttelettes sur des substrats à piliers, la similitude entre les gouttelettes et les piliers rend le traitement d'images plus compliqué. Par conséquent, un algorithme de traitement robuste a été développé pour la reconnaissance des gouttes sur les surfaces à piliers. Cet algorithme combine les informations géométriques, optiques et topologiques des images pour segmenter les gouttelettes. Il est capable de segmenter les gouttes dans une large gamme de rayons. En effet, au moyen d'une analyse d'histogramme, il peut estimer la taille de la goutte, diviser les gouttes en quatre tailles principales et utiliser un algorithme correspondant adapté à chaque gamme de taille. Une vérification manuelle de la capacité de détection de gouttes du présent algorithme comparée à des images réelles a été effectuée pour vérifier la précision de l'algorithme. Le paramètre F -mesure a permis

de quantifier la précision de la détection qui montre que cet algorithme a une grande précision pour les gouttes de plus de 0,05 mm.

Enfin, trois modèles numériques ont été développés pour décrire le comportement des gouttelettes sur des substrats plats et texturés. Les résultats de chaque algorithme ont été vérifiés par comparaison avec les données extraites des images d'échelles de gris. Pour chaque modèle analytique, l'algorithme pertinent a été introduit. Il est capable de simuler la nucléation et la croissance des gouttelettes à travers un processus de condensation par gouttelette.

Au début, un modèle traditionnel qui considère les gouttelettes comme des calottes sphériques a été expliqué. Ce modèle est plus adapté aux gouttelettes qui croissent sur les substrats plats. Les prédictions du modèle proposé pour l'évolution de la taille et de la densité des gouttelettes étaient en bon accord avec les résultats expérimentaux. De plus, la distribution spatiale estimée par le modèle était la même que les gouttelettes réelles selon la méthode de la fonction L de Ripley. Ce qui signifie que, aux étapes primaires, les très petites gouttelettes qui viennent de nucléer sont réparties selon une loi de Poisson mais lorsqu'elles commencent à croître par coalescence, leur distribution se change en processus de Matern II. Ceci est dû à la nature de la coalescence, qui ne laisse pas deux gouttelettes s'approcher plus près que la somme de leurs rayons que s'ils coalescent. Les gouttelettes simulées obéissent exactement à la même distribution que les vraies gouttelettes. En outre, l'effet de la température du substrat (T_w) et de la densité de nucléation initiale (N_D) sur le coefficient de transfert thermique moyen et le pourcentage de couverture de surface (ϕ) ont été étudiés. Il a été montré que bien que T_w n'affecte pas ϕ , N_D peut le diminuer. Ceci représente l'idée de contrôler la vitesse de condensation en changeant la disposition des gouttelettes sur la surface par l'intermédiaire de la texturation. De plus, dans cette étude, un nouveau modèle de description de la fonction de distribution de la taille des petites gouttelettes est introduit. Ce modèle est dérivé en écrivant le bilan de masse pour les petites gouttelettes entrant dans la taille donnée ($r_i, r_i + \Delta r$), et en considérant le modèle de Rose comme condition limite à $r = r_c$. Les résultats montrent une concordance acceptable avec les données expérimentales et simulation numériques en quatre différents N_D s et en quatre différents T_w s.

La comparaison des images d'échelle de gris prises à partir de substrats plats et texturés confirme le fait que sur les substrats texturés, les gouttelettes sont loin d'être de forme circulaire. En effet, les gouttelettes d'eau peuvent être facilement canalisées entre les motifs de texturation et former des formes plus elliptiques. Le premier effort pour modéliser des gouttelettes avec des formes elliptiques conduit au second modèle expliqué ici. Ce modèle considère les gouttelettes comme des billes ellipsoïdales pouvant se rapprocher dans une configuration tridimensionnelle et appliquées sur les gouttelettes qui se développent sur des substrats à piliers. Selon ce modèle, les gouttelettes ellipsoïdales se forment tout autour du substrat avec trois rayons a , b et c selon les axes X , Y et Z respectivement. Ensuite, ces gouttelettes commencent à se développer en raison de l'adsorption et de la coalescence sur trois dimensions et elles peuvent même couvrir plusieurs piliers aux stades finaux. Le modèle proposé est appliqué sur six surfaces à piliers différentes et son erreur moyenne est calculée sur toutes les surfaces à environ 10 % pour la densité des gouttelettes et à 2 % pour la taille des gouttelettes. La principale source d'erreur est la similarité entre l'apparence des gouttelettes et les piliers sur les images prises à partir de gouttelettes réelles, ce qui rend difficile l'identification du nombre exact de gouttelettes. De plus, ce modèle ne considère

pas l'effet de l'angle de contact de l'eau sur la surface. Mais, on peut affirmer que le modèle proposé a une bonne compréhension de la croissance des gouttelettes sur des substrats à piliers.

Le troisième modèle prend en compte à la fois la forme elliptique des gouttelettes sur les substrats texturés et l'effet de l'angle de contact des gouttelettes d'eau. Ce modèle considère les gouttelettes comme des semi-ellipsoïdes qui sont en fait un chapeau partiel coupé d'une ellipsoïde réelle. Ainsi, en connaissant l'angle de contact de la gouttelette elliptique sur le substrat, on pourra calculer son taux de croissance dû à l'adsorption et à la coalescence. La coalescence a été vérifiée en calculant l'existence d'une intersection réelle entre les équations projetées des deux ellipsoïdes sur chacun des plans $X - Y$, $X - Z$ et $Y - Z$. Les résultats de ce modèle sont bien ajustés par les résultats expérimentaux. De plus, la distribution des gouttelettes sur des motifs sinusoïdaux a été étudiée en utilisant la fonction K_{dir} de Ripley ainsi que la méthode de tracé de Fry. Comme prévu, bien que les plus petites et les très grosses gouttelettes ne sont pas conditionnées par la texturation, les gouttes coalescentes se sont formées de la même manière que par le motif sinusoïdal. Cela montre qu'en faisant des motifs de texturation sur les substrats, nous serons en mesure de changer la distribution spatiale des gouttelettes et, plus important encore, leur taux de croissance.

perspectives

As an outline of this work, the application of the texturing patterns on increasing the efficiency of illumination in the car light shields can be examined. The studies in this work were theoretical and have not been tested in real application. Also in this study, the surfaces were in an isolated chamber that is the case in the car light shields. But, it can be interesting to continue this work to study the effect of texturing pattern on the growth rate of droplets on the exterior substrates. In such cases, the effect of pollution can be very important specially under extreme conditions like what happens on the windows of airplanes.

Regarding the models presented here, developing the equations related to the size density functions ($f(r)$ and $F(r)$) for ellipsoidal and semi-ellipsoidal droplets can be interesting. Also, in this work we calculated the rate of droplets growth based on the assumption of Cassie-Baxter droplets. If we apply the hydrophobic coatings and the texturing patterns at the same time we can have the semi-ellipsoidal droplets that are in the form of Wenzel. Calculations for these kind of droplets are different and can lead to a more complicated model that has not been studied here.

Bibliography

- [1] N. Kovalchuk, A. Trybala, and V. Starov, "Evaporation of sessile droplets," *Current Opinion in Colloid & Interface Science*, vol. 19, no. 4, pp. 336–342, 2014.
- [2] M. Gazicki, W. James, and H. Yasuda, "Colloids and surfaces a: Physicochemical and engineering aspects," *Journal of Polymer Science: Letters Polymer Edition*, vol. 23, pp. 639–645, 1985.
- [3] L. Mishchenko, M. Khan, J. Aizenberg, and B. D. Hatton, "Spatial control of condensation and freezing on superhydrophobic surfaces with hydrophilic patches," *Advanced functional materials*, vol. 23, no. 36, pp. 4577–4584, 2013.
- [4] H. Lhuissier, D. Lohse, and X. Zhang, "Spatial organization of surface nanobubbles and its implications in their formation process," *Soft matter*, vol. 10, no. 7, pp. 942–946, 2014.
- [5] X. Liu and P. Cheng, "Dropwise condensation theory revisited part ii. droplet nucleation density and condensation heat flux," *International Journal of Heat and Mass Transfer*, vol. 83, pp. 842–849, 2015.
- [6] T. Rajala, C. Redenbach, A. Särkkä, and M. Sormani, "A review on anisotropy analysis of spatial point patterns," *arXiv preprint arXiv:1712.01634*, 2017.
- [7] T. A. Rajala, A. Särkkä, C. Redenbach, and M. Sormani, "Estimating geometric anisotropy in spatial point patterns," *Spatial Statistics*, vol. 15, pp. 100–114, 2016.
- [8] A. Kostinski and A. Jameson, "Fluctuation properties of precipitation. part i: On deviations of single-size drop counts from the poisson distribution," *Journal of the atmospheric sciences*, vol. 54, no. 17, pp. 2174–2186, 1997.
- [9] J. R. Maa, "Drop size distribution and heat flux of dropwise condensation," *The Chemical Engineering Journal*, vol. 16, no. 3, pp. 171–176, 1978.
- [10] E. E. Gose, A. Mucciardi, and E. Baer, "Model for dropwise condensation on randomly distributed sites," *International Journal of Heat and Mass Transfer*, vol. 10, no. 1, pp. 15–22, 1967.
- [11] B. Burnside and H. Hadi, "Digital computer simulation of dropwise condensation from equilibrium droplet to detectable size," *International journal of heat and mass transfer*, vol. 42, no. 16, pp. 3137–3146, 1999.

-
- [12] Y.-T. Wu, C.-X. Yang, and X.-G. Yuan, “Drop distributions and numerical simulation of dropwise condensation heat transfer,” *International Journal of Heat and Mass Transfer*, vol. 44, no. 23, pp. 4455–4464, 2001.
- [13] J. Rose and L. Glicksman, “Dropwise condensation—the distribution of drop sizes,” *International journal of heat and mass transfer*, vol. 16, no. 2, pp. 411–425, 1973.
- [14] J. E. Castillo, J. A. Weibel, and S. V. Garimella, “The effect of relative humidity on dropwise condensation dynamics,” tech. rep., Cooling Technologies Research Center, Purdue University, 2015.
- [15] D. Beysens, “The formation of dew,” *Atmospheric research*, vol. 39, no. 1-3, pp. 215–237, 1995.
- [16] R. D. Narhe, W. González-Viñas, and D. A. Beysens, “Water condensation on zinc surfaces treated by chemical bath deposition,” *Applied Surface Science*, vol. 256, no. 16, pp. 4930–4933, 2010.
- [17] D. Beysens, “Dew nucleation and growth,” *Comptes Rendus Physique*, vol. 7, no. 9-10, pp. 1082–1100, 2006.
- [18] D. Beysens, V. Pruvost, and B. Pruvost, “Dew observed on cars as a proxy for quantitative measurements,” *Journal of Arid Environments*, vol. 135, pp. 90–95, 2016.
- [19] M. Parsa, S. Harmand, and K. Sefiane, “Mechanisms of pattern formation from dried sessile drops,” *Advances in colloid and interface science*, 2018.
- [20] R. S. Volkov, G. V. Kuznetsov, and P. A. Strizhak, “The influence of initial sizes and velocities of water droplets on transfer characteristics at high-temperature gas flow,” *International Journal of Heat and Mass Transfer*, vol. 79, pp. 838–845, 2014.
- [21] M. Sadafi, I. Jahn, A. Stilgoe, and K. Hooman, “Theoretical and experimental studies on a solid containing water droplet,” *International Journal of Heat and Mass Transfer*, vol. 78, pp. 25–33, 2014.
- [22] J. Barrett and C. Clement, “Growth rates for liquid drops,” *Journal of Aerosol Science*, vol. 19, no. 2, pp. 223–242, 1988.
- [23] Y. Cheng, J. Xu, and Y. Sui, “Numerical investigation of coalescence-induced droplet jumping on superhydrophobic surfaces for efficient dropwise condensation heat transfer,” *International Journal of Heat and Mass Transfer*, vol. 95, pp. 506–516, 2016.
- [24] J. B. Boreyko, Y. Zhao, and C.-H. Chen, “Planar jumping-drop thermal diodes,” *Applied Physics Letters*, vol. 99, no. 23, p. 234105, 2011.
- [25] N. Miljkovic, R. Enright, and E. N. Wang, “Modeling and optimization of superhydrophobic condensation,” *Journal of Heat Transfer*, vol. 135, no. 11, p. 111004, 2013.

- [26] E. Schmidt, W. Schurig, and W. Sellschopp, "Versuche über die kondensation von wasserdampf in film-und tropfenform," *Technische Mechanik und Thermodynamik*, vol. 1, no. 2, pp. 53–63, 1930.
- [27] B. Qi, J. Wei, L. Zhang, and H. Xu, "A fractal dropwise condensation heat transfer model including the effects of contact angle and drop size distribution," *International Journal of Heat and Mass Transfer*, vol. 83, pp. 259–272, 2015.
- [28] X. Liu and P. Cheng, "Lattice boltzmann simulation for dropwise condensation of vapor along vertical hydrophobic flat plates," *International Journal of Heat and Mass Transfer*, vol. 64, pp. 1041–1052, 2013.
- [29] J. R. Lara and M. T. Holtzapple, "Experimental investigation of dropwise condensation on hydrophobic heat exchangers. part ii: Effect of coatings and surface geometry," *Desalination*, vol. 280, no. 1, pp. 363–369, 2011.
- [30] A. Cassie and S. Baxter, "Wettability of porous surfaces," *Transactions of the Faraday society*, vol. 40, pp. 546–551, 1944.
- [31] R. N. Wenzel, "Resistance of solid surfaces to wetting by water," *Industrial & Engineering Chemistry*, vol. 28, no. 8, pp. 988–994, 1936.
- [32] T. Koishi, K. Yasuoka, S. Fujikawa, T. Ebisuzaki, and X. C. Zeng, "Coexistence and transition between cassie and wenzel state on pillared hydrophobic surface," *Proceedings of the National Academy of Sciences*, vol. 106, no. 21, pp. 8435–8440, 2009.
- [33] S. Stylianou and J. Rose, "Drop-to-filmwise condensation transition: heat transfer measurements for ethanediol," *International Journal of Heat and Mass Transfer*, vol. 26, no. 5, pp. 747–760, 1983.
- [34] S. Vemuri and K. Kim, "An experimental and theoretical study on the concept of dropwise condensation," *International journal of heat and mass transfer*, vol. 49, no. 3, pp. 649–657, 2006.
- [35] T. Song, Z. Lan, X. Ma, and T. Bai, "Molecular clustering physical model of steam condensation and the experimental study on the initial droplet size distribution," *International Journal of Thermal Sciences*, vol. 48, no. 12, pp. 2228–2236, 2009.
- [36] H. R. T. Bahrami and H. Saffari, "Theoretical study of stable dropwise condensation on an inclined micro/nano-structured tube," *International Journal of Refrigeration*, vol. 75, pp. 141–154, 2017.
- [37] M.-G. Medici, A. Mongruel, L. Royon, and D. Beysens, "Edge effects on water droplet condensation," *Physical Review E*, vol. 90, no. 6, p. 062403, 2014.
- [38] J. Guadarrama-Cetina, A. Mongruel, M.-G. Medici, E. Baquero, A. Parker, I. Milimouk-Melnychuk, W. González-Viñas, and D. Beysens, "Dew condensation on desert beetle skin," *The European Physical Journal E*, vol. 37, no. 11, p. 109, 2014.

- [39] M. Qian and J. Ma, “The characteristics of heterogeneous nucleation on concave surfaces and implications for directed nucleation or surface activity by surface nanopatterning,” *Journal of Crystal Growth*, vol. 355, no. 1, pp. 73–77, 2012.
- [40] C.-H. Chen, Q. Cai, C. Tsai, C.-L. Chen, G. Xiong, Y. Yu, and Z. Ren, “Dropwise condensation on superhydrophobic surfaces with two-tier roughness,” *Applied Physics Letters*, vol. 90, no. 17, p. 173108, 2007.
- [41] C.-W. Lo, C.-C. Wang, and M.-C. Lu, “Spatial control of heterogeneous nucleation on the superhydrophobic nanowire array,” *Advanced Functional Materials*, vol. 24, no. 9, pp. 1211–1217, 2014.
- [42] J. F. Welch, *Microscopic study of dropwise condensation*. PhD thesis, University of Illinois at Urbana-Champaign, 1961.
- [43] J. Rose, “Dropwise condensation theory,” *International Journal of Heat and Mass Transfer*, vol. 24, no. 2, pp. 191–194, 1981.
- [44] R. N. Leach, F. Stevens, S. C. Langford, and J. T. Dickinson, “Dropwise condensation: experiments and simulations of nucleation and growth of water drops in alccoling system,” tech. rep., Physics Department, Washington State University, 2009.
- [45] M. Mei, F. Hu, C. Han, and Y. Cheng, “Time-averaged droplet size distribution in steady-state dropwise condensation,” *International Journal of Heat and Mass Transfer*, vol. 88, pp. 338–345, 2015.
- [46] P. Meakin, “Droplet deposition growth and coalescence,” *Reports on Progress in Physics*, vol. 55, no. 2, p. 157, 1992.
- [47] M. Abu-Orabi, “Modeling of heat transfer in dropwise condensation,” *International journal of heat and mass transfer*, vol. 41, no. 1, pp. 81–87, 1998.
- [48] X.-H. Ma, T.-Y. Song, Z. Lan, and T. Bai, “Transient characteristics of initial droplet size distribution and effect of pressure on evolution of transient condensation on low thermal conductivity surface,” *International Journal of Thermal Sciences*, vol. 49, no. 9, pp. 1517–1526, 2010.
- [49] A. Jameson and A. Kostinski, “What is a raindrop size distribution?,” *Bulletin of the American Meteorological Society*, vol. 82, no. 6, p. 1169, 2001.
- [50] A. Jameson and A. Kostinski, “Fluctuation properties of precipitation. part ii: Reconsideration of the meaning and measurement of raindrop size distributions,” *Journal of the atmospheric sciences*, vol. 55, no. 2, pp. 283–294, 1998.
- [51] A. Kostinski and A. Jameson, “On the spatial distribution of cloud particles,” *Journal of the atmospheric sciences*, vol. 57, no. 7, pp. 901–915, 2000.
- [52] M. L. Larsen, “Spatial distributions of aerosol particles: Investigation of the poisson assumption,” *Journal of Aerosol Science*, vol. 38, no. 8, pp. 807–822, 2007.

- [53] B. S. Sikarwar, S. Khandekar, and K. Muralidhar, “Mathematical modelling of dropwise condensation on textured surfaces,” tech. rep., Department of Mechanical Engineering, Indian Institute of Technology Kanpur, 2012.
- [54] X. Liu and P. Cheng, “Dropwise condensation theory revisited: Part i. droplet nucleation radius,” *International Journal of Heat and Mass Transfer*, vol. 83, pp. 833–841, 2015.
- [55] S. Kim and K. J. Kim, “Dropwise condensation modeling suitable for superhydrophobic surfaces,” *Journal of heat transfer*, vol. 133, no. 8, p. 081502, 2011.
- [56] M. Nosonovsky and B. Bhushan, “Phase behavior of capillary bridges: towards nanoscale water phase diagram,” *Physical Chemistry Chemical Physics*, vol. 10, no. 16, pp. 2137–2144, 2008.
- [57] H. Tanaka, “A theoretical study of dropwise condensation,” *ASME J. Heat Transfer*, vol. 97, no. 1, pp. 72–78, 1975.
- [58] H. Tanaka, “Measurements of drop-size distributions during transient dropwise condensation,” *Journal of Heat Transfer*, vol. 97, no. 3, pp. 341–346, 1975.
- [59] C. Redenbach, A. Särkkä, J. Freitag, and K. Schladitz, “Anisotropy analysis of pressed point processes,” *AStA Advances in Statistical Analysis*, vol. 93, no. 3, pp. 237–261, 2009.
- [60] J. Teichmann, F. Ballani, and K. G. van den Boogaart, “Generalizations of matérn’s hard-core point processes,” *Spatial Statistics*, vol. 3, pp. 33–53, 2013.
- [61] A. Marshak, Y. Knyazikhin, M. L. Larsen, and W. J. Wiscombe, “Small-scale drop-size variability: empirical models for drop-size-dependent clustering in clouds,” *Journal of the atmospheric sciences*, vol. 62, no. 2, pp. 551–558, 2005.
- [62] J. F. C. Kingman, *Poisson processes*, vol. 3. Clarendon Press, 1992.
- [63] P. Meakin, “The structure of two-dimensional witten-sander aggregates,” *Journal of Physics A: Mathematical and General*, vol. 18, no. 11, p. L661, 1985.
- [64] J. McCormick and J. Westwater, “Nucleation sites for dropwise condensation,” *Chemical Engineering Science*, vol. 20, no. 12, pp. 1021–1036, 1965.
- [65] M. Kiderlen and M. Hörig, “Matérn’s hard core models of types i and ii with arbitrary compact grains,” tech. rep., CSGB Research report, 2013.
- [66] M. Rosenberg, “Wavelet analysis for detecting anisotropy in point patterns,” *Journal of Vegetation Science*, vol. 15, no. 2, pp. 277–284, 2004.
- [67] N. Fry, “Random point distributions and strain measurement in rocks,” *Tectonophysics*, vol. 60, no. 1-2, pp. 89–105, 1979.
- [68] O. Nicolis, J. Mateu, and R. D’Ercole, “Testing for anisotropy in spatial point processes,” in *Proceedings of the Fifth International Workshop on Spatio-temporal Modelling (METMA5)*. Publisher Unidixital, Santiago de Compostela, pp. 1–4, 2010.

- [69] P. M. Dixon, “Ripley’s k function,” *Encyclopedia of environmetrics*, 2002.
- [70] S. N. Chiu, D. Stoyan, W. S. Kendall, and J. Mecke, *Stochastic geometry and its applications*. John Wiley & Sons, 2013.
- [71] B. Damit, C.-Y. Wu, and M.-D. Cheng, “On the validity of the poisson assumption in sampling nanometer-sized aerosols,” *Aerosol Science and Technology*, vol. 48, no. 5, pp. 562–570, 2014.
- [72] W. T. Scott, “Poisson statistics in distributions of coalescing droplets,” *Journal of the Atmospheric Sciences*, vol. 24, no. 2, pp. 221–225, 1967.
- [73] J. R. E.J. Le Fevre, “A theory of heat transfer by dropwise condensation,” in *Proceedings of 3rd International Heat Transfer*, pp. 362–375.
- [74] J. Rose, “On the mechanism of dropwise condensation,” *International Journal of Heat and Mass Transfer*, vol. 10, no. 6, pp. 755IN1757–756762, 1967.
- [75] C. Graham and P. Griffith, “Drop size distributions and heat transfer in dropwise condensation,” *International Journal of Heat and Mass Transfer*, vol. 16, no. 2, pp. 337–346, 1973.
- [76] J. Rose, “Dropwise condensation theory and experiment: a review,” *Proceedings of the Institution of Mechanical Engineers, Part A: Journal of Power and Energy*, vol. 216, no. 2, pp. 115–128, 2002.
- [77] T. Takaharu and H. Tanaka, “A theoretical study on the constriction resistance in dropwise condensation,” *International journal of heat and mass transfer*, vol. 34, no. 11, pp. 2779–2786, 1991.
- [78] M. El-Adawi and T. Felemban, “Dropsize function during dropwise condensation in relation to heat transfer intensification—statistical approach,” *Desalination and Water Treatment*, vol. 24, no. 1-3, pp. 244–250, 2010.
- [79] M. Mei, B. Yu, J. Cai, and L. Luo, “A fractal analysis of dropwise condensation heat transfer,” *International Journal of Heat and Mass Transfer*, vol. 52, no. 21, pp. 4823–4828, 2009.
- [80] M. Churchill, “Introduction to fractal geometry,” *Keble Summer Essay*, 2004.
- [81] N. Watanabe, M. Aritomi, and A. Machida, “Time-series characteristics and geometric structures of drop-size distribution density in dropwise condensation,” *International Journal of Heat and Mass Transfer*, vol. 76, pp. 467–483, 2014.
- [82] N. Watanabe and M. Aritomi, “Correlative relationship between geometric arrangement of drops in dropwise condensation and heat transfer coefficient,” *International Journal of Heat and Mass Transfer*, vol. 105, pp. 597–609, 2017.
- [83] L. R. Glicksman and A. W. Hunt, “Numerical simulation of dropwise condensation,” *International Journal of Heat and Mass Transfer*, vol. 15, no. 11, pp. 2251–2269, 1972.

-
- [84] G. Tammann and W. Boehme, “Die zahl der wassertröpfchen bei der kondensation auf verschiedenen festen stoffen,” *Annalen der Physik*, vol. 414, no. 1, pp. 77–80, 1935.
- [85] A. C. Peterson Jr, *Dropwise condensation of ethylene glycol*. PhD thesis, University of Illinois at Urbana-Champaign, 1965.
- [86] J. L. McCormick and E. Baer, “On the mechanism of heat transfer in dropwise condensation,” *Journal of Colloid Science*, vol. 18, no. 3, pp. 208–216, 1963.
- [87] D. Fritter, C. M. Knobler, D. Roux, and D. Beysens, “Computer simulations of the growth of breath figures,” *Journal of Statistical Physics*, vol. 52, no. 5-6, pp. 1447–1459, 1988.
- [88] E. Ruckenstein and G. O. Berim, “Kinetics of heterogeneous nucleation on a rough surface: Nucleation of a liquid phase in nanocavities,” *Journal of colloid and interface science*, vol. 351, no. 1, pp. 277–282, 2010.
- [89] G. O. Berim and E. Ruckenstein, “Kinetic theory of heterogeneous nucleation; effect of nonuniform density in the nuclei,” *Journal of colloid and interface science*, vol. 355, no. 1, pp. 259–264, 2011.
- [90] C. S. B. R. G. M. B. S. V. S. Pionnier N, Boroomandi Barati S, “Design of an environment controlled dew tracking setup to emphasize the role of the relative humidity on breath figures dynamics,” *EPJ journal of thecniques and instrumentation*, vol. 5, no. 2, 2018.
- [91] D. C. Montgomery and G. C. Runger, *Applied statistics and probability for engineers*. John Wiley & Sons, 2010.
- [92] M. V. Aragão, E. P. Frigieri, C. A. Ynoguti, and A. P. Paiva, “Factorial design analysis applied to the performance of sms anti-spam filtering systems,” *Expert Systems with Applications*, vol. 64, pp. 589–604, 2016.
- [93] S.-C. Pei and J.-H. Horng, “Circular arc detection based on hough transform,” tech. rep., Department of Electrical Engineering, National Tawan University, 1995.
- [94] X. Yu, D. Xing, T. Hazuku, T. Takamasa, T. Ishimaru, Y. Tanaka, and T. Akiba, “Measurement technique for solid-liquid two-phase flow using normal-line hough transform method,” tech. rep., Tokyo University of Marine Science and Technology - Research Institute for Cell Engineering Advanced Industrial Science and Technology, 2009.
- [95] T. J. Atherthon and D. J. Kerbyson, “Using phase to represent radius in the coherent circle hough transform,” tech. rep., Department of Computer Science, University of Warwick, 1993.
- [96] R. Muthukrishnan and M. Radha, “Edge detection technique for image segmentation,” tech. rep., Department of Statistics, Bharathiar University, 2011.

- [97] L. Shen, X. Song, M. Iguchi, and F. Yamamoto, "A method for recognizing particles in overlapped particle images," tech. rep., Department of Mechanical Engineering, Fukui University - Division of Materials Science and Engineering, Graduate School of Engineering, Hokkaido University, 1999.
- [98] M. Honkanen, "Turbulent multiphase flow measurements with particle image velocimetry: application to bubbly flows," tech. rep., Tampere University of Technology, 2002.
- [99] H. Freeman and L. S. Davis, "A corner-finding algorithm for chain-coded curves," tech. rep., IEEE Transactions on Computers, 1977.
- [100] C. Urdiales, A. Bandera, and F. Sandoval, "Non-parametric planar shape representation based on adaptive curvature functions," tech. rep., Dpto Technologica Electronica ETSI Telecomunicacion, Universidad de Malaga, 2002.
- [101] R. Lindken and W. Merzkirch, "A novel piv technique for measurements in multiphase flows and its application to two-phase bubbly flows," tech. rep., DHOchschule Bochum, Mecatronics and Mechanical Eengineering Department, 2002.
- [102] S. Beucher and F. Meyer, "The morphological approach to segmentation; the watershed transformation," tech. rep., Centre de morphologie mathematique, Ecole des Mines de Paris, 1990.
- [103] X. Zabulis, M. Papara, A. Chatziargyriou, and T. D. Karapantsios, "Detection of densely dispersed spherical bubbles in digital images based in template matching technique - application to wet foams," tech. rep., Division of Chemical Technology, School of Chemistry, Aristotelian University of Thessaloniki - University Box Informatics and Telematics Institute - Centre for Research and Technology Hellas, 2007.
- [104] Y. Fu and Y. Liu, "Development of a robust image processing technique for bubbly flow measurement in a narrow rectangular channel," tech. rep., Nuclear Engineering Program, Mechanical Engineering Department, Virginia Tech, 2016.
- [105] A. W. Fitzgibbon, M. Pilu, and R. B. Fisher, "Direct least-squares fitting of ellipses," tech. rep., Department of Artificial Intelligence, the University of Edinburgh, 1996.
- [106] T. Marosevic and R. Scitovski, "Multiple ellipse fitting by center-based clustering," tech. rep., Multiple ellipse fitting by center-based clustering, 2015.
- [107] A. L. Torre, L. Alonso-Nanclares, S. Muelas, J. M. Pena, and J. DeFelipe, "Segmentation of neuronal nuclei based on clump splitting and a two-step binarization of images," tech. rep., Instituto Cajal, Consejo Superior de Investigaciones - Laboratorio Cajal de Circuitos Corticales and Facultad de Informatica, Universidad Politecnica de Madrid, 2013.
- [108] W. X. Wang, "Binary image segmentation of aggregates based on polygonal approximation and classification of concavities," tech. rep., Dpto Technologica Electronica ETSI Telecomunicacion, Universidad de Malaga Division of Engineering Geology, Department of Civil and Environmental Engineering, Royal Institute of Technology, 1997.

- [109] D. Thompson, H. G. J. W. Haddad, and P. H. Bartels, "Scene segmentation in a machine vision system for histopathology," tech. rep., Optical Science Center, University of Arizona, 1990.
- [110] S. H. Ong and Jayasooriah, "Decomposition of digital clumps into convex parts by contour tracing and labelling," tech. rep., Optical Science Center, University of Arizona Department of Electrical Engineering, National University of Singapore, 1992.
- [111] A. Karn, C. Ellis, R. Arndt, and J. Hong, "An integrative image measurement technique for dense bubbly flows with a wide size distribution," tech. rep., Saint Anthony Falls Laboratory, University of Minnesota, 2015.
- [112] Q. Chen, X. Yang, and E. M. Petrucci, "Watershed segmentation for binary images with different distance transforms," tech. rep., University of Ottawa, Lakehead University, 2004.
- [113] Y. Gavet and J.-C. Pinoli, "Visual perception based automatic recognition of cell mosaics in human corneal endothelium microscopy images," *Image Analysis & Stereology*, vol. 27, no. 1, pp. 53–61, 2011.
- [114] D. Bradley and G. Roth, "Adaptive thresholding using the integral image," *Journal of Graphics Tools*, vol. 12, no. 2, pp. 13–21, 2007.
- [115] F. C. Crow, "Summed-area tables for texture mapping," *ACM SIGGRAPH computer graphics*, vol. 18, no. 3, pp. 207–212, 1984.
- [116] P. Viola and M. J. Jones, "Robust real-time face detection," *International journal of computer vision*, vol. 57, no. 2, pp. 137–154, 2004.
- [117] O. Veksler, "Fast variable window for stereo correspondence using integral images," in *Computer Vision and Pattern Recognition, 2003. Proceedings. 2003 IEEE Computer Society Conference on*, vol. 1, pp. I–I, IEEE, 2003.
- [118] J. Sauvola and M. Pietikäinen, "Adaptive document image binarization," *Pattern recognition*, vol. 33, no. 2, pp. 225–236, 2000.
- [119] F. Shafait, D. Keysers, and T. M. Breuel, "Efficient implementation of local adaptive thresholding techniques using integral images.," *DRR*, vol. 6815, p. 681510, 2008.
- [120] S. Beucher and C. Lantuéjoul, "Use of watersheds in contour detection," 1979.
- [121] Y. Gavet, *Perception visuelle humaine, complétion des mosaïques et application à la reconstruction d'images de l'endothélium cornéen humain en microscopie optique spéculaire*. PhD thesis, Ecole Nationale Supérieure des Mines de Saint-Etienne, 2008.
- [122] R. M. Haralick and L. Waston, "A facet model for image data," tech. rep., Computer Vision Graphics Image Process, 1981.
- [123] T. Ojala, M. Pietikinen, and D. Harwood, "Performance evaluation of texture measures with classification based on kullback discrimination of distributions," tech. rep., Department of Electrical Engineering, University of Ouu - Center for Automation Research, University of Maryland, 1994.

- [124] K. L. Lee and L. H. Chen, “A new method for coarse classification of textures and class weight estimation for texture retrieval,” tech. rep., Department of Computer and Information Science, National Chiao Tung University, 2002.
- [125] T. Fawcett, “An introduction to roc analysis,” tech. rep., Institute for the Study of Learning and Expertise, 2005.
- [126] P. B. Weisensee, Y. Wang, Q. Hongliang, D. Schultz, W. P. King, and N. Miljkovic, “Condensate droplet size distribution on lubricant-infused surfaces,” *International Journal of Heat and Mass Transfer*, vol. 109, pp. 187–199, 2017.
- [127] N. K. Battoo, B. S. Sikarwar, S. Khandekar, and K. Muralidhar, “Mathematical modeling and simulation of dropwise condensation and inclined surfaces exposed to vapor flux,” in *20th National and 9th International ISHMT-ASME Heat and Mass Transfer Conference*, pp. 1330–1336, 2010.
- [128] I. Tanasawa, “Advances in condensation heat transfer,” *Advances in heat transfer*, vol. 21, pp. 55–139, 1991.
- [129] S. Hatamiya and H. Tanaka, “A study on the mechanism of dropwise condensation,” *Tras. Jpn. Soc. Mech. Eng.(in Japanese)*, vol. 52, no. 477B, p. 2214, 1986.
- [130] S. FUJIKAWA and M. MAEREFAT, “A study of the molecular mechanism of vapour condensation,” *JSME international journal. Ser. 2, Fluids engineering, heat transfer, power, combustion, thermophysical properties*, vol. 33, no. 4, pp. 634–641, 1990.
- [131] S. Stylianou and J. Rose, “Dropwise condensation of ethanediol,” *Physico-Chemical Hydrodynamics 3*, vol. 199, 1982.
- [132] J. W. Rose, “Interphase matter transfer, the condensation coefficient and dropwise condensation,” in *Heat Transfer Conference*, vol. 1, pp. 89–104, 1998.
- [133] G. D. Bansal, S. Khandekar, and K. Muralidhar, “Measurement of heat transfer during drop-wise condensation of water on polyethylene,” *Nanoscale and Microscale Thermophysical Engineering*, vol. 13, no. 3, pp. 184–201, 2009.
- [134] R. Marek and J. Straub, “Analysis of the evaporation coefficient and the condensation coefficient of water,” *International Journal of Heat and Mass Transfer*, vol. 44, no. 1, pp. 39–53, 2001.
- [135] S. Zheng, F. Eimann, C. Philipp, T. Fieback, and U. Gross, “Modeling of heat and mass transfer for dropwise condensation of moist air and the experimental validation,” *International Journal of Heat and Mass Transfer*, vol. 120, pp. 879–894, 2018.
- [136] W. S. Amato and T. Chi, “Free convection heat transfer from isothermal spheres in water,” *International Journal of Heat and Mass Transfer*, vol. 15, no. 2, pp. 327–339, 1972.
- [137] H. Merk and J. Prins, “Thermal convection in laminar boundary layers ii,” *Applied Scientific Research, Section A*, vol. 4, no. 3, pp. 195–206, 1954.

- [138] P. Meakin, “Dropwise condensation: the deposition growth and coalescence of fluid droplets,” *Physica Scripta*, vol. 1992, no. T44, p. 31, 1992.
- [139] M. Nosonovsky, “Model for solid-liquid and solid-solid friction of rough surfaces with adhesion hysteresis,” *The Journal of chemical physics*, vol. 126, no. 22, p. 224701, 2007.
- [140] B. Lautrup, “Physics of continuous matter,” *Exotic and Everyday Phenomena in the Macroscopic World*, IOP, 2005.
- [141] J. W. Waldron and K. Wallace, “Objective fitting of ellipses in the centre-to-centre (fry) method of strain analysis,” *Journal of Structural Geology*, vol. 29, no. 9, pp. 1430–1444, 2007.
- [142] M. Brewster, “Evaporation and condensation of water mist/cloud droplets with thermal radiation,” *International Journal of Heat and Mass Transfer*, vol. 88, pp. 695–712, 2015.
- [143] G. Lorenzini and O. Saro, “Thermal fluid dynamic modelling of a water droplet evaporating in air,” *International Journal of Heat and Mass Transfer*, vol. 62, pp. 323–335, 2013.
- [144] G. J. Oberman and T. W. Farrell, “Modelling of the evaporation of a droplet suspended in a binary atmosphere,” *International Journal of Heat and Mass Transfer*, vol. 92, pp. 381–393, 2016.
- [145] C. Xie, J. Zhang, V. Bertola, and M. Wang, “Droplet evaporation on a horizontal substrate under gravity field by mesoscopic modeling,” *Journal of colloid and interface science*, vol. 463, pp. 317–323, 2016.
- [146] D. Hu, H. Wu, and Z. Liu, “Effect of liquid–vapor interface area on the evaporation rate of small sessile droplets,” *International Journal of Thermal Sciences*, vol. 84, pp. 300–308, 2014.
- [147] C. Mu, J. Pang, Q. Lu, and T. Liu, “Effects of surface topography of material on nucleation site density of dropwise condensation,” *Chemical Engineering Science*, vol. 63, no. 4, pp. 874–880, 2008.
- [148] J. McCormick and J. Westwater, “Drop dynamics and heat transfer during dropwise condensation of water vapor on a horizontal surface,” in *Chemical Engineering Progress Symposium Series*, vol. 62, pp. 120–134, 1966.
- [149] D. Condensation, “Experiments and simulations of nucleation and growth of water drops in a cooling system leach, rn; stevens, f.; langford, sc; dickinson, jt,” *Langmuir*, vol. 22, no. 21, pp. 8864–8872, 2006.
- [150] B. S. Sikarwar, K. Muralidhar, and S. Khandekar, “Simulation of dropwise condensation underneath a chemically textured substrate with a wettability gradient,” in *Proceeding 21 st National and 10 th International ISHMT-ASME heat and mass transfer conference, Chennai, India*, 2011.

- [151] J.-L. Brenguier, T. Bourriane, A. A. Coelho, J. Isbert, R. Peytavi, D. Trevarin, and P. Weschler, “Improvements of droplet size distribution measurements with the fast-fssp (forward scattering spectrometer probe),” *Journal of Atmospheric and Oceanic Technology*, vol. 15, no. 5, pp. 1077–1090, 1998.
- [152] M. L. Larsen, T. B. Hayward, and J. B. Teves, “Scaling properties of raindrop size distributions as measured by a dense array of optical disdrometers,” *Journal of Hydrology*, vol. 521, pp. 424–432, 2015.
- [153] M. L. Larsen and A. B. Kostinski, “Simple dead-time corrections for discrete time series of non-poisson data,” *Measurement Science and Technology*, vol. 20, no. 9, p. 095101, 2009.
- [154] D. Stoyan, “Simulation and characterization of random systems of hard particles,” *Image Anal Stereol*, vol. 21, no. Suppl 1, pp. 41–8, 2002.
- [155] P. Laurençot and S. Mischler, “On coalescence equations and related models,” in *Modeling and computational methods for kinetic equations*, pp. 321–356, Springer, 2004.
- [156] L. Černe, B. Simončič, and M. Željko, “The influence of repellent coatings on surface free energy of glass plate and cotton fabric,” *Applied Surface Science*, vol. 254, no. 20, pp. 6467–6477, 2008.
- [157] H. Gu, M. H. Duits, and F. Mugele, “Droplets formation and merging in two-phase flow microfluidics,” *International journal of molecular sciences*, vol. 12, no. 4, pp. 2572–2597, 2011.
- [158] M. Chiesa and J. Melheim, “Behaviour of water droplets falling in oil under the influence of an electric field,” *Behaviour*, vol. 13, p. 17, 2004.
- [159] L. P. Santos, T. R. Ducati, L. B. Balestrin, and F. Galembeck, “Water with excess electric charge,” *The Journal of Physical Chemistry C*, vol. 115, no. 22, pp. 11226–11232, 2011.
- [160] S. Sadhal, P. S. Ayyaswamy, and J. N. Chung, *Transport phenomena with drops and bubbles*. Springer Science & Business Media, 2012. Chapter 5.
- [161] M. François, *Computations of drop dynamics with heat transfer*. PhD thesis, University of Florida, 2002.
- [162] M. S. Amin, *Advanced Faraday cage measurements of charge, short-circuit current and open-circuit voltage*. PhD thesis, Massachusetts Institute of Technology, 2004.
- [163] J. Rose, “Condensation heat transfer fundamentals,” *Chemical Engineering Research and Design*, vol. 76, no. 2, pp. 143–152, 1998.
- [164] B. S. Sikarwar, S. Khandekar, and K. Muralidhar, “Mathematical modelling of drop-wise condensation on textured surfaces,” *Sadhana*, vol. 38, no. 6, pp. 1135–1171, 2013.

- [165] M. Mei, B. Yu, M. Zou, and L. Luo, “A numerical study on growth mechanism of dropwise condensation,” *International Journal of Heat and Mass Transfer*, vol. 54, no. 9, pp. 2004–2013, 2011.
- [166]
- [167] S. B. Barati, N. Pionnier, J.-C. Pinoli, S. Valette, and Y. Gavet, “Investigation spatial distribution of droplets and the percentage of surface coverage during dropwise condensation,” *International Journal of Thermal Sciences*, vol. 124, pp. 356–365, 2018.
- [168] S. B. Barati, J.-C. Pinoli, S. Valette, and Y. Gavet, “Differential and average approaches to rose and mei dropwise condensation models,” in *INASE-MMSSE 2017-The 2017 International Conference on Mathematical Methods, Mathematical Models and Simulation in Science and Engineering*, vol. 11, pp. 40–à, North Atlantic University Union, 2017.
- [169] H. Martin, S. B. Barati, J.-C. Pinoli, S. Valette, and Y. Gavet, “Segmentation of gray scale images of dropwise condensation on textured surfaces,” *World Academy of Science, Engineering and Technology, International Journal of Computer and Information Engineering*, vol. 5, no. 1, pp. 115–126, 2018.
- [170] D. Niu, L. Guo, H. Hu, and G. Tang, “Dropwise condensation heat transfer model considering the liquid-solid interfacial thermal resistance,” *International Journal of Heat and Mass Transfer*, vol. 112, pp. 333–342, 2017.
- [171] N. Pionnier, S. B. Barati, E. Contraires, R. Berger, M. Guibert, S. Benayoun, and S. Valette, “Design of an environment controlled dew tracking setup to emphasize the role of the relative humidity on breath figures dynamics,” *EPJ Techniques and Instrumentation*, vol. 5, no. 1, p. 2, 2018.
- [172] A. Ghosh, S. Beaini, B. J. Zhang, R. Ganguly, and C. M. Megaridis, “Enhancing dropwise condensation through bioinspired wettability patterning,” *Langmuir*, vol. 30, no. 43, pp. 13103–13115, 2014.
- [173] Y. A. Cengel, “Heat transfer - a practical approach,” tech. rep., International Edition, 1998.
- [174] J. W. Rose and L. R. Glicksman, “Dropwise condensation - the distribution of drop sizes,” tech. rep., Department of Mechanical Engineering, Massachusetts Institute of Technology, 1972.
- [175] R. N. Leach, F. Stevens, and J. T. Dickinson, “Dropwise condensation - experiments and simulations of nucleation and growth of water drops in a cooling system,” tech. rep., Physics Department, Washington State University, 2006.

NNT : 2018LYSEM018

Solmaz BOROOMANDI-BARATI

MODELING AND SIMULATION OF DROPWISE CONDENSATION ON TEXTURED
SUBSTRATES

Speciality : IMAGE, VISION, SIGNAL

Keywords : Dropwise condensation, Numerical modelling, Ellipsoidal droplets, Textured
substrate

Abstract :

The aim of this thesis is to develop a numerical simulation model to study the process of dropwise condensation on flat and textured substrates. The experimental part was carried out on the poly carbonate surfaces that were duplicated from a metallic mold textured using laser technology. The samples are mounted on a home-made condensation set-up. The results of these experiments are gray scale images that had to be binarized in order to get the information related to droplets growth rate, density and spatial distribution. Then, three different models were developed during this thesis to describe droplets behavior:

1. a classical method that considers droplets as spherical-caps growing on a flat substrate
2. a method that considers elliptical droplets (contact angle = 90°) growing on the textured substrates,
3. and a modified method that considers ellipsoidal-cap droplets (contact angle $\neq 90^\circ$) growing on the textured substrates.

The results of these three methods are validated by comparison with experimental data on a flat surface, 6 different configurations of pillared surfaces, and 6 configurations of sinusoidal patterns. The spatial distribution of droplets on both flat and textured substrates are studied using Fry plot and Ripley's K directional methods as well. Moreover, a method for studying the size distribution function of small droplets is proposed by modifying the method of Abu-Orabi for the unit surface.

The results show acceptable accordance between the models proposed and respective experimental data. Also regarding spatial distribution, the initial small droplets are distributed completely randomly, while the coalescing drops forms in the direction of texturing patterns on the substrate.

École Nationale Supérieure des Mines
de Saint-Étienne

NNT : 2018LYSEM018

Solmaz BOROOMANDI-BARATI

Modélisation et simulation de la condensation par gouttelettes sur substrats texturés

Spécialité: Image, Vision, Signal

Mots clefs : Condensation par gouttelette, Modélisation numérique, Gouttelettes ellipsoïdales, Substrat texturé

Résumé :

Le but de cette thèse est de développer un modèle de simulation numérique pour étudier le processus de condensation par gouttelette sur des substrats plats et texturés. La partie expérimentale a été réalisée sur des surfaces de polycarbonate qui ont été dupliquées à partir d'un moule métallique texturé en utilisant la technologie laser. Les échantillons sont montés sur une installation de condensation conçue dans le laboratoire. Les résultats de ces expériences sont des images en échelle de gris qui ont dû être binarisées afin d'obtenir les informations liées au taux de croissance des gouttelettes, à la densité et à la distribution spatiale. Ensuite, trois modèles différents ont été développés au cours de cette thèse pour décrire le comportement des gouttelettes:

1. une méthode classique qui considère les gouttelettes comme des calottes sphériques se développant sur un substrat plat,
2. une méthode qui considère les gouttelettes elliptiques (angle de contact = 90°) en croissance sur les substrats texturés,
3. et une méthode modifiée qui considère les gouttelettes à coiffe ellipsoïdale (angle de contact $\neq 90^\circ$) en croissance sur les substrats texturés.

Les résultats de ces trois méthodes sont validés par comparaison avec des données expérimentales sur une surface plane, 6 configurations différentes de surfaces à piliers et 6 configurations de motifs sinusoïdaux. La distribution spatiale des gouttelettes sur les substrats plats et texturés est étudiée à l'aide des méthodes Fry plot et K directionnel de Ripley. De plus, une méthode pour étudier la fonction de distribution de taille de petites gouttelettes est proposée en modifiant la méthode d'Abu-Orabi pour la surface unitaire.

Les résultats montrent une concordance acceptable entre les modèles proposés et les données expérimentales respectives. Toujours en ce qui concerne la distribution spatiale, les petites gouttelettes initiales sont distribuées de manière complètement aléatoire, tandis que les gouttes coalescentes se forment dans le sens des motifs de texturation sur le substrat.